Theoretical and experimental study of polymer melt dynamics: role of intermolecular dipolar interactions

Dissertation

zur Erlangung des akademischen Grades
Doctor rerum naturalium (Dr. rer. nat)

Vorgelegt dem Rat der
Fakultät für Mathematik und Naturwissenschaften
der Technischen Universität Ilmenau

von

M.Sc. Artur Lozovoi

1. Gutachter: Prof. Dr. rer. nat. habil. Siegfried Stapf
2. Gutachter: Prof. Dr. rer. nat. habil. Jörg Kröger
3. Gutachter: Prof. Dr. rer. nat. habil. Nail Fatkullin

Tag der Einreichung: 18.12.2017
Tag der wissenschaftlichen Aussprachen: 24.01.2018

urn:nbn:de:gbv:ilm1-2018000046

To my parents, Aida and Rudolf

Abstract

In this work dynamics of entangled polymer melts is extensively investigated by means of the novel versatile NMR formalism. Theoretical background for its application is presented and thoroughly discussed. It is thereby demonstrated that regime of the slow anomalous segmental diffusion inherent to the entangled polymer melts in a broad time scale can be probed by analyzing the contributions of the intermolecular dipolar interactions to the build-up functions of a special type. One of them combines the signals from three double-pulse spin-echo NMR pulse sequences and is called the *solid-echo build-up function.* The other one correlates the Hahn echo signals obtained at different time moments and is introduced as the *dipolar-correlation build-up function*. Both of them essentially reflect the features of the dipolar interactions between spins in a system. These interaction are, in turn, sensitive to the local segmental translation and reorientation, thus providing a way to investigate these motions.

The two introduced methods are implemented on the conventional low-field NMR spectrometers as well as on the high-temperature machine assembled in the course of this work. Using this equipment the proposed approach is applied to the study of entangled polybutadiene, poly(ethylene-alt-propylene) and polyethylene oxide melts. Obtained time dependencies of the segmental displacements are found to be in good agreement with the conventional techniques at short times. Moreover, the novel methods are capable of significantly extending the probed range of dynamics both in the time and in the displacement domain, thus providing information on the scale that is hardly accessible to the experimental methods established for the studies of entangled polymer melts. Therefore the introduced approach is considered to be a new powerful tool in the field of polymer physics.

Wide range of information provided by the dipolar-correlation and the solid-echo formalism allows a comprehensive experimental test of the validity of the *tube-reptation model* that is the most commonly used and well-established theoretical description of the entangled polymer melts. Time dependence of the mean squared segmental displacement obtained in poly(ethylene-alt-propylene) is found to be in good agreement with the corresponding predictions of the model. Three distinct power-laws are observed that are attributed to the Rouse, the incoherent and the coherent reptation regimes in the framework of the tube-reptation model. Importantly, the transition from the incoherent to the coherent reptation is reached for the first time in this polymer species of such a high molecular weight. On the other hand, segmental displacements obtained in the set of polyethylene oxide melts of different molecular weights displays no features of the extremely slow $\propto t^{0.25}$ dynamics predicted for the incoherent reptation. This result is consistent and is corroborated by other NMR techniques at shorter and longer times. This finding calls the universal applicability of the tube concept for all the polymer species in question.

Moreover, estimation of the relative contributions of the intra- and the intermolecular dipolar interactions to the transverse relaxation demonstrates similar behavior for all the studied polymer melts. Interestingly, this behavior is in contradiction with the prediction of the tube-reptation model and demonstrates no features expected for the highly anisotropic motion within the fictitious tube. The consistency of this result in all the samples investigated in this work allows one to raise an even more general question about the validity of the whole concept of the tube-reptation model.

Zusammenfassung

In dieser Arbeit wird die Dynamik verschränkter Polymerschmelzen mittels eines neuartigen vielseitigen NMR-Formalismus umfassend untersucht. Der theoretische Hintergrund für seine Anwendung wird vorgestellt und ausführlich diskutiert. Es wird gezeigt, dass das Regime der langsamen anomalen segmentalen Diffusion, die den verschränkten Polymerschmelzen in einem breiten Zeitraum innewohnt, durch Analyse der Beiträge der intermolekularen dipolaren Wechselwirkungen zu speziellen Varianten von Aufbaufunktionen untersucht werden kann. Einer von ihnen kombiniert die Signale von drei Doppelpuls-Spin-Echo-NMR-Impulsfolgen und wird als *Solid-echo Build-up Funktion* bezeichnet. Der andere korreliert die Hahn-Echosignale, die zu verschiedenen Zeitpunkten erhalten werden, und wird als *Dipolar-correlation Build-up* Funktion eingeführt. Beide spiegeln im Wesentlichen die Eigenschaften dipolarer Wechselwirkungen zwischen Spins in einem System wider. Diese Wechselwirkung ist wiederum empfindlich gegenüber der lokalen segmentalen Translation und Reorientierung, was eine Möglichkeit bietet, diese Bewegungen zu untersuchen.

Die beiden vorgestellten Methoden werden auf den konventionellen Niederfeld-NMR-Spektrometern und auch auf der im Rahmen dieser Arbeit aufgebauten Hochtemperatureinheit eingesetzt. Unter Verwendung dieser Ausrüstung wird der vorgeschlagene Ansatz auf die Untersuchung von Polybutadien, Poly(ethylen-alt-propylen) und Polyethylenoxidschmelzen angewendet. Die gefundene Zeitabhängigkeit der Segmentverschiebungen stimmt mit den Resultaten konventioneller Techniken bei kurzen Zeiten gut überein. Darüberhinaus sind die neuen Methoden geeignet, den untersuchten Dynamikbereich sowohl in der Zeit- als auch in der Verschiebungsdomäne signifikant zu erweitern und damit Informationen zu liefern, die für andere experimentelle Methoden kaum zugänglich sind. Daher wird der vorgestellte Ansatz als ein neues leistungsfähiges Werkzeug auf dem Gebiet der Polymerphysik angesehen.

Die breite Palette von Informationen, die durch den Dipolar-correlation und den Solid-echo Formalismus geliefert werden, erlaubt einen umfassenden experimentellen Test der Gültigkeit des *Tube-Reptation-Modells*, das die am häufigsten verwendete und wohletablierte theoretische Beschreibung der verschränkten Polymerschmelzen ist. Die Zeitabhängigkeit der Segmentverschiebung, die in Poly(ethylen-alt-propylen) erhalten wurde, stimmt gut mit den entsprechenden Vorhersagen des Modells überein. Es werden drei verschiedene Potenzgesetze beobachtet, die im Rahmen des Tube-Reptationsmodells dem Rouse-, den inkohärenten und den kohärenten Reptationsregimen zugeschrieben werden. Wichtig ist, dass der Übergang von der inkohärenten zur kohärenten Reptation bei dieser Polymerspezies mit einem so hohen Molekulargewicht zum ersten Mal experimentell beschrieben wird. Auf der anderen Seite zeigen Segmentverschiebungen, die in den Polyethylenoxidschmelzen mit unterschiedlichen Molekulargewichten erhalten werden, keine Merkmale der extrem langsamen $\propto t^{0.25}$ Dynamik, die für die inkohärente Reptation vorhergesagt wurde. Dieses Ergebnis ist konsistent und wird durch andere NMR-Techniken bei kürzeren und längeren Zeiten bestätigt. Dieser Befund stellt die universelle Anwendbarkeit des Konzepts der Röhre für alle weiteren Polymerspezies in Frage.

Darüber hinaus zeigt die Abschätzung der relativen Beiträge der intra- und intermolekularen dipolaren Wechselwirkungen zur transversalen Relaxation ein ähnliches Verhalten für alle untersuchten Polymerschmelzen. Interessanterweise steht dieses Verhalten im Widerspruch zur Vorhersage des Tube-Repation-Modells und zeigt keine Merkmale, die für die hoch anisotrope Bewegung innerhalb der fiktiven Röhre erwartet werden. Die Übereinstimmung dieses Ergebnisses in allen Proben lässt eine noch allgemeinere Frage nach der Gültigkeit des gesamten Konzeptes des Tube-Reptationsmodells aufkommen.

Table of Contents

Introduction

Natural polymeric materials, cotton and rubber, have been known and used by people since thousands of years and already in XIX century first experiments involving modification of properties of natural polymers, such as vulcanization of rubber with sulfur, were conducted. However, basic structure of this type of matter was not well understood until works of Staudinger in 1920s [1], who proposed the idea of covalently bond carbon chains and introduced the very concept of a *macromolecule*. Since then the field of polymer physics and chemistry has emerged and been featured by a lot of outstanding scientists, including Nobel prize winners: Paul J. Flory [4,5], Pierre-Gilles de Gennes [16,40] and Hermann Staudinger himself. However, in spite of the extensive research in this field, the significant advances in synthesizing artificial polymeric materials and their wide abundance in every area of human's life, there are still questions remaining unanswered. Among them is a problem of theoretical description of dynamics of polymeric liquids, or polymer melts. Their behavior is essentially different from simple liquids due to extreme lengths inherent to macromolecular chains. Each macromolecule possesses high number of internal degrees of freedom and is subject to interactions with a lot more neighbors than in the case of small molecules in a liquid state or in solids. Under these conditions exact calculation of all the interactions is practically impossible, however, use of statistical description of conformation and dynamics of a macromolecule is extremely beneficial, allowing to tackle the problem in a comparably simpler way. *Chapter 1* of this work is devoted to the overview of the theoretical models that are used today for this purpose: starting from a concept of the *ideal chain* and its equilibrium conformation to the sophisticated models of dynamics of entangled polymer melts. Derivations of the most important features and predictions for experimentally measurable quantities are given.

The main focus is set onto the so-called *tube-reptation model* that is based on the assumption that motion of a long macromolecule in a polymer melt, which is subject to entanglements, is effectively restricted by surrounding chains. This restriction is represented by a fictitious tube that is a core ansatz of this formalism. Tube-reptation model is the most widely used theoretical description of entangled polymer melt dynamics. Its predictions for the macroscopic melt's characteristics explain a lot of experimental results with a good precision. However, there is a number of controversies associated with the use of this model connected both with the variance of some of the predictions with the experimental findings, as well as with the criticism of the employed tube-existence assumption. These points are addressed in *Chapter 1* and generally throughout the work. One of the aims of the current research is to experimentally test the validity of the tube-reptation model. So what are the instruments that one can use to study polymer dynamics?

Today a wide range of different techniques is conventionally employed to obtain information about both structure and dynamics of polymers, ranging from scattering experiments (X-ray, neutron, light etc.) to rheological methods (viscosity, mechanical relaxation etc.). Investigation of translational dynamics in viscous polymer systems can be done with only few of these approaches. Their brief overview and comparison is given in *Chapter 3.5*. One of them and possibly the most versatile one is *nuclear magnetic resonance* (NMR). *Chapter 2* is devoted to a comprehensive description of this phenomenon and of its connection to microscopic segmental dynamics in a polymer melt. Actually, NMR spin relaxation reflects fluctuations of local magnetic fields that are caused by dipolar interactions between spins and are modulated by their thermal motion. Therefore investigation of the dipolar interactions in a polymer melt by means of NMR relaxometry has been for decades serving as a powerful tool for probing segmental dynamics.

However, the latest theoretical findings concerning the character of the dipolar interactions, which are summarized in the beginning of *Chapter 3*, demonstrate that their behavior is more complicated than it has been assumed before. Intermolecular and intramolecular dipolar interactions are shown to generally possess different time dependencies. Moreover, behavior of their ratio reflects the character of the motion in a system: isotropic or anisotropic. This provides an opportunity to check the validity of the tube concept in real polymer systems. Apart from that, investigation of the intermolecular dipolar interactions, which are almost exclusively modulated by the translational motion of the corresponding spins, can provide information about segment diffusion of macromolecules.

Chapter 3 is thus mostly devoted to the introduction and the thorough development of two novel methods based on NMR spin-spin relaxation. They imply an experimental construction of *solid-echo* and *dipolar-correlation build-up functions*. It is mathematically shown that these methods are capable of providing information about mean squared displacement of segments belonging to different macromolecules, or translation segmental diffusion, from the intermolecular contribution to the respective build-up functions. Comparison shows that the introduced approaches directly probe the time scale of polymer dynamics that is inaccessible to other conventional techniques that are suitable for studying segmental diffusion. The next step is application of these novel methods in real systems.

Although the developed techniques do not demand for the sophisticated hardware, NMR spectrometer capable of reaching high temperatures (up to $150°C$) is necessary in order to extend the time range of the probed segmental dynamics. Due to unavailability of such a device at the moment of this work, a new NMR spectrometer based on the accessible equipment is assembled. It is specifically suited for the high-temperature experiments. In *Chapter 4.1* its design and characteristics are described.

Experimental results are presented in *Chapter 4.2, 4.3* and *4.4.* Method based on the dipolar-correlation build-up function is first applied in highly entangled polybutadiene melts. The obtained results on the segmental diffusion are shown to be in good agreement with literature data, thereby confirming theoretical formalism of *Chapter 3*. Both of the introduced methods are then used to extensively study highly entangled poly(ethylene-alt-propylene) and polyethylene oxide melts. Whereas the probed segmental displacements coincide well with several other techniques in the overlapping time regimes, the approach described in this work allows to extend the accessible time scale by several decades. Part of the results actually corroborates well with the predictions of the tube-reptation model. At the same time, some crucial characteristics, such as time evolution of the inter- and the intramolecular dipolar interactions, are shown to be in contradiction with the corresponding model predictions, calling in question the validity of the tube concept. Detailed discussion of these findings from the point of view of NMR and polymer dynamics is presented in the end of *Chapter 4.*

Chapter 1. Properties of Polymers

Polymers are a class of soft matter objects that are defined as large macromolecules, consisting of repeating chemical blocks (based usually on atoms of carbon *C* or silicon *Si*) called *monomeric units*, which are connected with each other through covalent bonds. The number of monomers *N* is a degree of a polymerization of a macromolecule and can typically vary from ~100 up to ~10^6-10^9 units. A polymer chain can consist of a same repeating monomer, as polyethylene $[-CH_2 - CH_2-]_N$ or polyisoprene ("natural rubber") $[-CH_2 - CH = C(CH_3) - CH_2 -]_N$, then it is called *homopolymer*. Alternatively, a chain can be formed from a mixture of different monomers – *copolymer*. Typical examples are proteins – biomacromolecules, which consist of a particular sequence of amino acids and play a crucial role in the processes taking place in the human body. Further on, the monomers can be connected one-by-one forming a linear backbone allowing only for short sidechains and such a structure is known as *linear polymer*. In the case of the long sidechains a macromolecule is called *branched polymer*. Apart from that, polymer chains are differentiated on the basis of their flexibility, with extreme cases being a flexible *freely jointed chain* (to be discussed in *Chapter 1.2*) and a *rod-like chain*, which are illustrated in Figure 1.1. From now on, in this work all the theoretical description will be carried out for the case of linear flexible homopolymers.

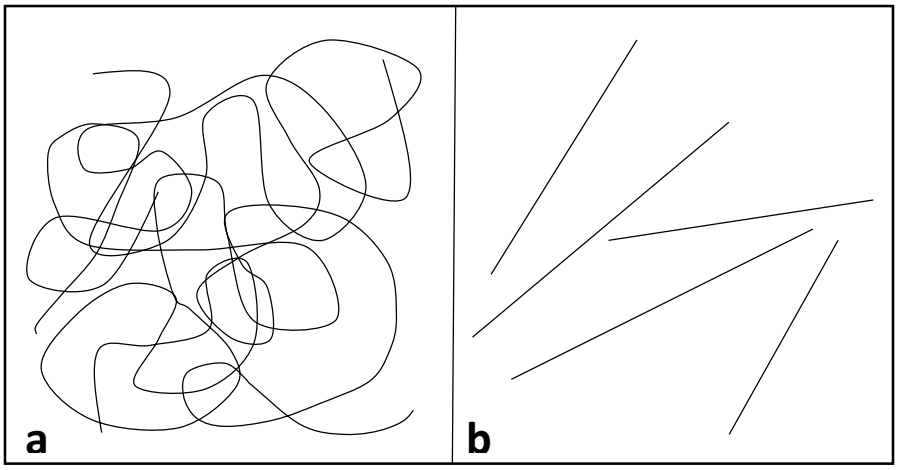

Figure 1.1. An illustrative sketch of an ensemble of freely jointed chains (a) and rod-like chains (b).

Among typical features of polymers is existence of the so-called *critical molecular weight* M_c, which was introduced on the basis of rheological experiments in melts of different polymer species. Evidently, molecular weight dependence of zero-shear macroscopic viscosity splits into two regions: $\propto M$ for low molecular weights and $\propto M^{3.4}$ for higher M [5,8]. This behavior is universal for flexible polymers. The molecular weight corresponding to the transition was named a critical molecular weight, it usually comprises several hundreds of monomer units [8,12]. As will be shown in *Chapter 1.5* this phenomenon is related to the occurrence of entanglements arising from the uncrossability of the long chains in polymer melts.

Analysis of a large assembly of atoms and chemical bonds occurring already in one macromolecule is usually performed based on a statistical description of its properties. In comparison, in the case of small molecules such an approach is only applicable to the ensemble comprising a high number of the

molecules. From the other side, huge length of polymer chains leads to a large number of available conformations, increasing with the degree of polymerization N as $\sim 3^N$, and a broad range of characteristic correlation times, varying from very fast local processes up to long-living correlations on the scale of the whole macromolecule. Under these circumstances, transitions between different conformations do not require a lot of energy, for instance, rotation around a chemical bond takes place already at room temperature. These crucial features determine unique properties of polymers, such as viscoelasticity and flexibility.

In addition to that, due to their size, macromolecules in any kind of media experience interactions with an extremely high number of neighboring molecules, e.g. solvent or other macromolecules, and it is reasonable to assume that these interactions are independent from each other and one can speak about a mean effect of the surrounding on the chain. This aspect significantly simplifies seemingly incalculable problem of the long chain's dynamics and interaction with the surrounding. This approach applied together with the statistical description of polymers, leads to an important outcome – macroscopic features of the long chains can be deduced independently from the detailed microstructure on the monomer level. The well-established way of describing the polymer molecule in this manner is realized through a *coarse-grained chain description*, which implies packing all the subsegmental properties of the macromolecule into one characteristic parameter – *Kuhn segment length*. Principles of this approach are explained and applied to investigation of chain's equilibrium conformation in *Chapter 1.1* and *1.2*.

Interestingly, despite of the apparent ideality of the formulated problem, predictions obtained on this basis are shown to be in good agreement with experimental findings. These results serve as an important starting point for extending the theory from equilibrium to dynamical problems. In Chapter 1.3 the most well-established model, namely Rouse model, is explicitly described. It is well confirmed experimentally and is commonly accepted as a fundamental model for polymer dynamics. In *Chapter 1.4, 1.5* and *1.6* substantial modifications of Rouse model adapted to real chains and entangled polymer melts are described. It will be shown throughout this *Chapter* that the majority of the important features of macromolecular conformation and dynamics bears universal character and depends mostly on the length of the chain and the Kuhn segment length, which comprises its microstructural properties.

1.1 Ideal chain

Consider a simple model of a single chain, which is subject to no external forces, with a backbone consisting of *n* chemical bonds, each of which is characterized by the length l_0 and by the corresponding molecular weight m_0. Curvilinear, or contour, length of this chain is equal to $L = nl_0$ and its overall molecular weight is $M = nm_0$. The coarse-grained description of this chain can be introduced through its splitting into *N* segments, containing the same number of chemical bonds. Each segment k is described by the position-vector of its beginning $\vec{R}_{k-1}$ and its end $\vec{R}_k$, consequently, the end-to-end vector of the segment is equal to $\vec{r}_k = \vec{R}_k - \vec{R}_{k-1}$. The end and the beginning of the whole chain are characterized by the position vectors $\vec{R}_0$ and $\vec{R}_N$, respectively. Segments are freely jointed meaning that free rotation relative to each other is permitted. The sketch of the chain described in this way and its segment's microstructure are illustrated in Figure 1.2.

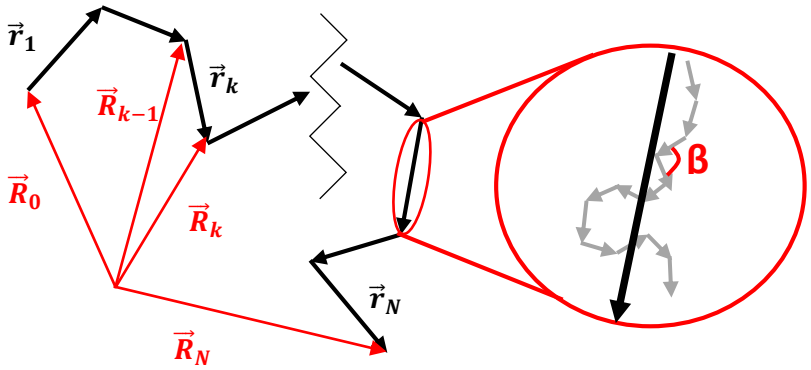

Figure 1.2. Coarse-grained representation of the chain.

Division of the macromolecular chain into the artificial segments $\{\vec{r}_1 \dots \vec{r}_N\}$ containing several backbone chemical bonds was first proposed by Werner Kuhn [1,3] and since then serves as a basis for a coarse-grained statistical description of the chain. The merit of this approach lies in the fact that all the stereochemical details (bond lengths and angles, rotation potential energies etc.) of the Kuhn segment structure can be packed into one parameter – Kuhn segment length b, given by:

$$b = \sqrt{\langle \vec{r}_i^2 \rangle} \ , \tag{1.1}$$

where the average is taken over all the segments in the chain. This assumption is justified if the length of the Kuhn segment is sufficiently large and it contains just enough chemical bonds, so that it is possible to assume no correlation between different Kuhn segments:

$$\langle \vec{r}_i \cdot \vec{r}_j \rangle = \delta_{ij} b^2 \ . \tag{1.2}$$

δ_{ij} is a Kronecker symbol, which is equal to 0 for $i \neq j$ and to 1 for $i = j$, and the average is taken over all the possible conformations. Although the interactions between the Kuhn segments are neglected in this consideration, there is a condition for their linear connectivity (end of $\vec{r}_i$ is attached to the beginning of $\vec{r}_{i+1}$ and so on). A chain defined in this way is usually called *random-walk model.* Thus, the macromolecule comprising n chemical bonds l_0 is now replaced by its coarse-grained representation, consisting of *N* Kuhn

segments b, which comprises a random sequence of rotational isomers (trans, gauche$^-$, gauche$^+$). As a next step, relevant properties of this chain should be examined.

Flory radius.

Important quantity describing the conformation of the macromolecule is its end-to-end vector, called *Flory radius* $\vec{R}_F$ [4,5]. Due to the fact that all the orientations of Kuhn segments are equally probable and are not correlated, the mean value of the Flory radius taken over all the conformations is $\langle \vec{R}_F \rangle = 0$. Therefore, it is more interesting to look at its mean squared value $\langle \vec{R}_F^2 \rangle$. To begin with, it is important to know the probability density $W(\vec{R}, N)$ of the chain's Flory radius being equal to $\vec{R}$. For the random-walk model this distribution is given by [5,17]:

$$W(\vec{R}, N) = \frac{1}{\left(\frac{2\pi}{3} N b^2\right)^{3/2}} exp\left(-\frac{3R^2}{2Nb^2}\right) \tag{1.3}$$

Using eq. (1.3) it is possible to calculate the mean squared value of the Flory radius:

$$\langle \vec{R}_F^2 \rangle = \int W(\vec{R}, N) \vec{R}^2 \, d^3\vec{R} = \frac{1}{\left(\frac{2\pi}{3} N b^2\right)^{\frac{3}{2}}} \int exp\left(-\frac{3R^2}{2Nb^2}\right) \vec{R}^2 \, d^3\vec{R} =$$

$$= \frac{1}{\left(\frac{2\pi}{3} N b^2\right)^{3/2}} \iiint exp\left(-\frac{3r^2}{2Nb^2}\right) \rho^4 \sin(\theta) \, d\rho d\varphi d\theta = \frac{8Nb^2}{3\sqrt{\pi}} \int_0^\infty e^{-x^2} x^4 dx = Nb^2 \tag{1.4}$$

Contour length L in this case can be rewritten as:

$$L = n l_0 = Nb \tag{1.5}$$

It is necessary to point out, that the calculation of the Flory radius according to eq. (1.4) implies the probability of it being larger than the contour length, which cannot occur in a real chain. However, in the limit of long chains $N \gg 1$, the deviations caused by this assumption are very small and the obtained result is valid with a good precision [6,7]. Since the contour length of the macromolecule can be calculated based on the knowledge of the chemical bonds' length and valence angles, and the Flory radius can be obtained from the experiment with the use of rheology [5,8], light [9], neutron [10] or X-ray scattering [11] techniques, combination of eq. (1.4) and eq. (1.5) provides a way to calculate the value of the Kuhn segment length as:

$$b = \frac{\langle \vec{R}_F^2 \rangle}{L} \tag{1.6}$$

The following parameter can be introduced:

$$C_N = \frac{\langle \vec{R}_F^2 \rangle}{n l_o^2} \tag{1.7}$$

It is called *characteristic ratio* and, as follows from its name, is peculiar for each polymer species, depending on the details of the local segment structure. In the limit of long chains $N \to \infty$ its value reaches the plateau and is denoted as C_∞. Equations (1.6) and (1.7) yield the connection between the Kuhn segment length, the chemical bond length and the characteristic ratio for a given polymer:

$$C_\infty = \frac{b}{l_0} \tag{1.8}$$

Higher values of the characteristic ratio correspond to the longer Kuhn segments, which means that correlations between the chemical bonds are preserved for the longer distances, thereby increasing the stiffness of the chain. For a freely jointed chain with no correlation between chemical bond orientations $C_\infty = 1$. For flexible chains C_∞ is usually in the range of 4-12. Typical values of C_∞ and b for different polymers can be found in literature [5,12,13].

It should be mentioned that equation (1.3) for the distribution of the chain's end-to-end vector is rather general and for high numbers of Kuhn segments $N \to \infty$ always approaches Gaussian statistics irrespectively of the probability density of Kuhn segment length $w(\vec{r})$: only its second moment $b^2 = \langle r^2 \rangle$ affects $W(\vec{R}, N)$.

Gaussian chain.

Consider the so-called *Gaussian chain*, which is characterized by the Gaussian distribution of the Kuhn segment length:

$$w(\vec{r}) = \frac{1}{\left(\frac{2\pi}{3}b^2\right)^{3/2}} exp\left(-\frac{3r^2}{2b^2}\right) \quad (1.9)$$

Effectively this model can be illustrated by $(N+1)$ beads sequentially connected by harmonic springs. A chain described in this way possesses a crucial property – vector $\vec{R}_n - \vec{R}_m$ connecting any two segments n and m is subject to the Gaussian distribution as well:

$$W(\vec{R}_n - \vec{R}_m) = \frac{1}{\left(\frac{2\pi}{3}|n-m|b^2\right)^{3/2}} exp\left(-\frac{3(\vec{R}_n - \vec{R}_m)^2}{2|n-m|b^2}\right) \quad (1.10)$$

The mean squared value of the end-to-end vector $\vec{R}_n - \vec{R}_m$ is

$$\langle (\vec{R}_n - \vec{R}_m)^2 \rangle = |n-m|b^2 \quad (1.11)$$

Thus, conformation of the coarse-grained flexible chain consisting of independent Kuhn segments, which is subject to no external constraints, is characterized by the Flory radius $|\bar{R}_F| = N^{1/2}b$. Conformation possessing these properties is called *random coil*. In contrast to a fully stretched conformation, orientation of each chemical bond in the random coil is equally probable and, therefore, the chain represents a sequence of the randomly oriented Kuhn segments, which reduces the value of its end-to-end vector: one can imagine this effect as the chain coiling.

Gyration radius.

In some cases, when it is not possible to define the Flory radius, such as in branched polymers, it is better to characterize the size of the macromolecule through its *radius of gyration* R_g, which is a root mean-squared distance from each segment to the macromolecule's center of mass averaged over all the conformations. It can be written in the form of:

$$R_g = \sqrt{\frac{1}{N}\sum_{i=1}^{N} \langle (\vec{R}_i - \vec{R}_{cm})^2 \rangle}, \quad (1.10)$$

where $\vec{R}_{cm} = \frac{1}{N}\sum_{i=1}^{N} \vec{R}_i$ is a center-of-mass position vector and $\vec{R}_i$ is the position vector of the ith segment. Consideration of eq. (1.9) and employing the property of the random coil to have Gaussian distribution of any end-to-end vector $\vec{R}_{nk}$ connecting the nth and the kth Kuhn segments [5], yields the following relation for the radius of gyration:

$$R_g^2 = \frac{R_F^2}{6} \quad (1.11)$$

Value of R_g^2, as will be shown in *Chapter 1.2-1.5*, plays an essential role in estimation of the segmental mean squared displacement (MSD) caused by the internal degrees of freedom of the macromolecule at a long-time limit.

Freely rotating chain.

Other models have been developed to describe the behavior of the ideal chain. For instance, *freely rotating chain* [14]. It consists of N chemical bonds of the same length with the fixed bond angle β (see Fig. 1.2), which results in the correlation between the neighboring segments (in contrast to a freely jointed chain):

$$\langle \vec{r}_i \vec{r}_{i+k} \rangle = {l_0}^2 (cos\beta)^k \quad (1.12)$$

All the isomeric conformations are assumed to be equally probable, thereby allowing for a free rotation around each chemical bond. Calculation of the Flory radius for this chain yields:

$$\langle \vec{R}_F^2 \rangle_{f.r.} = N {l_0}^2 \frac{1+cos\beta}{1-cos\beta} \quad (1.13)$$

Consequently, its characteristic ratio is equal to $C_\infty = \frac{1+cos\beta}{1-cos\beta}$.

Worm-like chain.

Alternative description can be given on the basis of *the worm-like chain model* [15]. Consider a chain consisting of N rigid rods with a length l_r. Contour length of this chain is $L = Nl_r$. Two points k and l on it are determined by their curvilinear coordinates $s_k = kl_r$ and $s_l = ll_r$ and their position vectors $\vec{R}(s_k)$ and $\vec{R}(s_l)$. Tangential unit vector at the corresponding position is the given by:

$$\vec{u}(s_k) = \frac{\partial \vec{R}(s_k)}{\partial s_k} \quad (1.14)$$

The correlation function of this tangential vector is assumed to be:

$$G(s_k, s_l) = \langle \vec{u}(s_k) \cdot \vec{u}(s_l) \rangle = \langle cos(\alpha_r) \rangle^{|k-l|}, \quad (1.15)$$

where $\langle cos(\alpha_r) \rangle$ is an average cosine of the angle between the two consecutive rods. This persistence of the chain manifests itself through this mean value (for a freely jointed chain it would be equal to zero). Further on, the correlation function $G(s_k, s_l)$ can be rewritten as:

$$G(s_k, s_l) = \langle cos(\alpha_r) \rangle^{|k-l|} = exp(|k-l| ln\langle cos(\alpha_r) \rangle) = exp\left(-\frac{|s_k - s_l|}{l_p}\right) \quad (1.16)$$

l_p is a parameter characterizing stiffness of the chain, called *persistence length*: $l_p = -\frac{l_r}{ln\langle cos(\alpha_r) \rangle}$. The mean squared value of the Flory radius in this case can be calculated from eq. (1.15) and (1.16):

$$\langle \vec{R}_F^2 \rangle_{pers.} = \iint_0^L ds_k ds_l \, \langle \vec{u}(s_k) \cdot \vec{u}(s_l) \rangle = 2Ll_p - 2{l_p}^2 \left(1 - exp\left(-\frac{L}{l_p}\right)\right) \quad (1.17)$$

In the limit of long flexible chains $N, \frac{L}{l_p} \to \infty$:

$$\langle \vec{R}_F^2 \rangle_{pers.} \approx 2Ll_p \quad (1.18)$$

Comparison of eq. (1.18) with eq. (1.4), given that the contour length of the chain is $L = Nb$, leads to a following connection between the persistence length and the Kuhn segment length:

$$b = 2l_p \quad (1.19)$$

Up to this point, all the models used for the description of polymer chain's conformation allowed for overlapping of the chain segments, which cannot take place in the real conditions. In the next paragraph this restriction is going to be considered. Nevertheless, it should be mentioned that scaling laws for the size of a polymer chain derived on the basis of the abovementioned model are remarkably close to the reality, given simplicity and ideality of the proposed picture. These results serve as a good starting point for further more complicated considerations of real chain's conformation.

1.2 Excluded volume effect

Consider a freely jointed chain consisting of N segments, which obeys a random-walk statistics as it was described previously. The probability of a given segment to cross another segment of the chain is rather small, however, as N increases, which is a point of interest in the case of a long polymer chain, this probability becomes sufficiently high to affect the macroscopical properties of the macromolecule's conformation, such as its Flory radius. When the segments approach each other they become subjected to attractive Van der Waals and repulsive Pauli and Coulomb interactions, which form a certain potential, describing the interaction between different segments. This interaction depends on the distance between them and is of a short-range nature in terms of the spatial separation, but for the curvilinear coordinates along the chain it effectively is long-range (Figure 1.3). Occurrence of the additional restrictions imposed by prohibition of self-crossing of the segments results in the increase of random coil's Flory radius [4,5,14].

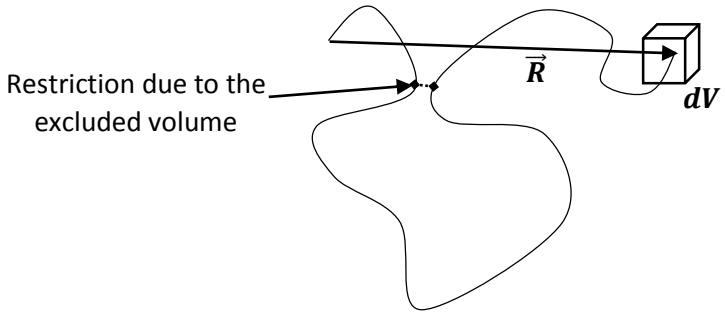

Figure 1.3. Illustration of the excluded volume effect

This problem can be treated on the basis of the Helmholtz free energy of a chain with the Flory radius $\vec{R}$. It can be written as:

$$A_H(\vec{R}) = U - TS, \tag{1.20}$$

where U is the internal energy, T is the temperature and S is the conformational entropy of the chain. The latter is given by:

$$S = k_b ln\left(\Omega(\vec{R})\right), \tag{1.21}$$

where k_b is a Boltzmann constant, $\Omega(\vec{R})$ is a number of the chain's conformations possible for a given end-to-end vector $\vec{R}$, corresponding to microstates of the system, which macrostate is set by $\vec{R}$. $\Omega(\vec{R})$ is proportional to the probability of the end-to-end vector to be pointing into the elementary volume element dV (see Figure 1.3). In the case of the Gaussian chain of the Kuhn segments the probability density is given by eq. (1.3) and $\Omega(\vec{R})$ can be written as:

$$\Omega(\vec{R}) \propto W(\vec{R}, N)dV = \frac{1}{\left(\frac{2\pi}{3}Nb^2\right)^{3/2}} exp\left(-\frac{3R^2}{2Nb^2}\right) dV \tag{1.22}$$

Consequently, expression for the entropy becomes:

$$S \propto k_b \frac{dV}{\left(\frac{2\pi}{3}Nb^2\right)^{3/2}} - k_b \frac{3R^2}{2Nb^2} = const - k_b \frac{3R^2}{2Nb^2} \tag{1.23}$$

The first term of this expression does not depend on $\vec{R}$ and therefore is denoted as a constant.

Consider now the first term in eq. (1.20) connected with the internal energy U. The repulsive interaction between two segments of the chain becomes effective when they both occur in the volume element δV, which can accommodate only two segments. The probability of finding exactly two Kuhn segments in this volume is equal to $\omega = \left(N\frac{\delta V}{V}\right)^2$, where V is the volume of the random coil and is connected with its Flory radius through a numerical coefficient: $V = \gamma\left|\vec{R}\right|^3$. The number of the Kuhn segment pairs interacting with each other, N_{pair}, is proportional to the probability ω and to the number of the volume segments $\frac{V}{\delta V}$:

$$N_{pair} = \omega\frac{V}{\delta V} = N^2\frac{\delta V}{V} \tag{1.24}$$

Mean contribution to the internal energy U of a pair of the interacting Kuhn segments is proportional to k_bT through a numerical factor α. Thus, combining eq. (1.20), (1.23) and (1.24), one can derive the following expression for the Helmholtz free energy:

$$A_H\left(\vec{R}\right) = \alpha k_bTN^2\frac{\delta V}{V} - const + k_bT\frac{3R^2}{2Nb^2} = k_bT\left(\alpha N^2\frac{\delta V}{\gamma\left|\vec{R}\right|^3} + \frac{3R^2}{2Nb^2} - const\right) \tag{1.25}$$

Flory radius of this chain can be calculated employing the condition of the minimum of Helmholtz free energy: $\frac{\partial A_H\left(\vec{R}\right)}{\partial\left|\vec{R}\right|} = 0$. The result is as follows:

$$\left|\vec{R}_F\right| = \left(\frac{\alpha\delta V}{\gamma}\right)^{\frac{1}{5}} b^{\frac{2}{5}}N^{\frac{3}{5}} \propto N^{\frac{3}{5}} \tag{1.26}$$

This is a very important consequence of the excluded volume effect. Eq. (1.4) for the Flory radius of the ideal chain yields the power law $\left|\vec{R}_F\right| \propto N^{\frac{1}{2}}$ in contrast to eq. (1.26), which means that the conformation of the real polymer chain is described by the larger value of the Flory radius than that of the ideal chain for a given number of segments N. It should be noted that the derivation given here is not exact and is based on the scaling laws, nevertheless, its prediction for the dependence of the Flory radius on N is in agreement with the results of more rigorous calculations, which can be found in literature [16-18]. The exponent close to $\frac{3}{5}$ has been indeed experimentally observed in light scattering studies of polystyrene solutions [19-21].

All the results obtained in *Chapter 1.1* and *1.2*, which are based on different theoretical models, describe an equilibrium average conformation of the polymer chain. Next step in understanding the macromolecule's behavior is to consider its dynamical properties. This problem is generally rather complicated and still today is far from being solved, especially in the case of entangled chains. However, there is a number of well-established polymer dynamics model, important features of which will be described in *Chapters 1.3-1.6*.

1.3 Rouse model

The most fundamental theoretical model of dynamics of a macromolecule in a viscous medium (polymer melt or solution) was first proposed by Kargin and Slonimskii in 1949 [22] and then independently described and established in more detail by Rouse in 1953 [23]. It is based on the coarse-grained consideration of a chain consisting of beads connected with springs (Fig. 1.4) and is commonly called the *Rouse model*.

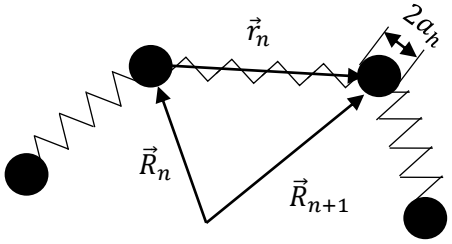

Figure 1.4. Bead-spring representation of a macromolecule in the Rouse model

This model is based on the dynamics of Brownian particles in the medium described by the Langevin equations, which are then generalized for the case of the particles with internal degrees of freedom. Consider a polymer chain consisting of N Kuhn segments. The mass of the chain is concentrated in $(N+1)$ beads on the backbone, characterized by the position vectors $\vec{R}_i$. Generally speaking, this picture is not realistic, since the mass is always distributed over the each Kuhn segment, rather than being localized at the ends. This assumption creates strong deviations of the model predictions from the real dynamics at times $t < \tau_s$, where τ_s is a segmental relaxation time, characterizing local conformational processes on the microlevel within the Kuhn segment. Segmental displacement at this time range is comparable with the Kuhn segment length b. Nevertheless, at longer times $t > \tau_s$, when displacements of the chain segments become much larger than b, the coarse-grained description is justified and, as will be shown further, provides predictions corroborated by the experimental results. It is noted that effects of the excluded volume (*Chapter 1.2*) are not taken into account by the Rouse model.

One can write the second Newton's law for the n^{th} bead:

$$m\ddot{\vec{R}}_n = \vec{F}_n^{intra}(t) + \vec{F}_n^{inter}(t), \tag{1.27}$$

where m is a mass of the each bead, $\vec{F}_n^{intra}$ and $\vec{F}_n^{inter}$ are intramolecular and intermolecular forces experienced by the n^{th} bead.

Intramolecular forces.

Intramolecular interactions between segments are of the entropic character and can be derived on the basis of the potential of mean force similar to the way it was done in *Chapter 1.2* while calculating the effect of the excluded volume, eq. (1.25). The difference is that in the Rouse model the excluded volume interaction is not considered, which means that the internal energy term in eq. (1.20) is equal to zero and the Helmholtz free energy for the current system is written as:

$$A_H(\vec{r}_1..\vec{r}_N) = -TS = -k_bTln\big(\Omega(\vec{r}_1..\vec{r}_N)\big), \tag{1.28}$$

where $\Omega(\vec{r}_1..\vec{r}_N)$ is a probability density of the chain to have a conformation defined by the set of vectors $\vec{r}_i = \vec{R}_{i+1} - \vec{R}_i$ corresponding to N Kuhn segments. Assuming that the chain is ideal, $\Omega(\vec{r}_1..\vec{r}_N)$ can be

represented as a product of the probability density functions $w(\vec{r}_i)$, since the orientations of the different Kuhn segments are not correlated. Then eq. (1.28) is translates to:

$$A_H(\vec{r}_1..\vec{r}_N) = -k_bT\sum_{i=1}^{N} ln\, w(\vec{r}_i) \quad (1.29)$$

The intramolecular force acting on the n^{th} bead is now given by the derivative of eq. (1.29):

$$\vec{F}_n^{intra}(t) = \frac{\partial A_H(\vec{R}_1-\vec{R}_0..\vec{R}_N-\vec{R}_{N-1})}{\partial \vec{R}_n} = -k_bT\sum_{i=1}^{N}\frac{\partial\left(ln\, w(\vec{R}_{i+1}-\vec{R}_i)\right)}{\partial \vec{R}_n} \quad (1.30)$$

Postulating that the probability density of the Kuhn segment $w\left(\vec{R}_{i+1}-\vec{R}_i\right)$ is Gaussian and is given by eq. (1.9) allows exact calculation of the intramolecular force:

$$\vec{F}_n^{intra}(t) = \frac{3k_bT}{b^2}\left(\vec{R}_{n+1}+\vec{R}_{n-1}-2\vec{R}_n\right) \quad (1.31)$$

The 0^{th} and the N^{th} beads have only one neighbor, therefore in this expression $\left(\vec{R}_0-\vec{R}_{-1}\right)$ and $\left(\vec{R}_{N+1}-\vec{R}_N\right)$ are set to be zero for $\vec{F}_0^{intra}$ and $\vec{F}_N^{intra}$ respectively. In the limit of high N, eq. (1.31) can be rewritten with n being a continuous variable:

$$\vec{F}_n^{intra}(t) = \frac{3k_bT}{b^2}\frac{\partial^2\vec{R}_n}{\partial n^2} \quad (1.32)$$

Thus, $\vec{F}_n^{intra}$ is an entropically elastic force acting on the bead n, characterized by the spring constant $K = \frac{3k_bT}{b^2}$.

Intermolecular forces.

Consider now the intermolecular term of eq. (1.27) $\vec{F}_n^{inter}$. It is determined by the contributions from the friction $\vec{F}_n^{fr}$ and the *stochastic Langevin force* $\vec{F}_n^L$, arising from the interaction of the n^{th} bead with the surrounding viscous medium. In accordance with the Stokes' law, the friction force experienced by a sphere moving in a viscous medium is given by:

$$\vec{F}_n^{fr} = -6\pi\eta_{mc}a_h\frac{\partial\vec{R}_n}{\partial t} = -\zeta\frac{\partial\vec{R}_n}{\partial t}, \quad (1.33)$$

where ζ is a segmental friction coefficient, η_{mc} is a microscopic viscosity, which is usually significantly lower than a macroscopic viscosity in polymer melts, a_h is an effective hydrodynamic radius. Stochastic Langevin force $\vec{F}_n^L$ is introduced in order to reflect the complicated random interaction of the Brownian particle with the neighboring solvent molecules. It can be also applied to the system of macromolecules in a melt, because the intermolecular forces considered in the Rouse model are of a short-range nature, acting on the scale of the Kuhn segment length b. This allows describing the interaction of the given Kuhn segment with the neighboring Kuhn segments of surrounding macromolecules, as if each of them was a molecule of a solvent. Stochastic Langevin force is a normal delta-correlated random process, which Cartesian components $\alpha, \beta = x, y, z$ are characterized by the following correlation function:

$$\langle\vec{F}_{n\alpha}^L(|t_2-t_1|)\vec{F}_{k\beta}^L(0)\rangle = 2k_bT\zeta\delta_{nk}\delta_{\alpha\beta}\delta(t_2-t_1) \quad (1.34)$$

Rouse equation of motion and normal modes.

After these considerations it is possible to rewrite the equation of motion (1.27) for the n^{th} bead as:

$$m\ddot{\vec{R}}_n = \frac{3k_bT}{b^2}\frac{\partial^2\vec{R}_n}{\partial n^2} - \zeta\frac{\partial\vec{R}_n}{\partial t} + \vec{F}_n^L(t) \quad (1.35)$$

This equation has a characteristic time constant $t = \frac{m}{\zeta}\sim 10^{-13}s$ for the typical values of the Kuhn segment mass m and the segmental friction coefficient ζ in real polymer melts. This characteristic time corresponds to the timescale of atomic tumbling, where the inertial term on the left-hand side of eq. (1.35) is playing an important role. However, at longer times accelerated motion becomes extremely

improbable due to the high density of the atoms in soft matter materials (such as polymers). Consequently, the inertial term $m\ddot{\vec{R}}_n$ becomes negligible, transforming the equation to the following form:

$$\frac{\partial \vec{R}_n}{\partial t} = \frac{3k_bT}{\zeta b^2}\frac{\partial^2 \vec{R}_n}{\partial n^2} + \frac{1}{\zeta}\vec{F}_n^L(t) \tag{1.36}$$

Together with the border conditions $\left.\frac{\partial \vec{R}_n}{\partial t}\right|_{n=0,N} = 0$, set of eq. (1.36) for all the segments of the chain is known as *Rouse equations* of motion. It can be shown, using methods of quantum mechanics [24], that $\vec{R}_n$ can be written in the form of a series of eigenfunctions $cos\left(\frac{\pi p}{N}n\right)$ with coefficients $\vec{X}_p(t)$:

$$\vec{R}_n(t) = \vec{X}_0(t) + \sum_{p=1}^{N}\vec{X}_p(t)cos\left(\frac{\pi p}{N}n\right), \tag{1.37}$$

where $\vec{X}_p(t)$ are the so-called *Rouse normal coordinates* or *normal modes* defined as:

$$\vec{X}_p(t) = \frac{1}{N}\int_0^N cos\left(\frac{\pi p}{N}n\right)\vec{R}_n dn \tag{1.38}$$

There is no correlation between the Rouse modes with different numbers p - they are orthogonal. Rouse equations of motion (1.36) can now be formulated for the normal coordinates:

$$\frac{d}{dt}\vec{X}_p(t) = -\frac{3\pi^2 k_bT}{\zeta b^2}\vec{X}_p(t) + \frac{1}{\zeta}\vec{F}_p^L(t), \tag{1.39}$$

where $\vec{F}_p^L(t) = \frac{1}{N}\int_0^N cos\left(\frac{\pi p}{N}n\right)\vec{F}_n^L dn$ is a Fourier transformation of the stochastic Langevin force. Furthermore, it is possible to write eq. (1.39) for the correlation function of the normal coordinates as:

$$\frac{d\langle \vec{X}_p(t)\vec{X}_q(0)\rangle}{dt} = -\frac{1}{\tau_p}\langle \vec{X}_p(t)\vec{X}_q(0)\rangle \tag{1.40}$$

Unlike the original form of the equation of motion for the position vectors $\vec{R}_n$, eq. (1.40) can be easily solved exactly and the result is

$$\langle \vec{X}_p(t)\vec{X}_q(0)\rangle = \langle \vec{X}_p(0)\vec{X}_q(0)\rangle exp\left(-\frac{t}{\tau_p}\right) = \frac{Nb^2}{2\pi^2 p^2}\delta_{pq}exp\left(-\frac{t}{\tau_p}\right) \tag{1.41}$$

This evolution of the correlation functions in time describes independent relaxation of the Rouse modes, characterized by the set of relaxation times:

$$\tau_p = \frac{\zeta b^2}{3\pi^2 k_bT}\left(\frac{N}{p}\right)^2 = \tau_s\left(\frac{N}{p}\right)^2, \tag{1.42}$$

where τ_s is the segmental relaxation time that was introduced before. It actually is the shortest Rouse relaxation time corresponding to the mode $p = N$ in the current representation. Mode number $p = 1$ is relaxing with the longest characteristic time $\tau_R = \tau_1 = \tau_s N^2$, usually called *Rouse or terminal relaxation time*. It should be noted, that according to eq. (1.42) the relaxation time of the mode $p = 0$ is infinite. However, this apparent divergence can be explained. Note, that the definition of $\vec{X}_p(t)$ in eq. (1.38) implies that $\vec{X}_0(t) = \frac{1}{N}\int_0^N \vec{R}_n dn$, which is a position vector $\vec{R}_{cm}$ of the macromolecule's center of mass, written in the continuous form. Therefore, 0^{th} mode corresponds to the translational motion of the center of mass and is not subject to the relaxation process. The fluctuations connected with the Rouse modes can be thought of as deformations of the chain on a different scale, starting with a Kuhn segment for $p = N$ up to the symmetrical fluctuations of the two halves of the chain with the fixed center for $p = 1$. These processes are illustrated in Figure 1.5, where eq. (1.37) is used to plot chain deformations described by the different Rouse modes.

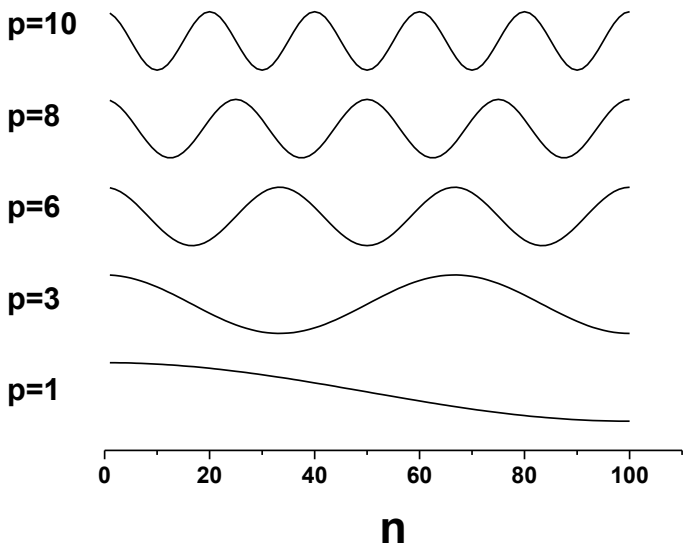

Figure 1.5. Chain deformations corresponding to the Rouse modes $p = 1, 3, 6, 8, 10$; n is an index of a Kuhn segment.

Thus, motion of a Kuhn segment in terms of the Rouse model is described by the superposition of Rouse modes. As a next step, some of the important properties resulting from this theoretical consideration are derived.

Tangent vector's orientation

Orientation of the Kuhn segments of the chain can be described through the correlation function $\langle \vec{b}_n(t)\vec{b}_n(0)\rangle$, where $\vec{b}_n = \frac{\partial \vec{R}_n}{\partial n}$ is a tangent end-to-end vector of the n^{th} Kuhn segment. Differentiating eq. (1.37) leads to the following expression for the segment orientation's correlation function:

$$\langle \vec{b}_n(t)\vec{b}_n(0)\rangle = \frac{b^2}{N}\sum_{p=1}^{N} exp\left(-\frac{t}{\tau_p}\right) = \begin{cases} \frac{\sqrt{\pi}}{2} b^2 \left(\frac{\tau_s}{t}\right)^{1/2}, & \tau_s \ll t \ll \tau_R \quad \text{(I)} \\ \frac{b^2}{N} exp\left(-\frac{t}{\tau_R}\right), & t \gg \tau_R \quad \text{(II)} \end{cases} \tag{1.43}$$

Time limit $t \ll \tau_s$ is not considered here, since the predictions of the coarse-grained Rouse model do not hold at the scale comparable or less than a Kuhn segment length b. Equations (1.42) are important for the determination of the frequency dependence (dispersion) of the intrasegment *spin-lattice relaxation rate* $\frac{1}{T_1}$ obtained in the *nuclear magnetic resonance* (NMR) experiments. Relationship between the orientational correlation function of a Kuhn segment and the spin-lattice relaxation rate will be discussed in detail in *Chapter 2.3*. For the moment, only the final result is given:

$$\frac{1}{T_1} \propto \begin{cases} -\tau_s ln(\omega\tau_s), & \frac{1}{\tau_R} \ll \frac{\omega}{2\pi} \ll \frac{1}{\tau_s} \quad \text{(I)} \\ \tau_s lnN, & \frac{\omega}{2\pi} \ll \frac{1}{\tau_R} \quad \text{(II)} \end{cases} \tag{1.44}$$

Frequency ω here corresponds to $\frac{\omega}{2\pi} = \frac{1}{t}$. Regime I of the $\frac{1}{T_1}$ dispersion is characterized by the logarithmic frequency dependence, whereas regime II predicts the frequency-independent plateau, which however depends on the length or, equivalently, the molecular weight of the chain. Both regimes I and II were observed experimentally in polymer melts with the molecular weights $M < M_c$ and in diluted polymer systems even for $M \gg M_c$ [25-30]. It should be mentioned that the Rouse dynamics is preserved in entangled polymer melts as well at the time scale, when thr segments do not sense restrictions imposed by the entanglements. It will be discussed in *Chapter 1.4* and *1.5.*

Segmental mean squared displacement.

The next point of interest is calculation of the mean squared displacement of Kuhn segments $\langle\left(\vec{R}_n(t) - \vec{R}_n(0)\right)^2\rangle$ as predicted by the Rouse model. For this purpose, expansion of $\vec{R}_n(t)$ given by eq. (1.37) is employed:

$$\langle\left(\vec{R}_n(t) - \vec{R}_n(0)\right)^2\rangle = \langle\left(\vec{X}_0(t) - \vec{X}_0(0)\right)^2\rangle + 4\sum_{p=1}^{N} cos^2\left(\frac{\pi p n}{N}\right)\langle\left(\vec{X}_p(t) - \vec{X}_p(0)\right)^2\rangle \quad (1.45)$$

The first term here is connected with the translational motion of the center of mass. Using eq. (1.34) and 1.39) it can be expressed as:

$$\langle\left(\vec{X}_0(t) - \vec{X}_0(0)\right)^2\rangle = \frac{6k_bT}{N\zeta}t = 6D_{cm}t \quad (1.46)$$

The second term of eq. (1.45) represents the motion of the Kuhn segments relatively to the center of mass and can be calculated using eq. (1.41). Then eq. (1.45) transforms to:

$$\langle\left(\vec{R}_n(t) - \vec{R}_n(0)\right)^2\rangle = 6Dt + 2\frac{Nb^2}{\pi^2}\sum_{p=1}^{N}\frac{1-exp\left(-\frac{tp^2}{N^2\tau_s}\right)}{p^2} = \begin{cases} \frac{2}{\pi^{3/2}}b^2\left(\frac{t}{\tau_s}\right)^{1/2}, \tau_s \ll t \ll \tau_R & \text{(I)} \\ 6D_{cm}t + \frac{Nb^2}{3}, \quad t \gg \tau_R & \text{(II)} \end{cases} \quad (1.47)$$

Again two time-limits of dynamics are distinguished. Note that the second term in expression (1.47) for regime II is actually connected with the radius of gyration, introduced in *Chapter 1.2*, $\frac{Nb^2}{3} = 2R_g^2$. Macromolecule in this regime undergoes normal diffusion with a diffusion coefficient of the center of mass depending on the chain length as $D_{cm} \propto N^{-1}$. Experimental study with the use of pulsed field-gradient NMR in polyethylene and polystyrene melts below the critical molecular weight $M < M_c$ confirmed this model prediction after additional consideration of the free volume connected with the chain-end dynamics [31].

Predictions of the Rouse model hold well for the non-entangled polymer melts, however, the model fails to describe correctly dynamics of macromolecules in dilute solutions and in entangled melts. The reason for the latter is that the effects of excluded volume are not considered in the Rouse model, resulting in overestimation of macromolecule's diffusion in an entangled melt. Theoretical approaches tackling this issue are presented in *Chapter 1.5-1.6*. On the other hand, hydrodynamic interactions, which are neglected in the Rouse model as well, play a crucial role when a macromolecule is moving in a solvent leading. This leads to strong deviations of the experimental results from the model predictions. The way to account for the hydrodynamic effects is presented in the next paragraph.

1.4 Zimm model

Hydrodynamic interactions between segments of a diluted macromolecule manifest themselves through a viscous drag, which facilitates a long-range effect of the given segment's motion on the dynamics of the other segments through the molecules of a solvent. Here a few words should be said about a conformation of a chain in a solvent. Excluded volume interactions, described in *Chapter 1.2*, should be in this case compared with the solvent-segment interactions. Their relative contributions depend on the type of solvent and strongly affect the conformation of the macromolecule. Generally, the Flory radius of the chain in a solvent can be written as:

$$R_F^2 = \alpha^2 N b^2, \tag{1.48}$$

where α is a temperature and molecular weight dependent swelling coefficient. At a certain temperature for a particular solvent condition $\alpha = 1$ can be achieved, which means that the excluded volume effect is exactly compensated by segment-solvent interactions and conformation of a macromolecule corresponds to the ideal chain (eq. 1.4). Such a condition is called θ-temperature and the solvent is, accordingly, called θ-solvent [4,32,33]. If $\alpha > 1$ the solvent is "good" and the chain's conformation is extended, being ultimately described by eq. (1.26), if $\alpha < 1$ the solvent is "poor" and the chain tends to form a globule. In this paragraph only dynamics of macromolecules in θ-solvents is discussed.

A model considering long-range hydrodynamic interactions in diluted polymer solutions was proposed by Zimm in 1956 [34]. The chain of N segments connecting $N + 1$ beads is considered, as in *Chapter 1.3* for the Rouse model. However, an additional force accounting for the hydrodynamic interactions is introduced. The second Newton's law for the n^{th} bead can be written without the inertial term in the following way:

$$\vec{F}_n^{intra}(t) + \vec{F}_n^{hydro}(t) + \vec{F}_n^{L}(t) = 0, \tag{1.49}$$

where $\vec{F}_n^{intra}(t)$ is an entropically elastic force given by eq. (1.31), $\vec{F}_n^{hydro}$ is a hydrodynamic force associated with the molecules of the solvent and $\vec{F}_n^{L}(t)$ is a stochastic Langevin force. According to the third Newton's law the bead is also acting on the solvent with the force, which has the same magnitude, but the opposite direction – $\vec{F}_n^{hydro}(t)$. This causes a flow of the solvent that affects other segments of the chain. Consequently, the hydrodynamic force experienced by the n^{th} bead consists of contributions from all the other beads, creating the viscous drag mentioned before. Velocity of the n^{th} bead acquired due to these interactions is given by:

$$\frac{d\vec{R}_n}{dt} = \sum_{k\neq n}\langle H_{\alpha\beta}(\vec{R}_{nk})\rangle\left(-\vec{F}_k^{hydro}(t)\right) = \sum_{k\neq n}\langle H_{\alpha\beta}(\vec{R}_{nk})\rangle\left(\vec{F}_k^{intra}(t) + \vec{F}_k^{L}(t)\right) \tag{1.50}$$

where summation is made over all the beads of the chain, $\langle H_{\alpha\beta}(\vec{R}_{nk})\rangle = \frac{\delta_{\alpha\beta}}{6\pi\eta}\langle\frac{1}{\vec{R}_{nk}}\rangle$ is a preaveraged Oseen tensor [35] with η being a viscosity of the solvent and $\vec{R}_{nk}$ – a vector connecting the beads n and k. Assuming the Gaussian chain, eq. (1.11) for $\vec{R}_{nk}$ can be employed. Then combination of eq. (1.49) and (1.50) yields the following equation of motion:

$$\frac{d\vec{R}_n}{dt} = \frac{3k_bT}{\sqrt{6\pi^3}\eta b^3}\sum_{k\neq n}\frac{1}{|n-k|^{1/2}}\left(\vec{R}_{k+1}(t) + \vec{R}_{k-1}(t) - 2\vec{R}_k(t) + \frac{b^2}{3k_bT}\vec{F}_k^{L}(t)\right) \tag{1.51}$$

Following the same approach as described in *Chapter 1.3* for the Rouse model, the border conditions are applied, $(\vec{R}_0 - \vec{R}_{-1}) = (\vec{R}_{N+1} - \vec{R}_N) = 0$, and n is treated as a continuous variable in the limit of long chains $N \gg 1$. Consequently, eq. (1.51) can be rewritten as:

$$\begin{cases} \frac{\partial \vec{R}_n}{\partial t} = \frac{3k_bT}{\sqrt{6\pi^3}\eta b^3}\int_0^N \frac{dk}{|n-k|^{1/2}}\left(\frac{\partial^2 \vec{R}_k}{\partial k^2} + \frac{b^2}{3k_bT}\vec{F}_k^L(t)\right) \\ \left.\frac{\partial \vec{R}_n}{\partial t}\right|_{n=0,N} = 0 \end{cases} \quad (1.52)$$

Using the Rouse-coordinate representation according to eq. (1.37) and following the same formalism, one obtains an equation of motion for the correlation function of the Rouse normal modes:

$$\langle \vec{X}_p(t)\vec{X}_q(0)\rangle = \langle \vec{X}_p(0)\vec{X}_q(0)\rangle exp\left(-\frac{t}{\tau_p^z}\right) = \frac{Nb^2}{2\pi^2p^2}\delta_{pq}exp\left(-\frac{t}{\tau_p^z}\right), \quad (1.53)$$

where $\tau_p^z = \tau_s^z\left(\frac{N}{p}\right)^{3/2}$ is the p^{th} Rouse mode's relaxation time and $\tau_s^z = \frac{\eta b^3}{\sqrt{3\pi}k_bT}$ is the segmental relaxation time. Thus, the terminal relaxation time in the Zimm model is characterized by a weaker chain length dependence $\tau_1^z \propto N^{3/2}$ than in the Rouse model ($\tau_1^R \propto N^2$).

Segmental mean squared displacement.

In the similar manner as in *Chapter 1.3*, the following predictions for the segmental mean squared displacement can be derived:

$$\left\langle\left(\vec{R}_n(t) - \vec{R}_n(0)\right)^2\right\rangle = \begin{cases} \frac{3}{\pi^2}\Gamma\left(\frac{1}{3}\right)b^2\left(\frac{t}{\tau_s^z}\right)^{\frac{1}{2}} & , \quad \tau_s^z \ll t \ll \tau_1^z \quad \text{(I)} \\ \frac{8k_bT}{3\sqrt{6\pi^3}\eta b N^{\frac{1}{2}}} + \frac{Nb^2}{3} = 6D_{cm}^z t + 2R_g^2 & , \quad t \gg \tau_1^z \quad \text{(II)} \end{cases} \quad (1.54)$$

Center-of-mass diffusion coefficient in the Zimm model has a weaker molecular weight dependence $D_{cm}^z \propto N^{-\frac{1}{2}}$ than in the Rouse model (eq. 1.46) $D_{cm}^R \propto N^{-1}$. This is an important feature, which has been experimentally observed with the use of dynamic light scattering in polystyrene diluted in θ-solvent [36,37]. Predictions for the scaling laws of the center-of-mass diffusion coefficient and the terminal relaxation time, eq. (1.53) and (1.54), suggest enhanced mobility due to the hydrodynamic interactions.

Tangent vector's orientation.

Calculation of the orientational correlation function for the tangential end-to-end vector of the Kuhn segment $\langle \vec{b}_n(t)\vec{b}_n(0)\rangle$ yields the following result:

$$\langle \vec{b}_n(t)\vec{b}_n(0)\rangle = \frac{b^2}{N}\sum_{p=1}^N exp\left(-\frac{t}{\tau_p^z}\right), \quad (1.55)$$

which following the same philosophy as for the Rouse model leads to two time limits:

$$\langle \vec{b}_n(t)\vec{b}_n(0)\rangle = \begin{cases} \frac{2}{3}\Gamma\left(\frac{2}{3}\right)b^2\left(\frac{\tau_s^z}{t}\right)^{2/3}, & \tau_s^z \ll t \ll \tau_1^z \quad \text{(I)} \\ \frac{b^2}{N}exp\left(-\frac{t}{\tau_1^z}\right) & , \quad t \gg \tau_1^z \quad \text{(II)} \end{cases} \quad (1.56)$$

The Zimm model successfully explains experimental results obtained in dilute polymer solutions in the case of θ-solvents by taking into account the long-range hydrodynamic interactions between the chain segments in addition to the Rouse formalism, approaching it in the limit of 100% concentration. In the next paragraphs dynamics of entangled polymer melts ($M > M_c$) will be considered and it will be shown that even though the Rouse model does not account for the entanglement effects, it can nevertheless serve as a valid basis for developing more elaborate models.

1.5 Entangled polymer melt. Tube-reptation model

Polymer chains in a molten state at high molecular weights $M > M_c$, tend to entangle, as was mentioned in *Chapter 1.1*. It is possible to roughly estimate M_e, molecular weight of a macromolecule, at which an entanglement occurs, based on a simple spatial consideration [38]. Assume that a macromolecule with a molecular weight M occupies a volume effectively given by a sphere of its radius of gyration. Employing eq. (1.4), (1.7) and (1.11) this volume is written as:

$$V^{eff} = \frac{4\pi}{3} R_g^3 = \frac{4\pi}{3} \left(\frac{6 C_\infty M l_0^2}{m_0} \right)^{\frac{3}{2}}, \tag{1.57}$$

where C_∞ is the characteristic ratio, l_0 is a length of a chemical bond and m_0 is a mass per chemical bond. Number of the identical macromolecules that can be packed into this volume is $N = \frac{\rho V^{eff} N_a}{M}$, where N_a is Avogadro number and ρ is the polymer's density. It is assumed that the entanglement takes place if $N = 2$. Using this condition together with eq. (1.57) allows estimation of the corresponding molecular weight M_e:

$$M_e = \left(\frac{m_0}{6 \left(\frac{2\pi}{3} \right)^{\frac{2}{3}} C_\infty l_0^2 \rho^{\frac{2}{3}} N_a^{\frac{2}{3}}} \right)^3 \tag{1.58}$$

It is noted, that this is only an illustrative simplified consideration and generally M_e is determined from the mechanical relaxation experiments and is related to the value of plateau shear modulus [17], which is observed in entangled polymer melts similar to permanently cross-linked systems. M_e is then described as a *molecular weight between entanglements* and is empirically connected to the critical molecular weight M_c as: $M_c = 1.4 \dots 3.5 M_e$ [13]. $N_e = \frac{M_e}{m_K}$ is a characteristic number of the Kuhn segments between the entanglements (m_K is a molecular weight of the Kuhn segment).

Segmental dynamics in the presence of the entanglements becomes sufficiently slowed down as compared to the Rouse model predictions, due to the restrictions superimposed by the surrounding macromolecules. In 1967 Edwards [39] treated this problem in the case of a tagged chain in a fixed network and calculated the free energy of such a system, as applied to rubber materials. A substantial step to better understanding of this phenomenon was made by de Gennes in 1971 [40]. He proposed the idea, that surrounding macromolecules form a tube, thereby creating a confinement for a tagged chain. Due to this, motion of the chain becomes highly anisotropic and represents *reptation*, which is similar to a creep along the tube. This problem was treated by de Gennes in the framework of the curvilinear diffusion of non-interacting defects of the tagged chain in the presence of the fixed obstacles. The proposed system is illustrated in Figure 1.7. This formalism allowed deriving important scaling laws for the center-of-mass diffusion coefficient and the terminal relaxation time: $D_{cm} \propto M^{-2}$, $\tau_1 \propto M^3$. These relations suggest significantly slower dynamics in entangled polymer melts than predicted by eq. (1.46) and (1.42) by the Rouse model.

Concept of the tube, curvilinear coordinates.

Extension of de Gennes' approach to polymer melts by taking into account the motion of the surrounding network was carried out by Doi and Edwards [17,41]. They distinguished several characteristic time limits, known as *Doi/Edwards limits*, which separate regimes of segmental dynamics. Consider a chain consisting of N Kuhn segments with length b. Its ends can be connected by a so-called *primitive chain, or primitive path* (dashed line in Figure 1.7), which bears the topology of the chain relative

to the tube. The motion of the chain at short times consists of wriggling around the primitive path, at longer times, however, the conformation of the primitive chain can change. The primitive chain itself is characterized by a contour length L. Position of its segment is then given by a curvilinear coordinate s and a position vector $\vec{R}(s)$. The primitive chain's conformation is described by the Gaussian statistics (eq. (1.10) and (1.11)) and it can move only back and forth along its own contour with a certain diffusion coefficient D_c, which essentially reflects reptative mechanism of the macromolecule's motion. As a consequence of the Gaussian statistics, the following relation for the two points s_1 and s_2 on the primitive chain holds:

$$\langle \vec{R}(s_1) - \vec{R}(s_2) \rangle^2 = a|s_1 - s_2|, \tag{1.59}$$

where a is a *step length* of the primitive chain, which is of the same order as the tube diameter $a \approx d_t$. From the connection of the experimentally measured value of the plateau shear modulus [8] with d_t and M_e the relation for the tube diameter is

$$d_t \cong \left(\frac{M_e}{M} N b^2\right)^{\frac{1}{2}} = N_e^{1/2} b, \tag{1.60}$$

which is equal to the Flory radius of the chain consisting of N_e Kuhn segments.

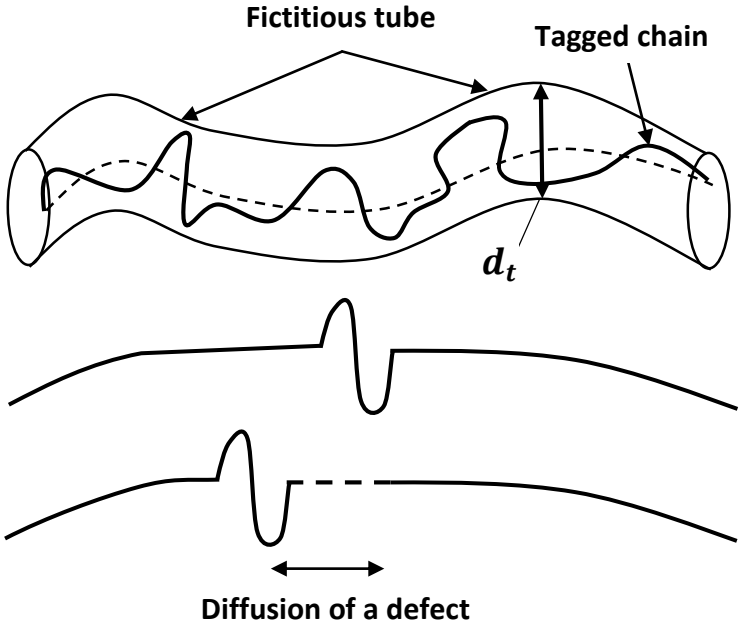

Figure 1.7 Sketch of a tagged chain confined in a fictitious tube of diameter d_t formed by surrounding macromolecules in a melt (dashed line represents a primitive chain). Below is a concept of a defect curvilinear diffusion along the chain in the tube, which causes reptation according to de Gennes [40].

Rouse dynamics $\tau_s < t < \tau_e$.

As the coarse-grained representation of the macromolecule is used, again dynamics on the scale of Kuhn segment and less, at times $t < \tau_s$ is not considered. When the displacement of the chain segments are small and the chain does not feel the constraints of the tube, dynamics is described by the Rouse model:

$$\left\langle \left(\vec{R}_n(t) - \vec{R}_n(0) \right)^2 \right\rangle \cong b^2 \left(\frac{t}{\tau_s}\right)^{1/2} \tag{1.61}$$

The time, at which the tube starts to impact the dynamics of the chain, is called the *entanglement time* τ_e. It can be estimated from eq. (1.61) as the time, at which the spatial displacement of the chain is of same order as the tube diameter d_t. Together with the use of eq. (1.60) it yields:

$$\tau_e \cong \tau_s N_e^2 \tag{1.62}$$

This characteristic time can be thought of as the Rouse relaxation time of a chain consisting of N_e Kuhn segments. The orientation correlation function of the tangent vector $\langle \vec{b}_n(t)\vec{b}_n(0)\rangle$ and the frequency dispersion of the intrasegment spin-lattice relaxation rate are given by eq. (1.43) and (1.44):

$$\langle \vec{b}_n(t)\vec{b}_n(0)\rangle = \frac{\sqrt{\pi}}{2} b^2 \left(\frac{\tau_s}{t}\right)^{1/2} \quad , \qquad \frac{1}{T_1} = -\tau_s ln(\omega\tau_s) \tag{1.63}$$

Reptation $\tau_e < t < \tau_d$.

At times $t > \tau_e$ motion of the chain perpendicular to the primitive path becomes restricted, whereas the reptative mobility along the tube is preserved. To describe segmental dynamics at this time range, the Rouse equations for the curvilinear coordinates s_n of $N+1$ beads have to be written:

$$\frac{\partial s_n}{\partial t} = \frac{3k_bT}{\zeta b^2}\frac{\partial^2 s_n}{\partial n^2} + \frac{1}{\zeta} f_n^L(t) \tag{1.64}$$

The only difference is the fact that the average value $\langle s_N - s_0\rangle = L$, unlike $\langle \vec{R}_N - \vec{R}_0\rangle = 0$ in the Rouse model. This modifies the border conditions at $n = 0$ and $n = N$, resulting in:

$$\left.\frac{\partial\langle s_n\rangle}{\partial n}\right|_{n=0,N} = \frac{L}{N} \tag{1.65}$$

Set of equations (1.64) with the conditions (1.65) is resolved in the terms of the normal modes as in *Chapter 1.3*. s_n can be then written as:

$$s_n(t) = X_0'(t) + 2\sum_{p=1}^{\infty} X_p'(t) cos\left(\frac{\pi p}{N} n\right) + \frac{nL}{N}, \tag{1.66}$$

where:

$$X_p'(t) = \frac{1}{N}\int_0^N cos\left(\frac{\pi p}{N} n\right)\left(s_n(t) - \frac{nL}{N}\right) dn \tag{1.67}$$

Analogously to the Rouse model, $X_0'(t)$ corresponds to the center of mass, but is defined in the curvilinear coordinates: $X_0'(t) = \frac{1}{N}\int_0^N s_n(t) dn$. Following the same formalism, the equation of motion for the correlation function of the normal modes is expressed as:

$$\langle X_p'(t)X_q'(0)\rangle = \langle X_p'(0)X_q'(0)\rangle exp\left(-\frac{tp^2}{\tau_R}\right) = \frac{Nb^2}{6\pi^2 p^2}\delta_{pq} exp\left(-\frac{tp^2}{\tau_R}\right) \tag{1.68}$$

Segmental curvilinear mean-squared displacement is then characterized by two regimes:

$$\langle (s_n(t) - s_n(0))^2\rangle \propto \begin{cases} \left(\frac{k_bTb^2t}{\zeta}\right)^{1/2}, & t \ll \tau_R \\ \frac{2k_bT}{N\zeta} t \quad , & t \gg \tau_R \end{cases} \tag{1.69}$$

According to eq. (1.59) the three-dimensional mean squared displacement is given by:

$$\langle (R_n(t) - R_n(0))^2\rangle = a|s_1 - s_2| \cong a\langle \left(s_n(t) - s_n(0)\right)^2\rangle^{\frac{1}{2}} \propto \begin{cases} a\left(\frac{k_bTb^2t}{\zeta}\right)^{1/4}, & t \ll \tau_R \\ a\left(\frac{2k_bT}{N\zeta} t\right)^{½}, & t \gg \tau_R \end{cases} \tag{1.70}$$

The Rouse relaxation time $\tau_R = \frac{\zeta b^2 N^2}{3\pi^2 k_bT}$ marks the transition from the regime of the so-called *incoherent reptation* to the regime of the *coherent reptation.* Power law $t^{1/4}$ in the regime of incoherent reptation, which was predicted by de Gennes [40] as well, represents a very peculiar type of the restricted anisotropic motion described by the Rouse modes for the curvilinear coordinates, with eq. (1.59) setting

the tube constraint. This motion is molecular weight independent, which underlines its local character. Due to an extremely low mobility of the chain in this regime, it is quite hard to observe it experimentally. However, the transition towards the exponent close to ¼ was measured by neutron spin echo [48] and novel transverse relaxation based methods [49] in poly(ethylene-alt-propylene), and by field-cycling NMR relaxometry in poly(ethylene-alt-propylene), polybutadiene and polydimethylsiloxane [50,51]. On the other hand, results obtained in polyethylene oxide show no signs of $t^{1/4}$ proportionality of the segmental MSD [52,53]. This will be discussed in detail in *Chapter 4*. The intrasegment spin-lattice relaxation rate is predicted to be proportional to: $\frac{1}{T_1} \propto \omega^{3/4}$ [40,54]. Such a frequency dispersion has never been observed in polymer melts, however, molecular dynamics simulations [55] and field-cycling NMR measurements [56] showed that this type of frequency dependence indeed occurs in polymer melts confined in pores of the diameter comparable to the charcteristic tube diameter d_t. It is necessary to underline, that this apparent controversy between the experimental results for segmental MSD and spin-lattice relaxation rate is connected with the significant contribution of the intermolecular dipolar interaction, consideration of which will be the focus of *Chapter* 3.

Normal diffusion $t > \tau_d$.

Coherent reptation at times $t \gg \tau_R$ is essentially a collective motion of the segments along the tube, which is described as a curvilinear normal diffusion with the diffusion coefficient $D_c = \frac{k_b T}{N\zeta}$ (eq. 1.69). Once the chain has diffused on a distance of the primitive chain's contour length L in the curvilinear coordinates, it means that the macromolecule has left the initial tube. The time interval, at which this condition is fulfilled is called *tube disengagement time* τ_d. Using eq. (1.59) and the fact that the end-to-end vectors of the tagged and the primitive chains are equal, it is possible to write: $L = \frac{Nb^2}{d_t}$. Then, τ_d can be estimated from the one-dimensional diffusion equation as:

$$\tau_d = \frac{L^2}{2D_c} \propto \frac{N^3}{N_e}\tau_s \tag{1.70}$$

As was pointed out by de Gennes, this characteristic time scales with the molecular weight in the manner close to that of the terminal relaxation time. Experimental results suggest exponent in the range 3…3.7 [8,42,43]. Frequency dependence of the intrasegment spin-lattice relaxation rate is: $\frac{1}{T_1} \propto N^{-1/2}\omega^{1/2}$ [54].

At times $t \gg \tau_d$ the macromolecule is released from the constraint and its motion becomes isotropic. Its center-of-mass diffusion coefficient D_{cm}^{tr}can be estimated from the condition that at the time moment τ_d the displacement in three-dimensional space should be equal to the Flory radius of the chain (it corresponds to the displacement L in one-dimensional curvilinear diffusion):

$$D_{cm}^{tr} = \frac{R_F^2}{6\tau_d} = \frac{Nb^2}{6\tau_d} \propto N^{-2} \tag{1.71}$$

This is a very important consequence of the tube-reptation model, which differs essentially from the Rouse model prediction ($D_{cm}^{R} \propto N^{-1}$). This molecular weight dependence was found in entangled polymer melts a number of times with the use of different techniques: infrared microdensitometry [44], field-gradient NMR [31,45,46], small-angle neutron scattering [47].

It is noted, that after the tube disengagement time $t \gg \tau_d$ all the correlations with the initial conformation are lost and the intrasegment spin-lattice relaxation rate $\frac{1}{T_1}$ becomes frequency independent, which corresponds to the so-called *extreme-narrowing limit* ($\omega\tau_d \ll 1$).

Summary.

The abovementioned considerations sum up the main mechanisms of chain dynamics in the framework of the tube-reptation formalism. Additional features were developed later on, which helped to explain some variance of the experimental results from the model predictions. For instance, accounting for the thermal fluctuation of the primitive chain's contour length [17,57] slightly modifies the molecular weight dependence of the center-of-mass diffusion coefficient and of the terminal relaxation time. In addition to that, conformational change of the tube due to the reptation of the surrounding chains affects the motion in the reptation regime and is considered through the so-called constraint release [58,59].

Predictions of the tube-reptation model for the segmental mean squared displacement and intrasegment spin-lattice relaxation rate with the characteristic times and distances are summarized in Figures 1.8 and 1.9. It is important to emphasize, that even though the tube-reptation model predicts the macroscopic observables well (viscosity, shear modulus, center-of-mass diffusion etc.), the microscopic features of polymer dynamics, which are mostly accessible by NMR and at certain conditions by neutron spin echo techniques (due to the extremely slow mobility and the long characteristic times), are not entirely in consistency with the theoretical outcome. A special attention will be paid to this issue throughout this work, corroborated by experimental results in *Chapter 4.*

More rigorous derivation of all the expressions and the detailed discussions of the additional features and of the limits of applicability of the tube-reptation formalism can be found in textbooks [16,17,18,60]. In the next paragraph another approach for the description of polymer dynamics in the presence of the entanglements, based on a memory function formalism, will be presented.

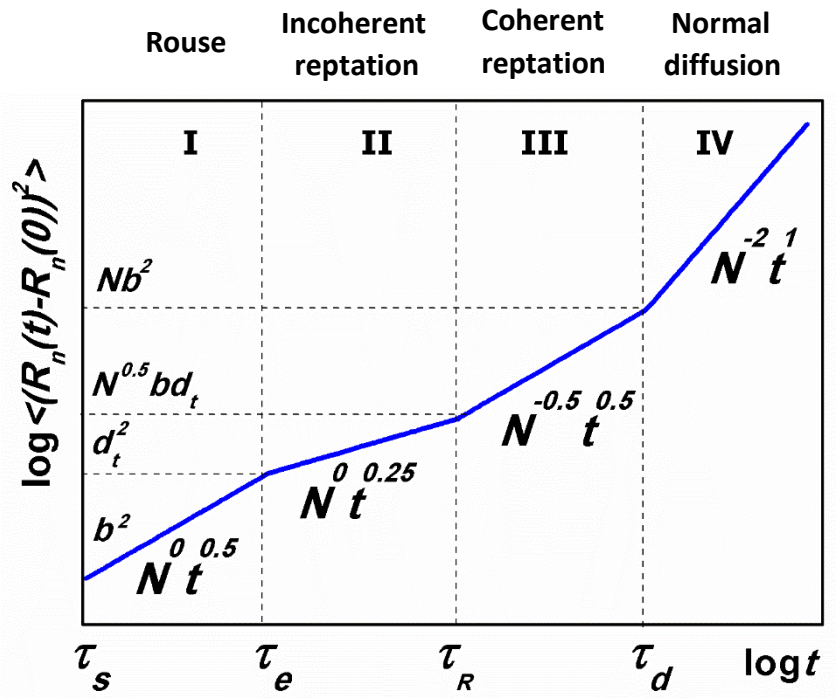

Figure 1.8 Segmental mean squared displacement as a function of time as predicted by the tube-reptation model with the characteristic time constants and displacements. N is a number of Kuhn segments in a chain, corresponding to its molecular weight.

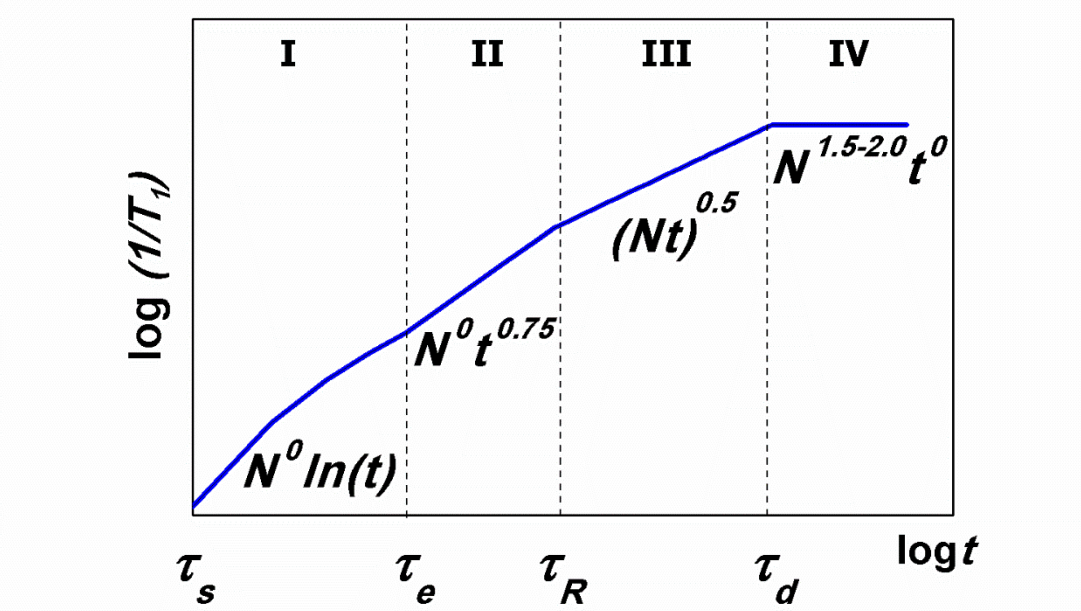

Figure 1.9 Intrasegment spin-lattice relaxation rate as a function of time as predicted by the tube-reptation model with the characteristic time constants. N is a number of Kuhn segments in a chain, corresponding to its molecular weight.

1.6 Entangled polymer melt. Renormalized Rouse model

Despite the ability to explain a lot of the experimental results, introduction of the tube as a physical representation of entanglements in polymer melts remains the most prominent disadvantage of the underlying formalism of the tube-reptation model. The derivations presented in the previous paragraph cannot be traced back to the microscopic level without the assumption being made about the nature of the entanglements. Therefore, demand for such a fundamental formalism is still high in the field of polymer dynamics. One of the alternative ways aimed to fulfill this goal was proposed by Schweizer [61,62]. It is based on the formulation of the *generalized Langevin equations* using the Mori-Zwanzig projection operator [63,64] for the Rouse-like polymer chain (*Chapter 1.3*). In this theoretical formalism no assumptions are made about the character of the entanglements, their effect manifests itself through the uncrossability of the chains. Intramolecular interactions are introduced through the potential of mean force, as was done previously in *Chapter 1.4* and *1.5.* The main challenge is determination of the memory matrix, which includes the intermolecular interactions bearing information about the entanglements.

The approximate form of the generalized Langevin equation for the n^{th} segment of the Gaussian chain, consisting of N Kuhn segments, with a position vector $\vec{r}_n$ is given by:

$$\frac{\partial^2 \vec{r}_n}{\partial t^2} = 0 = -\frac{\partial}{\partial \vec{r}_n} W(\vec{r}_n) - \sum_{k=1}^{N} \int_0^t d\tau \Lambda_{nk}(t-\tau) \frac{d\vec{r}_k(\tau)}{d\tau} + \vec{F}_n^Q(t) \tag{1.72}$$

Here $W(\vec{r}_n)$ is a potential of mean force, $\Lambda_{nk}(\tau, t-\tau) = \frac{1}{k_b T}\langle \vec{F}_n^Q(0)\vec{F}_k^Q(\tau)\rangle$ is the memory matrix, $\vec{F}_n^Q$ is a microscopic projected random force acting on the n^{th} segment of the chain. The inertial term is again neglected. Assuming that the local friction is described by the constant ζ and the intermolecular forces are represented by the fully repulsive interactions of hard spheres, the potential of mean force and the memory matrix can be rewritten as:

$$W(\vec{r}_n) = \frac{3k_bT}{2b^2}\sum_{i=1}^{N}(\vec{r}_i - \vec{r}_{i+1})^2 \quad , \quad \Lambda_{nk}(\tau, t-\tau) = \zeta\delta_{nk}\delta(\tau) + \frac{1}{k_bT}\langle \vec{F}_n^Q(0)\vec{F}_k^Q(\tau)\rangle \tag{1.73}$$

Then eq. (1.72) can be transformed to the expression similar to the Rouse equations of motion (eq. (1.36)) in the continuous representation:

$$0 = -\frac{3k_bT}{2b^2}\frac{\partial^2}{\partial n^2}\vec{r}_n - \zeta\frac{d\vec{r}_k(t)}{d\tau} - \frac{1}{k_bT}\sum_{k=1}^{N}\int_0^t d\tau \langle \vec{F}_n^Q(0)\vec{F}_k^Q(\tau)\rangle \ \frac{d\vec{r}_k(\tau)}{d\tau} + \vec{F}_n^Q(t) \tag{1.74}$$

At this point the problem lies in the calculation of the unknown correlation function $\langle \vec{F}_n^Q(0)\vec{F}_k^Q(\tau)\rangle$. In [61] it was shown that this function is connected with the projected segmental mean squared displacement $\langle\left(\vec{R}(t) - \vec{R}(0)\right)^2\rangle_Q$. The idea of the renormalization is to set this quantity to be equal to the segmental MSD predicted by the Rouse model in eq. (1.47). Then, eq. (1.74) can be resolved in terms of the Rouse normal modes. Details of this calculation can be found in [61,65]. In principle, renormalization can be done infinite number of times by assigning the segmental MSD predicted by $(n-1)^{\text{th}}$ renormalization to the projected MSD in the equation of motion for n^{th} renormalization. However, for $n > 3$ dynamical behavior of the memory matrix becomes incompatible with the assumptions made in the course of these considerations: its decay with time becomes too slow. Therefore, only once, twice and three times renormalized Rouse models can be applied to analyze the polymer dynamics. Predictions of the twice renormalized Rouse model are summarized in Table 1.1 [25,26,65]. It is noted that occurrence of different regimes of dynamics depends not only on time, but also on the mode number, which did not take place in the previously considered models. The characteristic times are given by:

$$\tau_p^{TRR} = \tau_s\left(\frac{N}{p}\right)^2\left(1 + 5.52\psi^2\frac{N}{p}\right), \qquad \tau_1^{TRR} \cong 5.52\psi^2\tau_s N^3 \quad \text{for} \quad p < \frac{N}{6\pi}, \tag{1.75}$$

where ψ is a parameter related to the presence of the entanglements in the system (defined in [61]).

Regime	Limits	$\langle\left(\vec{R}(t)-\vec{R}(0)\right)^2\rangle$	$\frac{1}{T_1^{intra}}$
Rouse	$\tau_s \ll t \ll \frac{\tau_s}{\psi}$	$\propto t^{1/2}$	$\propto -\tau_s ln(\omega\tau_s)$
$(I)_{TRR}$	$\frac{N}{6\pi} < p < 0.22N\sqrt{\psi}$ $\frac{\tau_s}{\psi} \ll t \ll (6\pi)^4\psi^2\tau_s$ $\psi \gg \frac{1}{\pi^2}$	$\propto t^{1/4}$	$\propto \omega^{-1/2}$
$(I)_{TRR}$	$p < \frac{N}{6\pi}$ $\frac{(6\pi)^4}{20}\psi\tau_s \ll t \ll \tau_1^{TRR}$	$\propto t^{1/3}$	$\propto \omega^{-1/3}$
$(III)_{TRR}$	$p < \frac{N}{6\pi}$ $t \gg \tau_1^{TRR}$	$\propto 6D_{cm}t \propto N^{-2}t$	$\propto \left(\frac{N^{-2}}{1+\omega^2}\right)$

Table 1.1 Predictions of the twice renormalized Rouse model for the segmental mean squared displacement and the intrasegment spin-lattice relaxation rate with the corresponding time and mode limits.

Experimental results obtained by the field-cycling NMR relaxometry, which probes the spin-lattice relaxation dispersion, can be fitted well with the use of the renormalized Rouse models [25,27,65]. However, the concept of renormalization is somewhat ambiguous and is not directly related to the fundamental physical principles of the chain's motion, thereby demanding for further development of this theoretical approach. In addition to that, previously mentioned viscoelastic behavior of polymer melts, which results in appearance of the shear modulus plateau, cannot be explained with the described approach, contrary to the tube-reptation model.

It should be emphasized as well, that the renormalized Rouse model is free from the topological restrictions and the segmental motion is therefore isotopic, whereas it is highly anisotropic in the regimes of incoherent and coherent reptation. This crucial feature will play an important role while considering the behavior of intra- and intermolecular dipolar interactions in *Chapter 3.*

Chapter 2. Nuclear Magnetic Resonance

In the beginning of the XXth century significant progress was achieved in understanding the structure and the properties of atom and of its nuclei. One of the groundbreaking experiments carried out during that time was performed by Stern and Gerlach in 1922 [66]. It was designed to check the Bohr's atom model [67] and, in particular, the quantization of the angular momentum, by studying the deflection of a beam consisting of silver atoms in a magnetic field. If the assumption that the angular momentum of an atom takes only certain allowed values is correct, then the magnetic moment, which is proportional to the angular momentum, should be quantized as well, resulting in a peculiar deflection pattern of the beam, different from the case of homogenous distribution of the magnetic moment predicted by the classical mechanics. This was indeed confirmed in the experiment: the beam was split into two directions, corresponding to two values of the spin angular momentum, $+\frac{1}{2}\hbar$ and $-\frac{1}{2}\hbar$. Based on the results of Stern and Gerlach, Rabi in 1938 [68] designed a setup where a molecular beam in a magnetic field was additionally subjected to the radiofrequency magnetic field, which at certain conditions caused transitions between different magnetic states of the nuclei. This was the first observation of the resonant absorption of the energy by the nuclei of the atoms in the beam, which were almost isolated from each other, detected through the change of their trajectories in the magnetic field – namely, *nuclear magnetic resonance*. In 1941 Zavoisky actually observed the nuclear magnetic resonance effect in a bulk matter, however, the results were not reproducible due to a very low sensitivity and were, eventually, discarded. Subsequently, NMR phenomenon was observed independently by Bloch in water [69] and Purcell in solid paraffin [70] in 1945 (both published in 1946), which later brought to them, as well as to Rabi, a Nobel Prize for these works.

Since its discovery NMR has been significantly developed and today, in spite of a high number of different variations, it can generally be divided into two big categories: the frequency-domain (spectroscopy) and the time-domain (relaxometry) NMR. The former is commonly used to elucidate the structure of molecules and is based on the Fourier transformation of the acquired signal and the subsequent analysis of its spectral characteristics, which reflect the position of the nuclei, the type of their surroundings, the distances between them etc. The time-domain NMR is usually utilized to investigate the dynamical properties of the nuclei through the analysis of the way the spin system is relaxing back to the thermal equilibrium after a perturbation (usually external). Nevertheless, both the spectroscopy and the relaxometry can be applied both to the structural, as well as the dynamical analysis of a system.

In this work, the time-domain NMR techniques are used to probe the dynamics of polymer melts. In the current chapter general concepts of the NMR phenomenon are given (*Chapter 2.1*), with particular focus on the dipole-dipole interaction between spins (*Chapter 2.2)*. The concept of spin relaxation and its connection with the microscopic motion of polymer melt's Kuhn segments are described in *Chapter 2.3.* Finally, the conventional experimental techniques suitable for the investigation of spin relaxation are presented in *Chapter 2.4*.

2.1 Concept and general principles

Spin operator $\hat{I}$, associated with a spin angular momentum (or equivalently, spin) with a value I, is described by its projections $\hat{I}_x$, $\hat{I}_y$ and $\hat{I}_z$. These operators do not commute with each other and obey the cycle rule $[\hat{I}_a, \hat{I}_b] = i\hat{I}_c$. As a consequence of the uncertainty principle, only one projection can be defined at a particular time moment. Let it be $\hat{I}_z$, then it is characterized by $2I + 1$ eigenvalues:

$$\hat{I}_z|I, m\rangle = m|I, m\rangle \quad (2.1)$$

Here $m = -I, -(I-1) \dots I-1, I$, and $|I, m\rangle$ are the eigenvectors of the operator $\hat{I}_z$. The value $2I + 1$ should be integer, therefore I can be either integer or half-integer. It is convenient to introduce two new operators instead of $\hat{I}_x$ and $\hat{I}_y$:

$$\begin{cases} \hat{I}^+ = \hat{I}_x + i\hat{I}_y \\ \hat{I}^- = \hat{I}_x - i\hat{I}_y \end{cases} \quad (2.2)$$

These are the *raising* and the *lowering* operators, respectively. They act on the eigenvectors $|I, m\rangle$ in the following way:

$$\begin{cases} \hat{I}^+|I, m\rangle = \sqrt{I(I+1) - m(m+1)}|I, m+1\rangle \\ \hat{I}^-|I, m\rangle = \sqrt{I(I+1) - m(m-1)}|I, m-1\rangle \end{cases} \quad (2.3)$$

As can be seen, these operators correspond to the transitions between the pure states of a spin, described by different m.

Spin in a constant magnetic field.

In order to introduce and investigate the nuclear magnetic resonance phenomenon, it is necessary to start with a problem of the behavior of a single spin I in a constant magnetic field. Generally, it is convenient to describe a spin system with a statistical operator, called the *density matrix*. It is defined as:

$$\hat{\rho} = \sum_n \omega_n \hat{p}_n \,, \quad (2.4)$$

where ω_n denotes a probability of the system to be in the pure state described by the eigenfunction $|\psi_n\rangle$ and $\hat{p}_n = |\psi_n\rangle\langle\psi_n|$ is the projection operator. The set of the probabilities ω_n obeys a condition: $\sum_n \omega_n = 1$ and the eigenfunctions $|\psi_n\rangle$ form an orthonormal basis. The density matrix thereby describes the mixed states of the spin system. Its time evolution is determined by the *Liouville-von Neumann* equation:

$$i\hbar \frac{\partial}{\partial t}\hat{\rho}(t) = [\hat{H}, \hat{\rho}(t)], \quad (2.5)$$

where $[..]$ denotes a commutator of two operators and $\hat{H}$ is a Hamiltonian of the system. This equation is analogous to the *Schrödinger's equation* for the pure quantum states. In this formalism the average value of the operator $\langle\hat{f}(t)\rangle$ that is the experimentally observable quantity is given by the following trace:

$$\langle\hat{f}(t)\rangle = Tr\big(\hat{f}\hat{\rho}(t)\big) \quad (2.6)$$

Consider now the solution of eq. (2.5), which is given by:

$$\hat{\rho}(t) = exp\left(-\frac{i\hat{H}t}{\hbar}\right)\hat{\rho}(0)exp\left(\frac{i\hat{H}t}{\hbar}\right) \quad (2.7)$$

Combination of eq. (2.6) and (2.7) results in the following expression for the average value of the observable quantity:

$$\langle\hat{f}(t)\rangle = Tr\big(\hat{f}(t)\hat{\rho}(0)\big), \quad (2.8)$$

where

$$\hat{f}(t) = exp\left(-\frac{i\hat{H}t}{\hbar}\right)\hat{f}(0)exp\left(\frac{i\hat{H}t}{\hbar}\right) \quad (2.9)$$

With the use of these equations, the time evolution of the observable average values of the spin projections $\hat{I}_x$, $\hat{I}_y$ and $\hat{I}_z$ can be derived. It is only necessary to define the Hamiltonian of the spin's interaction with the external magnetic field. Consider this field to be applied along the z-axis and have a value H_0. As was mentioned before, spin is associated with the angular momentum, which, in turn, is connected with the magnetic moment $\bar{\mu}$. In the case of nuclear spin (proton) it results in

$$\hat{\mu}_z = \frac{ge\hbar}{2m_pc}\hat{I}_z, \tag{2.10}$$

where g is the characteristic factor, which depends on the nuclear type, e is the elementary charge, m_p is the mass of proton, c is the speed of light. Then the Hamiltonian of the interaction with the external magnetic field is written as:

$$\widehat{H} = -\hat{\mu}_z\vec{H}_0 = -\frac{ge\hbar}{2m_pc}\hat{I}_zH_0 = \hbar\omega_0\hat{I}_z \tag{2.11}$$

It is called the *Zeeman interaction Hamiltonian*. Here $\omega_0 = -\frac{ge}{2m_pc}H_0 = -\gamma H_0$ is called the *Larmor frequency*, γ is the *gyromagnetic ratio*, depending on the nuclear species. Further on, the value of the magnetic field will be expressed interchangeably as H or $\omega = -\gamma H$. As can be seen from eq. (2.11), the gyromagnetic ratio also connects the magnetic moment with the spin angular momentum: $\hat{\mu} = \gamma\hbar\hat{I}$. Thus, the Hamiltonian is now defined through eq. (2.11), and eq. (2.9) can be rewritten for the α projection of the spin operator as:

$$\hat{I}_\alpha(t) = exp\left(-i\omega_0 t\hat{I}_z\right)\hat{I}_\alpha(0)exp\left(i\omega_0 t\hat{I}_z\right) \tag{2.12}$$

Employing eq. (2.6) and the properties of spin operators $\hat{I}_x$, $\hat{I}_y$ and $\hat{I}_z$, described in the beginning of this paragraph, the following set of equations can be derived:

$$\begin{cases} \langle\hat{I}_x(t)\rangle = cos(\omega_0 t)Tr\left(\hat{I}_x\hat{\rho}(0)\right) - sin(\omega_0 t)Tr\left(\hat{I}_y\hat{\rho}(0)\right) \\ \langle\hat{I}_y(t)\rangle = sin(\omega_0 t)Tr\left(\hat{I}_x\hat{\rho}(0)\right) + cos(\omega_0 t)Tr\left(\hat{I}_y\hat{\rho}(0)\right) \\ \langle\hat{I}_z(t)\rangle = Tr\left(\hat{I}_z\hat{\rho}(0)\right) \end{cases} \tag{2.13}$$

These equations describe a process of the precession of the spin I in the magnetic field H_0 applied along the z-axis in the case when the initial average value of the projections $\hat{I}_x$ and $\hat{I}_y$: $Tr\left(\hat{I}_x\hat{\rho}(0)\right)$ and $Tr\left(\hat{I}_y\hat{\rho}(0)\right)$ — are not zero. The sign of the Larmor frequency, thus, corresponds to the direction of the precession (positive – counterclockwise, negative - clockwise). For instance, a proton spin $I = \frac{1}{2}$ in the magnetic field of 1 Tesla is precessing clockwise around the direction of the field with a Larmor frequency $\omega_0 \approx 2.675 \cdot 10^8 \frac{rad}{s}$ or equivalently $\vartheta_0 = \frac{\omega_0}{2\pi} \approx 42.577\ MHz$.

In the thermodynamic equilibrium the density matrix is described by the Gibbs distribution of a canonical ensemble:

$$\hat{\rho}_{eq} = \frac{1}{Z}exp\left(-\frac{\hat{H}}{k_bT}\right), \tag{2.14}$$

where $Z = Tr\left(exp\left(-\frac{\hat{H}}{k_bT}\right)\right)$ is a partition function. In NMR experiments the so-called high-temperature approximation is employed, allowing to expand the exponent in eq. (2.14) into the Taylor series:

$$\hat{\rho}_{eq} \cong \frac{1}{Z}\left(1 - \frac{\hat{H}}{k_bT}\right) = \frac{1}{Z}\left(1 - \frac{\hbar\omega_0\hat{I}_z}{k_bT}\right) \tag{2.15}$$

Then, the average equilibrium value of the spin operator is defined as $\langle\hat{I}_\alpha\rangle_{eq} = Tr\left(\hat{I}_\alpha\hat{\rho}_{eq}\right)$. Using the relations $Tr\left(\hat{I}_\alpha\hat{I}_\beta\right) = \delta_{\alpha\beta}\frac{I}{3}(I+1)(2I+1)$, $Tr\left(\hat{I}_\alpha\right) = 0$ and $Tr(1) = 2I+1$ for a single spin, the following expressions can be derived:

$$\begin{cases} \langle \hat{I}_z \rangle_{eq} = -\frac{\hbar\omega_0}{k_b T}\frac{I}{3}(I+1) \\ \langle \hat{I}_x \rangle_{eq} = \langle \hat{I}_y \rangle_{eq} = 0 \end{cases} \quad (2.16)$$

This is a very important result demonstrating that in the state of the thermodynamic equilibrium the average values of spin operator's x- and y-projections are zero and the precession described by eq. (2.13) is not observable. This result is actually general and holds also for the system consisting of N spins. The z-projection of the spin operator $\langle \hat{I}_z \rangle_{eq}$ in this case is written as: $\langle \hat{I}_z \rangle_{eq} = -\frac{N\hbar\omega_0}{k_b T}\frac{I}{3}(I+1) = \frac{N\hbar\gamma H_0}{k_b T}\frac{I}{3}(I+1)$. The total (net) magnetization of the spin system is defined as a sum of the magnetic moments of the each spin and therefore equals to $\vec{M}_0 = \gamma\hbar\langle \hat{I}_z \rangle_{eq} = \frac{N\gamma^2\hbar^2\vec{H}_0}{k_b T}\frac{I}{3}(I+1)$. Thus, the equilibrium average z-projection of the spin operator and, consequently, the net magnetization of the spin system are inversely proportional to the temperature and are aligned in the same direction as the external magnetic field H_0, which is known as the *Curie law*.

Spin in constant and radiofrequency magnetic fields.

In order to observe the Larmor precession of the spin, it is necessary to perturb the system, thereby getting it out of the equilibrium state. This can be done by applying a specific radiofrequency magnetic field to the system, as was done by Rabi in his pioneer work [68]. Consider a situation, when the circular polarized RF field characterized by the frequency ω and the amplitude $H_1 = -\frac{\omega_1}{\gamma}$ is applied perpendicular to the constant magnetic field. In this case the Hamiltonian of the system consists of two parts, the Zeeman interaction Hamiltonian and the Hamiltonian of the interaction with the RF field:

$$\hat{H}(t) = \hat{H}_0 + \hat{H}_1(t) = \hbar\omega_0\hat{I}_z + \hbar\omega_1\left(cos(\omega t)\hat{I}_x + sin(\omega t)\hat{I}_y\right) \quad (2.17)$$

This Hamiltonian is time-dependent. The time evolution of the system is described by the Liouville-von Neumann equation, given by eq. (2.5). It is possible to introduce a new density matrix operator, which corresponds to the transformation into a frame rotating with the frequency ω:

$$\hat{\rho}'(t) = exp\left(i\omega t\hat{I}_z\right)\hat{\rho}(t)exp\left(-i\omega t\hat{I}_z\right) \quad (2.18)$$

Differentiating eq. (2.18) and employing eq. (2.5) yields:

$$\frac{\partial\hat{\rho}'(t)}{\partial t} = \left[i\omega\hat{I}_z, \hat{\rho}'(t)\right] + exp\left(i\omega t\hat{I}_z\right)\frac{\partial\hat{\rho}(t)}{\partial t}exp\left(-i\omega t\hat{I}_z\right) = \left[i\omega\hat{I}_z, \hat{\rho}'(t)\right] +$$
$$+exp\left(i\omega t\hat{I}_z\right)\left[\hat{H}(t), \hat{\rho}(t)\right]exp\left(-i\omega t\hat{I}_z\right) = \left[i\omega\hat{I}_z, \hat{\rho}'(t)\right] + \frac{1}{i\hbar}\left[\hat{H}'(t), \hat{\rho}'(t)\right] \quad (2.19)$$

$\hat{H}'(t)$ denotes the Hamiltonian in the rotating frame and can be calculated with the use of eq. (2.17) and eq. (2.2) for the raising and lowering operators:

$$\hat{H}'(t) = exp\left(i\omega t\hat{I}_z\right)\hat{H}(t)exp\left(-i\omega t\hat{I}_z\right) = exp\left(i\omega t\hat{I}_z\right)\left(\hbar\omega_0\hat{I}_z + \frac{\hbar\omega_1}{2}\left(\hat{I}^+exp(-i\omega t) +\right.\right.$$
$$\left.\left.+\hat{I}^-exp(i\omega t)\right)\right)exp\left(-i\omega t\hat{I}_z\right) = \hbar\omega_0\hat{I}_z + \hbar\omega_1\hat{I}_x \quad (2.20)$$

As a consequence of the transformation into the frame rotating at the frequency of the RF magnetic field, the Hamiltonian $\hat{H}'$ becomes time-independent. Combination of eq. (2.19) and (2.2) results in the following equation of motion:

$$i\hbar\frac{\partial\hat{\rho}'(t)}{\partial t} = \left[\hbar\omega\hat{I}_z, \hat{\rho}'(t)\right] - \left[\hbar\omega_0\hat{I}_z, \hat{\rho}'(t)\right] + \left[\hbar\omega_1\hat{I}_x, \hat{\rho}'(t)\right] = \left[\hbar(\omega-\omega_0)\hat{I}_z + \hbar\omega_1\hat{I}_x, \hat{\rho}'(t)\right] \quad (2.21)$$

This equation describes a nutation of the spin I in the laboratory frame. It consists of the precession around the z-axis with the frequency ω in the laboratory frame and the precession around the vector

$\frac{\omega_1}{\sqrt{(\omega-\omega_0)^2+\omega_1^2}}\vec{e}_x + \frac{\omega-\omega_0}{\sqrt{(\omega-\omega_0)^2+\omega_1^2}}\vec{e}_z$ with the frequency $\sqrt{(\omega-\omega_0)^2+\omega_1^2}$ in the rotating frame. For the typical experimental conditions $\omega_1 \ll \omega_0$, therefore the z-projection dominates the behavior of the spin. Importantly, if the frequency of the RF field $\omega = \omega_0$, then the motion is effectively represented by the precession around the x-axis in the rotating frame. In this case the z-projection is periodically changing with time with the largest amplitude, which corresponds to the absorption and the emission of the RF energy. Thus, $\omega = \omega_0$ is the resonant condition for the spin in the constant magnetic field of the value $H_0 = -\frac{\omega_0}{\gamma}$ applied along the z-axis, which is subject to the RF magnetic field circularly polarized at frequency ω in the transverse plane.

The same problem can be tackled with the help of the perturbation theory, widely used in quantum mechanics. Consider a system with a Hamiltonian:

$$\hat{H} = \hat{H}_0 + \hat{V}(t), \tag{2.22}$$

where $\hat{H}_0$ is the Zeeman interaction Hamiltonian, satisfying $\hat{H}_0|n\rangle = E_n|n\rangle$, and $\hat{V}(t)$ is a time-dependent Hermitian operator, representing the perturbation caused by the rotating RF field:

$$\hat{V}(t) = \frac{\hbar\omega_1}{2}\left(\hat{I}^+ exp(-i\omega t) + \hat{I}^- exp(i\omega t)\right) \tag{2.23}$$

The quantum perturbation theory in this case yields the following result for the probability of a transition from the state n to k per time unit, known as *Fermi's golden rule* [74]:

$$W_{kn} = \frac{2\pi}{\hbar}\left|\langle n|\hat{V}(t)|k\rangle\right|^2 \rho(\Delta E_{kn}), \tag{2.24}$$

where $\Delta E_{kn} = \hbar\omega_{kn}$ is the energy difference between the states n and k, $\rho(\Delta E_{kn})$ is its distribution function, normalized as $\int \rho(\Delta E_{kn}) d\Delta E_{kn} = 1$. Assuming that the energy difference is constant, the following relation holds: $\rho(\Delta E_{kn}) = \rho(\hbar\omega_{kn}) = \delta(\hbar\omega_{kn}) = \frac{\delta(\omega_{kn})}{\hbar}$. Employing eq. (2.23), eq. (2.24) can be rewritten as:

$$W_{kn} = \frac{\pi\omega_1^2}{2}\left(\langle k|\hat{I}^+|n\rangle\langle n|\hat{I}^-|k\rangle\delta(\omega_{kn}-\omega) + \langle k|\hat{I}^-|n\rangle\langle n|\hat{I}^+|k\rangle\delta(\omega_{kn}+\omega)\right) \tag{2.25}$$

This equation describes the probabilities of the transitions between the states n and k. Due to the properties of the operators $\hat{I}^+$ and $\hat{I}^-$, given by eq. (2.3), the transition can occur only between the states with the same I, while m is allowed to change by 1. Therefore, the transition $|I,m\rangle$ -> $|I,m+1\rangle$ is determined by the first term of eq. (2.25) and corresponds to the absorption of the RF energy $\hbar\omega = \hbar\omega_{kn}$, whereas the second term of eq. (2.25) stands for the emission of the energy quantum $\hbar\omega$ and the transition $|I,m\rangle$ -> $|I,m-1\rangle$. The probability of the both processes are equal, complying with the law of the conservation of energy. In this description the nuclear magnetic resonance phenomenon occurs exactly at the frequency $\omega_{kn} = \frac{\Delta E_{kn}}{\hbar}$, due to delta-functions in eq. (2.25). In reality, the difference between the energy levels of the system is characterized by a certain distribution, resulting in the spectrum of the frequencies, at which the absorption takes place.

Bloch equations.

Liouville-von Neumann equation, eq. (2.5), describes the evolution of the density matrix in time, which is not an experimentally measurable quantity. However, the behavior of the observable average value of the spin $\langle\hat{I}(t)\rangle$ in the external magnetic field $\vec{H}_0 = -\frac{\vec{\omega}_0}{\gamma}$ can be explicitly given by the Euler equation:

$$\frac{d\langle\hat{I}(t)\rangle}{dt} = \vec{\omega}_0 \times \langle\hat{I}(t)\rangle \tag{2.26}$$

In the case of the magnetic field having only z-component equal to $-\frac{\omega_0}{\gamma}$, eq. (2.26) translates to:

$$\begin{cases} \frac{d\langle \hat{I}_x(t)\rangle}{dt} = -\omega_0 \langle \hat{I}_y(t)\rangle \\ \frac{d\langle \hat{I}_y(t)\rangle}{dt} = \omega_0 \langle \hat{I}_x(t)\rangle \\ \frac{d\langle \hat{I}_z(t)\rangle}{dt} = 0 \end{cases} \quad (2.27)$$

This set of equations leads to the previously derived eq. (2.13), which describes the precession around the z-axis. In a real system this precession will be affected by the internal magnetic fields, caused by the surrounding nuclei and electrons in addition to $\vec{H}_0$. Interactions with these fields result in the relaxation of the spin components to their equilibrium values. This effect was accounted for by Bloch [75] via the introduction of the relaxation terms into eq. (2.27):

$$\begin{cases} \frac{d\langle \hat{I}_x(t)\rangle}{dt} = -\omega_0 \langle \hat{I}_y(t)\rangle - \frac{1}{T_2}\langle \hat{I}_x(t)\rangle \\ \frac{d\langle \hat{I}_y(t)\rangle}{dt} = \omega_0 \langle \hat{I}_x(t)\rangle - \frac{1}{T_2}\langle \hat{I}_y(t)\rangle \\ \frac{d\langle \hat{I}_z(t)\rangle}{dt} = -\frac{1}{T_1}\left(\langle \hat{I}_z(t)\rangle - \langle \hat{I}_z(t)\rangle_{eq}\right) \end{cases} \quad (2.28)$$

Here $\frac{1}{T_2}$ is called the *spin-spin*, or *transverse, relaxation rate* and corresponds to the relaxation of x- and y-projections of the spin to their equilibrium value – zero. $\frac{1}{T_1}$ is the *spin-lattice, or longitudinal, relaxation rate* and it characterizes the relaxation of the z-projection to its equilibrium value $\langle \hat{I}_z(t)\rangle_{eq}$. In *Chapter 2.3* the spin-lattice and the spin-spin relaxation phenomena and their connection with spin dynamics will be discussed in more detail.

It should be noted that the formalism based on the density matrix is very general and can be applied to the evaluation of the behavior of the macroscopic magnetization of a spin ensemble as well. Consequently, the Euler and the Bloch equations are also valid for the macroscopic magnetization vector and its projections.

2.2 Dipolar coupling

Consider now a system consisting of two spins I_1 and I_2, subject to the dipolar interactions with each other, in a constant external magnetic field with a Hamiltonian:

$$\widehat{H} = \widehat{H}_0 + \widehat{H}_{dd} = \hbar\omega_0\left(\hat{I}_{1z} + \hat{I}_{2z}\right) + \frac{\gamma^2\hbar^2}{r_{12}^3}\left(\hat{I}_1\hat{I}_2 - \frac{3(\vec{r}_{12}\hat{I}_1)(\vec{r}_{12}\hat{I}_2)}{r_{12}^2}\right) \quad (2.29)$$

The second term of this equation is a well-known expression for the magnetic interaction between two dipoles, with $\vec{r}_{12}$ being a vector between them. Rewriting this term using lowering and raising operators leads to the notation of the dipoalr interaction in terms of the Van Fleck components [76]:

$$\begin{aligned}
&\widehat{H}_{dd} = A\hat{I}_{1z}\hat{I}_{2z} + B\left(\hat{I}_1^+\hat{I}_2^- + \hat{I}_1^-\hat{I}_2^+\right) + C\left(\hat{I}_{1z}\hat{I}_2^+ + \hat{I}_1^+\hat{I}_{2z}\right) + D\left(\hat{I}_{1z}\hat{I}_2^- + \hat{I}_1^-\hat{I}_{2z}\right) + E\hat{I}_1^+\hat{I}_2^+ + F\hat{I}_1^-\hat{I}_2^- \\
&A = \frac{\gamma^2\hbar^2}{r_{12}^3}\left(1 - 3cos^2(\theta_{12})\right) \\
&B = -\frac{\gamma^2\hbar^2}{4r_{12}^3}\left(1 - 3cos^2(\theta_{12})\right) \\
&C = -\frac{3\gamma^2\hbar^2}{2r_{12}^3}cos(\theta_{12})sin(\theta_{12})exp(-i\varphi_{12}) \\
&D = -\frac{3\gamma^2\hbar^2}{2r_{12}^3}cos(\theta_{12})sin(\theta_{12})exp(i\varphi_{12}) \\
&E = -\frac{3\gamma^2\hbar^2}{4r_{12}^3}sin^2(\theta_{12})exp(-2i\varphi_{12}) \\
&F = -\frac{3\gamma^2\hbar^2}{4r_{12}^3}sin^2(\theta_{12})exp(2i\varphi_{12}),
\end{aligned} \quad (2.30)$$

where θ_{12} is the angle between $\vec{r}_{12}$ and $\vec{H}_0$ and φ_{12} is the angle between the projection of $\vec{r}_{12}$ onto the XY-plane and the x-axis. Term A with the operators $\hat{I}_{1z}\hat{I}_{2z}$ does not cause any transitions in the system. Term B is responsible for the *zero-quantum transitions*: operators $\hat{I}_1^+\hat{I}_2^-$ result in the change of the state $\Delta m_1 = 1$ and $\Delta m_2 = -1$, $\hat{I}_1^-\hat{I}_2^+$ lead to $\Delta m_1 = 1$ and $\Delta m_2 = -1$. In the both cases $\Delta m = \Delta m_1 + \Delta m_2 = 0$. These are called the *flip-flop transitions* and cause the process of the *spin diffusion*, which leads to the spatial equilibration of the magnetic moment in the system. Terms C and D are responsible for the *single-quantum* transitions $\Delta m = \pm 1$. Finally, terms E and F correspond to the *double-quantum* transitions $\Delta m = \pm 2$. First two terms A and B form the so-called *secular part* of the dipole-dipole Hamiltonian $\widehat{H}_{dd}^{sec} = \frac{\gamma^2\hbar^2}{r_{12}^3}\left(1 - 3cos^2(\theta_{12})\right)\left(\hat{I}_{1z}\hat{I}_{2z} - \frac{1}{4}\left(\hat{I}_1^+\hat{I}_2^- + \hat{I}_1^-\hat{I}_2^+\right)\right)$, which commutates with the Zeeman interaction Hamiltonian: $\left[\widehat{H}_0, \widehat{H}_{dd}^{sec}\right] = 0$.

Consider the simplest case of two spins $I_1 = I_2 = \frac{1}{2}$. Both of the spins separately are characterized by $2I + 1 = 2$ pure states with the possible values for m_1 and m_2 being $\pm\frac{1}{2}$. Consequently, the system of these two spins has 4 possible states: $|++\rangle, |+-\rangle, |-+\rangle$ and $|--\rangle$. In the absence of the Zeeman interaction, all the states are degenerate. Adding the Zeeman interaction by "switching on" the external magnetic field, results in the following relations for these states (using eq. (2.2) and (2.3)):

$$\begin{aligned}
\langle++|\widehat{H}_0|++\rangle &= \hbar\omega_0 \\
\langle-+|\widehat{H}_0|+-\rangle &= 0 \\
\langle+-|\widehat{H}_0|-+\rangle &= 0 \\
\langle--|\widehat{H}_0|--\rangle &= -\hbar\omega_0
\end{aligned} \quad (2.31)$$

All the cross terms are zero, therefore $|++\rangle$, $|+-\rangle, |-+\rangle$ and $|—\rangle$ are the eigenfunctions of the Zeeman interaction Hamiltonian. In this case two states $|+-\rangle$ and $|-+\rangle$ are degenerate. Considering

now separately the effect of the dipole-dipole interaction, given by the Hamiltonian eq. (2.30), leads to the following result:

$$\begin{aligned}
\langle + + |\hat{H}_{dd}| + + \rangle &= \tfrac{1}{4}A & \langle + - |\hat{H}_{dd}| + - \rangle &= B \\
\langle + - |\hat{H}_{dd}| - + \rangle &= -\tfrac{1}{4}A & \langle - + |\hat{H}_{dd}| - + \rangle &= B \\
\langle - + |\hat{H}_{dd}| + - \rangle &= -\tfrac{1}{4}A & & \\
\langle - - |\hat{H}_{dd}| - - \rangle &= \tfrac{1}{4}A & &
\end{aligned} \tag{2.32}$$

Importantly, the cross terms shown in the right column of eq. (2.32) are non-zero. This means that the Zeeman Hamiltonian's eigenstates are not the eigenstates of the dipole-dipole Hamiltonian. However, after the diagonalization of the matrix formed by eq. (2.32), a new basis can be introduced, which consists of three states $|T;1\rangle = |+ +\rangle$, $|T;0\rangle = \frac{1}{\sqrt{2}}(|+ -\rangle + |- +\rangle)$ and $|T;-1\rangle = |- -\rangle$ called the *triplet states,* which coincide with the eigenstates of the spin $I = 1$, and $|S;0\rangle = \frac{1}{\sqrt{2}}(|+ -\rangle - |- +\rangle)$ called the *singlet state*, which can be compared to the eigenstate of the spin $I = 0$. In this basis the eigenvalues of $\hat{H}_0$ are the same as in eq. (2.31), and for $\hat{H}_{dd}$ they are given by:

$$\begin{aligned}
\langle 1;T|\hat{H}_{dd}|T;1\rangle &= \tfrac{1}{4}A \\
\langle 0;T|\hat{H}_{dd}|T;0\rangle &= -\tfrac{1}{2}A \\
\langle 0;S|\hat{H}_{dd}|S;0\rangle &= 0 \\
\langle -1;T|\hat{H}_{dd}|T;-1\rangle &= \tfrac{1}{4}A
\end{aligned} \tag{2.33}$$

All the cross terms here are equal to zero – the matrix is diagonalized. The degeneracy of the states is eliminated by the effect of the dipole-dipole interaction. The graphical scheme of the energy level splitting for the two-spin $I = \frac{1}{2}$ system is illustrated in Figure 2.1.

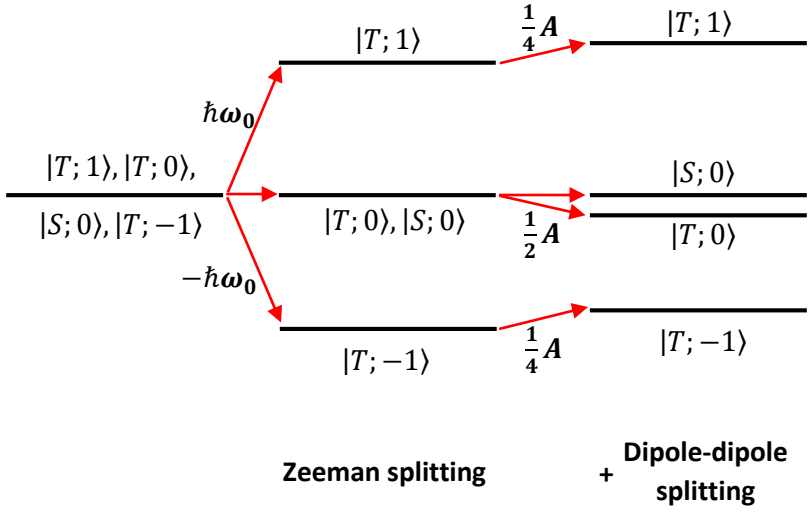

Figure 2.1. Illustrative scheme of the energy level splitting of the two coupled spins $I = \frac{1}{2}$. On the left side the levels are degenerate in the absence of the magnetic field, then the spins are subjected to the Zeeman interaction with the external magnetic field $H_0 = -\frac{\omega_0}{\gamma}$ and finally also to the dipole-dipole interaction between each other.

According to the Fermi's golden rule (eq. 2.24) the transition between the triplet states $|T;1\rangle$, $|T;0\rangle$ and $|T;-1\rangle$ are allowed with the frequencies corresponding to the difference between the respective energy levels.

In the course of this consideration the effect of the exchange interaction between the spins, which occurs through the electrons of the chemical bonds, known as the *indirect dipole-dipole coupling* or the *J-coupling*, was not taken into account. Rigorous discussion of its impact onto the energy levels of a two-spin system can be found in literature [73].

Evidently, dipole-dipole interactions bear information about the spatial positions of the spins through the dependence on $\vec{r}_{12}$, θ_{12} and φ_{12}. Therefore, probing the dipolar interaction in the experiment is a powerful tool of analyzing both the structure and the dynamics of molecules. Interestingly, while paying closer attention to the factor $\left(1-3cos^2(\theta_{12})\right)$, it becomes apparent that if the interspin vector and the magnetic field vector form a certain angle $\theta_{12} \cong 54.74$, called a *magic angle*, then the secular part of the dipole-dipole Hamiltonian becomes zero. This feature is often used in the NMR spectroscopy. On the other hand, the same factor $\left(1-3cos^2(\theta_{12})\right)$ is subject to the motional averaging due to the rotation of the molecule in the case of the intramolecular spin coupling and due to the translation of the corresponding molecules in the case of the intermolecular coupling. For instance, simple liquids are characterized by the fast isotropic motion, which leads to: $\langle\left(1-3cos^2(\theta_{12})\right)\rangle = \frac{1}{2}\int_0^{\pi} sin(\theta_{12})\left(1-3cos^2(\theta_{12})\right)d\theta_{12} = 0$, where $sin(\theta_{12})$ and $\frac{1}{2\pi}$ appear due to the transformation into the spherical coordinates and the integration over the solid angle. Contrary, in solids the dipolar interactions result in the distinct level splitting as discussed above. There is also an intermediate situation, usually encountered in soft matter, when the dipolar interaction are averaged out only partly and one speaks about the *residual dipolar interactions.*

In the next paragraph it will be shown that the dipole-dipole interactions affect the spin relaxation process and thereby can be evaluated through the NMR relaxation experiments.

2.3 Spin relaxation

Consider a spin system, which can be described by the Euler equation:

$$\frac{d\langle \hat{I}(t)\rangle_q}{dt} = \left(\left(\omega_0 + \omega_1^z(t)\right)\vec{e}_z\right) \times \langle \hat{I}(t)\rangle_q \,, \tag{2.34}$$

where $\langle \hat{I}(t)\rangle_q = Tr\left(\hat{I}\rho(t)\right)$ is a quantum average observable, ω_0 is the Larmor frequency corresponding to the external magnetic field $\vec{H}_0$ aligned along the z-axis and $\omega_1^z(t)$ is associated with a random magnetic field much weaker than $\vec{H}_0$, which also is collinear with the z-axis. In this case, eq. (2.34) for the z-projection of the spin transforms to $\frac{d\langle \hat{I}_z(t)\rangle}{dt} = 0$. Thus, the random magnetic field along the z-axis does not cause the spin-lattice relaxation of $\langle \hat{I}_z(t)\rangle$. This is a simplified situation, which, nevertheless, helps to describe the important features of the transverse relaxation. Eq. (2.34) can be written for the raising and the lowering operators in the following way:

$$\begin{cases} \frac{d\langle \hat{I}^+(t)\rangle_q}{dt} = i\left(\omega_0 + \omega_1^z(t)\right)\langle \hat{I}^+(t)\rangle_q \\ \frac{d\langle \hat{I}^-(t)\rangle_q}{dt} = -i\left(\omega_0 + \omega_1^z(t)\right)\langle \hat{I}^-(t)\rangle_q \end{cases} \tag{2.35}$$

Equations (2.35) are equivalent and further on only the evolution of the raising operator $\langle \hat{I}^+(t)\rangle_q$ will be considered. The solution of eq. (2.35) after additional averaging over all the realizations of the random variable $\omega_1^z(t)$ yields:

$$\langle \hat{I}^+(t)\rangle = exp(i\omega_0 t)\,\langle exp\left(i\int_0^t \omega_1^z(t_1)dt_1\right)\rangle\,\langle \hat{I}^+\rangle_0 \tag{2.36}$$

It is noted that eq. (2.36) assumes that $\langle \omega_1^z(t)\rangle = 0$, otherwise the non-zero average value of $\omega_1^z(t)$ contributes to the shift of the resonance frequency $\omega_0 \to (\omega_0 + \langle \omega_1^z(t)\rangle)$. The factor $exp(i\omega_0 t)$ corresponds to the Larmor precession in the laboratory frame. In the rotating frame eq. (2.36) can be rewritten as:

$$g(t) = \left(\frac{\langle \hat{I}^+(t)\rangle}{\langle \hat{I}^+\rangle_0}\right)_{rot} = \langle exp\left(i\int_0^t \omega_1^z(t_1)dt_1\right)\rangle \tag{2.37}$$

The time-dependent function $g(t)$ describes relaxation in the transverse XY-plane and is called the *free induction decay* (FID). Expanding eq. (2.37) into the Taylor series and assuming that $\omega_1^z(t)$ is a stochastic stationary variable, which correlation functions of high orders can be rewritten through the binary correlation functions, eq. (2.37) translates to:

$$g(t) = exp\left(-\frac{1}{2}\iint_0^t dt_1 dt_2 \langle \omega_1^z(t_2 - t_1)\omega_1^z(0)\rangle\right) = exp\left(-\int_0^t (t-\tau)\langle \omega_1^z(\tau)\omega_1^z(0)\rangle\, d\tau\right) \tag{2.38}$$

Thus, the FID depends on the convolution of the binary correlation function of the magnetic field, randomly fluctuating along the z-axis, causing the transverse relaxation in the spin system. Very often the main origin of this field fluctuation is the dipole-dipole interactions between the spins.

The binary correlation function $\langle \omega_1^z(\tau)\omega_1^z(0)\rangle$ can be characterized by the *correlation time* $\tau_c = \frac{\int_0^\infty \langle \omega_1^z(\tau)\omega_1^z(0)\rangle d\tau}{\langle \omega_1^z\rangle}$. Then, eq. (2.38) can be further evaluated in two time limits. If $t \ll \tau_c$, the free induction decay is transformed to:

$$g(t) = exp\left(-\frac{1}{2}\langle (\omega_1^z)^2\rangle t^2\right) \tag{2.39}$$

which is called the *Gaussian decay.* It is usually encountered in solids, soft matter and viscous liquids. On the other hand, if $t \gg \tau_c$, $g(t)$ is an exponential function and corresponds to an exponential decay

$$g(t) = exp\left(-t\int_0^\infty \langle \omega_1^z(\tau)\omega_1^z(0)\rangle\, d\tau\right) = exp\left(-\frac{t}{T_2}\right) \tag{2.40}$$

This relaxation regime appears in the short correlation time limit ($T_2 \gg \tau_c$). In the case, when τ_c is of the same order as the transverse relaxation time T_2, transition from the Gaussian to the exponential decay is observed. Experimental results obtained in entangled polymer melts presented in *Chapter 4* will display this feature.

Spin relaxation in a constant and a random isotropic magnetic field.

The results obtained for the transverse relaxation in a constant and a random magnetic field along the same axis are very important for the demonstration of its certain features and behavior. However, a more general case of a random isotropic field $\vec{\omega}_1(t)$, which is normally caused by the dipole-dipole interactions between the spins, should be considered to model a situation closer to the real one. Cartesian components of the random field $\omega_1^x(t)$, $\omega_1^y(t)$, $\omega_1^z(t)$ are assumed to obey the following relation:

$$\langle \omega_1^\alpha(t_1)\omega_1^\beta(t_2)\rangle = \frac{\delta_{\alpha\beta}}{3}\langle \vec{\omega}_1(t_2-t_1)\vec{\omega}_1(0)\rangle \quad (2.41)$$

The Euler equation in the rotating frame is then written as:

$$\frac{d\langle \hat{I}^{rot}(t)\rangle_q}{dt} = \vec{\omega}_1^{rot}(t) \times \langle \hat{I}^{rot}(t)\rangle_q, \quad (2.42)$$

where the components of $\vec{\omega}_1^{rot}$ are:

$$\begin{cases} \omega_1^{x;rot}(t) = cos(\omega_0 t)\omega_1^x(t) + sin(\omega_0 t)\omega_1^y(t) \\ \omega_1^{y;rot}(t) = -sin(\omega_0 t)\omega_1^x(t) + cos(\omega_0 t)\omega_1^y(t) \\ \omega_1^{z;rot}(t) = \omega_1^z(t) \end{cases} \quad (2.43)$$

Eq. (2.42) is independent of the constant magnetic field $\vec{H}_0$. The solution of this equation is given by:

$$\langle \hat{I}^{rot}(t)\rangle_q = \int_0^t \vec{\omega}_1^{rot}(t_1) \times \langle \hat{I}^{rot}(t_1)\rangle_q \, dt_1 + \langle \hat{I}^{rot}(0)\rangle_q \quad (2.44)$$

This expression can be further substituted into eq. (2.42), yielding, after averaging over all the realizations of the stochastic variable $\vec{\omega}_1(t)$, the following relation:

$$\frac{d\langle \hat{I}^{rot}(t)\rangle}{dt} = \int_0^t \langle \vec{\omega}_1^{rot}(t) \times \left(\vec{\omega}_1^{rot}(t_1) \times \hat{I}^{rot}(t_1)\right)\rangle \, dt_1 \quad (2.45)$$

This equation can be transformed to the following form for the Cartesian components $\hat{I}_\alpha^{rot}(t)$:

$$\frac{d\langle \hat{I}_\alpha^{rot}(t)\rangle}{dt} =$$

$$= -\int_0^t \langle \sum_{\beta=x,y,z}\left(\sum_{k=x,y,z}\left(\omega_1^{k;rot}(t)\omega_1^{k;rot}(t_1)\right)\delta_{\alpha\beta} - \left(\omega_1^{\beta;rot}(t)\omega_1^{\alpha;rot}(t_1)\right)\right)\hat{I}_\beta^{rot}(t_1)\rangle \, dt_1 \quad (2.46)$$

In order to evaluate the complex correlation function in the integral of eq. (2.46) $\langle\left(\sum_{k=x,y,z}\left(\omega_1^{k;rot}(t)\omega_1^{k;rot}(t_1)\right)\delta_{\alpha\beta} - \left(\omega_1^{\beta;rot}(t)\omega_1^{\alpha;rot}(t_1)\right)\right)\hat{I}_\beta^{rot}(t_1)\rangle$ it is necessary to make an assumption about the character of the stochastic fluctuations of the magnetic field. Such an assumption is called the *Redfield limit* (or the short correlation time limit) and postulates that the fluctuations of the magnetic field characterized by the correlation time τ_c are much faster than the spin relaxation time, i.e. fluctuation of $\hat{I}_\beta^{rot}$. This approximation and formalism were introduced and rigorously described in the series of works by Bloch and Wangness [77-79], and separately by Redfield [80]. In this case the abovementioned complex function can be rewritten as:

$$\langle\left(\sum_{k=x,y,z}\left(\omega_1^{k;rot}(t)\omega_1^{k;rot}(t_1)\right)\delta_{\alpha\beta} - \left(\omega_1^{\beta;rot}(t)\omega_1^{\alpha;rot}(t_1)\right)\right)\hat{I}_\beta^{rot}(t_1)\rangle =$$

$$= \langle\left(\sum_{k=x,y,z}\left(\omega_1^{k;rot}(t)\omega_1^{k;rot}(t_1)\right)\delta_{\alpha\beta} - \left(\omega_1^{\beta;rot}(t)\omega_1^{\alpha;rot}(t_1)\right)\right)\rangle \langle \hat{I}_\beta^{rot}(t_1)\rangle \quad (2.47)$$

Employing the property of the correlation function of the stationary process for the first term

$$\left\langle \left(\sum_{k=x,y,z} \left(\omega_1^{k;rot}(t)\omega_1^{k;rot}(t_1) \right) \delta_{\alpha\beta} - \left(\omega_1^{\beta;rot}(t)\omega_1^{\alpha;rot}(t_1) \right) \right) \right\rangle \langle \hat{I}_\beta^{rot}(t_1) \rangle =$$

$$= \left\langle \left(\sum_{k=x,y,z} \left(\omega_1^{k;rot}(t-t_1)\omega_1^{k;rot}(0) \right) \delta_{\alpha\beta} - \left(\omega_1^{\beta;rot}(t-t_1)\omega_1^{\alpha;rot}(0) \right) \right) \right\rangle \langle \hat{I}_\beta^{rot}(t_1) \rangle \quad (2.48)$$

Using this result and the property of the convolution, eq. (2.46) translates to:

$$\frac{d\langle \hat{I}_\alpha^{rot}(t) \rangle}{dt} = -\int_0^t \sum_{\beta=x,y,z} \left(\sum_{k=x,y,z} \left(\omega_1^{k;rot}(t_1)\omega_1^{k;rot}(0) \right) \delta_{\alpha\beta} - \right.$$

$$\left. - \left(\omega_1^{\beta;rot}(t_1)\omega_1^{\alpha;rot}(0) \right) \right) \langle \hat{I}_\beta^{rot}(t - t_1) \rangle \, dt_1 \quad (2.49)$$

In the abovementioned Redfield limit $t \gg t_1$ and $\langle \hat{I}_\beta^{rot}(t-t_1) \rangle \approx \langle \hat{I}_\beta^{rot}(t) \rangle$. Then the right-hand side of eq. (2.49) can be modified to:

$$\frac{d\langle \hat{I}_\alpha^{rot}(t) \rangle}{dt} =$$

$$= -\sum_{\beta=x,y,z} \left(\int_0^\infty \left(\sum_{k=x,y,z} \left(\omega_1^{k;rot}(t_1)\omega_1^{k;rot}(0) \right) \delta_{\alpha\beta} - \left(\omega_1^{\beta;rot}(t_1)\omega_1^{\alpha;rot}(0) \right) \right) dt_1 \right) \langle \hat{I}_\beta^{rot}(t) \rangle =$$

$$= -\sum_{\beta=x,y,z} w_{\alpha\beta} \langle \hat{I}_\beta^{rot}(t) \rangle, \quad (2.50)$$

where $w_{\alpha\beta}$ is the matrix of the kinetic coefficients. Its diagonal elements describe the spin relaxation times and the off-diagonal elements correspond to the shift of the resonance frequency. Therefore, the spin-spin and the spin-lattice relaxation times can be calculated using the property of the stochastic function eq. (2.41) and the connection between the laboratory and the rotating frames eq. (2.43):

$$\begin{cases} w_{xx} = w_{yy} = \frac{1}{T_2} = \frac{2}{3}\int_0^\infty \left(1 + cos(\omega_0 t)\right) \langle \vec{\omega}_1(t)\vec{\omega}_1(0) \rangle dt \\ w_{zz} = \frac{1}{T_1} = \frac{2}{3}\int_0^\infty cos(\omega_0 t) \langle \vec{\omega}_1(t)\vec{\omega}_1(0) \rangle dt \end{cases} \quad (2.51)$$

The short correlation time limit with respect to the spin-spin and the spin-lattice relaxation times means that $T_1 \gg min\left(\tau_c, \frac{1}{\omega_0}\right)$ and $T_2 \gg \tau_c$. The condition for T_1 can be satisfied even in the case of the long correlation time τ_c provided that the value of the constant external magnetic field $H_0 = -\frac{\omega_0}{\gamma}$ is increased. However, the condition for T_2 is stricter, due to the occurrence of the term independent of ω_0 in the integral in eq. (2.51) that does not contribute additionally to the decay of the correlation function $\langle \vec{\omega}_1(t)\vec{\omega}_1(0) \rangle$ unlike in the case of the spin-lattice relaxation.

The more detailed consideration of the problem of a spin in a constant and a randomly fluctuating magnetic field, based on the similar approach as well as the quantum mechanical treatment, can be found in textbooks [71,72,81].

Spin relaxation in a constant and a random isotropic magnetic field caused by dipole-dipole interactions.

As was mentioned before, in real systems a relevant, often encountered situation is represented by the case when the randomly fluctuating magnetic field $\vec{\omega}_1(t)$ is caused by the dipole-dipole interactions between the spins. This problem was first treated by Bloembergen, Purcell and Pound in their work of 1948 [82] based on the quantum perturbation theory. The expressions for the spin-spin and the spin-lattice relaxation times are derived in terms of the *spectral densities*

$$J^{(k)}(\omega) = \int_{-\infty}^{\infty} G^{(k)}(\tau)\, exp(-i\omega\tau) d\tau, \quad (2.52)$$

which are the Fourier transformations of the dipolar correlation functions:

$$G^{(0)}(t) = \langle \frac{\left(1-3cos^2(\theta_{12}(t))\right)}{r_{12}^3(t)} \frac{\left(1-3cos^2(\theta_{12}(0))\right)}{r_{12}^3(0)} \rangle$$
$$G^{(1)}(t) = \langle \frac{cos(\theta_{12}(t))sin(\theta_{12}(t))exp(i\varphi_{12}(t))}{r_{12}^3(t)} \frac{cos(\theta_{12}(0))sin(\theta_{12}(0))exp(-i\varphi_{12}(0))}{r_{12}^3(0)} \rangle \quad (2.53)$$
$$G^{(2)}(t) = \langle \frac{sin^2(\theta_{12}(t))exp(2i\varphi_{12}(t))}{r_{12}^3(t)} \frac{sin^2(\theta_{12}(0))exp(-2i\varphi_{12}(0))}{r_{12}^3(0)} \rangle$$

The correlation functions given by eq. (2.53) correspond to the correlation functions of the Van Fleck components of the dipole-dipole Hamiltonian, eq. (2.30). In these terms the spin-lattice and the spin-spin relaxation rates for the spin I in the constant magnetic field $H_0 = -\frac{\omega_0}{\gamma}$ due to the dipolar interactions are written as:

$$\begin{cases} \frac{1}{T_1} = \frac{3}{2}\gamma^4\hbar^2 I(I+1)\left(J^{(1)}(\omega_0) + J^{(2)}(2\omega_0)\right) \\ \frac{1}{T_2} = \frac{3}{8}\gamma^4\hbar^2 I(I+1)\left(J^{(0)}(0) + 10J^{(1)}(\omega_0) + J^{(2)}(2\omega_0)\right) \end{cases} \quad (2.54)$$

Here again the crucial difference between two spin relaxation processes is clear: spin-lattice relaxation occurs through the components of the magnetic field induced by dipolar interactions, magnitude of which corresponds to ω_0 and $2\omega_0$, whereas spin-spin relaxation, in addition to this, is sensitive to the zero-frequency processes, which are caused by slow motions. As in the previous paragraph, the short correlation time limit is assumed in eq. (2.54). For entangled polymer melts, which constitute the focus of the current work, the expression for $\frac{1}{T_1}$ can be used to evaluate the experimental results at conventional magnetic fields ($T_1 \gg min\left(\tau_c, \frac{1}{\omega_0}\right)$). Consequently, the spin-lattice relaxation is exponential. However, the assumption $T_2 \gg \tau_c$ is not valid in these systems (see the typical time scale of the polymer dynamics in *Chapter 1*), therefore consideration of the spin-spin relaxation demands for a different approach, which will be discussed in *Chapter 3*.

Dipolar correlation function and Kuhn segment's orientation.

Consideration of the spins belonging to the same molecule (in the case of small molecules) or to the same segment of the macromolecule allows assuming the fixed interspin distance $r_{12} = r$. In this case the correlation functions given by eq. (2.53) can be rewritten in terms of the *spherical harmonics* $Y_{m,n}(t)$:

$$G^{(0)}(t) = \frac{16}{5\pi r^6}\langle Y_{2,0}(t)Y_{2,0}(0)\rangle \ , \ Y_{2,0}(t) = -\sqrt{\frac{5}{16\pi}}\left(1-3cos^2(\theta_{12}(t))\right)$$
$$G^{(1)}(t) = \frac{8}{15\pi r^6}\langle Y_{2,1}(t)Y_{2,-1}(0)\rangle \ , \ Y_{2,\pm1}(t) = -\sqrt{\frac{15}{8\pi}}cos(\theta_{12}(t))sin(\theta_{12}(t))exp(\pm i\varphi_{12}(t)) \quad (2.55)$$
$$G^{(2)}(t) = \frac{32}{15\pi r^6}\langle Y_{2,2}(t)Y_{2,-2}(0)\rangle \ , \ Y_{2,\pm2}(t) = \sqrt{\frac{15}{32\pi}}sin^2(\theta_{12}(t))exp(\pm 2i\varphi_{12}(t))$$

In this representation the correlation functions of interest are the autocorrelation functions of the spherical harmonics. As was discussed in the previous paragraph, only the spin-lattice relaxation rate can be evaluated using eq. (2.54) due to the requirement for the short correlation times. Therefore, only the functions $G^{(1)}(t)$ and $G^{(2)}(t)$, which are included in the expression for $\frac{1}{T_1}$ will be discussed further. Their time dependence is determined by $\langle Y_{2,1}(t)Y_{2,-1}(0)\rangle$ and $\langle Y_{2,2}(t)Y_{2,-2}(0)\rangle$, which can be rewritten based on eq. (2.55) using the relation of the trigonometric functions with the Cartesian components of the interspin vector $\vec{r}_{12}$:

$$\langle Y_{2,1}(t)Y_{2,-1}(0)\rangle = \frac{15}{8\pi}\left(\langle\frac{r_x(t)r_x(0)r_z(t)r_z(0)}{r^4}\rangle + \langle\frac{r_y(t)r_y(0)r_z(t)r_z(0)}{r^4}\rangle\right)$$

$$\langle Y_{2,2}(t)Y_{2,-2}(0)\rangle = \frac{15}{32\pi}\left(\langle\frac{r_x^2(t)r_x^2(0)}{r^4}\rangle + \langle\frac{r_y^2(t)r_y^2(0)}{r^4}\rangle - 2\langle\frac{r_x^2(t)r_y^2(0)}{r^4}\rangle - 2\langle\frac{r_y^2(t)r_x(0)r_y(0)}{r^4}\rangle + \right.$$
$$\left. +4\langle\frac{r_x(t)r_y(t)r_x(0)r_y(0)}{r^4}\rangle\right) \quad (2.56)$$

Consider now a chain consisting of N Kuhn segments, properties of which were thoroughly discussed in *Chapter* 1. At times $t > \tau_s$ the average orientation of the interspin vector $\vec{r}_{12}$ is parallel to the tangent end-to-end vector $\vec{b}_n$ of the n^{th} Kuhn segment, which contains both the spins. Then, the terms $\frac{r_\alpha}{r}$ in eq. (2.56) can be substituted by the terms $\frac{b_{n\alpha}}{b_n}$, where b_α are the Cartesian components of the Kuhn segment's tangent end-to-end vector equal to $b_{n\alpha} = \frac{\partial R_{n\alpha}}{\partial n}$ with $R_{n\alpha}$ being the Cartesian components of the chain's end-to-end vector. Consequently, $b_{n\alpha}$ can be expressed through the Rouse normal coordinates as was demonstrated in *Chapter 1.3* using eq. (1.37):

$$b_{n\alpha} = \frac{\partial R_{n\alpha}}{\partial n} = -\frac{2\pi}{N}\sum_{p=1}^{N} pX_{p\alpha}(t)sin\left(\frac{\pi p}{N}n\right) \quad (2.57)$$

Then, the correlation function of the type $\langle b_{n\alpha}(t)b_{n\beta}(0)b_{n\gamma}(t)b_{n\delta}(0)\rangle$ with $\alpha,\beta,\gamma,\delta = x,y,z$, which are relevant for calculation of eq. (2.56), are given by:

$$\langle b_{n\alpha}(t)b_{n\beta}(0)b_{n\gamma}(t)b_{n\delta}(0)\rangle =$$
$$\left(\frac{2\pi}{N}\right)^4\sum_{p_1,p_2,p_3,p_4=1}^{N} p_1p_2p_3p_4 sin\left(\frac{\pi p_1}{N}n\right)sin\left(\frac{\pi p_2}{N}n\right)sin\left(\frac{\pi p_3}{N}n\right)sin\left(\frac{\pi p_4}{N}n\right)*$$
$$\langle X_{p_1\alpha}(t)X_{p_2\beta}(0)X_{p_3\gamma}(t)X_{p_4\delta}(0)\rangle \quad (2.58)$$

Using the orthogonality of the normal modes and the fact that the averages of each of its Cartesian components are equal, one can transform eq. (2.58) to:

$$\langle b_{n\alpha}(t)b_{n\beta}(0)b_{n\gamma}(t)b_{n\delta}(0)\rangle = \langle b_{n\alpha}(t)b_{n\beta}(0)\rangle^2 = \frac{1}{9}\langle\vec{b}_n(t)\cdot\vec{b}_{n\beta}(0)\rangle^2 \quad (2.59)$$

Substitution of this result into eq. (2.56) and (2.55) and averaging over all the segments leads to the following relation:

$$G^{(1)}(t) = 4G^{(2)}(t) = \frac{5}{12\pi}\langle\vec{b}(t)\cdot\vec{b}(0)\rangle^2 \quad (2.60)$$

It can be used to rewrite eq. (2.54) for the intrasegment (in the sense of the Kuhn segment) spin-lattice relaxation rate through the Kuhn segment's tangent vector's orientational correlation function:

$$\frac{1}{T_1^{intra}} = \frac{3}{2}\gamma^4\hbar^2 I(I+1)\left(\int_{-\infty}^{\infty}\langle\vec{b}(\tau)\cdot\vec{b}(0)\rangle^2 e^{-i\omega\tau}d\tau + 4\int_{-\infty}^{\infty}\langle\vec{b}(\tau)\cdot\vec{b}(0)\rangle^2 e^{-i2\omega\tau}d\tau\right) \quad (2.61)$$

Since the autocorrelation functions in the integrals are even by their nature, eq. (2.61) can be translated to the following simpler form, including only the real parts of the Fourier transformations:

$$\frac{1}{T_1^{intra}} = 3\gamma^4\hbar^2 I(I+1)\left(\int_0^{\infty}\langle\vec{b}(\tau)\cdot\vec{b}(0)\rangle^2 cos(\omega\tau)d\tau + 4\int_0^{\infty}\langle\vec{b}(\tau)\cdot\vec{b}(0)\rangle^2 cos(2\omega\tau)d\tau\right) \quad (2.62)$$

This expression provides a direct connection between the fluctuations of the Kuhn segment orientation in the macromolecule and the intrasegment spin-lattice relaxation rate. It serves as a basis for the calculation of the corresponding quantities for different polymer dynamics models in *Chapter 1*.

In the next paragraph conventional experimental NMR methods, which allow measurements of the spin-lattice and the spin-spin relaxation, will be discussed.

2.4 Experimental NMR methods for measuring spin relaxation

In *Chapter 2.1* it was explicitly shown that the spin operator projections tend to relax to their equilibrium values $\langle \hat{I}_z \rangle_{eq} = -\frac{\hbar\omega_0}{k_b T}\frac{I}{3}(I+1)$, $\langle \hat{I}_x \rangle_{eq} = \langle \hat{I}_y \rangle_{eq} = 0$, once they are perturbed by the radiofrequency magnetic field. Consider the pulse of the RF field, which is circularly polarized at frequency ω and is applied along the x'-axis in the rotating frame. If the resonance condition $\omega = \omega_0 = -\gamma H_0$ is satisfied, the spin in the rotating frame is then precessing around the x'-axis with a frequency ω_1. The equations of motion for the spin operator projections in the rotating frame are derived from the Euler equation and are similar to the set of eq. (2.27) with the only difference being the value and the direction of the external magnetic field. These equations can be rewritten in terms of the net magnetization M of a system consisting of N spins I:

$$\begin{cases} \frac{dM_{x'}(t)}{dt} = 0 \\ \frac{dM_{y'}(t)}{dt} = \omega_1 M_z(t) \\ \frac{dM_z(t)}{dt} = -\omega_1 M_{y'}(t) \end{cases}, \tag{2.63}$$

where $M_{x'}(t)$ and $M_{y'}(t)$ are the average components of the magnetization in the rotating frame. The effects of the spin relaxation are assumed to be negligible, since the typical duration of the RF pulses is very short ($\sim 1-10\ \mu s$) compared to the spin relaxation times. Taking into account the initial equilibrium values of the magnetization components $M_{x',y'}(0) = 0$ and $M_z(0) = \frac{N(\gamma\hbar)^2 H_0}{k_b T}\frac{I}{3}(I+1)$, solution of eq. (2.63) is given by:

$$\begin{cases} M_{x'}(t) = 0 \\ M_{y'}(t) = M_z(0)sin(\omega_1 t) \\ M_z(t) = M_z(0)cos(\omega_1 t) \end{cases} \tag{2.64}$$

It is clear that if the duration and the amplitude of the RF pulse satisfy the condition $\omega_1\tau = \frac{\pi}{2}$, then $M_{y'}(\tau) = M_z(0)$ and $M_z(\tau) = M_{x'}(\tau) = 0$. Therefore, after the switching off of the RF field the average Cartesian components of the magnetization in the laboratory frame are equal to:

$$\begin{cases} M_x(\tau) = -M_z(0)sin(\omega_0 t) \\ M_y(\tau) = M_z(0)cos(\omega_0 t) \\ M_z(\tau) = 0 \end{cases} \tag{2.65}$$

These are the initial conditions at the time moment $t = \tau$ for the free induction decay, described in *Chapter 2.3* and *2.4*. The equilibrium magnetization $M_z(0)$ is thereby transferred into the transverse plane. The magnetization components $M_x(\tau)$ and $M_y(\tau)$ are experimentally detectable quantities, conventionally measured through the induction current created in the RF coil by the alternating magnetic field.

Consider now the RF pulse applied again along the x'-axis (the same philosophy works for all the other directions in the XY-plane), which value and duration satisfy the condition $\omega_1\tau = \pi$. In this case the average Cartesian components of the net magnetization at the time moment $t = \tau$ right after the pulse are given by:

$$\begin{cases} M_x(\tau) = 0 \\ M_y(\tau) = 0 \\ M_z(\tau) = -M_z(\tau) \end{cases} \tag{2.66}$$

The transverse components of the magnetization are zero and the z-component is inverted. RF pulses satisfying the conditions $\omega_1\tau = \frac{\pi}{2}$ and $\omega_1\tau = \pi$, are called the $\frac{\pi}{2}$ (or 90°) and the π (or 180°) pulse, respectively. Further on in this work they will be addressed as the operators $\hat{P}_\alpha^{\pi/2}$ and $\hat{P}_\alpha^{\pi}$, where α denotes the axis in the rotating frame, along which the corresponding RF pulse is applied. These pulses serve as a core basis for the majority of the NMR pulse sequences.

Transverse magnetization decay measurement.

Theoretically the simplest way of measuring spin-spin relaxation is obtaining the free induction decay after the $\hat{P}_\alpha^{\pi/2}$ RF pulse. However, practically that is not usually possible. The reason for this is the fact that the transverse magnetization decay is subject to the homogenous and the inhomogeneous effects, corresponding to the homogeneous and the inhomogeneous spectral line broadening. The homogeneous effects are responsible for the "true" spin-spin relaxation and are associated with the fluctuations of the microscopic magnetic field, for instance, due to the dipolar interactions. The inhomogeneous effects, in turn, are caused by the macroscopic magnetic field gradient, appearing due to the magnetic system's imperfection as well as the local magnetic susceptibility changes in the sample, which lead to a difference between the magnetic fields sensed by the spins depending on their spatial position. An important difference between these two types of phenomena lies in the fact that the additional relaxation caused by the inhomogeneous effects can be recovered by means of the *Hahn echo* pulse sequence [83], thereby allowing for the measurement of the "true" transverse relaxation. Description of the effect of this pulse sequence onto the net magnetization and of the connection of the obtained signal with the dipolar interactions between the spins in polymer melts are among the main goals of this work and will be thoroughly discussed in *Chapter 3.* It can be briefly explained now, that the Hahn echo pulse sequence consists of $\hat{P}_x^{\pi/2}$ and $\hat{P}_{x,y}^{\pi}$ RF pulses separated by the time interval τ. During that time the transverse components of the magnetization are relaxing due to both the inhomogeneous and the homogeneous effects. After application of the $\hat{P}_{x,y}^{\pi}$ the precession of $\langle M_x \rangle$ and $\langle M_y \rangle$ is effectively reversed, which results in the formation of the *spin echo* (a symmetric signal consisting of two specular free induction decays) with a top exactly at the time moment $t = 2\tau$, called the *echo time* (usually measured from the middles of the RF pulses). The transverse magnetization decay to its equilibrium value $M_{x_{eq}} = M_{y_{eq}} = 0$ is then composed from the signal amplitudes at the echo tops measured at different echo times $2\tau_1$, $2\tau_2$ …, yielding a decay function: $M_{xy} = M_{xy}(2\tau)$. This pulse sequence is illustrated in Figure 2.2.

There is a number of the modifications of the Hahn echo pulse sequence, which are aimed to overcome some of its drawbacks or to provide additional information, such as: *Carr-Purcell-Meiboom-Gill* pulse sequence [84,85], consisting of a train of $\hat{P}_{x,y}^{\pi}$ RF pulses, which is used to exclude the effects of the diffusion. Another pulse sequence, namely *solid echo* $\hat{P}_x^{\pi/2} - \tau - \hat{P}_y^{\pi/2}$ [86], refocuses not only the homogeneous effects, but also the decay due to the secular part of the dipolar Hamiltonian. This is the beneficial feature for the investigation of the residual dipolar interactions in polymer melts and it will be discussed extensively in *Chapter 3*. The scheme of the solid echo is presented in Figure 2.3. A good overview of other conventional pulse sequences can be found, for instance, in [87].

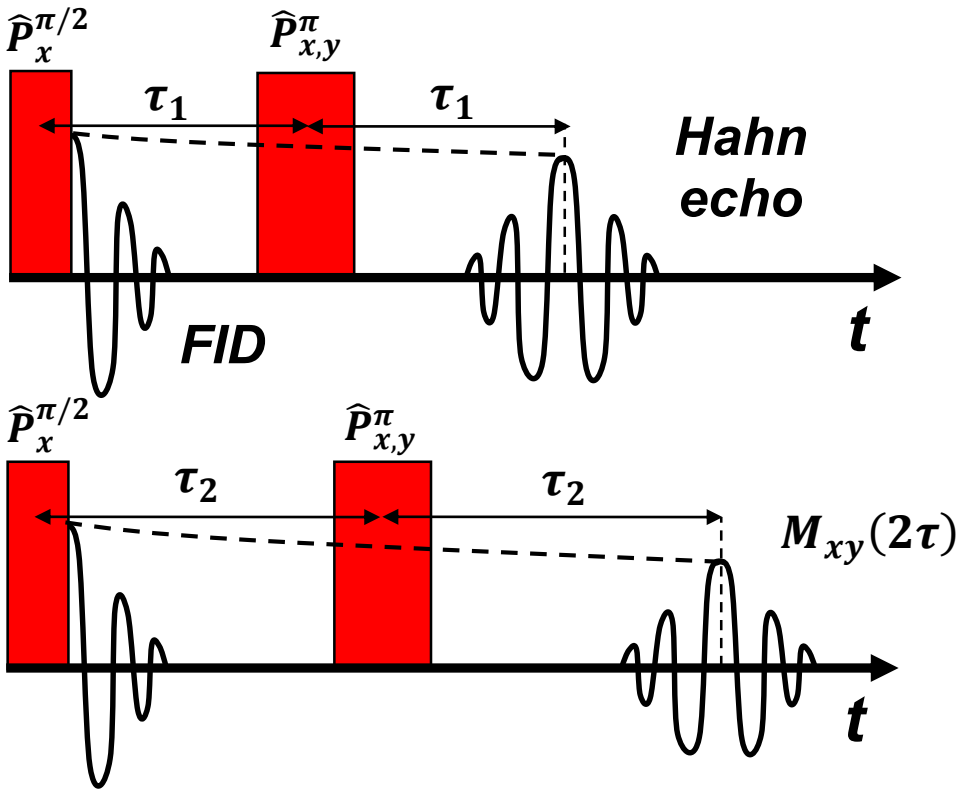

Figure 2.2. Graphical representation of the Hahn echo pulse sequence. The dashed line shows how the transverse magnetization decay composed of the echo tops is being obtained.

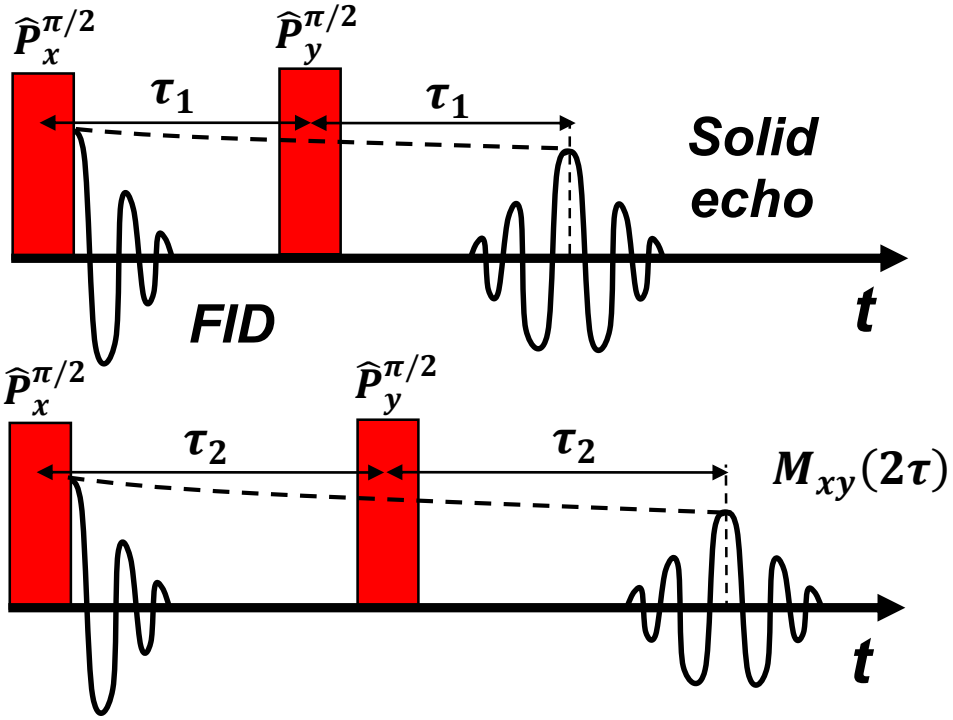

Figure 2.3. Graphical representation of the solid echo pulse sequence. The dashed line shows how the transverse magnetization decay composed of the echo tops is being obtained.

Longitudinal magnetization decay measurement. Field-cycling NMR relaxometry.

Knowledge of the spin-lattice relaxation time's frequency dispersion is a powerful tool for the investigation of polymer melt dynamics, providing relevant information about the microscopic motion, as was shown in *Chapter 2.3*. Experiments allowing for conventional measurements of spin-lattice relaxation at different magnetic fields (as a consequence, at different frequencies) can be performed by means of the *field—cycling NMR relaxometry* [88-90]. The typical scheme of the experiment is shown in Figure 2.4.

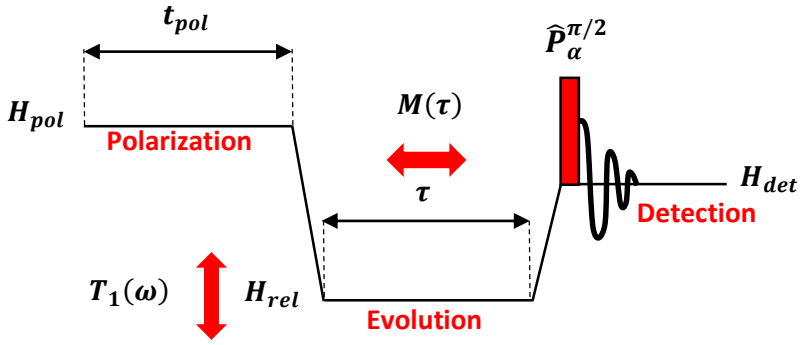

Figure 2.4. Scheme of the field-cycling spin-lattice relaxation measurement. Red arrows denote the changing evolution times τ, providing the longitudinal magnetization decay, and the variable relaxation field, which allows obtaining the frequency profile $T_1(\omega)$.

A spin system is first polarized in the polarization field H_{pol}, which is chosen to be high in order to create the larger Curie magnetization in the system $M_0(H_{pol}) = \frac{N\gamma^2\hbar^2 H_{pol}}{k_b T}\frac{I}{3}(I+1)$. For this purpose, polarization time is set to $\sim 5T_1(\omega_{pol})$. After that, the magnetic field is rapidly $(2-3ms)$ switched to the relaxation field H_{rel}. Neglecting the effect of magnetization loss during the switching time, one can assume that the initial value of the magnetization after the field switch is $M_0(H_{pol})$. Further on, the evolution of the net magnetization towards its equilibrium value in the magnetic field H_{rel} during the time interval τ is described by the Bloch equation with the solution given by:

$$M(\tau) = M_0(H_{rel}) + \left(M_0(H_{pol}) - M_0(H_{rel})\right) exp\left(-\frac{\tau}{T_1(H_{rel})}\right) \quad (2.67)$$

After the time interval τ the magnetic field is switched to the detection field H_{det}. Again assuming no losses during the switching time, the net magnetization is equal to $M(\tau)$ given by eq. (2.67). Immediate subjection of the spin system to the $\hat{P}_{\alpha}^{\pi/2}$ RF pulse allows recording the FID signal, initial value of which is equal to $M(\tau)$, as discussed earlier.

Thus, repeating such an experimental cycle with the different evolution times τ in the same relaxation field allows obtaining the spin-lattice relaxation curve and the value of T_1. Employing this sequence of experiments in the different relaxation fields provides the Larmor frequency profile of the spin-lattice relaxation time $T_1(\omega)$. In *Chapter 3* contributions from the intramolecular and the intermolecular dipolar interactions to such a profile will be discussed, and in *Chapter 4* the corresponding experimental results obtained in entangled polymer melts will be presented.

Double-quantum spectroscopy.

Double-quantum NMR pulse sequences are widely used to directly probe dipolar couplings in different systems, which are characterized by the non-averaged dipole-dipole interactions, such as solids [91,92], polymeric materials [93,94] etc. Unlike in the previously discussed experiments, the aim of the double-quantum pulse sequence is to create the conditions, when the spin system is evolving under the so-called *double-quantum Hamiltonian* [95]. Despite of a variety of the existing pulse sequences, most of them in the case of a system containing N spins I lead to the same form of this Hamiltonian, given in the rotating frame by:

$$\hat{H}_{DQ} = \frac{\gamma^2\hbar^2(3cos^2(\theta_{ij})-1)}{2r_{ij}^3}\sum_{i<j}\left(\hat{I}_i^+\hat{I}_j^+ - \hat{I}_i^-\hat{I}_j^-\right) = \frac{\gamma^2\hbar^2(3cos^2(\theta_{ij})-1)}{2r_{ij}^3}\sum_{i<j}\left(\hat{I}_{ix}\hat{I}_{jx} - \hat{I}_{iy}\hat{I}_{jy}\right) \quad (2.68)$$

This expression contains only the double-quantum terms in contrast to the secular part of the full dipole-dipole interaction Hamiltonian, eq. (2.30). These terms can actually cause coherent transitions between the energy levels of the even number of spins – this is called a *multiple-quantum coherence* (*double-quantum coherence* in the case of a single spin pair). In *Chapter 4* results obtained in polymer melts with the use of the modified double-quantum pulse sequence [96] based on the experiment originally suggested by Baum and Pines [92] are presented. Both of these pulse sequences are illustrated in Figure 2.5.

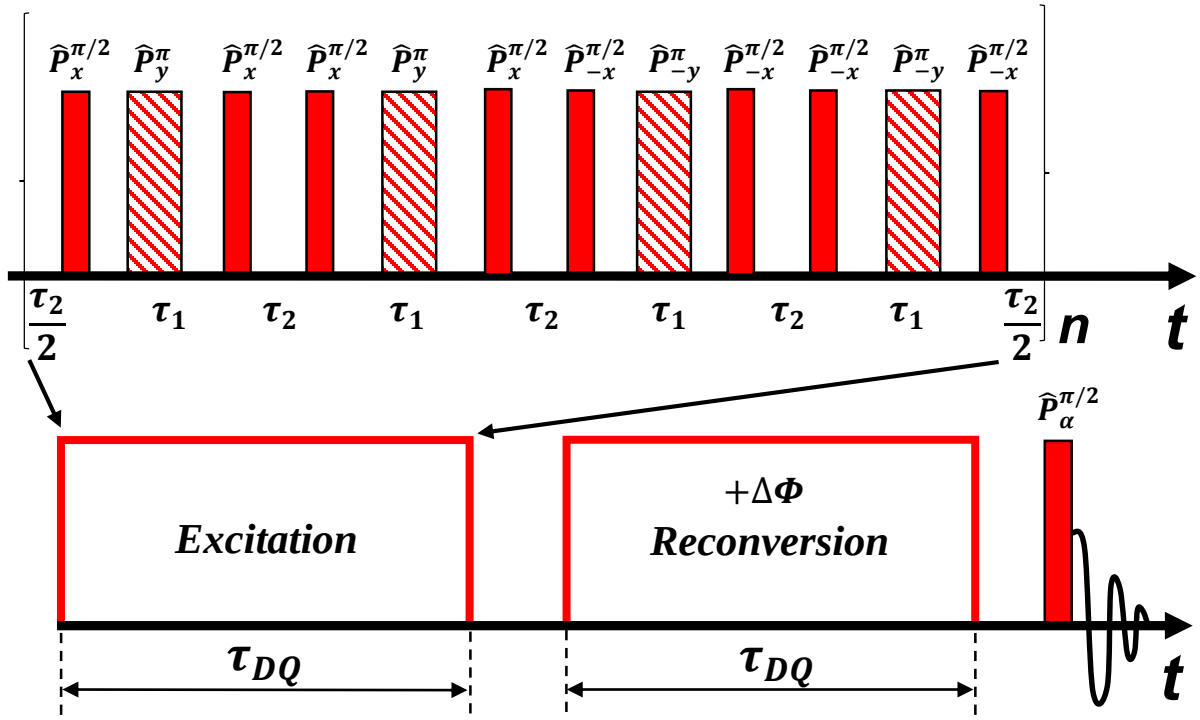

Figure 2.5. Graphical representation of the Baum-Pines pulse sequence. Excitation and reconversion periods consist of the same number of cycles n illustrated on the upper sketch, with a phase shift $\Delta\Phi$ of the RF pulses during the reconversion. τ_1 is a separation between the 1st and the 2nd $\frac{\pi}{2}$ pulse and so on, τ_2 is a separation between the 2nd and the 3rd $\frac{\pi}{2}$ pulse and so on. The dashed π pulses inserted in the middle between the corresponding $\frac{\pi}{2}$ pulses represent the modification of the classic Baum-Pines sequence, introduced in [96].

The pulse sequence consists of the two periods: excitation and reconversion. The excitation period represents n time cycled pulse train illustrated on the upper sketch of Figure 2.5 and creates the double-quantum Hamiltonian, given by eq. (2.68). Its duration τ_{DQ} defines the time scale of the experiment and is determined by the combination of the number of cycles n and the separation between the RF pulses: $\tau_1 = 2\tau_2 + d_{\pi/2}$, where $d_{\pi/2}$ is a duration of the $\hat{P}_\alpha^{\pi/2}$ pulse. The reconversion pulse train has the same structure and duration as the excitation, however, all the phases of the RF pulses are shifted by $\Delta\Phi$, which is incremented in a four-step phase cycle. The last $\hat{P}_\alpha^{\pi/2}$ converts the dipolar multi-quantum coherences into the observable transverse magnetization. Modification of this sequence, according to [96] implies inserting $\hat{P}_\alpha^{\pi}$ pulses in the middle between the $\hat{P}_\alpha^{\pi/2}$ pulses, as is shown in Figure 2.5. This change is able to improve the stability of the experiment at long times by canceling the offset effects, as well as by compensating the RF pulses imperfections.

Depending on the phase cycle of the receiver phase, this pulse sequence can yield the *double-quantum build-up curve* I^{DQ} or the so-called reference signal I^{ref}, which comprises all the magnetization that has not evolved into the double-quantum coherences. Then, the normalized double-quantum build-up function can be constructed: $I^{nDQ} = \frac{I^{DQ}}{I^{DQ}+I^{ref}}$. It is free of the effects caused by the transverse relaxation and the long-time instrumental errors, therefore providing more reliable information. This function is connected to the residual, not averaged dipolar couplings in the system (for instance, in isotropic liquids it equals to zero). Therefore, the double-quantum spectroscopy serves as a good tool for probing molecular dynamics in entangled polymer melts. In *Chapter 3* a devoted formalism for the evaluation of the double-quantum build-up function with a special focus on the effects of the intermolecular dipolar interactions will be discussed.

Chapter 3. Intermolecular Dipolar Interactions

In the previous chapters it was shown that one of the key parameters characterizing polymer melt dynamics, namely Kuhn segment orientational correlation function $\langle \vec{b}(\tau) \cdot \vec{b}(0) \rangle$, affects the shape of the NMR spin-lattice and spin-spin relaxation curves through the modulation of the dipolar interactions between the spins, thereby providing a way to probe the segmental dynamics by means of the NMR relaxation experiments. Special focus was set onto the case of spin $I = \frac{1}{2}$, since it is especially relevant for polymeric macromolecules, which normally contain a large number of interacting hydrogen atoms.

Evaluation of the spin relaxation data is carried out in terms of the pairwise interactions between the spins. As was shown in *Chapter 2.3*, taking into account only the spins belonging to the same Kuhn segment leads to a relatively simple expression for the intrasegment spin-lattice relaxation rate $\frac{1}{T_1^{intra}}$, given by eq. (2.62). During the long history of NMR in polymer melts it was actually almost always assumed that the intrasegment contribution dominates the spin-lattice relaxation, as well as the spin-spin relaxation, and that the intersegment and intermolecular dipolar interaction are too weak to have a considerable impact on the experimental results [93,96,97,98]. This is a well-known assumption commonly used in the solid-state NMR, where the dipolar interactions are determined by the closest neighbors in a rigid lattice [81].

However, a series of works published throughout the last two decades showed theoretical and experimental evidence that called this assumption into question. In the work [99] the intramolecular and the intermolecular dipolar interactions were evaluated separately in polybutadiene and polyethylene oxide melts. It was shown with the use of the field-cycling NMR relaxometry that even though the intrasegment contribution to the spin-lattice relaxation is prevalent at short times/high Larmor frequencies, considerable impact of the intermolecular interactions arises at long times/short Larmor frequencies. Later on, these effects were studied in more detail and the theoretical formalism providing the connection between the intermolecular spin-lattice relaxation rate and the mean squared displacement of the spins belonging to the different macromolecules was developed [100,101]. This is possible due to the fact that the intrasegment dipolar interaction is almost exclusively governed by the rotational motion of the Kuhn segment, due to the approximately fixed distance between the interacting spins. In turn, the intermolecular dipolar interaction is mostly modulated by the translation of the segments, especially, at longer times, when they become more relevant.

It should be also mentioned that it was theoretically shown [102] and experimentally proved in polyethylene oxide melts [103] that the intermolecular dipolar interactions play an important role in the process of the spin diffusion in polymer melts.

The illustration of the situation typically encountered in the entangled polymer melts is shown in Figure 3.1. It demonstrates the spatial positions of the spins contributing to the intrasegment and the intermolecular dipolar interactions, and also the character of the interactions between the spin pairs. In [104,105] the dipolar correlation functions for the case of the intrasegment, intersegment and intermolecular interactions in polymer melts were calculated for the different models of polymer dynamics. A brief overview of these results will be given and the way they can be used to discriminate between the polymer dynamics models will be discussed in *Chapter 3.1*. More details about the inter- and the intramolecular interactions in different systems can be found in the recent review articles [30,106].

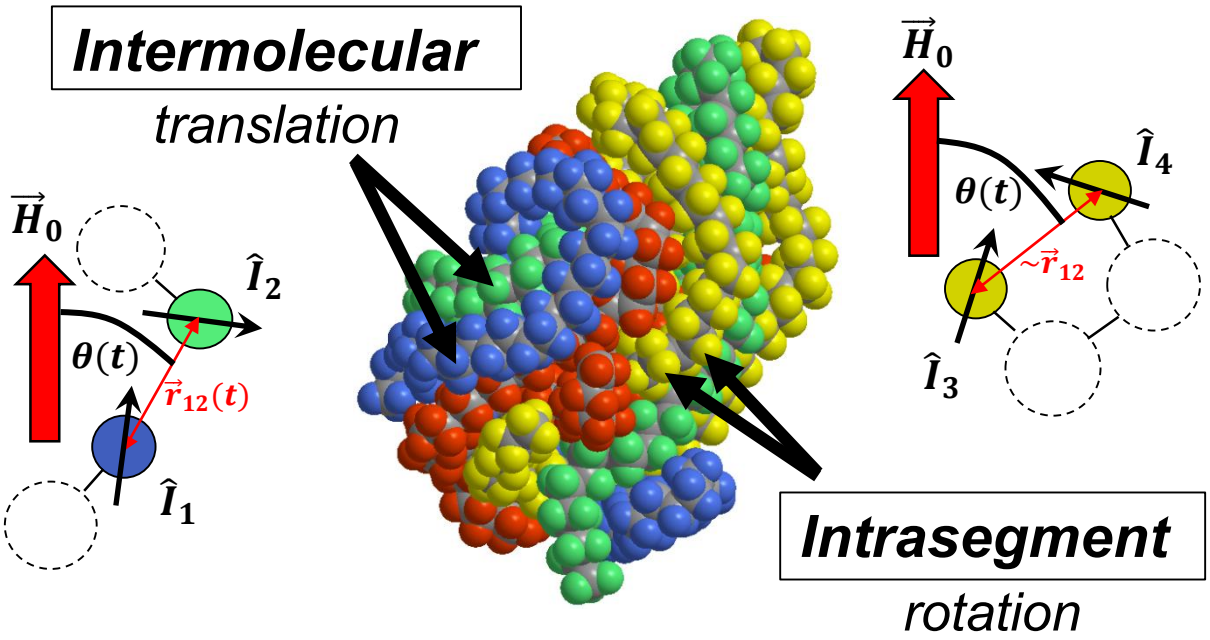

Figure 3.1. Illustration of the spatial positions of the dipolar coupled spins in an entangled polymer melt. This conformation is modeled in *Chem3D* for 4 similar linear macromolecules, consisting of 75 backbone carbon atoms, which are marked with grey. Hydrogen atoms are marked with blue, yellow, green and red for the respective macromolecules. The enlarged detailed sketches correspond to the two cases of the dipolar interactions.

Development of the formalism taking into account all the spins in the system while evaluating the spin-lattice relaxation in polymer melts and the first proofs of it, mentioned above, led to the emerge of the series of the experimental works, in which the field-cycling NMR relaxometry was successfully applied to the investigation of the segmental diffusion and of the orientational correlation function in polymer melts at the time scale $10^{-9} - 10^{-4}\ s$ (to be cited further on).

The same theoretical approach was also used in [105,107] to evaluate the transverse magnetization decay and the double-quantum build-up function. A brief description of the important theoretical outcomes applied to all the three methods (field cycling, transverse relaxation and double-quantum spectroscopy) will be presented in *Chapter 3.4* and *3.5.* Part of the experimental results shown and discussed in *Chapter 4* are obtained and evaluated by means of these techniques.

However, the main focus of *Chapter 3* is set on the introduction of the two novel NMR methods, based on the spin-spin relaxation measurements. One method is uses the so-called *solid echo build-up function* and is described in detail in *Chapter 3.2.* The other method benefits from the construction of the *dipolar-correlation build-up function* and is thoroughly discussed in *Chapter 3.3.* Both of them reflect the features of the polymer segmental dynamics and are shown to be able to serve as an indicator of the validity of the different theoretical models. It is actually demonstrated that these NMR methods can directly provide information about the segmental translation in a time range of milliseconds, which is hardly accessible to the conventional experimental techniques. Properties of the solid-echo and the dipolar-correlation build-up functions and their comparison with other methods, usually applied in polymer melts, are presented in *Chapter 3.4 and 3.5.* These two methods were first introduced, discussed and experimentally applied in polymer melts in [49,108,109].

3.1. Revisiting time dependence of the dipolar correlation function

In *Chapter 2* it was discussed that the knowledge of the dipolar correlation function, eq. (2.53) and (2.55), and of its connection with the NMR spin relaxation allows for the determination of the features of polymer melt dynamics from the experimental data. However, the formalism presented before considered the dipole-dipole interaction only between the two spins belonging to the same Kuhn segment, i.e. the interspin distance is constant and the dipolar correlation function is determined by the orientation of the spin pair. This theoretical approach was often applied to evaluation of the experimental data on the spin-lattice relaxation using eq. (2.62) [25-27]. There is a number of prominent works, in which the similar formalism based on the consideration of the intrasegment spin-pair interaction, was applied to the investigation of the features of the spin-spin relaxation in polymer melts [97,98,110-114].

Nevertheless, after the appearance of the experimental evidence of the non-negligible effect of the intermolecular dipolar interaction had been presented (mentioned in the introduction to this *Chapter*), demand for the rigorous theoretical reconsideration of the character of the dipolar interactions in polymer melts arose. This problem was successfully tackled by Fatkullin *et al.* in the works [104,105]. Important predictions for the intrasegment $A_0^{d;intra}$, the intersegment (segments of the same macromolecule) $A_0^{d;ss}$ and the intermolecular $A_0^{d;inter}$ contributions to the total dipolar correlation function A_0^d were made for the isotropic renormalized Rouse model and for the anisotropic regimes II and III of the tube-reptation model of polymer dynamics.

The total dipole-dipole correlation function is connected with $G^{(0)}(t)$ introduced in eq. (2.53), as:

$$A_0^d(t) = \frac{1}{N_s}\sum_{km} G_{km}^{(0)}(t) = \frac{1}{N_s}\sum_{km} \langle \frac{\left(1-3cos^2(\theta_{km}(t))\right)}{r_{km}^3(t)} \frac{\left(1-3cos^2(\theta_{km}(0))\right)}{r_{km}^3(0)} \rangle \tag{3.1}$$

The summation can be split into the abovementioned contributions:

$$A_0^d(t) = A_0^{d;intra} + A_0^{d;ss} + A_0^{d;inter} \tag{3.2}$$

It was shown that the intrasegment contribution $A_0^{d;intra}$ is given by:

$$\begin{cases} A_0^{d;intra} \propto \dfrac{S_{ij}^2 b^5}{\left(r_{ij}^{near}\right)^6 d_t^3 \langle r^2(t)\rangle}, & anisotropic\ motion \\ A_0^{d;intra} \propto \dfrac{5\beta^2 S_{ij}^2 b^4}{12\pi^3\left(r_{ij}^{near}\right)^6 \langle r^2(t)\rangle^2}, & isotropic\ motion \end{cases} \tag{3.3}$$

Here r_{ij}^{near} denotes the distance between the nearest protons in a macromolecule, b is the Kuhn segment length, d_t is the tube diameter, β is the model-specific coefficient connecting the segmental mean squared displacement with the correlation function of the Kuhn segment's tangent vector $\langle \vec{b}(t)\vec{b}(0)\rangle$, i.e. for the twice renormalized Rouse model $\beta = \frac{2}{3sin\left(\frac{\pi}{3}\right)} \cong 0.77$. S_{ij} is the spin-segment coupling parameter, describing the orientation of the spin pair relatively to the corresponding Kuhn segment's tangent vector ($0 \le S_{ij} \le 1$) depending on its microstructure.

The intersegment contribution $A_0^{d;ss}$ is given by:

$$\begin{cases} A_0^{d;ss} \propto \dfrac{\tilde{N}_s}{b^2 d_t^2 \langle r^2(t)\rangle}, & anisotropic\ motion \\ A_0^{d;ss} \propto \dfrac{9\tilde{N}_s}{5\pi^4\beta b^2 \langle r^2(t)\rangle^2} ln\left(\dfrac{25\pi^4\beta^2\langle r^2(t)\rangle^2}{18b^2}\right), & isotropic\ motion \end{cases} \tag{3.4}$$

Here $\widetilde{N}_s$ is the number of spins per Kuhn segment. Comparison of eq. (3.3) and (3.4) leads to the following relations:

$$\begin{cases} \frac{A_0^{d;ss}}{A_0^{d;intra}} \propto \frac{\widetilde{N}_s d_t}{b S_{ij}^2} \left(\frac{r_{ij}^{near}}{b}\right)^6, & anisotropic\ motion \\ \frac{A_0^{d;ss}}{A_0^{d;intra}} \propto \frac{108 \widetilde{N}_s}{25\pi\beta^3 S_{ij}^2} \left(\frac{r_{ij}^{near}}{b}\right)^6 ln\left(\frac{25\pi^4\beta^2\langle r^2(t)\rangle^2}{18b^2}\right), & isotropic\ motion \end{cases} \quad (3.5)$$

Factor $\left(\frac{r_{ij}^{near}}{b}\right)^6$ is a very small quantity on the order of $10^{-6} - 10^{-3}$ and $ln\left(\frac{25\pi^4\beta^2\langle r^2(t)\rangle^2}{18b^2}\right)$ is the function that increases very slowly with time. Therefore, for any typical values of the parameters included in eq. (3.5), both the expressions for anisotropic and isotropic models of motion tend to decay to zero at times $t \gg \tau_s$. Thus, the intramolecular contribution to the total dipolar correlation function is dominated by its intrasegment part $A_0^{d;intra}$, independently of the character of the motion. This was experimentally proven in entangled polyethylene oxide and polybutadiene melts in [101].

Consider now the intermolecular contribution $A_0^{d;inter}$, which is actually independent of the model of polymer dynamics and is determined by:

$$A_0^{d;inter} = \sqrt{\frac{2}{3\pi}} \frac{16\pi}{5} \frac{n_s}{\left(\sigma^* + \langle \tilde{r}^2(t)\rangle^{\frac{1}{2}}\right)^3}, \quad (3.6)$$

where n_s is the concentration of spins in the system, σ^* is the effective diameter of the macromolecular chain, $\langle \tilde{r}(t)\rangle$ is the relative segmental mean squared displacement. Generally, determination of the connection between the absolute and the relative MSD is a complicated problem, which is not solved. Nevertheless, it is possible to point out some limiting cases. If the two segments are rigidly connected and move together $\langle \tilde{r}(t)\rangle = 0$. On the other hand, if the motions of the each segment are not correlated with each other, then $\langle \tilde{r}(t)\rangle = 2\langle r(t)\rangle$. This situation takes place in entangled polymer melts at times $t \ll \tau_s$ and $t \gg \tau_1$. Therefore, it is justified to assume that in the intermediate cases $\langle r(t)\rangle = \tilde{\alpha}\langle \tilde{r}(t)\rangle$, where $0 < \tilde{\alpha} < 2$. As was described in *Chapter 1.5*, in the framework of the tube-reptation model each chain is moving inside its own tube, which means that this model predicts uncorrelated motion of the different chains, consequently, $\tilde{\alpha} = 2$ for the whole time scale. Therefore the experimental data evaluation in *Chapter 4* will be carried out assuming that $\tilde{\alpha} = 2$. In spite of the fact that this assumption is rather justified and that the value of $\tilde{\alpha}$ can lie exclusively in a narrow region $0 \leq \tilde{\alpha} \leq 2$ thus only slightly affecting the value of the MSD, its application should be kept in mind.

Comparison of eq. (3.3) and (3.6) leads to the important outcome:

$$\begin{cases} \frac{A_0^{d;inter}}{A_0^{d;intra}} \propto \langle r^2(t)\rangle^{-\frac{1}{2}}, & anisotropic\ motion \\ \frac{A_0^{d;inter}}{A_0^{d;intra}} \propto \langle r^2(t)\rangle^{\frac{1}{2}}, & isotropic\ motion \end{cases} \quad (3.7)$$

The dependence of the relative ratio of the inter- and the intramolecular contributions to the total dipole-dipole correlation function on the segmental mean squared displacement is essentially different in the case of anisotropic ($\propto \langle r^2(t)\rangle^{\frac{1}{2}}$) and isotropic ($\propto \langle r^2(t)\rangle^{-\frac{1}{2}}$) motion. This feature can serve as a powerful indicator that reflects the character of the segmental motion in a polymer melt and can help to discriminate between the models of polymer dynamics. The experimental separation of the inter- and the

intra- contributions is possible by means of the isotopic dilution technique. Protonated polymer chains are diluted and homogeneously mixed with the deuterated chains of the same polymer species, of the same or similar molecular weight. Eventually, a sample consisting of the tagged protonated chains in the deuterated matrix is created. The intermolecular dipolar interaction between the protons in this sample are decreased. Extrapolation to the zero proton concentration yields the pure intramolecular contribution $A_0^{d;intra}$ to the total dipolar correlation function. Comparison with the reference fully protonated sample, which comprises both intra- and inter- contributions, allows to obtain $A_0^{d;inter}$. This procedure will be described in detail for polyethylene oxide in *Chapter 4.4.*

In Figure 3.2 the time dependence of the intermolecular $A_0^{d;inter}$ and the intramolecular $A_0^{d;intra}$ dipolar correlation functions, as predicted by the tube-reptation model, is plotted. Long-time limit $t \gg \tau_d$ of $A_0^{d;intra}$ is given by the exponential correlation function for the isotropic rotational diffusion with a correlation time τ_r.

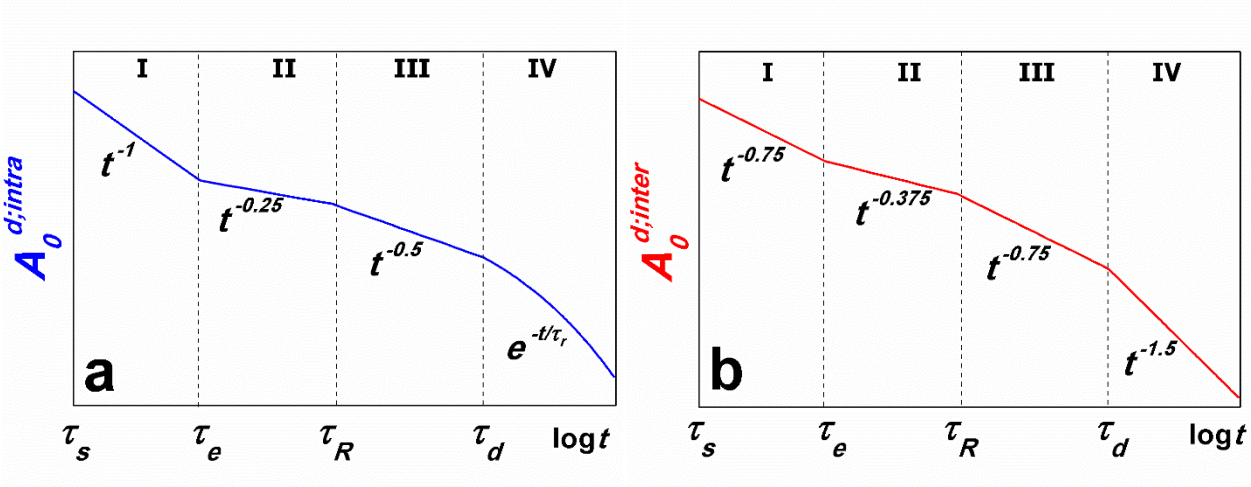

Figure 3.2. Time dependence of the intermolecular $A_0^{d;inter}$ (a) and the intramolecular $A_0^{d;intra}$ (b) dipolar correlation functions as predicted by the tube-reptation model.

3.2. Solid echo build-up function

In order to extract information about the time-dependence of the proton dipole-dipole correlation function and the segmental mean-squared displacement in a polymer melt, a special function should be considered, which is constructed from the signals given by the three different spin echo experiments:

- $S_1 - \left(\hat{P}_x^{\pi/2} - \tau - \hat{P}_y^{\pi/2}\right)$, known as *solid echo* (Figure 2.3)
- $S_2 - \left(\hat{P}_x^{\pi/2} - \tau - \hat{P}_x^{\pi/2}\right)$
- $S_2 - \left(\hat{P}_x^{\pi/2} - \tau - \hat{P}_y^{\pi}\right)$, known as *Hahn echo* (Figure 2.2)

The proposed function is named the *solid-echo build-up function* and is defined by the following equation:

$$I^{SE}(t) = \frac{S_1(t)+S_2(t)-S_3(t)}{S_1(t)+S_2(t)} \tag{3.8}$$

In this expression $t = 2\tau$ is the time moment at which the spin echo is observed and τ is the interval between the two RF pulses. If the system is characterized by the fully averaged out dipolar interactions and its spin-spin relaxation decay is exponential, then the solid-echo build-up function equals zero. It will be shown that the initial rise of this function contains additive contributions from the intra- and the intermolecular dipolar interactions, with the latter comprising the information about the translational motion of the segments. Derivation presented in this paragraph follows closely the derivation published in [49] and [109].

Calculation of solid echo S_1 signal.

Consider a system described by the following Hamiltonian:

$$\hat{H} = \hat{H}_s + \hat{H}_L + \hat{H}_{dd}^{sec} \tag{3.9}$$

In this expression $\hat{H}_s = \sum_k \hbar\omega_0 \hat{I}_{kz}$ is the Zeeman spin Hamiltonian describing the interaction of proton spins with the external magnetic field H_0, $\omega_0 = -\gamma H_0$ is the Larmor frequency corresponding to that magnetic field, $\hat{H}_L$ is the Hamiltonian of the lattice degrees of freedom related to the motion of the macromolecules in space, and $\hat{H}_{dd}^{sec}$ is the secular part of the dipole-dipole interaction Hamiltonian, where only homonuclear interactions of ^1H nuclei are considered further on. The latter gives the main contribution to the transverse relaxation at high frequencies and can be expressed in the following way, generalizing the expression given in *Chapter 2.3* for all the spin pairs in the system:

$$\hat{H}_{dd}^{sec} = \frac{1}{2}\sum_{k,l} A_{kl}\left(\hat{I}_{kz}\hat{I}_{lz} - \frac{1}{4}\left(\hat{I}_k^+\hat{I}_l^- + \hat{I}_k^-\hat{I}_l^+\right)\right), \tag{3.10}$$

where for $k \neq l$

$$A_{kl} = \frac{\gamma^2\hbar^2}{r_{kl}^3}\left(1 - 3cos^2(\theta_{kl})\right) \tag{3.11}$$

Here k and l are the indices enumerating the spins, r_{kl} is the distance between spins k and l, θ_{kl} is the angle between the direction of H_0 and r_{kl}, $A_{kk} = 0$. Factor $\frac{1}{2}$ appears, in contrast to the expression given in *Chapter 2.3* for a single spin pair, due to the summation in eq. (3.10) and the fact that $A_{kl} = A_{lk}$. For the better representation, the expression for $\hat{H}_{dd}^{sec}$ can be rewritten as follows:

$$\hat{H}_{dd}^{sec} = \frac{3}{4}\sum_{k,l} A_{kl}\hat{I}_{kz}\hat{I}_{lz} - \frac{1}{4}\sum_{k,l}\tilde{A}_{kl}\hat{I}_k \cdot \hat{I}_l \tag{3.12}$$

In eq. (3.12), $\hat{I}_k \cdot \hat{I}_l = \hat{I}_{kx}\hat{I}_{lx} + \hat{I}_{ky}\hat{I}_{ly} + \hat{I}_{kz}\hat{I}_{lz}$ and $\tilde{A}_{kl} = A_{kl} - 2J_{kl}$, where J_{kl} is the constant of an exchange interaction between spins k and l. The scalar part of eq. (3.12) is usually neglected for the sake of simplification of the calculations in the framework of the Anderson-Weiss approximation, used in the cases where incomplete motional narrowing conditions take place and the Redfield limit is not satisfied [115]. The scalar term comprises the spin diffusion phenomenon due to the presence of the zero-quantum transitions, causing the interspin flip-flop interactions. In [105] it was shown that taking into account the scalar term leads to a deviation from the standard Anderson-Weiss approach of less than 10% for times $t \leq 2T_2^{eff}$, where T_2^{eff} is the effective spin-spin relaxation time (time by which magnetization decays by *e* times) of a spin system governed by the Hamiltonian given by eq. (3.10). It means that in this time range neglecting the scalar term while analyzing the experimental data is acceptable.

Now consider the response of the spin system to the RF pulse sequence $\left(\hat{P}_x^{\pi/2} - \tau - \hat{P}_y^{\pi/2}\right)$, previously described in *Chapter 2.4* and depicted in Figure 2.3 - solid echo. At the time origin, the state of the total (spin + lattice) system is described by the equilibrium density matrix:

$$\hat{\rho}_{eq} = \frac{1}{Z} exp\left(-\frac{\hat{H}}{k_b T}\right) \cong \hat{\rho}_{eq}^{s}\hat{\rho}_{eq}^{L} = \frac{1}{Z_s} exp\left(-\frac{\hat{H}_s}{k_b T}\right)\hat{\rho}_{eq}^{L} \cong \frac{1}{Z_s}\left(1 - \frac{\hbar\omega_0}{k_b T}\hat{I}_z\right)\hat{\rho}_{eq}^{L} \quad (3.13)$$

In this expression $\hat{\rho}_{eq}^{L}$ is the equilibrium density matrix of the lattice, $Z_S \cong (2I+1)^{N_S}$ is the statistical sum of the spin system in the high-temperature approximation, i.e. $\frac{\hbar\omega_0}{k_b T} \ll 1$, which is valid with high accuracy at any temperature above $\sim 10\, mK$, N_s is the total number of spins with the resonance frequency ω_0 and $\hat{I}_z = \sum_k \hat{I}_{kz}$. After application of the first RF pulse $\hat{P}_x^{\pi/2}$, rotating the spins by an angle $\frac{\pi}{2}$ about the x-axis, the equilibrium matrix $\hat{\rho}_{eq}$ turns into:

$$\hat{\rho}_0 = \hat{P}_x^{\pi/2}\hat{\rho}_{eq} = exp\left(-i\frac{\pi}{2}\hat{I}_x\right)\hat{\rho}_{eq} exp\left(i\frac{\pi}{2}\hat{I}_x\right) \cong \frac{1}{Z_s}\left(1 + \frac{\hbar\omega_0}{k_b T}\hat{I}_y\right)\hat{\rho}_{eq}^{L} \quad (3.14)$$

The system now follows the free evolution determined by the Hamiltonian in eq. (3.9) and the density matrix of the total system at the time moment t is equal to:

$$\hat{\rho}(t) = \hat{S}(t)\hat{\rho}_0 = exp\left(-it\hat{L}_H\right)\hat{\rho}_0, \quad (3.15)$$

where, for the purpose of abbreviation, the Liouville space formalism is used (see, for example [72]), i.e. $\hat{S}(t)$ is the superoperator of the evolution caused by the Hamiltonian $\hat{H} = \hat{H}_s + \hat{H}_L + \hat{H}_{dd}^{sec}$, which, by definition, is acting in accordance with the following rule:

$$\hat{S}(t)\hat{\rho}_0 = exp\left(-i\hat{H}t\right)\hat{\rho}_0 exp\left(i\hat{H}t\right) \quad (3.16)$$

$\hat{L}_H$ is the Liouville operator defined by the relation:

$$\hat{L}_H\hat{\rho} = \frac{1}{\hbar}\left[\hat{H};\hat{\rho}\right] \quad (3.17)$$

After that, at time $t = \tau$, the second RF pulse $\hat{P}_y^{\pi/2}$ acts on the spin system and rotates the magnetization by an angle $\frac{\pi}{2}$ about the y-axis. Considering the situation when the experimentally measurable quantity $S_1(t)$ is the y-component of the total spin of the system $\langle \hat{I}_y \rangle$, its value at the time moment *t* can be calculated with the help of the statistical operator $\hat{\rho}(t)$ in accordance with its description in *Chapter 2.1* and eq. (3.14) and (3.15) , yielding the following expression:

$$S_1(t) = \langle \hat{I}_y(t) \rangle = Tr\left(\hat{I}_y\hat{\rho}(t)\right) \cong \frac{\hbar\omega_0}{k_b T(2I+1)^{N_S}} Tr\left(\hat{I}_y\hat{S}(t-\tau)\hat{P}_y^{\pi/2}\hat{S}(\tau)\hat{I}_y\hat{\rho}_{eq}^{L}\right), \quad (3.18)$$

where $Tr(\dots)$ is the trace operation over all the spin and lattice variables, and $\hat{I}_z = \sum_k \hat{I}_{kz}$. Within the accuracy of the high-temperature approximation, eq. (3.18) is exact. Its further evaluation demands

approximations due to the presence of the multi-particle interaction term $\widehat{H}_{dd}^{sec}$ given by eq. (3.10) in the total Hamiltonian (eq. (3.9)). Subsequently, the modified Anderson-Weiss approximation is going to be used, details of which can be found in [105].

A first step of this approximation is based on the transition to the interaction, or Dirac, representation. The main difference from the usual standard schemes is contained in choosing the so-called "Zero Hamiltonian", which in the present case includes the scalar part of the Hamiltonian $\widehat{H}$ and is defined as:

$$\widehat{H}_0 = \widehat{H}_S + \widehat{H}_L - \frac{1}{4}\sum_{k,l} \tilde{A}_{kl}\hat{I}_k \cdot \hat{I}_l \tag{3.19}$$

Consequently, in this case the role of perturbation is assumed by the following Hamiltonian:

$$\widehat{H}_{dd}^{sec;zz} = \frac{3}{4}\sum_{k,l} A_{kl}\hat{I}_{kz}\hat{I}_{lz} \tag{3.20}$$

Eq. (3.18) can be rewritten as:

$$S_1(t) = \frac{\hbar\omega_0}{k_b T(2I+1)^{N_S}} Tr\left(\hat{I}_y \hat{\tilde{S}}_{dd}^{sec}(t-\tau;\tau)\hat{S}_0^{-1}(\tau)\hat{P}_y^{\pi/2}\hat{S}_0(\tau)\hat{\tilde{S}}_{dd}^{sec}(\tau;0)\hat{I}_y\hat{\rho}_{eq}^{L}\right) \tag{3.21}$$

Here $\hat{S}_0(\tau) = exp\left(-it\hat{L}_0\right)$ is the superoperator of evolution created by the Hamiltonian $\widehat{H}_0$ given by (A11) and

$$\hat{\tilde{S}}_{dd}^{sec}(t_2,t_1) = \hat{T}exp\left(-i\int_{t_1}^{t_2}\hat{\tilde{L}}_{dd}^{sec;zz}(t')\,dt'\right) \tag{3.22}$$

is the superoperator of evolution created by the Hamiltonian $\widehat{H}_{dd}^{sec;zz}$, given by eq. (3.20), in the interaction representation, where $\hat{T}$ denotes the Dyson time ordering operator.

As a next step, for the calculation with the superoperator $\hat{\tilde{S}}_{dd}^{sec}(t_2,t_1)$ one can use the standard quantum statistical perturbation theory, truncating the series decomposition on terms having the second order of magnitude with respect to $\int_{t_1}^{t_2}\hat{\tilde{L}}_{dd}^{sec;zz}(t')\,dt'$. In this case contributions of the higher orders of magnitude can be recovered using the second cumulant, i.e. the Anderson-Weiss, approximation for calculating the spin echo signal. For realization of this procedure it is necessary to be able to calculate the time evolution of the operators having the structure:

$$\hat{S}_0^*(t)\hat{I}_{kz}\hat{I}_{lz} = exp\left(i\frac{\widehat{H}_0}{\hbar}t\right)\hat{I}_{kz}\hat{I}_{lz}exp\left(-i\frac{\widehat{H}_0}{\hbar}t\right) \tag{3.23}$$

In the present case the Zero Hamiltonian $\widehat{H}_0$ includes the scalar part of the spin-spin interactions and, due to that, the right part of eq. (3.23) cannot be calculated exactly. The approximation suggested in [105] implies replacing the right-hand side of eq. (3.23) by its projection in the sense of Zwanzig-Mori [63,64,81]:

$$\hat{S}_0^*(t)\hat{I}_{kz}\hat{I}_{lz} \cong \hat{P}_{kl}^{zz}\hat{S}_0^*(t)\hat{I}_{kz}\hat{I}_{lz} = \hat{I}_{kz}\hat{I}_{lz}\frac{Tr\left(\hat{I}_{kz}\hat{I}_{lz}\hat{S}_0^*(t)\hat{I}_{kz}\hat{I}_{lz}\hat{\rho}_{eq}^{L}\right)}{Tr_s(\hat{I}_{kz}\hat{I}_{lz})^2} = \hat{I}_{kz}\hat{I}_{lz}P_{kl}^{fl}(t), \tag{3.24}$$

where $Tr_s(\ldots)$ is the trace operation over all the spin variables.

Note that experimentally measurable quantities are the time-dependent correlation functions having structures similar to eq. (3.21). They do not depend on the choice of the initial moment of time. The approximation given by eq. (3.24) obviously does not possess this feature, therefore it should be applied with the additional instructions to keep the discussed property. First of all, the time-dependent correlation functions should be rewritten into "normal form", which means that the argument t_i of the spin operators $\hat{S}_0^*(t_i)\hat{I}_{kz}\hat{I}_{lz}$ at the initial moment of time is zero. Then the approximation given by eq. (3.24) should be applied to these time-dependent correlation functions written in the "normal form". For instance, consider how to calculate a quantity, which has the structure of the form:

$$J(t_2;t_1) = Tr\left(\left(\hat{S}_0^*(t_i)\hat{I}_{kz}\hat{I}_{lz}\right)\hat{B}\left(\hat{S}_0^*(t_i)\hat{I}_{kz}\hat{I}_{lz}\right)\hat{\rho}_{eq}^{L}\right), \tag{3.25}$$

where $\hat{B}$ is a time-independent operator. Taking advantage of a translational invariance it can be represented in the normal form as follows:

$$J(t_2;t_1) = Tr\left(\left(\hat{S}_0^*(t_2-t_1)\hat{I}_{kz}\hat{I}_{lz}\right)\hat{B}\hat{I}_{kz}\hat{I}_{lz}\hat{\rho}_{eq}^L\right) \quad (3.26)$$

It is possible now to apply eq. (3.24) and obtain:

$$J(t_2;t_1) = P_{kl}^{fl}(t_2-t_1)Tr\left(\hat{I}_{kz}\hat{I}_{lz}\hat{B}\hat{I}_{kz}\hat{I}_{lz}\hat{\rho}_{eq}^L\right) \quad (3.27)$$

Here $P_{kl}^{fl}(t)$ can be considered as the probability for a given pair of spins with numbers k and l not to participate in the flip-flop processes during the time interval t. For protons, which have a spin $I = \frac{1}{2}$, the mutual flip-flop transitions between the spins with numbers k and l do not give a contribution to the probability P_{kl}^{fl}. The expression for this probability was derived with the use of the standard Anderson-Weiss approximation in [105]:

$$P_{kl}^{fl}(t) = exp\left(-\int_0^t (t-\tau)\frac{I(I+1)}{6\hbar^2}\sum_m\left(\langle\tilde{A}_{km}(\tau)\tilde{A}_{km}(0)\rangle_{eq} + \langle\tilde{A}_{lm}(\tau)\tilde{A}_{lm}(0)\rangle_{eq}\right)d\tau\right) \quad (3.28)$$

Eq. (3.21) for the signal $S_1(t)$ can be rewritten in the following form:

$$S_1(t) = \frac{\hbar\omega_0}{k_bT(2I+1)^{N_s}}Tr\left(\hat{S}_0(\tau)\left(\hat{\hat{S}}_{dd}^{sec}(t-\tau;\tau)\right)^{-1}\hat{S}_0^{-1}(t)\hat{I}_y\hat{P}_y^{\pi/2}\hat{S}_0(\tau)\hat{\hat{S}}_{dd}^{sec}(\tau;0)\hat{I}_y\hat{\rho}_{eq}^L\right) \quad (3.29)$$

Employing the approximation given by eq. (3.24) action of the evolution superoperators on the spin variables $\hat{S}_0(\tau)\left(\hat{\hat{S}}_{dd}^{sec}(t-\tau;\tau)\right)^{-1}\hat{S}_0^{-1}(t)\hat{I}_y$ and $\hat{S}_0(\tau)\hat{\hat{S}}_{dd}^{sec}(\tau;0)\hat{I}_y$ can be calculated exactly. Then, using properties of the spin $I = \frac{1}{2}$, symmetry arguments such as the isotropy of system, considering motions of lattice variables classically, after quantum statistical calculations, which were described in detail in [105], one obtains the following result:

$$S_1(t) =$$
$$= \frac{\hbar\omega_0}{4k_bT}\sum_{kl}\langle cos\left(\tilde{\varphi}_l(t-\tau)\right)cos\left(\varphi_k(\tau)\right)\left(\delta_{kl} + 4\frac{\partial^2}{\partial\tilde{\varphi}_{kl}^d\partial\varphi_{kl}^d}\right)\prod_m cos\left(\frac{\tilde{\varphi}_{lm}^d(t-\tau)}{2}\right)cos\left(\frac{\varphi_{km}^d(\tau)}{2}\right)\rangle, \quad (3.30)$$

where

$$\varphi_{kl}^d(\tau) = \frac{3\gamma^2\hbar}{2}\int_0^\tau\frac{1-3cos^2(\theta_{kl}(t_1))}{r_{kl}^3(t_1)}P_{kl}^{fl}(t_1)dt_1, \quad (3.31)$$

$$\tilde{\varphi}_{kl}^d(t-\tau) = \frac{3\gamma^2\hbar}{2}\int_\tau^t\frac{1-3cos^2(\theta_{kl}(t_1))}{r_{kl}^3(t_1)}P_{kl}^{fl}(t_1)dt_1, \quad (3.32)$$

the phases $\tilde{\varphi}_l(t-\tau) = \omega_s(t-\tau)$ and $\varphi_k(\tau) = \omega_k\tau$ are connected with either the chemical shift differences of the different protons or different Larmor frequencies caused by external magnetic field gradient (ω_s and ω_k), the latter being assumed small enough for neglecting diffusion effects. The bracket $\langle\ldots\rangle$ denotes the equilibrium averaging over the lattice variables. The quantities $\varphi_{kl}^d(\tau)$ and $\varphi_{kl}^d(t-\tau)$, where $\varphi_{kk}^d(\tau) = \varphi_{kk}^d(t-\tau) = 0$, are related to motions of the proton spins in the local dipolar fields after the first and the second RF pulses, respectively. They contain information about polymer segmental dynamics through the time dependence of the factors $\frac{1-3cos^2(\theta_{kl}(t_1))}{r_{kl}^3(t_1)}$ inside the integrals at the right-hand side of eq. (3.31) and (3.32). In the course of formal partial differentiations over $\tilde{\varphi}_{lm}^d(t-\tau)$ and $\varphi_{km}^d(\tau)$, these quantities should be considered as independent variables. After that, it is necessary to use eq. (3.31) and (3.32), and perform a statistical averaging. Due to the factors $cos\left(\tilde{\varphi}_l(t-\tau)\right)cos\left(\varphi_k(\tau)\right)$ and

$cos\left(\frac{\tilde{\varphi}^d_{lm}(t-\tau)}{2}\right)cos\left(\frac{\varphi^d_{km}(\tau)}{2}\right)$, the signal $S_1(t)$ possess a maximum at the time moment $t = 2\tau$, thereby leading to a spin echo formation. Note that the spin echo can be observed even in the situations, which are actually rather difficult to realize experimentally, when the phases $\tilde{\varphi}_l(t-\tau)$ and $\varphi_k(\tau)$ are very small, but motion of spins before and after the second RF pulse are correlated due to the factor $cos\left(\frac{\tilde{\varphi}^d_{lm}(t-\tau)}{2}\right)cos\left(\frac{\varphi^d_{km}(\tau)}{2}\right)$.

Calculation of the solid-echo build-up function I^{SE}.

Both the signals $S_2(t)$ and $S_3(t)$ can be calculated following the same philosophy as in the case of the signal $S_1(t)$, yielding:

$$S_2(t) = \frac{\hbar\omega_0}{4k_bT}\times$$
$$\times \sum_{kl}\langle sin\big(\tilde{\varphi}_l(t-\tau)\big)sin\big(\varphi_k(\tau)\big)\left(\delta_{kl} + 4(1-\delta_{kl})\frac{\partial^2}{\partial\tilde{\varphi}^d_{kl}\partial\varphi^d_{kl}}\right)\prod_m cos\left(\frac{\tilde{\varphi}^d_{lm}(t-\tau)}{2}\right)cos\left(\frac{\varphi^d_{km}(\tau)}{2}\right)\rangle \quad (3.33)$$
$$S_3(t) = \frac{\hbar\omega_0}{4k_bT}\sum_k\langle cos\big(\tilde{\varphi}_k(t-\tau) - \varphi_k(\tau)\big)\prod_m cos\left(\frac{\tilde{\varphi}^d_{km}(t-\tau)}{2} + \frac{\varphi^d_{km}(\tau)}{2}\right)\rangle \quad (3.34)$$

The most important difference between the Hahn echo, signal $S_3(t)$, and the two variations of the spin echo, signal $S_1(t)$, which is named the solid echo, and signal $S_2(t)$, occurs in the factor $cos\left(\frac{\tilde{\varphi}^d_{km}(t-\tau)}{2} + \frac{\varphi^d_{km}(\tau)}{2}\right)$ appearing in a product operator, which implies that the influence of the local dipolar fields on the spin evolution under the Hahn echo pulse sequence is additive, as this expression contains the sum of phases $\left(\frac{\tilde{\varphi}^d_{km}(t-\tau)}{2} + \frac{\varphi^d_{km}(\tau)}{2}\right)$, where the factors $\frac{1}{2}$ reflect the fact that spin $I = \frac{1}{2}$ is treated.

Now consider the sum of two echo signals $S_1(t)$ and $S_2(t)$, which were calculated before:

$$S_{12}(t) = S_1(t) + S_2(t) =$$
$$= \frac{\hbar\omega_0}{4k_bT}\sum_{kl}\langle cos\big(\tilde{\varphi}_l(t-\tau) - \varphi_k(\tau)\big)\left(\delta_{kl} + 4\frac{\partial^2}{\partial\tilde{\varphi}^d_{kl}\partial\varphi^d_{kl}}\right)\prod_m cos\left(\frac{\tilde{\varphi}^d_{lm}(t-\tau)}{2}\right)cos\left(\frac{\varphi^d_{km}(\tau)}{2}\right)\rangle \quad (3.35)$$

The sum of two signals has the same echo forming factor $cos\big(\tilde{\varphi}_l(t-\tau) - \varphi_k(\tau)\big)$ as the Hahn echo signal given by eq. (3.34). Using this feature and the fact that all the discussed signals have a maximal value at the time moment $t = 2\tau$, the normalized function, which reflects the difference between the solid and the Hahn echoes, $I^{SE}(t)$ is defined:

$$I^{SE}(t) = \frac{S_{12}(t) - S_3(t)}{S_{12}(t)}. \quad (3.36)$$

At the time moment $t = 2\tau$, when one can neglect the effects caused by the difference of chemical shifts between different spins, the value $cos\big(\tilde{\varphi}_l(t-\tau) - \varphi_k(\tau)\big) \cong 1$. Therefore one can derive from eq. (3.34), (3.35) and (3.36):

$$I^{SE}(t) = 1 - \frac{\sum_k\langle\prod_m cos\left(\frac{\tilde{\varphi}^d_{km}(\tau)}{2} + \frac{\varphi^d_{km}(\tau)}{2}\right)\rangle}{\sum_{kl}\langle\left(\delta_{kl} + 4\frac{\partial^2}{\partial\tilde{\varphi}^d_{kl}\partial\varphi^d_{kl}}\right)\prod_m cos\left(\frac{\tilde{\varphi}^d_{lm}(\tau)}{2}\right)cos\left(\frac{\varphi^d_{km}(\tau)}{2}\right)\rangle} \quad (3.37)$$

Then, employing the following approximation for the cosine function in eq. (3.37):

$$cos(x) = 1 - \frac{1}{2}x^2 + \cdots \cong exp\left(-\frac{1}{2}x^2\right), \tag{3.38}$$

Eq. (3.36) can be finally evaluated to the form:

$$I^{SE}(t) = 1 - \frac{\sum_k exp\left(-\frac{1}{8}\sum_m \langle\left(\tilde{\varphi}^d_{km}(\tau)+\varphi^d_{km}(\tau)\right)^2\rangle\right)}{\sum_k exp\left(-\frac{1}{8}\sum_m \langle\left(\tilde{\varphi}^d_{km}(\tau)-\varphi^d_{km}(\tau)\right)^2\rangle\right)} \tag{3.39}$$

It is noted that the solid-echo build-up function is experimentally obtained from the same signals as the $\beta(2\tau;\tau)$ function, described in [113,114], with a difference in the denominator of eq. (3.36): $S_{12}(t)$ is replaced with its initial value $S_{12}(0)$. However, the formalism presented here for the evaluation of the corresponding signals considers all the spins in the system, whereas in [113,114] treatment is restricted to a single pair of protons. Therefore, $I^{SE}(t)$ can be considered as a many-spin generalization of the function $\beta(2\tau;\tau)$. Moreover, use of $S_{12}(t)$, as compared to $S_{12}(0)$, simplifies the evaluation of the data, since the latter signal is not straightforwardly determined in the experiment (zero-time extrapolation is necessary). In addition to that, somewhat similar functions based on spin-spin relaxation were used and discussed in several works [98,111,112]. Importantly, all of them are evaluated only for a case of the dipolar interactions between a single spin pair.

Application in polymer melts.

Consider now the application of the solid-echo build-up function in polymer melts. For chains of high molecular weight the assumption of equivalency of proton spins is often justified, and it helps to simplify the theoretical calculations. It results in the dependence of each contribution inside the sums in eq. (3.31) and (3.32) on the spin number k being weak, i.e. the contributions are equal to each other. Therefore it is possible to transform eq. (3.39) to:

$$I^{SE}(t) = 1 - \frac{1}{N_s}\sum_k exp\left(-\frac{1}{2}\sum_m \langle\tilde{\varphi}^d_{km}(\tau)\varphi^d_{km}(\tau)\rangle\right) = 1 - exp\left(-\frac{1}{2N_s}\sum_{k\neq m}\langle\tilde{\varphi}^d_{km}(\tau)\varphi^d_{km}(\tau)\rangle\right) \tag{3.40}$$

The main assumption made in the course of this derivation is the modified Anderson-Weiss approximation, which is exact at times $t < T_2^{eff}$ [105]. In this time limit the argument in the exponential in eq. (3.40) is small, thereby enabling one to decompose this expression into the Taylor series. Keeping only the terms quadratic in phase yields:

$$I^{SE}(t) = \frac{1}{2N_s}\sum_{k\neq m}\langle\tilde{\varphi}^d_{km}(\tau)\varphi^d_{km}(\tau)\rangle + \cdots \tag{3.41}$$

At times $t < \tau_{fl}$ term $P^{fl}_{kl}(t) \approx 1$ in eq. (3.31) and (3.32), which essentially means that no flip-flop processes are taking place. Characteristic flip-flop time τ_{fl} is of the same order as T_2^{eff} and will be discussed in more detail in *Chapter 3.4*. Thus, employing the translational invariance of the time-dependent correlation functions in eq. (3.31) and (3.32), eq. (3.41) can be rewritten in terms of the total dipolar correlation functions:

$$I^{SE}(t) = \frac{9}{8}\gamma^4\hbar^2\int_0^\tau(\tau - t_1)\left(A_0^d(\tau + t_1) + A_0^d(\tau - t_1)\right)dt_1 + \cdots \tag{3.42}$$

where A_0^d is given by eq. (3.1) and was thoroughly discussed in *Chapter 3.1*. The intermolecular contribution to A_0^d is given by eq. (3.6). For times much longer than the segmental relaxation time $t \gg \tau_s$, the relative segmental MSD becomes much larger than the effective chain diameter σ^*. Therefore, $A_0^{d;inter}$ can be connected with the relative MSD of proton spins from different macromolecules $\langle\tilde{r}^2(t)\rangle$ in a slightly more straightforward fashion than in eq. (3.6):

$$A_0^{d;inter}(t) = \sqrt{\frac{2}{3\pi}}\frac{16\pi}{5}\frac{n_s}{\langle\tilde{r}^2(t)\rangle}, \tag{3.43}$$

Consequently, the experimentally measurable function $I^{SE}(t)$ can be as well represented as a sum of the intramolecular and the intermolecular contributions:

$$I^{SE}(t) = I^{SE;intra}(t) + I^{SE;inter}(t) \tag{3.44}$$

Using eq. (3.43) it is possible to demonstrate that the intermolecular part of the solid-echo build-up function is connected in a rather simple way with the relative MSD of the polymer segments from the different macromolecules:

$$I^{SE;inter}(t) = \frac{18\pi}{5}\sqrt{\frac{2}{3\pi}}\gamma^4\hbar^2 n_s \int_0^\tau (\tau - t_1)\left(\frac{1}{\langle\tilde{r}^2(\tau+t_1)\rangle} + \frac{1}{\langle\tilde{r}^2(\tau-t_1)\rangle}\right)dt_1 + \cdots \tag{3.45}$$

In the case when the relative mean squared displacement of polymer segments from different macromolecules can be described by a time-independent exponent α, i.e. $\langle\tilde{r}^2(t)\rangle \propto t^\alpha$, integration of the right-hand side of eq. (3.45) can be performed exactly with the assumption that $\alpha < \frac{2}{3}$, yielding:

$$I^{SE;inter}(t) = \frac{18\pi}{5}f(\alpha)\sqrt{\frac{2}{3\pi}}\gamma^4\hbar^2 n_s \frac{t^2}{\langle\tilde{r}^2(t)\rangle^{\frac{3}{2}}} + \cdots, \tag{3.46}$$

where

$$f(\alpha) = \frac{2^{\frac{3\alpha}{2}}\left(2^{1-\frac{3\alpha}{2}}-1\right)}{4\left(1-\frac{3\alpha}{2}\right)\left(1-\frac{3\alpha}{4}\right)} \tag{3.47}$$

Using the first term of eq. (3.46), which is connected only with the expressions of the type $\langle\tilde{\varphi}_{km}^d(\tau)\varphi_{km}^d(\tau)\rangle$ in the Taylor expansion of $I^{SE}(t)$, one can obtain the relative mean squared displacement of the polymer segments belonging to the different polymer chains as:

$$\langle\tilde{r}^2(t)\rangle = \left(\frac{18\pi}{5}f(\alpha)\sqrt{\frac{2}{3\pi}}\gamma^4\hbar^2 n_s \frac{t^2}{I^{SE;inter}(t)}\right)^{\frac{2}{3}} \tag{3.48}$$

This is the main result of this theoretical derivation and it will be used for the evaluation of the experimental data obtained in entangled polymer melts in *Chapter 4.* Treatment of the α-dependent numerical coefficient $f(\alpha)$ is presented in the next paragraph.

3.3. Dipolar-correlation build-up function

In this paragraph the second method for investigation of the segmental diffusion in entangled polymer melts based on the NMR transverse relaxation is presented. It implies introduction of the *dipolar-correlation build-up function* $I^{DC}(t)$, which is defined as:

$$I^{DC}(t) = \frac{S^{HE}(t)S^{HE}(0)}{\left(S^{HE}\left(\frac{t}{2}\right)\right)^2}, \tag{3.49}$$

where $S^{HE}(t)$ is a signal from the Hahn echo pulse sequence $\hat{P}_x^{\pi/2} - \tau - \hat{P}_y^{\pi}$ (Figure 2.2) at the time moment $t = 2\tau$. $I^{DC}(t)$ thereby correlates Hahn echo signals at two different time moments t and $\frac{t}{2}$. It is illustrated in Figure 3.3. As in the case of the solid-echo build-up function, $I^{DC}(t) = 0$ for any exponential Hahn echo decay. Mathematical derivation presented in this paragraph was first described in [108] and [109].

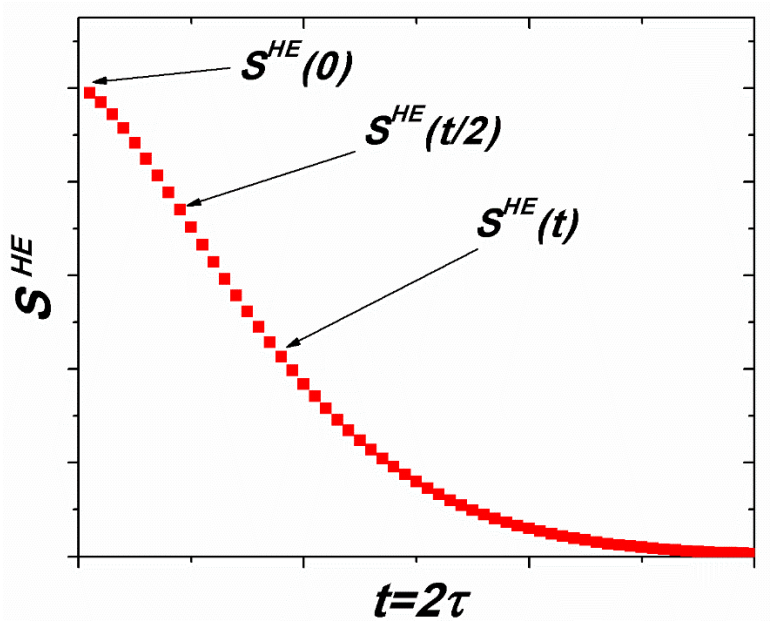

Figure 3.3. Hahn echo signals that are used to construct the dipolar-correlation build-up function $I^{DC}(t) = \frac{S^{HE}(t)S^{HE}(0)}{\left(S^{HE}\left(\frac{t}{2}\right)\right)^2}$. The decay is modeled by a function $g(t) = exp\left(-\left(\frac{t}{T_2'}\right)^{\frac{3}{2}}\right)$, often obtained in entangled polymer melts.

In order to calculate how I^{DC} is connected with the features of the segmental motion in a polymer melt, consider a system described by the following Hamiltonian

$$\hat{H} = \hat{H}_s + \hat{H}_L + \hat{H}_{dd}^{sec}, \tag{3.50}$$

Using the result obtained with the same formalism as in the previous paragraph, the response of the spin system to the Hahn echo pulse sequence is written as:

$$S^{HE}(t) = S_3(t) = \frac{\hbar\omega_0}{4k_bT}\sum_k \langle cos\left(\tilde{\varphi}_k(t-\tau) - \varphi_k(\tau)\right)\prod_m cos\left(\frac{\tilde{\varphi}_{km}^d(t-\tau)+\varphi_{km}^d(\tau)}{2}\right)\rangle, \tag{3.51}$$

where

$$\varphi_{kl}^d(\tau) = \frac{3\gamma^2\hbar}{2}\int_0^\tau \frac{1-3cos^2(\theta_{kl}(t_1))}{r_{kl}^3(t_1)} P_{kl}^{fl}(t_1)dt_1 \tag{3.52}$$

$$\tilde{\varphi}_{kl}^{d}(t-\tau)=\frac{3\gamma^2\hbar}{2}\int_{\tau}^{t}\frac{1-3cos^2(\theta_{kl}(t_1))}{r_{kl}^3(t_1)}P_{kl}^{fl}(t_1)dt_1 \tag{3.53}$$

Consider eq. (3.51) in more detail for a situation at the time moment $t=2\tau$. If the external magnetic field gradient, created by the imperfection of a spectrometer, is small enough, i.e. one can neglect the effect of a thermal diffusion of polymer segments, the cosine function inside the brackets of eq. (3.51) is $cos\left(\tilde{\varphi}_k(t-\tau)-\varphi_k(\tau)\right)\cong 1$. Therefore, function $S^{HE}(t)$ experiences a sharp maximum at the time moment $t=2\tau$ and its structure is essentially simplified:

$$S^{HE}(t)=\frac{\hbar\omega_0}{4k_bT}\sum_k\langle\prod_m cos\left(\frac{\tilde{\varphi}_{km}^{d}(\tau)+\varphi_{km}^{d}(\tau)}{2}\right)\rangle. \tag{3.54}$$

Now consider the Hahn echo signal at the time moment $t=\tau$, which is actually the response of the spin system to the pulse sequence $\hat{P}_x^{\pi/2}-\frac{\tau}{2}-\hat{P}_y^{\pi}$. The expression for the signal amplitude in this case is written analogously in the following way:

$$S^{HE}\left(\frac{t}{2}\right)=\frac{\hbar\omega_0}{4k_bT}\sum_k\langle\prod_m cos\left(\frac{\tilde{\varphi}_{km}^{d}\left(\frac{\tau}{2}\right)+\varphi_{km}^{d}\left(\frac{\tau}{2}\right)}{2}\right)\rangle \tag{3.55}$$

From eq. (3.52) and (3.53) it is possible to see that:

$$\varphi_{kl}^{d}(\tau)=\tilde{\varphi}_{kl}^{d}\left(\frac{\tau}{2}\right)+\varphi_{kl}^{d}\left(\frac{\tau}{2}\right) \tag{3.56}$$

Using this relation, eq. (3.55) can be rewritten as follows:

$$S^{HE}\left(\frac{t}{2}\right)=\frac{\hbar\omega_0}{4k_bT}\sum_k\langle\prod_m cos\left(\frac{\varphi_{km}^{d}(\tau)}{2}\right)\rangle \tag{3.57}$$

Employing the approximation for the cosine function given by eq. (3.38), expressions for $S^{HE}(t)$ and $S^{HE}\left(\frac{t}{2}\right)$ can be written as:

$$S^{HE}(t)=\frac{\hbar\omega_0}{4k_bT}\sum_k exp\left(-\frac{1}{8}\sum_m\langle\left(\tilde{\varphi}_{km}^{d}(\tau)+\varphi_{km}^{d}(\tau)\right)^2\rangle\right) \tag{3.58}$$

and

$$S^{HE}\left(\frac{t}{2}\right)=\frac{\hbar\omega_0}{4k_bT}\sum_k exp\left(-\frac{1}{8}\sum_m\langle\left(\varphi_{km}^{d}(\tau)\right)^2\rangle\right) \tag{3.59}$$

Note that due to the translational invariant symmetry with respect to the displacement at the initial time moment the following relation holds:

$$\langle\left(\varphi_{km}^{d}(\tau)\right)^2\rangle=\langle\left(\tilde{\varphi}_{km}^{d}(\tau)\right)^2\rangle \tag{3.60}$$

Eq. (3.58) and (3.59) now can be substituted into eq. (3.49). Another signal that is necessary for the determination of I^{DC} is $S^{HE}(0)$. It can be calculated from eq. (3.58) using the fact the summation is carried out for all N_s spins of the system:

$$S^{HE}(0)=\frac{\hbar\omega_0}{4k_bT}N_s \tag{3.61}$$

Combining eq. (3.58), (3.59) and (3.61) the expression for $I^{DC}(t)$ can be rewritten as:

$$I^{DC}(t)=1-\frac{N_s\sum_k exp\left(-\frac{1}{8}\sum_m\langle\left(\tilde{\varphi}_{km}^{d}(\tau)+\varphi_{km}^{d}(\tau)\right)^2\rangle\right)}{\left(\sum_k exp\left(-\frac{1}{8}\sum_m\langle\varphi_{km}^{d}(\tau)^2\rangle\right)\right)^2} \tag{3.62}$$

At the initial time moment $t=0$ the dipolar-correlation build-up function $I^{DC}(t)$ is equal to zero by definition. Its initial rise at times $t<T_2^{eff}$ can be calculated via decomposing expressions eq. (3.58), (3.59) and (3.62) into the Taylor series. Assuming equivalency of the spins and keeping only the terms quadratic in phases provides the following result:

$$I^{DC}(t)=\frac{1}{4N_s}\sum_{k\neq m}\langle\tilde{\varphi}_{km}^{d}(\tau)\varphi_{km}^{d}(\tau)\rangle+\cdots \tag{3.63}$$

Application in polymer melts.

$I^{DC}(t)$ can be rewritten in terms of dipolar correlation functions using eq. (3.1), (3.31) and (3.32) for times $t < \tau_{fl}$:

$$I^{DC}(t) = \frac{9}{16}\gamma^4\hbar^2 \int_0^\tau (\tau - t_1)\left(A_0^d(\tau + t_1) + A_0^d(\tau - t_1)\right) dt_1 + \cdots \quad (3.64)$$

As was discussed previously, the total dipolar correlation function can be separated into:

$$A_0^d(t) = A_0^{d;intra} + A_0^{d;inter} \quad (3.65)$$

Consequently, the initial rise of the $I^{DC}(t)$ build-up function can be represented as the sum of the intramolecular and the intermolecular contributions analogously to I^{SE}:

$$I^{DC}(t) = I^{DC;intra}(t) + I^{DC;inter}(t) \quad (3.66)$$

Using eq. (3.43) for the intermolecular dipolar correlation function and eq. (3.64), it is possible to determine the connection between the intermolecular part of the dipolar-correlation build-up function $I^{DC;inter}(t)$ and the relative mean squared displacement of the polymer segments from the different macromolecules:

$$I^{DC;inter}(t) = \frac{9\pi}{5}\sqrt{\frac{2}{3\pi}}\gamma^4\hbar^2 n_s \int_0^\tau (\tau - t_1)\left(\frac{1}{\langle\tilde{r}^2(\tau+t_1)\rangle} + \frac{1}{\langle\tilde{r}^2(\tau-t_1)\rangle}\right) dt_1 + \cdots \quad (3.67)$$

The right-hand side of eq. (3.67) can be integrated in the case when the exponent α describing the time-dependence of the segmental MSD corresponds to the regime of the anomalous diffusion with $\alpha < \frac{2}{3}$. Then eq. (3.67) translates to:

$$I^{DC;inter}(t) = \frac{9\pi}{5}f(\alpha)\sqrt{\frac{2}{3\pi}}\gamma^4\hbar^2 n_s \frac{t^2}{\langle\tilde{r}^2(t)\rangle^{\frac{3}{2}}} + \cdots, \quad (3.68)$$

where $f(\alpha)$ is the same numerical coefficient as in eq. (3.47).

From eq. (3.68) one can obtain the relative mean squared displacement of the polymer segments belonging to the different polymer chains:

$$\langle\tilde{r}^2(t)\rangle = \left(\frac{9\pi}{5}f(\alpha)\sqrt{\frac{2}{3\pi}}\gamma^4\hbar^2 n_s \frac{t^2}{I^{DC;inter}(t)}\right)^{\frac{2}{3}} \quad (3.69)$$

This is the second important theoretical outcome of this work, which connects the segmental MSD in polymer melts with the experimentally measurable intermolecular part of the dipolar-correlation build-up function. Eq. (3.69) will be used for the evaluation of the experimental data in *Chapter 4*.

Numerical coefficient $f(\alpha)$.

In order to determine the segmental MSD with the help of both eq. (3.48) and (3.69), it is necessary to know the numerical coefficient $f(\alpha)$, which is generally different depending on the regime of polymer dynamics. In *Chapter 4* evaluation of the experimental data is first done with an arbitrary value of α, chosen either from the middle of the interval $\frac{1}{4} \leq \alpha \leq \frac{1}{2}$ or based on the educated guess about the features of polymer dynamics at the given conditions. Since $f(\alpha)$ does not affect the slope of $\langle\tilde{r}^2(t)\rangle$, its true value can be extracted from the MSD time dependence for any α used in the beginning. The slope of $\langle\tilde{r}^2(t)\rangle$ is in turn described by the power law $\langle\tilde{r}^2(t)\rangle \propto t^\alpha$ and therefore yields a true value of α. This new value of α is then used again for the calculation of the corrected values of $\langle\tilde{r}^2(t)\rangle$. This iterative method allows the straightforward evaluation of the experimental data.

Consider now the situation, when the transition between different power laws of $\langle \tilde{r}^2(t) \rangle$ is encountered. For instance, in the framework of the tube-reptation model $\alpha = \frac{1}{2}$ in the Rouse regime, $\alpha = \frac{1}{4}\ and\ \frac{1}{2}$ in the regimes of incoherent and coherent reptation and $\alpha = 1$ in the regime of normal diffusion. In general, for all the models, the regime of anomalous diffusion is characterized by the power law exponent lying in the interval $\frac{1}{4} \leq \alpha \leq \frac{1}{2}$. It is therefore important to know the variation of $f(\alpha)$, or even more precisely $\left(f(\alpha)\right)^{\frac{2}{3}}$, since it is included into eq. (3.69) and (3.48) in power $\frac{2}{3}$. In order to illustrate it, the ratio $\left(\frac{f(\alpha)}{f\left(\frac{1}{4}\right)}\right)^{\frac{2}{3}}$ is plotted in Figure 3.4. For example, transition from the regime I ($\alpha = \frac{1}{2}$) to the regime II ($\alpha = \frac{1}{4}$) of the tube-reptation model corresponds to the change in the numerical factor in eq. (3.48) and (3.69): $\left(\frac{f\left(\frac{1}{2}\right)}{f\left(\frac{1}{4}\right)}\right)^{\frac{2}{3}} \cong 1.3$. In this work experimental data obtained in the region of transitions is evaluated assuming a smooth linear change of α, which actually provides a good qualitative picture of the transition. Additional mathematical treatment is necessary for the precise consideration of this problem.

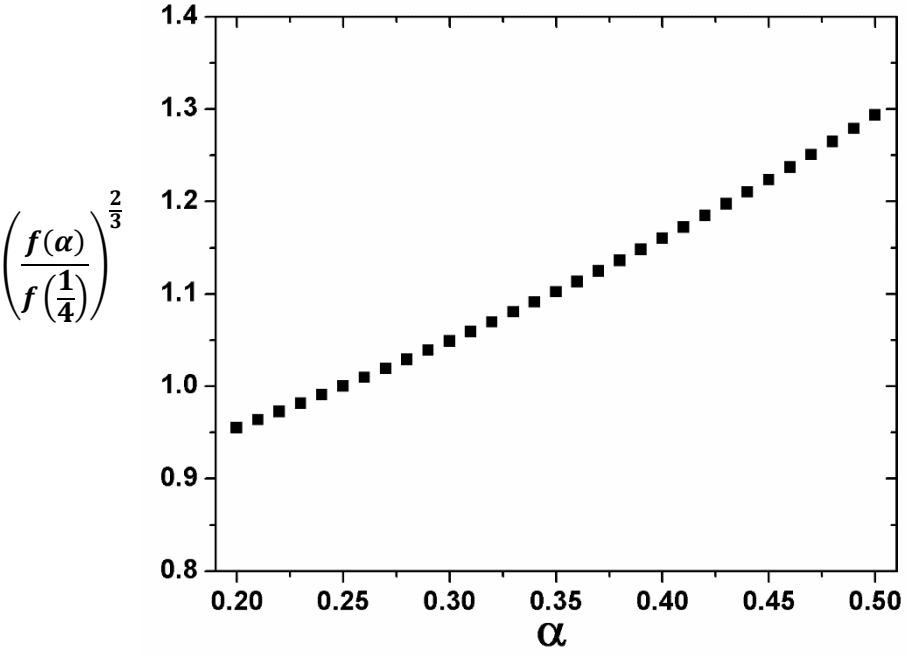

Figure 3.4. Ratio $\left(\frac{f(\alpha)}{f\left(\frac{1}{4}\right)}\right)^{\frac{2}{3}}$ that reflects the degree of variation of the factor $f(\alpha)$ and consequently of the relative segmental MSD given by eq. (3.48) and (3.69). For the transition from $\alpha = \frac{1}{2}$ to $\alpha = \frac{1}{4}$ it is equal to ≈ 1.3.

3.4. Features of build-up functions

Discussion of the certain properties of the build-up functions follows closely the argumentation presented in [109]. Expression for the initial rise of the solid-echo and the dipolar-correlation build-up functions at times $t < T_2^{eff}$, given by eq. (3.43) and (3.63) can be compared with the expression for the initial rise of the double-quantum build-up function $I_{nDQ}(\tau_{DQ})$ measured by the double-quantum NMR methods, discussed in *Chapter 2.4*. $I_{nDQ}(\tau_{DQ})$ was derived for a many-spin system within a framework of the Anderson-Weiss approximation in [107]:

$$I_{nDQ}(\tau_{DQ}) = \frac{\sum_k sinh\left(\sum_m \langle \varphi_{km}^{ex}(\tau_{DQ})\varphi_{km}^{rec}(\tau_{DQ})\rangle\right)}{\sum_k exp\left(\sum_m \langle \varphi_{km}^{ex}(\tau_{DQ})\varphi_{km}^{rec}(\tau_{DQ})\rangle\right)}, \quad (3.70)$$

where

$$\varphi_{kl}^{ex}(\tau_{DQ}) = \frac{\gamma^2\hbar}{2}\int_0^{\tau_{DQ}} \frac{1-3cos^2(\theta_{kl}(t_1))}{r_{kl}^3(t_1)}\, dt_1, \quad (3.71)$$

$$\varphi_{kl}^{rec}(\tau_{DQ}) = \frac{\gamma^2\hbar}{2}\int_{\tau_{DQ}}^{2\tau_{DQ}} \frac{1-3cos^2(\theta_{kl}(t_1))}{r_{kl}^3(t_1)}\, dt_1, \quad (3.72)$$

where τ_{DQ} is the duration of the DQ excitation and reconversion periods, which represents the experimentally controlled parameters, i.e. the DQ evolution time. One can consider τ_{DQ} as the analog of the parameter τ in the spin-echo experiment and, consequently, substitute $\varphi_{kl}^{ex}(\tau_{DQ})$ and $\varphi_{kl}^{rec}(\tau_{DQ})$ by $\varphi_{kl}^{d}(\tau)$ and $\tilde{\varphi}_{kl}^{d}(\tau)$ given by eq. (3.31) and (3.32). In this case, following the same approach as previously, at times $t < T_2^{eff}$ eq. (3.70) can be rewritten as:

$$I_{nDQ}(t) = \frac{1}{9N_s}\sum_{k\neq m}\langle \tilde{\varphi}_{km}^{d}(\tau)\varphi_{km}^{d}(\tau)\rangle. \quad (3.73)$$

It is clear that eq. (3.73) differs from eq. (3.43) and (3.63) for $I^{SE}(t)$ and $I^{DC}(t)$ only in the numerical coefficient.

Different time limits. System of equivalent spins.

Eq. (3.43), (3.63) and (3.73) for the dipolar-correlation, the double-quantum and the solid-echo build-up functions show that their initial rise contains additive contributions from the intermolecular and the intramolecular dipolar interactions. For times $t < T_2^{eff}$, this result is accurate and represents a direct consequence of the high-temperature approximation for the distribution of spin variables, eq. (3.13). The first non-additive corrections at short times cannot have order of magnitude higher than $\left\|\frac{\hat{H}_{dd}}{k_BT}\right\| \ll 1$. This can be verified by direct calculations of the corresponding NMR signals with a density matrix defined as: $\hat{\rho}_{eq} = \frac{1}{Z_s}\left(1 - \frac{\hbar\omega_0}{k_bT}\hat{I}_z - \frac{\hat{H}_{dd}^{sec}}{k_BT}\right)\hat{\rho}_{eq}^{L}$.

At longer times $t \geq T_2^{eff}$, contributions from the inter- and intramolecular dipolar interactions to the discussed build-up functions do not remain additive. The main source of this deviation is the scalar term in the Hamiltonian given by eq. (3.12). It induces flip-flop transitions between the different spin pairs, which lead to the spin diffusion and make time dependence of the build-up functions sensitive to many-spin dynamical correlations. This problem can be partially resolved for solids, where it is possible to neglect thermal displacements of the spin-bearing nuclei in comparison with the equilibrium distance between them. The calculation can be carried out using the method of moments or actually solving dynamics for a limited number of spins, for example, for a three-spin system, as was considered in [116]. In the case of polymer melts this problem cannot be generally resolved in a quantitatively accurate

manner. This is caused by the fact that no theoretical models exist that describe dynamical correlations between three and more polymer segments from different macromolecules for times shorter than the polymer chain's terminal relaxation time. Nevertheless, some qualitative instructive conclusions can be made on the basis of the Anderson-Weiss approximation.

For the situation when all the spins are equivalent, i.e. terms inside the sums in eq. (3.40), (3.62) and (3.70) do not depend on k, these equations can be simplified:

$$\begin{aligned} I^{SE}(t=2\tau) &= 1-exp\left(-\frac{1}{2N_s}\sum_{k\neq m}\langle\tilde{\varphi}^d_{km}(\tau)\varphi^d_{km}(\tau)\rangle\right) \\ I^{DC}(t=2\tau) &= 1-exp\left(-\frac{1}{4N_s}\sum_{k\neq m}\langle\tilde{\varphi}^d_{km}(\tau)\varphi^d_{km}(\tau)\rangle\right) \\ I_{nDQ}(t=2\tau) &= \frac{1}{2}\left(1-exp\left(\frac{2}{9N_s}\sum_{k\neq m}\langle\tilde{\varphi}^d_{km}(\tau)\varphi^d_{km}(\tau)\rangle\right)\right) \end{aligned} \tag{3.74}$$

From eq. (3.34) it can be seen that in the same approximation of spin's equivalency, the normalized Hahn echo signal is given by:

$$g^{HE}(t)=\frac{S^{HE}(t=2\tau)}{S^{HE}(0)}=exp\left(-\frac{1}{8N_s}\sum_{k\neq m}\langle\left(\tilde{\varphi}^d_{km}(\tau)+\varphi^d_{km}(\tau)\right)^2\rangle\right) \tag{3.75}$$

At times $t \geq T_2^{eff}$ eq. (3.75) in the framework of the modified Anderson-Weiss approximation is non-additive, however a quantity defined as:

$$ln\left(\frac{1}{1-I^{DC}(t)}\right)=\frac{1}{4N_s}\sum_{k\neq m}\langle\tilde{\varphi}^d_{km}(\tau)\varphi^d_{km}(\tau)\rangle \tag{3.76}$$

is still additive.

As was mentioned before, $P_{kl}^{fl}(t)$ given by eq. (3.28) describes the probability of two spins k nad l not to participate in flip-flop transitions. It is a two-spin dynamical quantity and can be approximated as $P_{kl}^{fl}(t) \cong P_{fl}^2(t)$, where $P_{fl}(t)$ is the probability for a certain spin not to undergo a flip-flop transition and it is written as [105]:

$$P_{fl}^2(t)=exp\left(-\int_0^t(t-\tau)\frac{I(I+1)}{6\hbar^2N_s}\sum_{m\neq k}\langle\tilde{A}_{km}(\tau)\tilde{A}_{km}(0)\rangle\,d\tau\right) \tag{3.77}$$

Consider the normalized Hahn echo signal given by eq. (3.75). It can be written in the following way, which is typical for polymer melts at short times:

$$g^{HE}(t)=exp\left(-\left(\frac{t}{T_2^{eff}}\right)^{\bar{\alpha}}\right) \tag{3.78}$$

Then, using eq. (3.11) for A_{km}, eq. (3.51)- (3.53) for the Hahn echo signal and eq. (3.77), it is possible to obtain the following time dependence of the probability $P_{fl}(t)$:

$$P_{fl}(t)=exp\left(-\left(\frac{t}{\tau_{fl}}\right)^{\bar{\alpha}}\right) \tag{3.79}$$

Comparing eq. (3.74) and (3.79) for the cases when one can neglect the contribution from the exchange interactions, it is possible to establish the following relation between T_2^{eff} and τ_{fl}:

$$\tau_{fl} \cong \left(\frac{9}{2}\right)^{1/\bar{\alpha}} T_2^{eff} \tag{3.80}$$

Typically for high molecular mass polymer melts the exponent is $1 \leq \bar{\alpha} \leq 2$, therefore $2.1T_2^{eff} \leq \tau_{fl} \leq 4.5T_2^{eff}$. Note, that actually a numerical coefficient connecting T_2^{eff} and τ_{fl} should be slightly larger, because, as it was argued in the works [104,105], the main contribution to the intermolecular part of the total dipolar correlation function in high molecular wight polymer melts comes from the spins at

different macromolecules separated from each other by the distances on the order of $\langle r^2\left(T_2^{eff}\right)\rangle^{\frac{1}{2}}$. This is a direct consequence of the anomalous character of the segmental diffusion, i.e. $\frac{1}{4} \leq \alpha \leq \frac{1}{2}$ in the power law of the MSD time dependence. Typically, the effective spin-spin relaxation time in such polymer melts is around few millisecond and $\langle r^2\left(T_2^{eff}\right)\rangle^{\frac{1}{2}} \approx 20 - 200$ Å, see, for example, the latest experimental results [49]. The displacement of this order is significantly larger than the typical distances between the nearest spins on the same macromolecule $r_{ij}^{near} \approx 1.5 - 3$Å [13]. Therefore flip-flop transitions between these spins are negligible in comparison with the flip-flop transitions between the spins from the different macromolecules. This allows for replacing the total effective spin-spin relaxation time by its intermolecular part $T_2^{inter} > T_2^{eff}$ in eq. (3.80). In addition to that, the following connection between two exponents $\bar{\alpha} = \frac{4-3\alpha}{2}$ can be established with the help of eq.

Different time limits. System of non-equivalent spins.

Consider now the situation when protons possess different chemical environment, for example, as protons in CH_2 and CH_3 groups. Let the index i enumerate different types of protons and φ_i define the fraction of protons of the corresponding sort: $\sum_i \varphi_i = 1$. Then, as it follows from eq. (3.58), the normalized Hahn echo amplitude $g(t) = \frac{S^{HE}(t)}{S^{HE}(0)}$ can be written as:

$$g(t) = \sum_i \varphi_i \, exp\left(-\frac{1}{8}\sum_m \langle\left(\tilde{\varphi}_{im}^d(\tau)+\varphi_{im}^d(\tau)\right)^2\rangle\right) \tag{3.81}$$

As an illustrative example, from now on consider a system with two types of spins, the HE signal of which is described by the following relation:

$$g(t) = \varphi_1 exp\left(-\left(\frac{t}{T_2^{eff,a}}\right)^{\alpha_1}\right) + \varphi_2 exp\left(-\left(\frac{t}{T_2^{eff,b}}\right)^{\alpha_2}\right), \tag{3.82}$$

where α_1 and α_2 are exponents depending on the dynamics of the spin-bearing polymer segments, $\alpha_1 \geq \alpha_2$ and $T_2^{eff,a} \leq T_2^{eff,b}$.

Dipolar-correlation build-up function.

The DC build-up function for this system can be calculated using its definition by eq. (3.49). The short-time and the long-time limits of it are illustrated in Figure 3.5 and are given by the following equations:

$$I^{DC}(t) = \begin{cases} \left(1 - \frac{1}{2^{\alpha_1 - 1}}\right)\varphi_1\left(\frac{t}{T_2^{eff,a}}\right)^{\alpha_1} + \left(1 - \frac{1}{2^{\alpha_2 - 1}}\right)\varphi_2\left(\frac{t}{T_2^{eff,b}}\right)^{\alpha_2}, & t < T_2^{eff,a} \\ 1, & t \to \infty \end{cases}, \tag{3.83}$$

where $\alpha_1 \geq \alpha_2 > 1$. At times $t > T_2^{eff,b}$ behavior of $I^{DC}(t)$ can be rather complex, possibly resulting in the negative values, see Figure 3.5. The situation, when $\alpha_1 \geq \alpha_2 = 1$, which models the existence of a highly mobile low molecular weight compound in the system with a proton fraction of $\varphi_2 = 1 - \varphi_1 > 0$, has a different long-time limit:

$$I^{DC}(t) = \begin{cases} \left(1 - \frac{1}{2^{\alpha_1 - 1}}\right)\varphi_1\left(\frac{t}{T_2^{eff,a}}\right)^{\alpha_1}, & t < T_2^{eff,a} \\ -\frac{\varphi_1}{1-\varphi_1}, & t \to \infty \end{cases} \tag{3.84}$$

It becomes clear that the low molecular weight component does not contribute to the initial rise of the DC build-up function, its existence only changes the normalization of the function through the factor φ_1. This is an important finding considering the ubiquitous presence of small amounts (< 1%) of highly mobile impurities in many polymer melt samples.

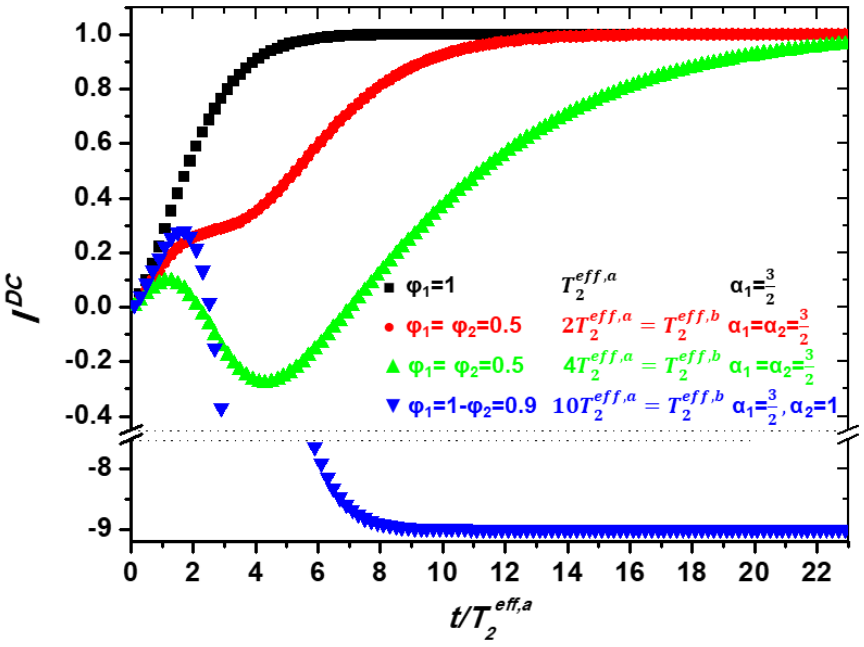

Figure 3.5. Dipolar-correlation build-up functions $I^{DC}(t)$ for the case of a one-component system with an exponent $\alpha_1 = \frac{3}{2}$ (black), a two-component system with exponents $\alpha_1 = \alpha_2 = \frac{3}{2}$ and different decay constants (red and green), and a two-component system with an exponential contribution modelling a low molecular weight, highly mobile fraction (blue). The lower part of the graph shows the long-time limit behavior of the blue curve.

Solid-echo build-up function.

The solid-echo (SE) build-up function in the case of the system described by eq. (3.82) is given by the following equation:

$$I^{SE}(t) = 1 - \frac{\varphi_1 exp\left(-\left(\frac{t}{T_2^{eff,a}}\right)^{\alpha_1}\right) + \varphi_2 exp\left(-\left(\frac{t}{T_2^{eff,b}}\right)^{\alpha_2}\right)}{\varphi_1 exp\left(\left(1-\frac{1}{2^{\alpha_1-1}}\right)\left(\frac{t}{T_2^{eff,a}}\right)^{\alpha_1}\right) + \varphi_2 exp\left(\left(1-\frac{1}{2^{\alpha_2-1}}\right)\left(\frac{t}{T_2^{eff,b}}\right)^{\alpha_2}\right)} \tag{3.85}$$

Its behavior at the limits in the cases, when $\alpha_1 \geq \alpha_2 > 1$, is determined by the following relations:

$$I^{SE}(t) = \begin{cases} 2\left(1-\frac{1}{2^{\alpha_1-1}}\right)\varphi_1\left(\frac{t}{T_2^{eff,a}}\right)^{\alpha_1} + 2\left(1-\frac{1}{2^{\alpha_2-1}}\right)\varphi_2\left(\frac{t}{T_2^{eff,b}}\right)^{\alpha_2}, & t < T_2^{eff,a} \\ 1, & t \to \infty \end{cases} \tag{3.86}$$

Again the situation with $\alpha_2 = 1$ has a different long-time behavior:

$$I^{SE}(t) = \begin{cases} 2\left(1 - \frac{1}{2^{\alpha_1 - 1}}\right)\varphi_1 \left(\frac{t}{T_2^{eff,a}}\right)^{\alpha_1}, & t < T_2^{eff,a} \\ 1, & t \to \infty \end{cases} \quad (3.87)$$

In Figure 3.6 the behavior of the SE build-up function is illustrated, showing all the described features at long- and short-time limits.

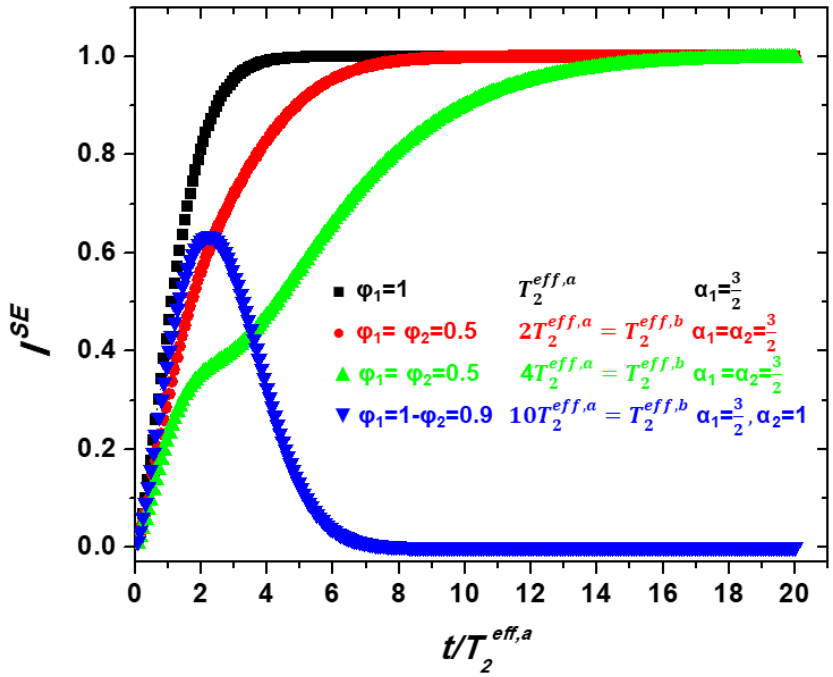

Figure 3.6 Solid-echo build-up functions $I^{SE}(t)$ for the case of a one-component system with an exponent $\alpha_1 = 3/2$ (black), a two-component system with exponents $\alpha_1 = \alpha_2 = 3/2$ and different characteristic decay constants (red and green), and a two-component system with an exponential contribution modelling a low molecular weight highly mobile fraction (blue).

Note, that taking into account the effects of the flip-flop transitions will result in the long-time limits in eq. (3.83) and (3.86) being less than 1. The consideration of this problem is out of scope of the current work.

The important outcome of the presented calculations is the fact that the slope of the initial rise of the DC and SE build-up functions at times $t < T_2^{eff}$ is not affected by the small fractions of the highly mobile impurities, which possess an exponential transverse magnetization decay (for instance, traces of solvent or low molecular weight polymer chains). However, in the situation when several spin groups, characterized by different spin-spin relaxation times, are present in the system, initial rise remains the same only at much shorter times (as is shown in Figure 3.5 and 3.6). This effect restricts the limits of the applicability of the presented formalism for extracting the segmental mean-squared displacement from the initial rise of the build-up functions. This restriction is more severe in the case of the dipolar-correlation build-up function $I^{DC}(t)$ (compare the same regimes in Figure 3.5 and 3.6).

3.5. Comparative discussion

Summarizing all the discussion of the possible applications of the DC, DQ and SE build-up functions to the investigation of the entangled polymer systems [49,108,109], it should be emphasized that all the three methods in ideal case provide equivalent information about the translational motion of the polymer segments from the theoretical point of view. Comparison of eq. (3.33), (3.63) and (3.73), which describe the respective build-up functions, shows that all of them differ only in a numerical coefficient.

However, construction of each of these build-up functions demands for a different experimental rendering. The most simple approach, consisting of a single Hahn echo NMR experiment, is required for the determination of I^{DC}, but accuracy of this method at short times depends on the precision of determining $S^{HE}(0)$ - Hahn echo signal at the initial time moment, see eq. (3.49). The combination of three spin-echo pulse sequences, which is necessary for the calculation of I^{SE}, is more complicated to apply and demands for a high quality of RF pulse's shape and phase stability [49]. However, as it can be seen from eq. (3.8), the knowledge of the initial values of spin-echo signals is not required in this case. Double quantum NMR technique represents a further sophistication of the experimental conditions, taking use of a high number of consequent RF pulses during the excitation and reconversion periods (see Figure 2.5), which create the DQ Hamiltonian. Here again as for I^{SE}, one does not need to obtain the initial values of the corresponding NMR signals, see eq. (3.73) Moreover, the time range of applicability of this expression is almost twice as large, as that of eq. (3.43) for I^{SE}. However, taking use of this advantage of DQ technique is only possible if one is able to implement the RF-pulse trains creating the DQ Hamiltonian with gaps between the pulses sufficiently short in order to neglect the spin displacements during them in comparison with the displacements during the whole excitation and reconversion periods. This issue has not been yet investigated with a necessary accuracy to be able to draw certain conclusions.

Since typical values of T_2^{eff} in polymer melts are on the order of milliseconds [98,108,111-114], segmental mean squared displacements in polymer melts directly probed by the methods based on I^{SE} and I^{DC}, proposed in this work, cover the time range $\sim 100\mu s < t < \sim(1-10)ms$. This range is limited by the receiver's dead time on the one hand and by the requirement $t < T_2^{eff}$, discussed in detail previously in the course of derivations. This time scale can be virtually extended utilizing the so-called *time-temperature superposition* principle (TTS), which is commonly used in rheological studies of polymer melt's mechanical relaxation [117,118]. Since, the segmental mean squared displacement in a polymer melt can be universally described by the relation $\langle r^2(t)\rangle \propto b^2\left(\frac{t}{\tau_s}\right)^{\alpha}$ [17,25], it follows that MSD temperature dependence is determined by $\tau_s(T)$ if it is assumed for the Kuhn segment length that $b(T) \cong b$, which is a justified approximation. This essentially means that varying temperature is equivalent to varying the time scale of the experiment, which results in the fact that the abovementioned experimental time-window of the measured mean squared displacements can actually probe different regions of polymer dynamics at different temperatures. Change of the temperature corresponds to a shift in the time domain, which is determined by the temperature dependence of the segmental relaxation time $\tau_s(T)$ that is known for a large number of linear polymers [13,119]. Thereby the so-called master curve of the MSD's time dependence can be constructed, which comprises all the experiments performed at different temperatures. This method is proved to be extremely useful in entangled polymer melts as applied to the spin-lattice relaxation dispersion [50,51,120] and the double-quantum NMR [121-124]

experiments. In *Chapter 4* it will be as well used to analyze the segmental mean squared displacement. In particular, in poly(ethylene-alt-propylene) TTS allows extension of the probed time scale to over 6 decades: $10^{-6} - 10^{0}\ s$.

Field-cycling relaxometry.

Segmental mean squared displacement that is obtained by means of the presented formalism via the construction of the intermolecular parts of the dipolar-correlation and the solid-echo build-up functions, according to eq. (3.48) and (3.69), is an important quantity, which reflects dynamics of a system. As was mentioned before, it can be also obtained from the field-cycling NMR relaxometry. Following the same idea of the separation of the intra- and intermolecular contributions to the total dipolar correlation function, in [100,101] it was shown that segmental MSD can be extracted from the intermolecular part of the spin-lattice relaxation rate $\frac{1}{T_1^{inter}}$. The relationship is given by:

$$\langle \tilde{r}^2 \left(t = \frac{2\pi}{\omega}\right)\rangle = \left(\frac{12}{5}\sqrt{\frac{\pi}{6}} f^{FC}(\alpha)\gamma^4\hbar^2 n_s \frac{T_1^{inter}}{\omega}\right)^{\frac{2}{3}}, \tag{3.88}$$

where

$$f^{FC}(\alpha) = \frac{\pi\left(1+2\cdot 2^{\frac{3\alpha}{2}}\right)}{2cos\left(\frac{3\pi\alpha}{4}\right)\Gamma\left(\frac{3\alpha}{2}\right)} \tag{3.89}$$

and

$$\frac{1}{T_1^{inter}} = \frac{\frac{1}{T_1} - \frac{1}{T_1^{intra}}}{\frac{8}{3}(1-\beta_H)(1-\frac{\gamma_D}{\gamma_H})^2 f_1^{FC}(\alpha)} \tag{3.90}$$

Here β_H is a fraction of protonated polymer chains, γ_D and γ_H are the gyromagnetic ratios of deuteron and proton, correspondingly, numerical coefficient $f_1^{FC}(\alpha)$ is given by:

$$f_1^{FC}(\alpha) = \frac{1+2\left(1+\frac{\gamma_D}{\gamma_H}\right)^{\frac{3\alpha-2}{2}} + \frac{1}{3}\left(1-\frac{\gamma_D}{\gamma_H}\right)^{\frac{3\alpha-2}{2}}}{1+2\cdot 2^{\frac{3\alpha}{2}}} \tag{3.91}$$

Similar to the methods introduced in this work, integration leading to eq. (3.88) assumes the exponent of the MSD power law $< \frac{2}{3}$. In the course of the derivation of this expression dipolar interaction between deuterons and protons was taken into account in addition to the pure proton-proton interactions. Its contribution is, however, rather small, depending on the value of $\left(\frac{\gamma_D}{\gamma_H}\right)^2 \cong 0.023$.

This method allows directly probing segmental dynamics in entangled polymer melts at times $10^{-9} - 10^{-4}s$. Employing a sophisticated hardware that can reach lower magnetic fields extends the higher limit of this time scale up to $\sim 10^{-3}s$ [125]. However, experiments at extremely low fields can result to the violation of the Redfield limit, which leads to the deviations in the measured relaxation rates. A number of work devoted to the extensive study of polymer dynamics with the use of this formalism was carried out [50,51,30,126,127]. Part of the data on polyethylene oxide presented in *Chapter 4* is as well obtained from the field-cycling relaxometry with the use of the mentioned approach.

Transverse relaxation.

Methods proposed in *Chapter 3.2* and *3.3* are based on different combination of the spin-echo signals. However, in [105] a way to determine segmental mean-squared displacement in entangled polymer melts from the intermolecular contribution to the Hahn echo signal was suggested. It should be noted that calculations were actually done for the free induction decay with the assumption of absence of the inhomogeneous effects discussed in *Chapter 2.4.* Practically, this condition is fulfilled only when the inhomogeneous effects are refocused in the Hahn echo pulse sequence, therefore the proposed approach is equally valid when applied to the transverse magnetization decay. Segmental MSD is then obtained with the help of the following expression:

$$\langle \tilde{r}^2(t) \rangle = \left(\frac{36\pi}{5(2-3\alpha)(4-3\alpha)} \sqrt{\frac{2}{3\pi}} \gamma^4 \hbar^2 n_s \frac{t^2}{\ln\left(\frac{1}{g^{inter}(t)}\right)} \right)^{\frac{2}{3}}, \tag{3.92}$$

where $g^{inter}(t)$ is the intermolecular part of the normalized Hahn echo signal. Here again the exponent of the MSD power law is assumed to be $\alpha < \frac{2}{3}$. However, another expression can be obtained with the use of this approach for the regime of normal diffusion $t > \tau_1$. In *Chapter 1* it was shown that all the polymer dynamics models predict segmental displacement due to the internal motions caused by relaxation of the Rouse modes to be on the order of $2R_g^2$ at the time moment $t \sim \tau_1$. At longer times diffusion becomes dominated by the center-of-mass translation that is characterized by the Einstein equation $\langle r^2(t) \rangle = 6D_{cm}t$. Given, that the relation $\langle \tilde{r}^2(t) \rangle = 2\langle r^2(t) \rangle$ is valid in the normal diffusion regime, the relative segmental MSD for times $t > \tau_1$ can be expressed as:

$$\langle \tilde{r}^2(t) \rangle = 2\langle r^2(t) \rangle = 4R_g^2 + 12D_{cm}t, \tag{3.93}$$

Now this expression can be used to evaluate the integrals in the equation derived in [105]:

$$g^{inter}(t) = exp\left(-\sqrt{\frac{2\pi}{3}} \frac{9}{5} \gamma^4 \hbar^2 n_s \int_0^t \frac{(t-\tau)d\tau}{\langle \tilde{r}^2(\tau) \rangle^{\frac{3}{2}}} \right) = exp\left(-\sqrt{\frac{2\pi}{3}} \frac{9}{5} \gamma^4 \hbar^2 n_s \int_0^t \frac{(t-\tau)d\tau}{\left(4R_g^2 + 12D_{cm}\tau\right)^{\frac{3}{2}}} \right) \tag{3.94}$$

This leads to the following connection between the center-of-mass diffusion coefficient and the intermolecular part of the Hahn echo decay at times $t > \tau_1$:

$$D_{cm} = \left(\frac{\sqrt{2\pi}\gamma^4 \hbar^2 n_s R_g}{5\sqrt{3} ln\left(g^{inter}(t)\right)} \right)^{1/2} - t \frac{\sqrt{6\pi}\gamma^4 \hbar^2 n_s}{20 R_g ln\left(g^{inter}(t)\right)} \tag{3.95}$$

Possible disadvantage of this formalism is that it is prone to effects connected with the exponential decay caused by highly mobile impurities, if they are present, unlike the solid-echo and the dipolar-correlation build-up functions (as was shown in the previous paragraph). Nevertheless, this approach will be shown to provide valuable results in *Chapter 4* for $t > \tau_1$.

Other techniques.

- Conventional NMR method probing translational displacement in different types of matter, in particular in polymer melts, is a *field-gradient NMR diffusometry* [87, 128]. It is based on the spatial encoding of spins in a system by applying an additional magnetic field (constant in time or pulsed), which creates a gradient across the sample either in one, or in several dimensions. Motion of the spins contributes additionally to the transverse relaxation rate, since it is sensitive to the low-frequency/long-time processes (see *Chapter 2.3*). This effect can be measured by a number of different, spin-echo based

pulse sequences. This method has been widely applied in polymer melts [25,31,44-46,125], however, it is subject to certain limitations. First, the minimal values of MSD accessible by field-gradient NMR are limited by the hardware, namely by the strength of the magnetic field gradient. Typically that sets the lower limit of measurable displacements at $\sqrt{\langle r^2(t)\rangle}\sim 200\text{Å}$. Second, polymer melts of high molecular weight are sometimes characterized by diffusion coefficients on the order of $10^{-15}\ \frac{m^2}{s}$, which then becomes comparable to a spin diffusion process due to the flip-flop transitions [129]. Interplay of these two effects complicates determination of a "real" segment displacement.

- Another widely used method that yields information about the translational segmental displacement is incoherent *quasi-elastic neutron scattering* (QENS) and, in particular, one of its types - *neutron spin echo* (NSE) [130,131]. In contrast to the classical QENS experiment, the difference in velocities, or times of flight, of individual neutron spins before and after the scattering event in a sample is registered in NSE through their Larmor precession in the magnetic field. Segmental MSD in this method is directly related to the scattering function that is obtained experimentally. In the assumption of the Gaussian diffusion propagator (Gaussian probability distribution of the displacement), the relation is

$$S_{inc}(Q,t) = exp\left(-\frac{1}{6}Q^2\langle r^2(t)\rangle\right), \tag{3.96}$$

where Q is a wave vector. Typical MSD obtained with NSE in polymer melts do not exceed 30 Å at times not longer than 100ns and are limited by the maximal achievable values of the wave vector. It should be mentioned as well that the neutron spin echo technique demands for an extremely sophisticated and expensive hardware, at the present time only less than 10 spectrometers suited for this purpose exist.

- Dynamic light scattering is commonly applied to determine the macro characteristics of polymer chains in solutions, such as radius of gyration or center-of-mass diffusion coefficient [9]. However, interpretation of the data obtained in polymer melts is excessively complicated from a theoretical point of view, therefore this technique is not relevant in the scope of this work.
- There is a number of other conventional methods, such as X-ray scattering, rheology, dielectric spectroscopy etc. that are used for the investigation of different properties of polymer melts, but they do not provide information about translational segmental dynamics.

In Figure 3.7 a graphical summary of the abovementioned experimental methods that provide information about segmental dynamics in entangled polymer melts and their time scales are presented. It should be noted that novel methods presented in this *Chapter* actually cover the time range inaccessible directly by other conventional techniques.

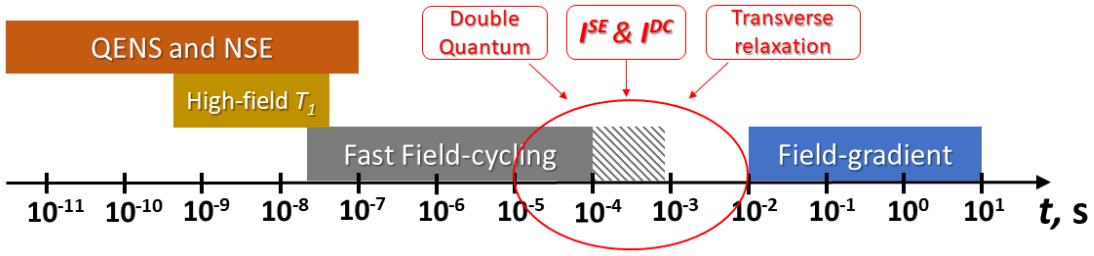

Figure 3.7. Time scale of an entangled polymer melt's segmental dynamics directly accessible by different techniques. The hatched part of the FFC rectangle represents the time range covered with the help of the ultra-low field-cycling NMR experiments [125]

Chapter 4. Experiment and Discussion

In *Chapter 4* theoretical formalism developed in *Chapter 3* is applied to investigation of a number of polymer melts. In order to exclude the effects of the proton chemical shift's difference, which is present in the majority of polymer species, all the experiments are performed at low magnetic fields (17, 19, 20 and 40 MHz). In these conditions possible modulation of the signal due to the chemical shift difference, which is proportional to the magnetic field H_0, is negligible when compared to the transverse relaxation rate: $\Delta\delta \ll \frac{1}{T_2^{eff}}$. For instance, in cis-polybutadiene-1,4 chemical shift difference between aliphatic and olefinic protons is 3.36 ppm [132], which means that characteristic time scale of its effect is $\sim 1ms$ at 300 MHz and $\sim 15ms$ at 20 MHz, whereas T_2^{eff} possesses a very weak frequency dependence and in both cases is on the order of $\sim 2 - 4ms$ at ambient temperatures.

As was mentioned in the previous *Chapter*, extensive study of polymer melt dynamics with the solid-echo and dipolar-correlation build-up functions benefits from the application of the time-temperature superposition principle. This demands for experiments within a broad temperature range above the polymer's melting point, which allows probing a larger time interval of the segmental dynamics. In order to circumvent the problem of inaccessibility of high temperatures (up to $\sim 150°\mathrm{C}$) on the available conventional NMR spectrometers at the moment of this work, a decision to construct an NMR device specifically suited for this purpose was taken. In *Chapter 4.1* all the details of its design and the important characteristics are given.

In *Chapter 4.2* the first experimental application of the dipolar-correlation build-up function in entangled cis-polybutadiene-1,4 melts with molecular weight $M_w = 196\ kg/mol$ is presented. These results were published in [108]. Obtained segmental mean squared displacement is compared with data from the independent field-cycling NMR relaxometry measurements on the same samples. Relative contribution of the inter- and intramolecular dipolar interactions is analyzed as well.

Chapter 4.3 contains a thorough investigation of entangled poly(ethylene-alt-propylene) melts with molecular weight $M_w = 200\ kg/mol$. Here the solid-echo build-up function is applied for the first time and the obtained results are compared with the ones yielded by the dipolar-correlation build-up function. The findings of these methods are not only corroborated by the conventional techniques at shorter times, but also considerably increase the probed time scale by several decades in time, thus providing an opportunity for a detailed discussion of polymer dynamics features. Time dependence of the relative contribution of the intermolecular dipolar interactions displays a well-pronounced variance with the predictions of the tube-reptation model. Results of this research were published in [49].

Finally, *Chapter 4.4* is devoted to an extensive study of polyethylene oxide melts of different molecular weights ($M_w = 10 \ldots 220\ kg/mol$). Several techniques, namely, field-cycling relaxometry, solid-echo and dipolar-correlation build-up functions, and the formalism based on the transverse relaxation (see *Chapter 3.5)*, are applied, providing an access to a wide range of segmental displacements. The obtained time dependence of the segmental MSD, as well as of the relative contribution of the intermolecular dipolar interactions, raises a question of applicability of the tube-reptation model for the explanation of the microscopic dynamics in polyethylene oxide.

4.1 Equipment

As was mentioned in the introduction, the main purpose of assembling a new spectrometer was an extension of the accessible temperature range up to at least $\sim 150°C$, in order to be able to effectively apply the time-temperature superposition principle for polymer melt dynamics investigation. An external constant magnetic field H_0 is created with the use of the field adjustable *Halbach magnet* [133,134], which is schematically shown in Figure 4.1. It consists of two nested MANDHALA rings, which are both composed of smaller dipolar magnets, made of *FeNdB* Grade 45 (N-45) coated with nickel and oriented in the Halbach array. The diameter of the borehole is $10\ cm$. The outer ring can be rotated, thereby changing the direction and the strength of the magnetic field, as is shown in a vector representation in Figure 4.1. The created magnetic field corresponds to the one of a dipolar magnet and is aligned in the transverse plane relatively to the axis of the two rings/cylinders. Magnetic field strength can be set in the range: $0.1 \dots 0.45$ T. It is decided to use the maximal magnetic field, corresponding to the proton Larmor frequency $\vartheta_0 = 19.2MHz$, for the sake of a better signal-to-noise ratio ($\vartheta_0 = 17MHz$ was used in some experiments). In this configuration the zone of the best magnetic-field homogeneity ($\sim 150ppm$) is located far off the center – it is determined by measuring the FID NMR signal at different positions with the use of the 3D-positioning system of a NMR probe, specifically designed for this purpose.

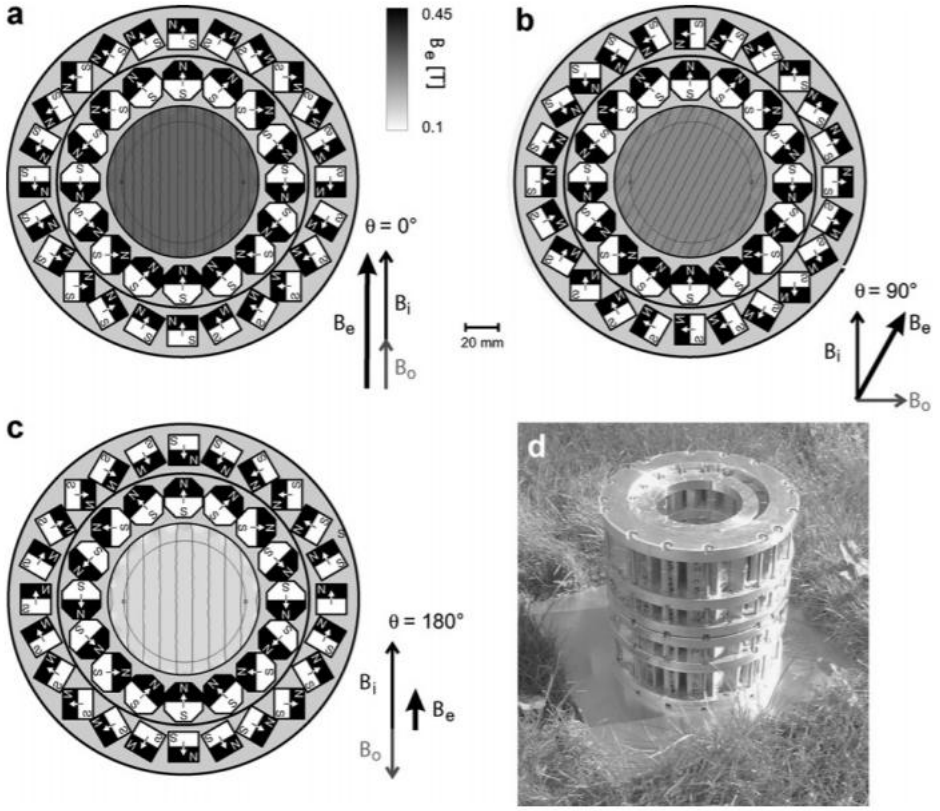

Figure 4.1. Schematic illustration of the Halbach magnet. It consists of two nested rings that create magnetic fields, the outer one can be rotated, thereby changing the value and the direction of the magnetic field, as is shown in a vector representation. *Reprinted from [135] with permission from Elsevier*

3D-Positioning system.

The 3D-positioning system is constructed with the highly-appreciated help of Robert Dyer. It operates in cylindrical coordinates, since it is a natural frame of choice for a cylindrical borehole of the magnet. Movement along each of the axis is provided with stepper motors, all of which are controlled by Pololu Micro Maestro 6-Channel USB Servo Controller, which in turn is operated through a serial port from a PC with the use of Pololu PC Maestro Interface. Step resolution of $\sim 1mm$ along z-axis and r-axis is achieved. Rotation around z-axis is performed with the use of a gear with the smallest possible angle increment of $\sim 0.01\ rad$. This movement covers only a half of a full revolution ($0 \dots 180°$), the full spatial span is reached by translation along the r-axis from $-r_m$ to r_m, where r_m is a radius of the magnet's borehole.

Photographs of the positioning system mounted under the magnet table and detached are shown in Figure 4.2 (a) and (b). Moving parts corresponding to each dimension are marked with numbers on the photograph (b). The probe is mounted on the top of the construction into a probe holder 3D-printed from polylactic acid (4). Current coordinates of the probe's position are detected with the use of potentiometers.

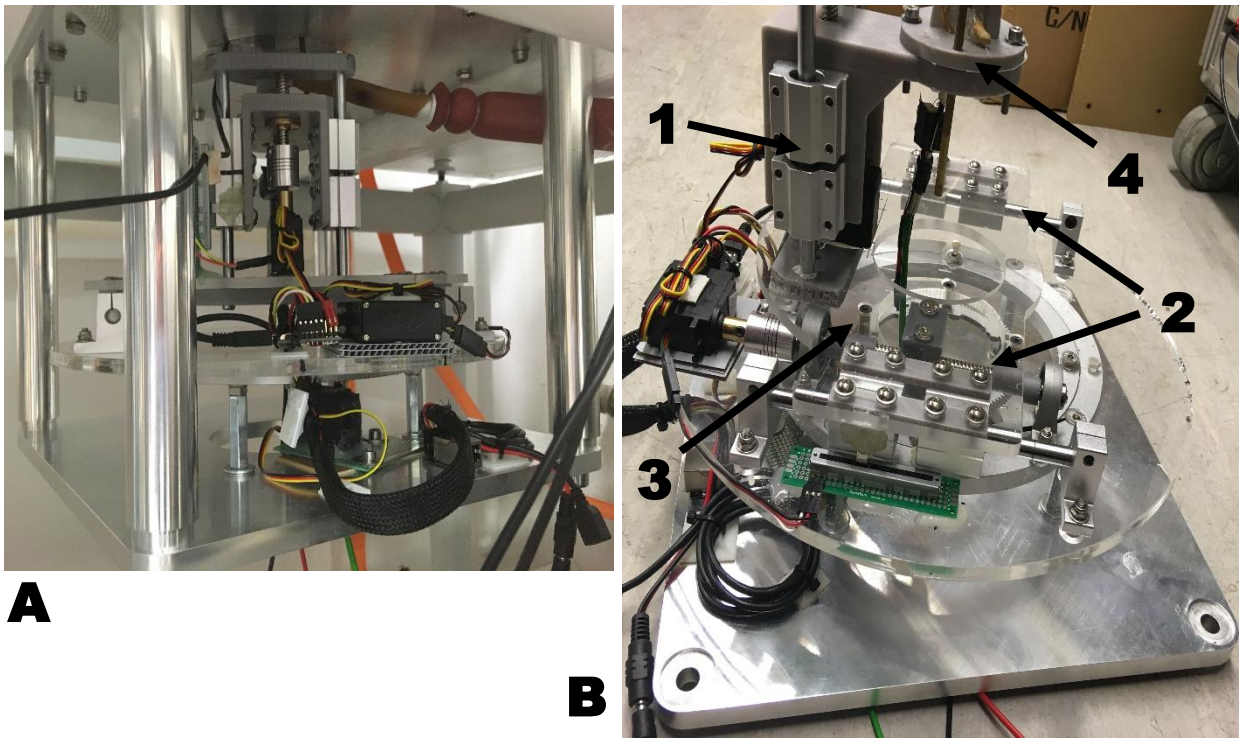

Figure 4.2. NMR probe 3D-positioning system, mounted under the magnet table (a) and separate (b). 3 dimensions on cylindrical coordinates are marked in (b): (1) – vertical movement along z-axis, (2) – horizontal movement along r-axis, and (3) – rotation around z-axis with use of a gear. (4) is a 3D-printed probe holder.

Thermal insulation of the magnet.

Using the permanent magnet for the NMR experiments inevitably leads to the problem of its temperature stability. For instance, for the *FeNdB* magnets used here change in temperature of $1K$ results in change of the material's magnetization by $\sim 1\%$ [133]. Situation is even more complicated if reaching high temperatures inside of the probe is intended. Therefore, it is decided to create an insulated thermal bath that will encapsulate the magnetic system. Temperature is stabilized at $30°C$ by Bruker Variable Temperature Unit B-VT 1000 via a pair of constantan heaters placed inside of the bath. Insulation is made of extruded polystyrene foam with a thickness of $10cm$. Photographs of the insulation box are shown in Figure 4.3. Holes are left on the top and on the bottom side of the box to provide access to the magnet's borehole.

The inner walls of the magnet are the most complicated parts to thermally isolate because they are in the closest proximity to the probe that is going to be heated. Another limitation arising in this case is the diameter of the borehole and the necessity for the probe to be able to move in order to find the optimal magnetic field homogeneity position. Practically, this means that the thickness of the insulation should not exceed $1.5 - 2\ cm$. To satisfy these conditions, an active insulation system based on the thermally controlled flowing water is used. A hollow copper spiral matching the diameter of the borehole with a water flow, temperature of which is kept by MGW Lauda RC 6 at $30°C$, is placed inside. It is shown in Figure 4.3 (b).In order to improve the thermal insulation inside the borehole, additional air exhaust by means of a powerful computer fan connected to the pipe on the top of the box is implemented (marked in Figure 4.3 (a).

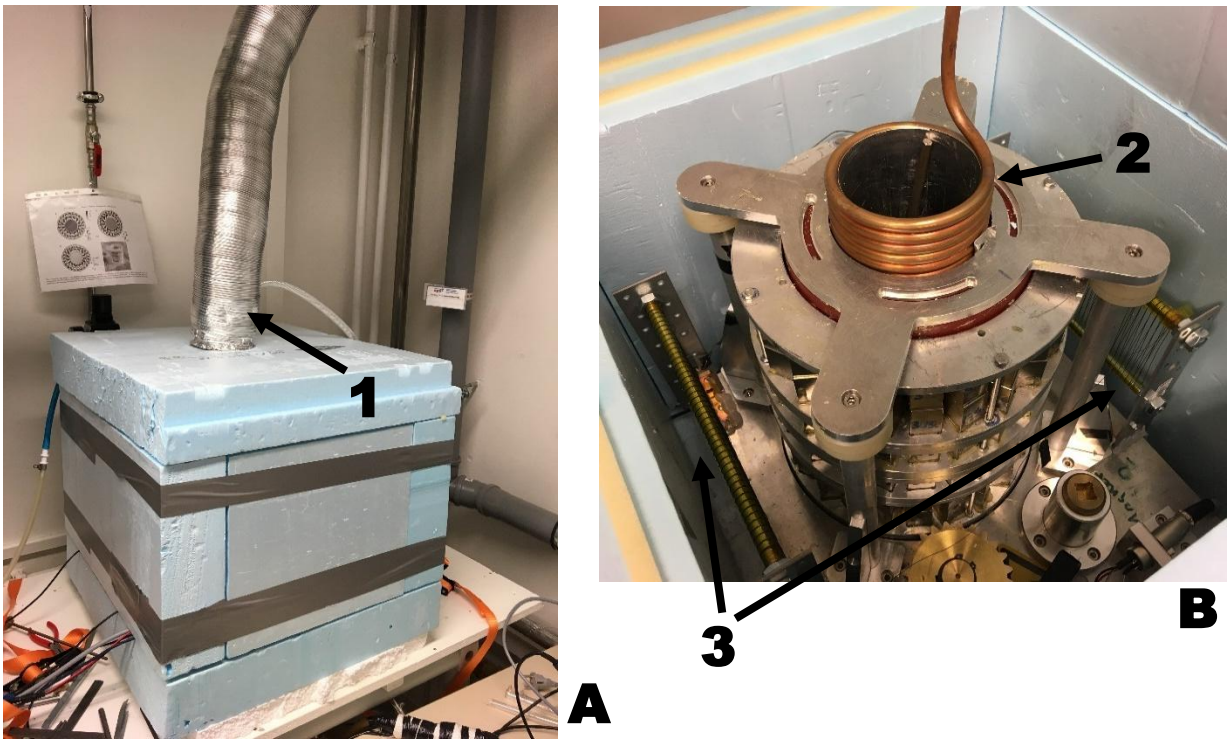

Figure 4.3. Photographs of the magnet insulation system. (a) the closed box, (b) view inside. (1) is an air exhaust system, (2) is a water thermal insulation, (3) is a pair of constantan heaters controlling the temperature of the magnet.

Stability of the magnet's temperature that is achieved with this insulation system is estimated through the stability of the proton Larmor frequency ϑ_0 determined in the NMR experiments, which corresponds to the magnetic field strength. Without the sample heating almost no significant change of ϑ_0 over 12 hours is observed, which is remarkably good. When the sample is heated to $\theta = 150°C$ the Larmor frequency becomes a subject to fluctuations around the equilibrium value with an amplitude of $\sim 2 - 3\ kHz$ and the period of $\sim 10\ hours$. These conditions are actually not critical in terms of data acquisition, since all the measurements that are performed in this work are based on the spin echo refocusing and therefore only the tops of the echoes that are not sensitive to moderate frequency offsets are acquired.

NMR probe.

In order to isolate the air flow that heats the sample from the magnet, it is decided to place the NMR radiofrequency coil inside the evacuated glass dewar. It has been made by Björn Herrnberger in the Glass Workshop of TU Ilmenau. Outer diameter of the dewar is $17mm$, inner diameter is $11mm$. The walls are less than $1mm$ thick and space between them is evacuated and vacuum sealed. Photograph of the dewar is shown in Figure 4.4 (a). The resonant circuit that is shown in Figure 4.4 (b) is a parallel oscillator circuit (see the circuit in Figure 4.4 (d)). It consists of the copper RF coil with $5mm$ inner diameter, the variable and the constant tuning capacitors C_1 and C_2, and the variable matching capacitor C_3. All the capacitors are characterized by the high Q-factors and by the high maximal voltage (1000V). The bandwidth of this circuit when tuned at $19.2\ MHz$ is $\sim 100 kHz$.

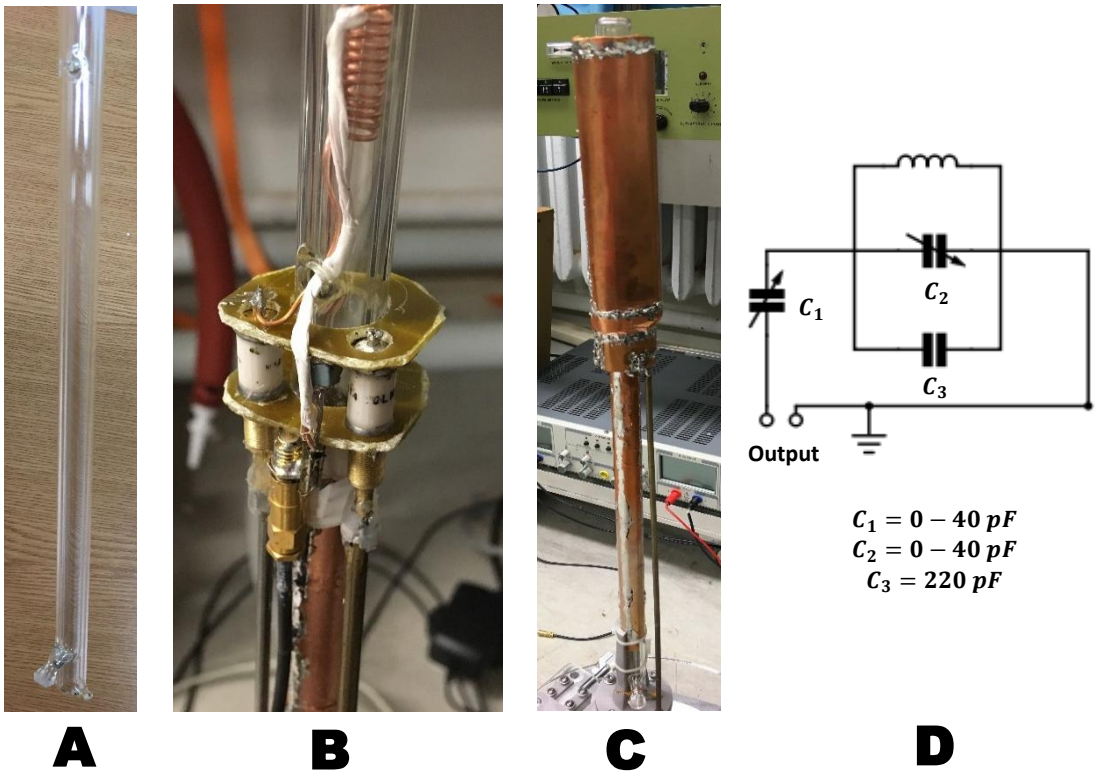

Figure 4.4. Construction of the NMR probe. (a) – the evacuated glass dewar that provides additional thermal insulation, (b) – the RF resonant circuit, consisting of the solenoid coil, the tuning and the matching capacitors, (c) – the whole probe with the copper noise shielding.

Copper shielding for the noise reduction is implemented around the resonant circuit that is shown in Figure 4.4 (d). It allows obtaining a signal-to-noise ratio of over 200 during a single scan of FID in a water sample completely filling the RF coil.

Heating of the sample is provided with a dry air flow, which is first preheated to $60°\mathrm{C}$ and then enters the dewar from the bottom passing through another heating system inside of it. Both the heaters are made of a nichrome wire and together allow reaching the temperatures up to $150°\mathrm{C}$. Temperature control is performed by regulating the current through the second heater by means of Delta Temperature Controller that is operating a transistor in a switching regime. Stability of the sample temperature achieved in this setup is $\pm 0.3°\mathrm{C}$.

Magnetic field homogeneity.

After the NMR probe, 3D-positioning system for it and the thermally insulated magnetic system with the desired characteristics have been designed, Magritek KEA NMR spectrometer together the Tomco RF Pulse amplifier are used to perform NMR experiments. Search for the best magnetic field homogeneity zone is carried out by measuring the length of the FID signal in a water solution of $Cu(SO)_4$. Unfortunately, as was mentioned previously, it is found to be far off the geometrical center of the magnetic system, which is an unfavorable condition due to the complexity of the thermal insulation in the case of the probe being too close to the magnet. Therefore, coarse shimming is applied by placing a magnetic rod with a diameter $\sim 5mm$ inside of the borehole. It obviously sticks to one of the poles, however, gentle manipulation with the rod's orientation and position allows shifting the homogeneity zone almost exactly to the center of the borehole.

Homogeneity of $< 50ppm$ is obtained under these conditions in a small ($1 - 2mm$ high) sample. However, magnetic field homogeneity along the z-axis for the larger samples is rather poor, which leads to a strongly non-exponential FID. This is a crucial problem since most of the isotopically diluted polymer melt samples are made rather big in order to increase the NMR signal. The only way to circumvent this effect without applying sophisticated shimming systems is to find a compromise and to deliberately work in the less homogeneous field. FID with slight distortions at short times at the homogeneity of $\sim 130ppm$ is shown in Figure 4.5. Eventually, optimal conditions are found to be when the homogeneity is $\sim 250ppm$. This experimental setup is used to obtain results presented in *Chapter 4.3* and *4.4.*

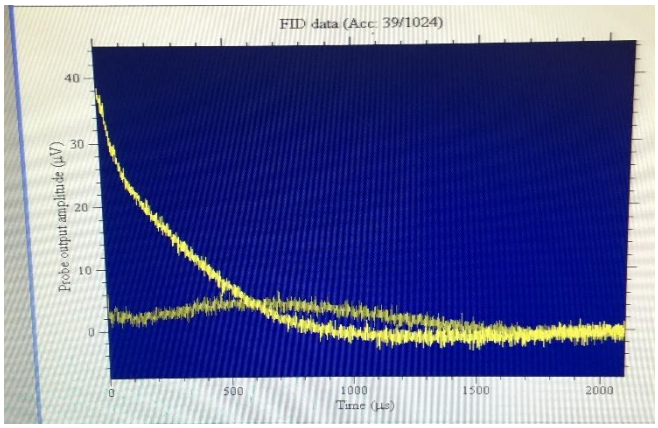

Figure 4.5. FID with slight distortions at short times obtained in a water solution of $Cu(SO)_4$ in the magnetic field with homogeneity of $\sim 130ppm$.

4.2 Polybutadiene

Experimental results presented in this paragraph were first published in [108]. In order to prove the feasibility of the method based on the dipolar-correlation build-up function presented in *Chapter 3*, experiments with fully protonated and isotopically diluted cis-polybutadiene-1,4 (PB) melts are carried out. Chemical structure of the PB monomeric unit is shown in Figure 4.6. Samples were prepared in the group of Ernst Rössler in Bayreuth University [50]. Fully protonated samples have $M_w = 196000\frac{g}{mol}$, isotopically diluted mixture consists of protonated chains with $M_w = 196000\frac{g}{mol}$ and deuterated chains with $M_w = 191000\frac{g}{mol}$ ($\frac{M_w}{M_n} = 1.02$, purchased from Polymer Standards Service GmbH, Mainz, Germany). Proton molar concentration in the mixture is 15%. Details of the isotopical dilution procedure will be further discussed in *Chapter 4.4* for polyethylene oxide samples.

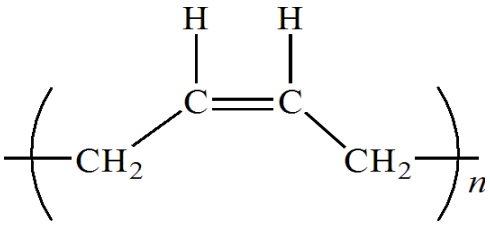

Figure 4.6. Chemical structure of cis-polybutadiene-1,4 monomeric unit.

Experiments are carried out on Minispec mq40 (Bruker, Germany) at a proton Larmor frequency of $40\ MHz$ at two distinct temperatures $308K$ and $338K$, controlled by a thermal bath within $0.1K$. A Hahn echo pulse sequence with $\hat{P}_x^{\pi/2}$ pulse length of $2.5\ \mu s$ and a $\hat{P}_y^{\pi}$ pulse length of $5\ \mu s$ is used. CYCLOPS phase cycling is implemented in order to minimize the unwanted effect of pulse and receiver channel imperfections.

Figure 4.7 (a) shows the normalized Hahn echo decay curves $g^{HE}(t)$ of the two PB samples at two different temperatures. The effect of deuteration is clearly observed. The effective relaxation time T_2^{eff} increases from $1.5\ ms$ for the protonated sample to $2.7\ ms$ for the deuterated sample at 308K, and from $1.9\ ms$ to $4.5\ ms$ at 338K. This increase in relaxation times remarks that in both the cases the intermolecular dipolar interactions play an important role, and evidently cannot be considered as negligible (this was thoroughly discussed from the theoretical point of view in *Chapter 3)*. From the Hahn echo signals shown in Figure 4.7 (a), the dipolar-correlation build-up functions $I^{DC}(t)$ are constructed using eq. (3.49) and are displayed in figure 4.7 (b). It can be seen that the characteristic behavior of the build-up functions at long times $t > T_2^{eff}$ can be attributed to the effect of the spin non-equivalency inherent to polybutadiene, explicitly discussed in *Chapter 3.4.*

Comparing the DC build-up function of the fully protonated sample $I_p^{DC}(t)$ with that of the isotopically diluted mixture $I_\beta^{DC}(t)$ with a corresponding proton content β, obtained at the same temperature, provides a way to extract the intermolecular contribution to the DC build-up function $I^{DC;inter}(t)$. In order to do that, it is assumed that the intermolecular contribution to the total DC build-up function is decaying proportionally with decreasing proton content in the melt. It means that the following relation should hold for arbitrary β:

$$I_\beta^{DC}(t) = 1 - exp\left(A'^{intra}(t) + \beta \cdot A'^{inter}(t)\right) \tag{4.1}$$

In *Chapter 4.4* it will be demonstrated in the series of the isotopically diluted polyethylene oxide samples that this proportionality is indeed valid. It is possible to derive the following expression for $I^{DC;inter}(t)$:

$$I^{DC;inter}(t) = 1 - \left(\frac{1-I_p^{DC}(t)}{1-I_\beta^{DC}(t)}\right)^{\frac{1}{1-\beta}} \tag{4.2}$$

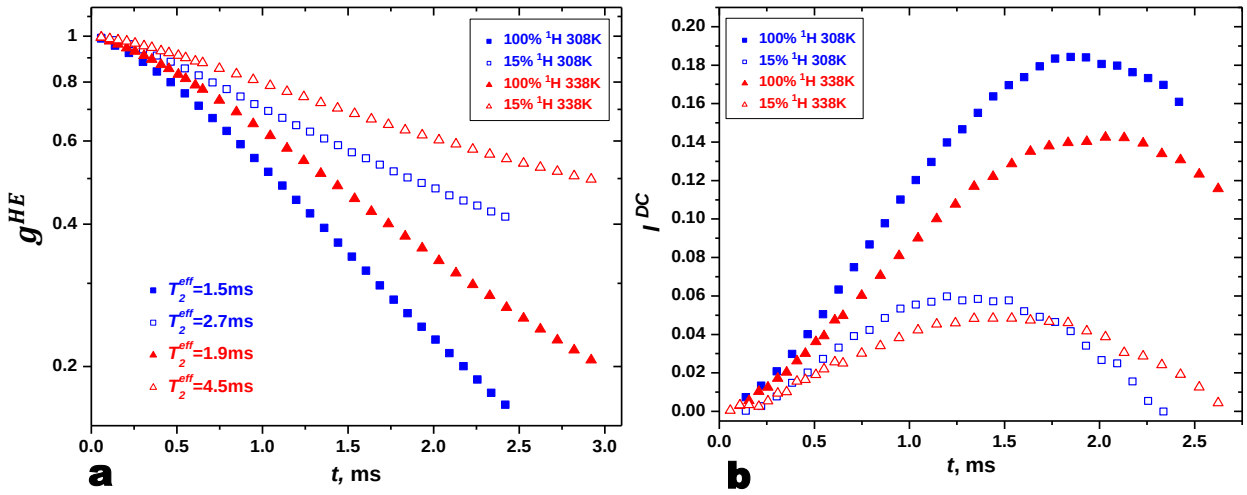

Figure 4.7. (a) Normalized Hahn echo decay and (b) dipolar-correlation build-up functions $I^{DC}(t)$ for the fully protonated polybutadiene $M_w = 196\ kg/mol$ (100% ^{1}H) and the mixture of protonated and deuterated polybutadiene $M_w = 191\ kg/mol$ (15% ^{1}H) at T=308K and T=338K.

Segmental mean squared displacement.

Eq. (3.69) can be used to calculate the relative segmental mean squared displacement. Assuming that motions of segments are statistically independent, the relative MSD $\langle \tilde{r}^2(t) \rangle$ is connected with the absolute MSD $\langle r^2(t) \rangle$ as $\langle r^2(t) \rangle = \frac{1}{2}\langle \tilde{r}^2(t) \rangle$ (see the discussion in *Chapter 3.1*). Taking $\beta = 0.15$, $n_s = 5.75 \cdot 10^{22} cm^{-3}$[38] and using the iterative approach described previously for the determination of the numerical coefficient $f(\alpha)$, the time dependence of $\langle r^2(t) \rangle$ is calculated. It is displayed in Figure 4.8 (a). Note that only the time region $t < T_2^{eff}$ of the Hahn echo signals is used for calculation of the segmental MSD. As expected, the MSD at 338K is larger than that at 308K. In the time interval $1 \cdot 10^{-4} - 2 \cdot 10^{-3} s$ the root mean-squared displacement (RMSD) between 35 Å and 75 Å is found. In the case of PB196000 the entanglement length, known as the tube diameter, is $d_t \cong 40$Å [38]. Therefore, in this temperature interval, according to the tube-reptation model, the range of the MSD reflects the crossover from the non-entangled to the entangled dynamics (from the Rouse regime I to the incoherent reptation regime II).

In figure 4.8 (b) the master curve of the segmental MSD that is composed from Figure 4.8 (a) using the time-temperature superposition principle is shown. The reference temperature is set at $338\ K$. The applied shifting factor was taken from the temperature dependence of the segmental relaxation time $\tau_s(T)$ for polybutadiene reported in [131]. An exponent of the power law $\alpha = 0.32 \pm 0.03$ is found, which is an intermediate value between the regime I (Rouse) $\alpha = 0.5$ and the regime II (incoherent reptation) $\alpha = 0.25$ of the tube-reptation model.

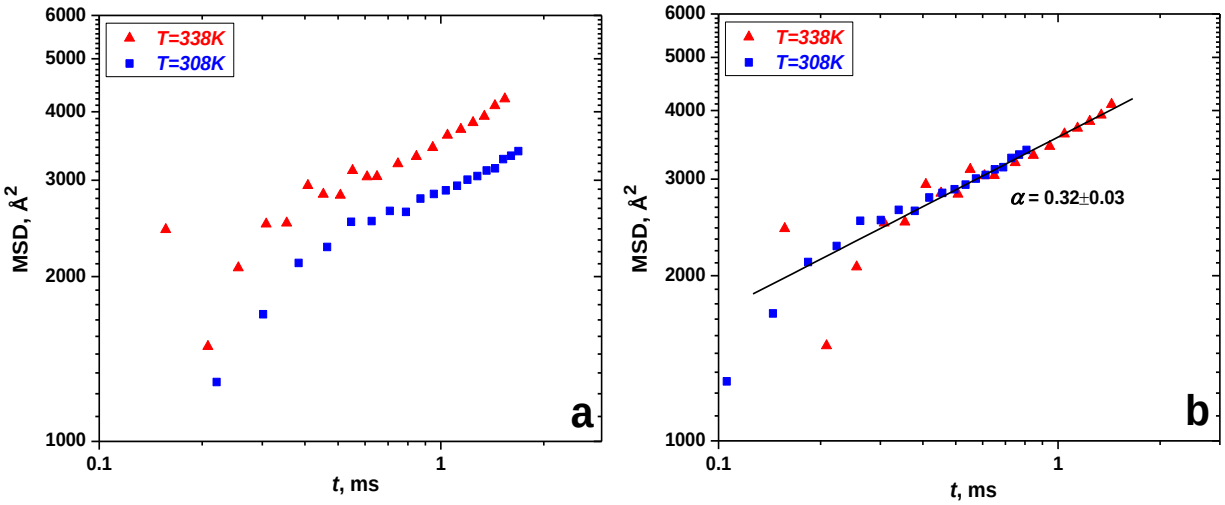

Figure 4.8 (a) Segmental mean squared displacement in polybutadiene $M_w = 196\ kg/mol$ calculated from $I^{DC;inter}(t)$ at $T = 308K$ and $T = 338K$. (b) as in (a), but superimposed using the time-temperature superposition principle. The resulting data is fitted by a power law with an exponent $\alpha = 0.32 \pm 0.03$.

Direct measurements of the MSD at the discussed time region $1 \cdot 10^{-4} - 2 \cdot 10^{-3} s$ for such a high molecular weight of PB has never been reported earlier. As was discussed in *Chapter 3.5* conventional techniques, namely, field-cycling relaxometry, field gradient NMR and neutron scattering, possess certain limitation, which makes this displacement and time interval inaccessible to the direct measurements. However, the data obtained with the dipolar-correlation build-up function can be, nevertheless, compared with the FC results if the time window is shifted again by applying the TTS. In Figure 4.9, results provided by the DC method are plotted together with the MSD derived from the field-cycling NMR relaxometry on the very same samples, [50], shifted to the reference temperature of $391K$. Clearly, both the absolute values of the MSD and its time dependence coincide with only minimal deviation.

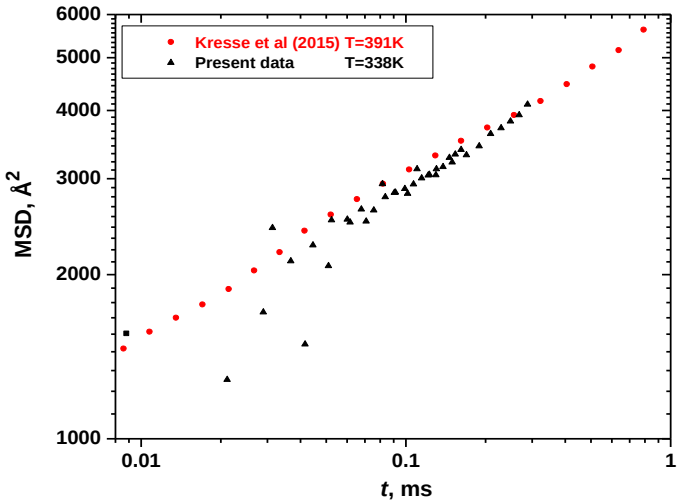

Figure 4.9 Segmental mean squared displacement extracted from the field-cycling NMR relaxometry data [50] for polybutadiene at $T = 391K$ compared with the MSD calculated for the same samples at $T = 338K$ in this work, superimposed with the use of the time-temperature superposition principle.

Inter- and intramolecular dipole-dipole interactions.

Another important feature that can be studied using the formalism introduced in *Chapter 3* is a relative contributions of the inter- and intramolecular dipolar interactions. It follows from eq. (3.58) that these contributions are contained in the exponent of the normalized Hahn echo decay and are expressed through the convolution of the corresponding dipolar correlation functions with time (similar to eq. (3.64)). Assuming again that decrease of the intermolecular contribution is proportional to the proton content, the following expression for $\frac{A^{inter}}{A^{intra}}$ is derived:

$$\frac{A^{inter}}{A^{intra}} = \frac{L_p(t) - L_\beta(t)}{L_\beta(t) - \beta L_p(t)}, \tag{4.3}$$

where $L_p(t)$ and $L_\beta(t)$ are the logarithms of the normalized Hahn echo signals of the fully protonated and the isotopically diluted samples, respectively. A^{inter} and A^{intra} should be distinguished from A'^{inter} and A'^{intra} used in eq. (4.1), which reflect analogous contributions to the exponent of $I_\beta^{DC}(t)$.

In Figure 4.10 the ratio $\frac{A^{inter}}{A^{intra}}$ is plotted as a function of the RMSD, $\langle r^2(t)\rangle^{\frac{1}{2}}$. As can be seen, intermolecular contribution dominates at longer times and $\frac{A^{inter}}{A^{intra}}$ grows steadily in the whole range. This is at variance with the theoretical predictions of the tube-reptation model. As was established from the MSD data, the probed regime of the dynamics corresponds to the transition from isotropic to anisotropic motion (Rouse to incoherent reptation). According to eq. (3.7) $\frac{A^{inter}}{A^{intra}} \propto \frac{A_0^{d;inter}}{A_0^{d;intra}} \propto \langle r^2(t)\rangle^{-\frac{1}{2}}$ in the regime of the anisotropic motion, however this is not observed in the current results. Any apparent tendency to reaching the plateau of $\frac{A^{inter}}{A^{intra}}$ would indicate the beginning of the transition towards reptation dynamics. In this case the relative intermolecular contribution should reach a maximum and start to decrease as $\propto \langle r^2(t)\rangle^{-\frac{1}{2}}$.

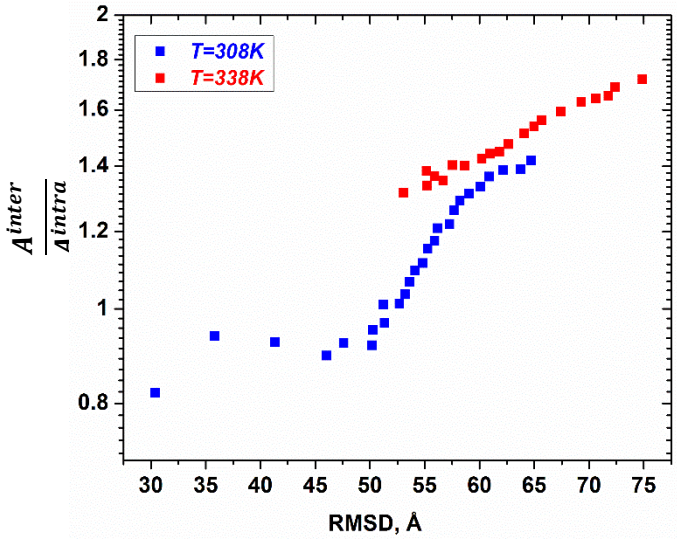

Figure 4.10. Ratio of inter- over intramolecular contributions to the Hahn echo decay $\frac{A^{inter}}{A^{intra}}$ in polybutadiene $M_w = 196\ kg/mol$ at T=308K and T=338K calculated based on eq. (4.3) and plotted as a function of the root mean squared displacement $\langle r^2(t)\rangle^{\frac{1}{2}}$.

Summary.

The novel method introduced and explicitly described in *Chapter 3* that is based on the dipolar-correlation build-up function is shown to be feasible for probing dynamics of entangled polybutadiene melts $M_w = 196\ kg/mol$. Separation of the inter- and intramolecular dipolar interactions is effectively performed using isotopical dilution technique. Segmental mean squared displacement corresponding to translation of segments from different macromolecules is extracted from the intermolecular part of the DC build-up function and is compared with the conventional field-cycling relaxometry data using the time-temperature superposition principle, showing good agreement between the techniques, which is interpreted as a proof of feasibility of the dipolar-correlation build-up function formalism.

Segmental MSD are directly probed in a time scale of $1 \cdot 10^{-4} - 2 \cdot 10^{-3} s$, which is not accessible by other experimental techniques (neutron spin echo, field-cycling NMR relaxometry, field-gradient NMR). Therefore, the presented method can be considered as a powerful tool for investigation of entangled polymer melt dynamics that provides unique information about the segmental translation.

The observed exponent of the power law of the MSD time-dependence $\alpha = 0.32 \pm 0.03$ and the probed time/temperature interval correspond to the transition between the Rouse and incoherent reptation dynamics in the framework of tube-reptation model. However, the obtained dependence of the ratio of the inter- and intramolecular dipolar interactions $\frac{A^{inter}}{A^{intra}}$ on the root mean squared displacement is at variance with the tube-reptation model prediction for the regime of anisotropic motion. Importantly, it is shown that intermolecular contribution prevails over the intramolecular one at longer times that corroborates theoretical results discussed in *Chapter 3*.

At the time period when that experimental work was conducted the high-temperature NMR spectrometer described in *Chapter 4.1* was not yet assembled. Therefore, the maximal temperature used corresponds to the maximal accessible temperature for the Bruker Minispec mq40, $T = 338K$. In the next paragraph an extensive investigation of poly(ethylene-alt-propylene) melts is presented with the use of the high-temperature equipment.

4.3 Poly(ethylene-alt-propylene)

Poly(ethylene-alt-propylene) (PEP) with a narrow molar mass distribution ($M_w/M_n < 1.06$) was synthesized in the group of D. Richter (Forschungszentrum Jülich, Germany) and kindly provided by E. Rössler (Bayreuth University, Germany). The polymer combines a very simple structure shown in Figure 4.11, a low glass transition temperature of $T_g \cong 206K$ [127] and only a weak tendency to crystallize. Two samples are used: one of them represents fully protonated PEP with a molar mass of $M_w = 200\ kg/mol$. The second sample is an isotopic mixture composed by fully protonated and fully deuterated PEP of the same molecular weight $M_w = 200\ kg/mol$, with weight fractions of 10% ^{1}H and 90% ^{2}H, respectively. Both samples are in a highly entangled state due to the molecular weight M_w significantly exceeding the critical mass of PEP, $M_c \cong 2\ kg/mol$ [38], therefore the anomalous segmental diffusion regime is expected in a broad range of time, representing the point of interest for this work. Most of the results presented in this paragraph were first published in [49].

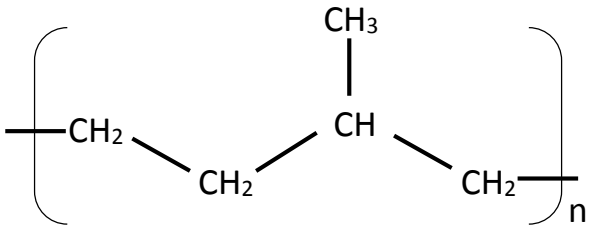

Figure 4.11. Chemical structure of poly(ethylene-alt-propylene) monomeric unit.

Transverse NMR relaxation experiments are performed in a broad temperature range $T = 283K$-$-440K$ with the use of three different NMR spectrometers. The measurements at temperatures $T = 283K-338K$ are carried out on a Minispec mq40 (Bruker, ^{1}H $40\ MHz$). The intermediate temperature range $T = 338K-400K$ is covered on the Minispec mq20 (Bruker, ^{1}H $20\ MHz$) in the group of K. Saalwächter (University of Halle, Germany). Finally, high temperatures above $400K$ are covered with the use of a homemade spectrometer described in *Chapter 4.1* at the Larmor frequency of $17\ MHz$. The results of all the measurements at different temperatures are treated in the same way, since the analysis of the data based on the formalism developed in *Chapter 3* is independent from the Larmor frequency. In order to calculate the solid-echo build-up function $I^{SE}(t)$ according to eq. (3.1) one needs to obtain signals S_1, S_2 and S_3 resulting from three different pulse sequences $\left(\hat{P}_x^{\pi/2} - \tau - \hat{P}_y^{\pi/2}\right)$, $\left(\hat{P}_x^{\pi/2} - \tau - \hat{P}_x^{\pi/2}\right)$ and $\left(\hat{P}_x^{\pi/2} - \tau - \hat{P}_y^{\pi}\right)$, as was discussed earlier. In principle, the numerator of $I^{SE}(t)$, namely $S_1 + S_2 - S_3$, can be obtained in one single experiment, using the pulse sequence $\left(\hat{P}_x^{\pi/2} - \tau - \hat{P}_{k_1}^{\pi/2}\hat{P}_{k_2}^{\pi/4}\hat{P}_{k_3}^{\pi/4}\right)$ with a proper phase cycling for k_1, k_2 and k_3, so that the $\hat{P}_\alpha^{\pi/4}$ RF pulses are either in phase (Hahn echo S_3) or cancel each other (S_1 and S_2). However, this type of experiment demands for a high homogeneity of the RF field, otherwise artifacts connected with a non-perfect angle of a magnetization flip following the RF pulse can appear. Therefore, in this work, signals S_3 and $S_{12} = S_1 + S_2$ (with the use of phase cycling) are measured separately and are then combined in order to obtain the SE build-up function. As an example, in Figure 4.12 the solid-echo build-up function $I^{SE}(t)$ is plotted as a function of time $t = 2\tau$ for the fully protonated and the diluted sample at $T = 333K$.

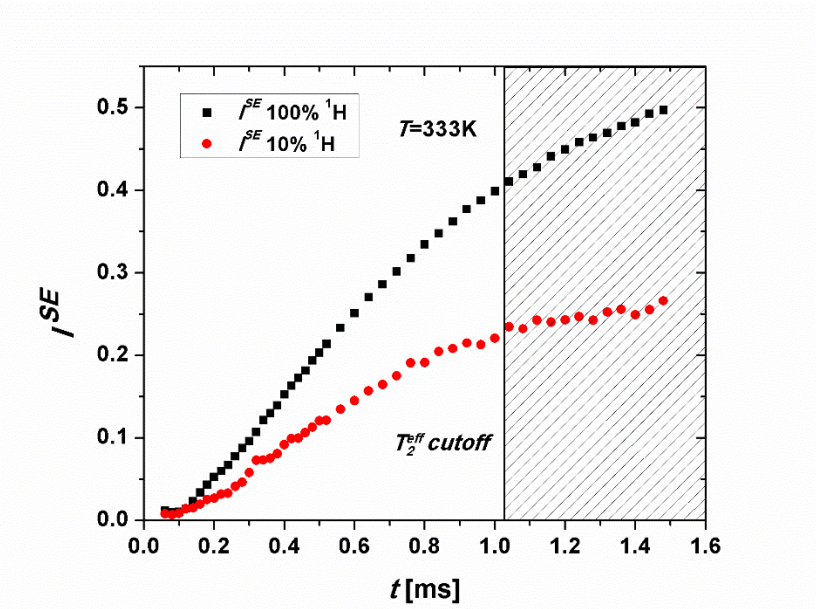

Figure 4.11. Proton solid-echo build-up function $I^{SE}(t)$ as a function of time for the protonated (100% ^{1}H) and diluted (10% ^{1}H) PEP 200k. The vertical line marks the T_2^{eff} characteristic time of a transverse magnetization decay for the protonated sample.

Segmental mean squared displacement.

The representation of this data into the relative mean-squared displacements according to eq. (3.48) is valid only for times $t < T_2^{eff}$. Thus, the area of the curves which is not used for analysis is marked on the plot, corresponding to T_2^{eff} of the protonated sample, as it is always lower than T_2^{eff} of the diluted one, due to the almost full elimination of the intermolecular proton dipole-dipole interactions in the latter. The intermolecular part of the build-up function $I^{SE;inter}$, which is necessary for obtaining the segmental MSD, can be extracted from this data via extrapolation to the zero proton content in the same way as for $I^{DC;inter}$:

$$I^{SE;inter}(t) = 1 - \left(\frac{1-I_p^{SE}(t)}{1-I_\beta^{SE}(t)}\right)^{\frac{1}{1-\beta}}, \tag{4.4}$$

where, β is the proton concentration in the diluted sample, $I_p^{SE}(t)$ and $I_\beta^{SE}(t)$ are solid-echo build-up functions of the protonated and the diluted samples, respectively. Again relation $\langle r^2(t)\rangle = \frac{1}{2}\langle \tilde{r}^2(t)\rangle$ is assumed and the segmental mean-squared displacement, which is calculated using eq. (3.48) with $n_s = 7.36 \cdot 10^{22} cm^{-3}$[38] at different temperatures $T = 283K - 440K$, is plotted in Figure 4.12.

The long-time limitations of validity of the curves for each temperature are connected with the values of T_2^{eff}, which is increasing with the temperature. On the other hand, the short-time limit is determined by the difference between the values of I_β^{SE} and I_p^{SE}, which is becoming too small, leading to a high uncertainty of the calculated $I^{SE;inter}$ and, consequently, of $\langle r^2(t)\rangle$.

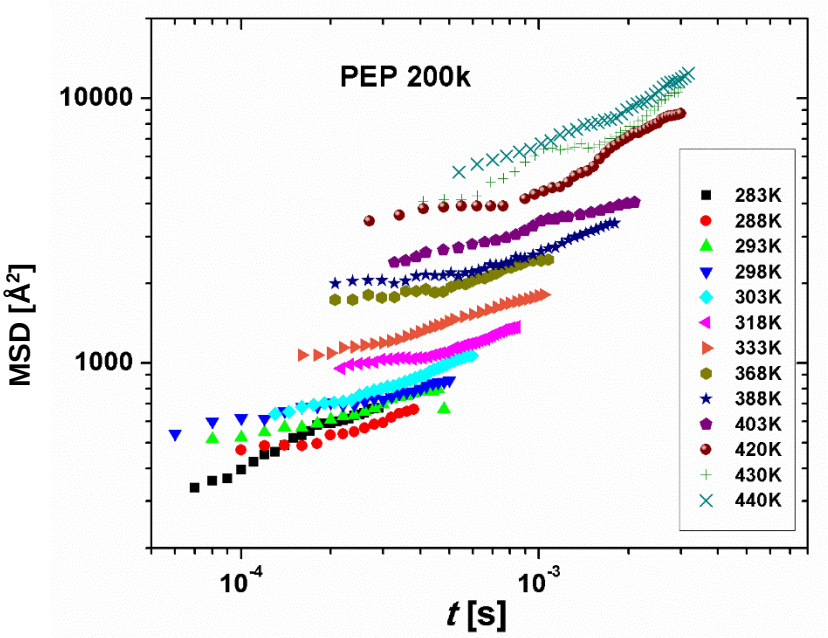

Figure 4.12. Segmental mean-squared displacements $\langle r^2(t)\rangle$ of PEP 200k for different temperatures.

In order to illustrate the actual interval of the measured displacements in time, the time-temperature superposition (TTS) principle is applied. The temperature dependent coefficients used for the horizontal (i.e. time) shift of MSD curves in Figure 4.12 relative to the reference temperature are taken from the segmental relaxation time temperature dependence data $\tau_s(T)$ obtained by shear rheology, dielectric spectroscopy and FC NMR, presented in [126] and shown in Figure 4.15 as well. The reference temperature is set to be 333K and results are compared with the MSD of PEP with $M_w = 80\ kg/mol$ measured by means of neutron spin echo spectroscopy carried out by Wischnewsky et al. at the $T = 492K$ [136]. In order to perform such a comparison the extrapolation of the $\tau_s(T)$ to $T = 492K$ is done and the value of τ_s obtained in this way (marked in Figure 4.15) is used for the temperature shift of the NSE data. The result of this superposition yields a master curve shown in Figure 4.13.

One can see that data obtained by the SE method coincides well with NSE data in the time interval $t \approx 10^{-6} - 10^{-5}s$, and extends significantly the probed time range of the segmental mean-squared displacements up to $t \approx 1s$ at $T = 333K$. Three power-law regimes are revealed. Two transition times were estimated from the intersections of the power laws: $\tau_e \cong 4.6\mu s$, corresponding to the transition between the Rouse (I) and the incoherent reptation (II) regimes, and $\tau_R \cong 47ms$, marking the transition between the incoherent reptation (II) and the coherent reptation (III) regimes in the framework of the tube-reptation model. It is noted that to the best of the author's knowledge, the latter transition in PEP 200k was observed for the first time.

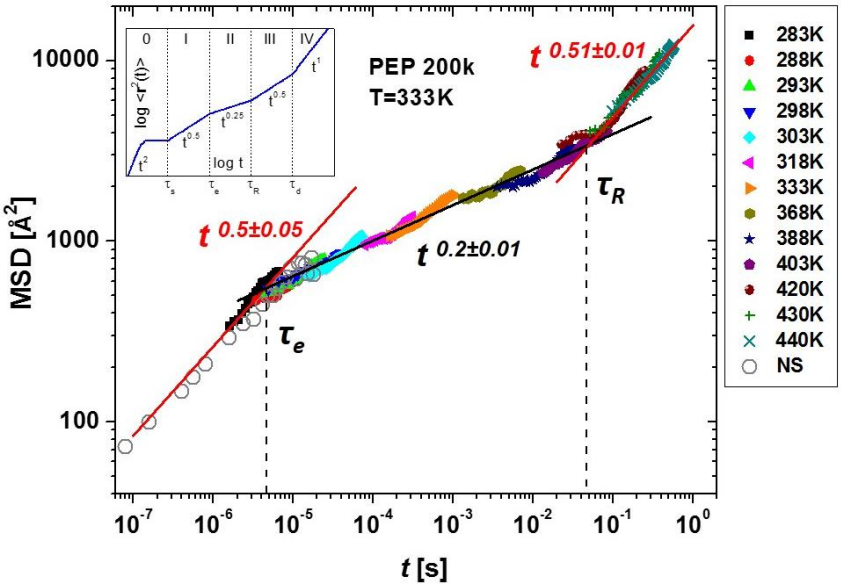

Figure 4.13. PEP 200k MSD time dependence obtained via time-temperature superposition of the curves in Figure 4.12, and MSD of PEP 80K measured using neutron spin echo (NSE) spectroscopy [136]. Three different power-law regimes are revealed with exponents as indicated. The crossover times τ_e and τ_R are determined from the intersections of the power laws. The inset shows the predictions of the tube-reptation model for the MSD time dependence.

The exponents of the power laws in regimes (I) $\alpha = 0.5 \pm 0.05$, and (III) $\alpha = 0.51 \pm 0.01$, respectively, are in good agreement with the values predicted by the tube-reptation model ($\alpha = 0.5$), whereas in regime (II) the observed exponent $\alpha = 0.2 \pm 0.01$ is lower than the theoretical value of $\alpha = 0.25$. Model prediction for the ratio between τ_R and τ_e for the case of PEP is $\frac{\tau_R}{\tau_e} = \left(\frac{N}{N_e}\right)^2 \cong 8000$. The data displayed in Figure 4.12 yields the value $\frac{\tau_R}{\tau_e} \cong 10000$, which is remarkably close to the theoretically predicted one.

With these results, it is possible to estimate the characteristic tube diameter d_t of poly(ethylene-alt-propylene) using the value of τ_e: $\langle r^2(\tau_e)\rangle^{\frac{1}{2}} = \sqrt{\frac{2}{\pi^{3/2}}}\, d_t$ [17]. It results in $d_t \cong 3.9nm$, which is in good agreement with the calculated value $4.88\ nm$ [38] and the NS data yielding $4\ nm$ from [136].

In [126] the same polymer PEP 200k was studied with the field-cycling NMR relaxometry and the values of $\alpha \cong 0.5$ for regime I and $\alpha \cong 0.2$ in the beginning of regime II were obtained, as well as the tube diameter of $4.6\ nm$. In Figure 4.14 the MSD obtained from the SE method presented in Figure 4.12 is compared to the FC relaxometry and NSE data, and to the results from the method based on the dipolar-correlation build-up function using eq. (3.69). For the latter, again the principle of the time-temperature superposition was applied for constructing the master curve using the same temperature shift factors as previously.

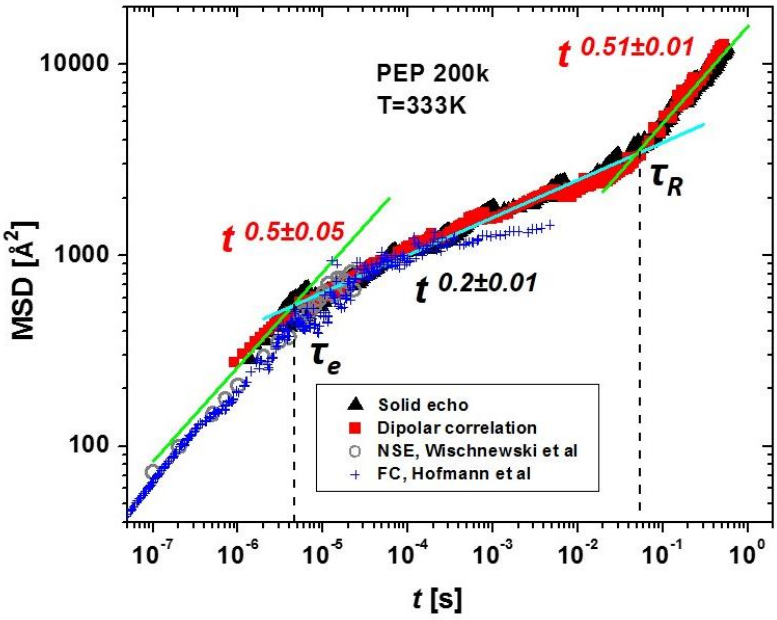

Figure 4.14. PEP 200k MSD time dependence obtained through $I^{SE}(t)$ (SE formalism) and $I^{DC}(t)$ (DC formalism) is compared with FC data in PEP 200k [126] and the MSD of PEP 80K measured with the use of NSE [136].

Exceeding the time range of NSE spectroscopy and FFC relaxometry, the presented SE and DC methods are able to reach regime III of the tube-reptation model. $I^{DC}(t)$ data clearly yields 3 regimes of the time-dependent segmental MSD with exponents close to the ones observed with the use of $I^{SE}(t)$. The difference of absolute values of the MSD between these two methods is satisfactory, the tube diameter calculated from the DC data is slightly higher than the one calculated before $d_t \cong 4.2nm$.

In addition to that, it should be taken into account that the $I^{SE}(t)$ build-up function has an amplitude two times higher than that of the $I^{DC}(t)$ build-up function, which can be seen from the comparison of eq. (3.41) and (3.63). This leads to a better signal-to-noise ratio for the SE method. At the same time, construction of $I^{DC}(t)$ is technically simpler, demanding only for performing a Hahn echo experiment. Contrary, for the construction of the $I^{SE}(t)$ function, a series of double pulse experiments with perfectly tuned receiver phase and RF pulses of a high quality is necessary.

Characteristic time constants.

In Figure 4.15 the temperature dependencies of all the characteristic time constants of the tube-reptation model in PEP are presented: segmental relaxation time τ_s, entanglement time τ_e, Rouse relaxation time τ_R and tube disengagement relaxation time τ_d. The graph is based on Figure 7 from [127] with the addition of the data obtained in the present work by the novel SE and DC methods. Values of $\tau_e(T)$ are provided by ^{1}H FC NMR, shear-stress rheology [126], dielectric spectroscopy and solid-state ^{2}H NMR [137] for different molecular weights of PEP, since τ_s is molecular weight-independent. $\tau_s(T)$ data is interpolated by a four-parameter function [119] and this function is vertically shifted to intersect τ_e, τ_R and τ_d values. The presented values of the entanglement time τ_e for PEP 200k are obtained with the use of NSE [136], ^{1}H FC NMR [126] and the SE and DC methods. It is clearly seen that τ_e provided for $T =$

$333K$ by the methods introduced in this work is in good agreement with the other two experimental values. Furthermore, the SE and DC approach is the only one providing the value of the Rouse relaxation time τ_R for PEP 200k. In addition to this, temperature dependence of the terminal relaxation time for PEP 200k $\tau_d(T)$ obtained with the use of shear-stress rheology [127] is shown for the complete illustration of the relaxation times map in PEP.

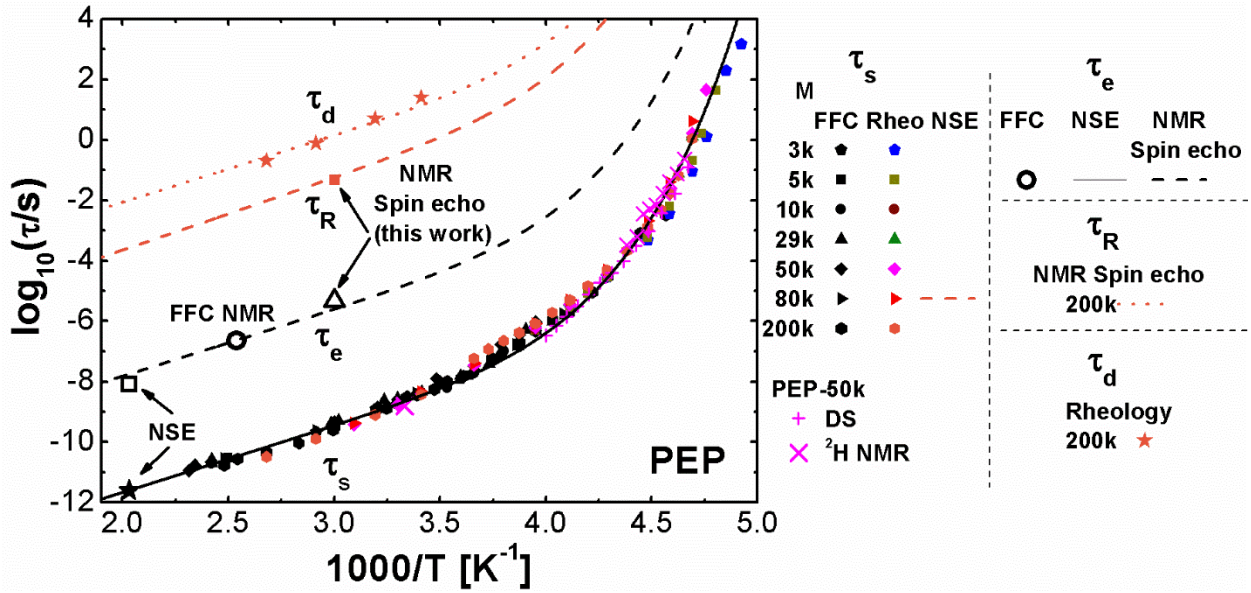

Figure 4.15. Relaxation map of PEP: $\tau_s(T)$, $\tau_e(T)$, $\tau_R(T)$ and $\tau_d(T)$ obtained by different methods.

Inter- and intramolecular dipolar interactions.

Investigation of the relative contributions of the inter- and intramolecular dipolar interactions to the total dipole-dipole correlation function is performed similarly to the previous paragraph. Eq. (4.3) is used to calculate the ratio $\frac{A^{inter}}{A^{intra}}$ from the Hahn echo signals with $\beta = 0.1$. It is plotted as a function of the RMSD in Figure 4.16 (a). The whole time scale is separated into 3 regimes of segmental dynamics based on the MSD data and is fitted in regimes I and II (black line). Blue line represents the prediction of the tube-reptation model.

The exponent of the $\frac{A^{inter}}{A^{intra}}$ dependence on RMSD in regime I is 1.28 ± 0.08, which is sufficiently close to the theoretical prediction for isotropic motion. Interestingly, the behavior of $\frac{A^{inter}}{A^{intra}}$ in regimes II and III is completely different from what follows from the model prediction: here the function grows as a function of RMSD with the exponent of the power law 0.47 ± 0.02 in regime II, tending to reach a plateau in regime III. In the previous paragraph similar situation during the transition from regime I to regime II was demonstrated in polybutadiene melt.

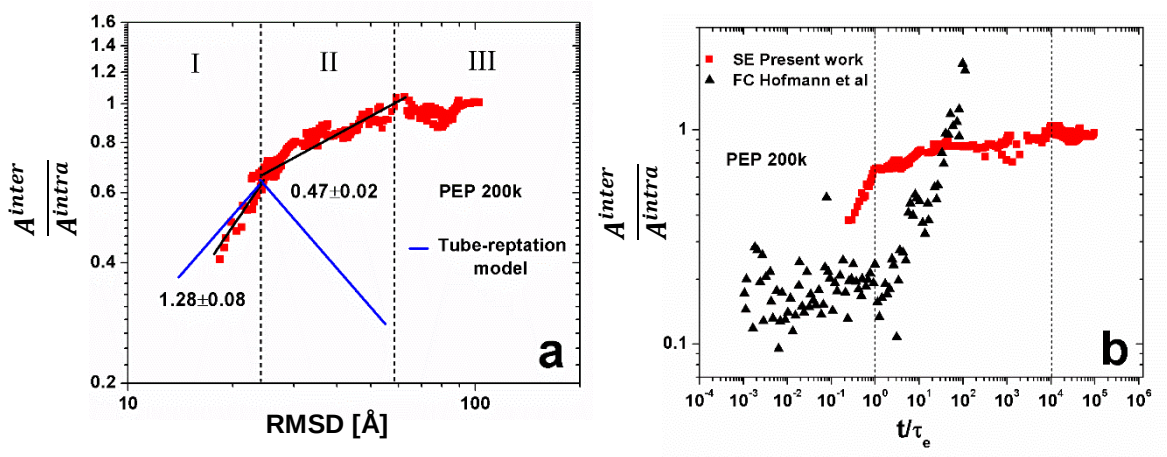

Figure 4.16. (a) Ratio of inter- over intramolecular contributions to the Hahn echo decay $\frac{A^{inter}}{A^{intra}}$ in PEP 200k calculated based on eq. (4.3) and plotted as a function of the root mean squared displacement $\langle r^2(t)\rangle^{\frac{1}{2}}$. (b) comparison of $\frac{A^{inter}}{A^{intra}}$ obtained in this work with the FC data [127] as a function of $\frac{t}{\tau_e}$.

Calculation of the reorientational and translational dipolar correlation functions for PEP 200k employing FFC relaxometry data was as well performed in [127] for regime I and the beginning of regime II. The comparison of this data to the results obtained in this work is shown in Figure 4.16 (b). Here the ratio $\frac{A^{inter}}{A^{intra}}$ is plotted as a function of the normalized time t/τ_e, showing essentially different behaviour of the data provided by different methods for times $\frac{t}{\tau_e} \approx 10^{-1} - 10^{3}$. Preliminary explanation of this phenomenon can rely on two reasons. First, both techniques provide the ratio $\frac{A^{inter}}{A^{intra}}$ based on different integral transformations of the total proton magnetic dipole-dipole correlation function. In the case of FC relaxometry, it is a weighted sum of Fourier transformations of the dipole-dipole correlation functions at the resonance and double resonance frequencies, whereas in the case of the spin-echo method one deals with a convolution of the discussed dipole-dipole correlation function with time. This leads to a possible difference in the numerical coefficients and even in a functional behavior during the crossover between different regimes of macromolecular motion. However, it is emphasized that the ratio $\frac{A^{inter}}{A^{intra}}$ does not affect the MSD results, as according to eq. (3.48), MSD depends only on the intermolecular part of the solid-echo (or dipolar-correlation) build-up function. Secondly, both methods can be subjects to additional disturbing effects at long times/low frequencies: FC in regime II, at frequencies on the order of $100Hz$, approaches the Redfield limit (see *Chapter 2*) and the methods introduced in this work are affected by the spin non-equivalency and highly mobile impurities at high temperatures (see *Chapter 3*). Moreover, results provided by the multi-quantum resonance method differ from the both sets of data presented here, yielding weaker isotope-dilution effects [138]. Therefore, FC and time-domain (transverse-evolution) approaches such as MQ, Hahn echo or solid echo have been already observed to provide different results for $\frac{A^{inter}}{A^{intra}}$. However, the significant uncertainties related to this ratio do not challenge the consistent MSD result.

Comparison with the double-quantum build-up function.

As can be seen from eq. (3.41), (3.63) and (3.73), the solid-echo, dipolar-correlation and double-quantum build-up functions contain the same information about the dipolar interactions in a spin system, encoded into the phases accumulated during the evolution periods. However, they differ in a numerical coefficient that results into the following relation:

$$\frac{\frac{I^{SE}(t)}{I^{DC}(t)}}{I^{nDQ}(t)} = \frac{\frac{4.5}{2.25}}{1} \tag{4.5}$$

$I^{DQ}(t)$ and $I^{ref}(t)$ are measured on Minispec mq20 with the modified Baum-Pines pulse sequence following the protocol described in *Chapter 2.4.* $I^{nDQ}(t)$ is then constructed from the double-quantum and the reference signal according to equation: $I^{nDQ} = \frac{I^{DQ}}{I^{DQ}+I^{ref}}$. Comparison of the three build-up functions $I^{SE}(t)$, $I^{DC}(t)$ and $I^{nDQ}(t)$ obtained in the protonated PEP 200k at $T = 358K$ is shown in Figure 4.17. Matching is obtained by applying rescaling coefficients to $I^{DC}(t)$ and $I^{nDQ}(t)$. Ratio $\frac{I^{SE}(t)}{I^{DC}(t)}$ is found to be ≈ 2.2, which is close to the theoretical value of 2. Deviation at longer times can be caused by the effects of spin non-equivalency and possible highly mobile impurities in the sample. Ratio $\frac{I^{SE}(t)}{I^{nDQ}(t)}$ is calculated to be ≈ 1.5, which is far off the theoretical value of 4.5. Possible explanation for this striking difference can be attributed to the difference of the experimental techniques. Absence of the spin motion is assumed in the time period between the consecutive RF pulses in the DQ pulse train. Its presence can invalidate the theoretical formalism used to obtain eq. (3.73). Rigorous investigation of this problem lies out of the scope of the current work.

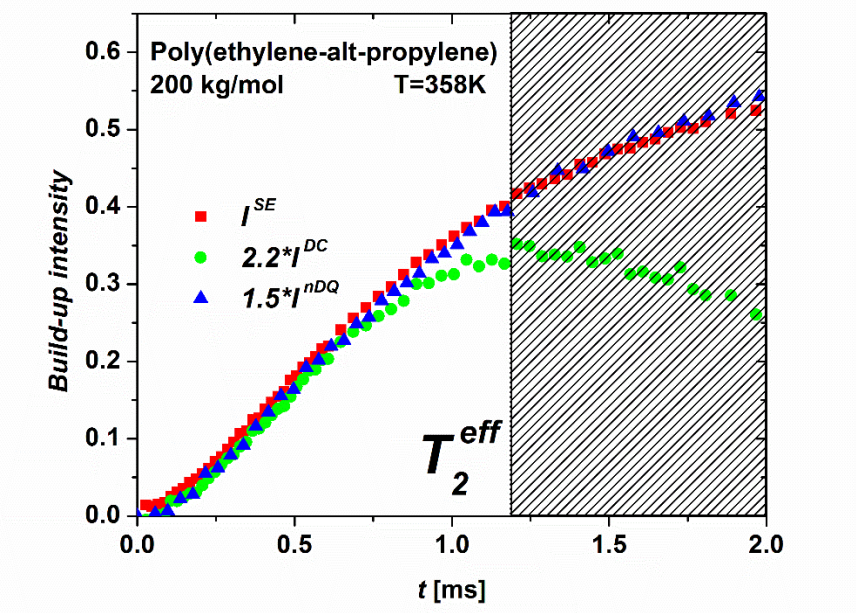

Figure 4.17. Solid-echo $I^{SE}(t)$, rescaled dipolar-correlation $I^{DC}(t)$ and rescaled double-quantum $I^{nDQ}(t)$ build-up functions obtained in the protonated PEP 200k.

Summary.

In this paragraph it is shown that the method based on the solid-echo build-up function provides the results in poly(ethylene-alt-propylene) that are consistent with the previously verified dipolar-correlation build-up function based approach. Moreover, these two methods are able to extend the time scale of polymer dynamics probed by conventional techniques by several orders of magnitude towards the longer times/lower frequencies, being in good agreement with them in the overlapping regions. For the first time in PEP $M_w = 200\ kg/mol$ transition from the incoherent to the coherent reptation in terms of the tube-reptation model is observed. Experimental simplicity of the proposed methods (SE and DC) and the large accessible time range (6 decades in time) should promote them as powerful tools of investigating segmental motion in entangled polymer melts.

Similar to the case of polybutadiene melts analyzed in the previous paragraph, intermolecular dipolar interactions are shown to play a significant role in the transverse relaxation in PEP $200\ kg/mol$. Again the dependence of the ratio of the inter- over intramolecular dipolar interactions exhibits no signs of anisotropic motion that should be inherent to the segmental dynamics in the probed time range (regions II and III) according to the tube-reptation model. Despite apparent inconsistencies between the field-cycling NMR relaxometry, methods proposed in this work and multi-quantum NMR spectroscopy, first two of them repeatedly hint at the fact that tube-reptation concept of the restricted motion in entangled polymer melts is not able to explain observed features of the dipolar interactions.

In the next paragraph solid-echo and dipolar-correlation build-up functions formalism will be applied together with the field-cycling NMR relaxometry in a series of polyethylene oxide melts of different molecular weights.

4.4. Polyethylene oxide

Part of the results presented in this paragraph are submitted for publication [53]. Polyethylene oxide (PEO) is a perfect polymer for the application of the solid-echo and dipolar-correlation build-up functions formalism developed in *Chapter 3*, due to the fact that it contains only magnetically equivalent protons. Structure of the PEO monomeric unit is shown in Figure 4.18. At ambient temperatures PEO is solid, its melting point is at $T_m \approx 338K$, which means that only high-temperature measurements are beneficial and therefore experiments are carried out on the homemade Halbach spectrometer described previously ($\vartheta_0 = 19.2MHz$).

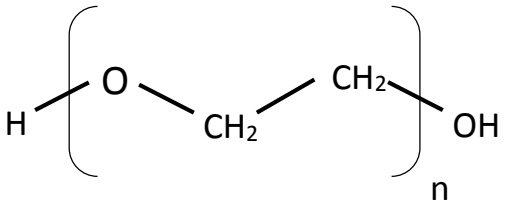

Figure. 4.18. Chemical structure of polyethylene oxide monomeric unit.

Isotopic dilution.

As was briefly mentioned before, isotopic dilution is a procedure of diluting protonated chains of a particular polymer species in deuterated (all protons are replaced by deuterium) chains of the same polymer. This results in a gradual decrease of the intermolecular dipolar interactions upon decreasing the proton concentration in a mixture. Thereby the intramolecular dipolar interactions can be estimated by extrapolation to the zero proton content. Comparison with the reference protonated sample yields the intermolecular part of the dipolar interactions.

Fully protonated and fully deuterated PEO of different molecular weights M_w and different polydispersity indexes $\frac{M_w}{M_n}$ were purchased from Polymer Standards Service GmbH (Mainz, Germany). In Table 4.1 all the molecular weights and corresponding proton molar concentration in the prepared isotopically diluted mixtures are listed.

Protonated M_w	$\frac{M_w}{M_n}$	Deuterated M_w	$\frac{M_w}{M_n}$	Proton Content, β
$220\ kg/mol$	1.11	$867\ kg/mol$	2.46	100%, 85%,77%, 44%
$94.6\ kg/mol$	1.16	$74.1\ kg/mol$	1.21	100%, 19.6%
$41.3\ kg/mol$	1.30	$49.4\ kg/mol$	1.13	100%, 50%, 31%, 16%, 10%, 4.9%
$17.9\ kg/mol$	1.20	$22\ kg/mol$	1.07	100%, 19.2%
$10\ kg/mol$	1.12	$11\ kg/mol$	1.09	100%, 21%

Table 4.1. Characteristics of the purchased polyethylene oxide and list of the prepared isotopically diluted mixtures.

In order to prepare homogeneous mixtures, protonated PEO and its deuterated counterpart are dissolved in chloroform $CHCl_3$ (stabilized with ethanol), creating a dilute solution ($< 5\%$ weight concentration) inside a glass flask. After that a stir bar is immersed into a mixture, the flask is closed and placed onto a magnetic stirrer. The mixture is then being stirred for 72 hours at a moderate frequency of

$< 2 - 3\ Hz$. NMR measurements of the same PEO, pure and after stirring, demonstrates no apparent effects of the chemical interaction between the sample and the stir bar.

Mixing by means of the mechanical shaking for 72 hours was attempted as well, however, it was noticed that samples tend to deteriorate if the shaking speed exceeds certain values $\sim 500\ rev/min$. Deterioration revealed itself in the change of the spin relaxation times and $T_1(\omega_0)$ Larmor frequency dispersion, as well as through appearance of an additional peak on the NMR spectrum, which altogether hinted at some structural changes in the polymer. Shearing action of high speed is mentioned as a cause of PEO degradation, especially at high M_w, in [139]. Therefore, all the samples are prepared with the aid of magnetic stirrer.

After 72 hours of mixing solvent is extracted in a rotatory evaporator at $T = 323K$ during ~6 hours. By the end of this procedure sample is almost evenly distributed on the walls of the flask, nevertheless it can be easily extracted due to the low adhesion to the glass. It is then placed into a $5mm$ NMR tube, evacuated for several hours in a turbomolecular vacuum pump and eventually flame sealed. In order to ensure the validity of this preparation procedure a series of different concentration of PEO-h $M_w = 41.3\ kg/mol$ in PEO-d $M_w = 49.4\ kg/mol$ are made (see Table 4.1) following the protocol described above. Hahn echo decays are obtained at $T = 353K$ and are shown in Figure 4.19 (a). All of them are monoexponential in the observed time range, which corresponds to the regime of normal diffusion $t > \tau_d$ and $\langle r^2(t)\rangle > 2R_g^2$. In Figure 4.19 (b) corresponding transverse relaxation rates are plotted as a function of proton concentration β. Linear dependence is observed as is expected for the proper homogeneous mixtures of the deuterated and the protonated chains. This proves the preparation protocol and application of eq. (4.1)-(4.4).

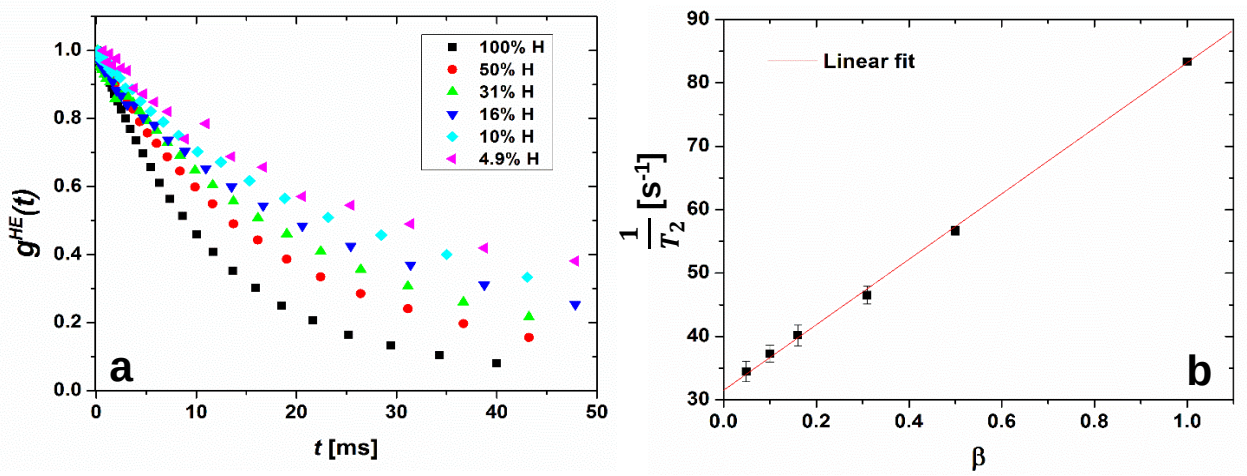

Figure 4.19 (a) Normalized Hahn echo decays in different mixtures of PEO-h $M_w = 41.3\ kg/mol$ in PEO-d $M_w = 49.4\ kg/mol$ at $T = 353K$. (b) Linear dependence of the transverse relaxation rate $\frac{1}{T_2}$ on the proton concentration β in a mixture.

The same investigation is carried out for the case of PEO-h $M_w = 220\ kg/mol$ in PEO-d $M_w = 863\ kg/mol$ to check the proportionality of dilution when the deuterated matrix consists of a priori much larger chains. In Figure 4.20 (a) the normalized Hahn echo decays, which are pseudogaussian (exponent $\bar{\alpha}$ of the decay function is in the range $1 \ldots 2$), and (b) $\frac{1}{T_2^{eff}}$ as a function of the proton concentration are

plotted. Linear proportionality is found in this case as well, which justifies the use of deuterated matrix of a larger M_w. Since both the protonated and the deuterated chains are in a highly entangled state ($M_w \gg M_c \cong 3.6\, kg/mol$ [13]), larger value of M_w of the deuterated chains can only affect the tube disengagement time τ_d of the mixed samples, the other time constants do not depend on the dynamics of the matrix and are mostly determined by the characteristics of the protonated chains.

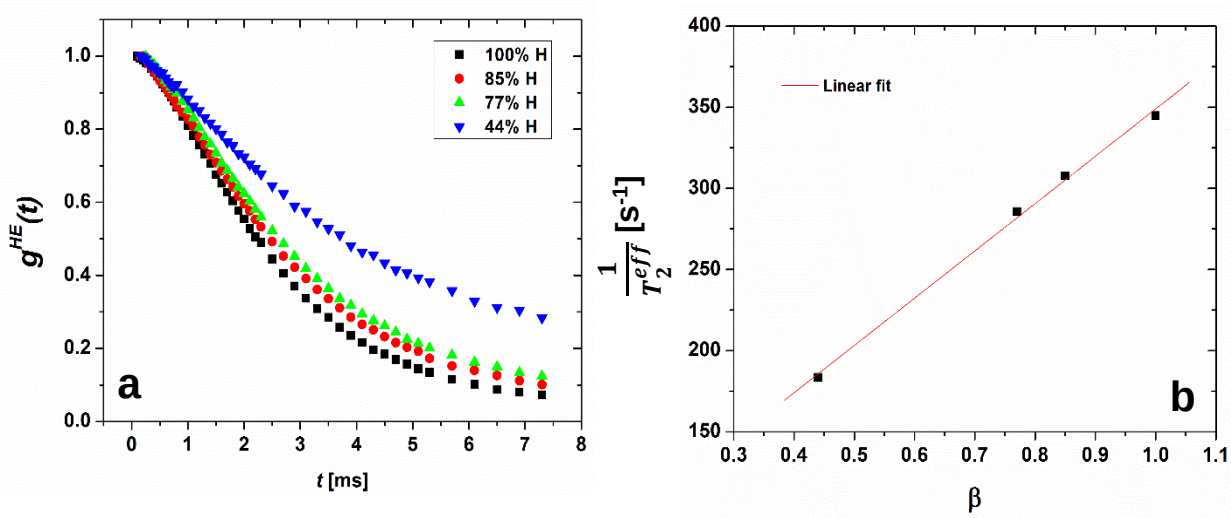

Figure 4.20 (a) Normalized Hahn echo decays in different mixtures of PEO-h $M_w = 220\, kg/mol$ in PEO-d $M_w = 867\, kg/mol$ at $T = 353K$. (b) Linear dependence of transverse relaxation rate $\frac{1}{T_2^{eff}}$ on the proton concentration β in a mixture.

In Table 4.2 characteristic times, calculated center-of-mass diffusion coefficients and gyration radii for all the samples are summarized. The center-of-mass diffusion coefficients are extrapolated from the reference value $D_{cm}\left(12.3\frac{kg}{mol}\right) = 3 \cdot 10^{-13}\frac{m^2}{s}$ as $D_{cm} \propto M_w^2$ [140,141]. Tube disengagement time τ_d is calculated as $\tau_d = \frac{R_F^2}{3\pi^2 D_{cm}}$ [17], where $R_F^2 = Nb^2$ and $b = 11$Å [12]. Characteristic times τ_R, τ_e and τ_s are obtained from τ_d using equations from *Chapter 1* and the value of $N_e = 15$ [12,13]. Gyration radii are extrapolated using proportionality $R_g^2 \propto N$ from the value of $\langle R_g^2\rangle^{\frac{1}{2}} = 119.5$Å obtained with small-angle neutron scattering for PEO of $M_w = 110\, kg/mol$ in [142]. All the used values correspond to $T = 353K$.

Protonated M_w	$\langle R_g^2\rangle^{\frac{1}{2}}$ [Å]	$D_{cm;calc}\left[\frac{m^2}{s}\right]$	τ_e [s]	τ_R [s]	τ_d [s]
$220\, kg/mol$	171	$9.4 \cdot 10^{-16}$	$1.9 \cdot 10^{-8}$	$2.2 \cdot 10^{-4}$	$7 \cdot 10^{-2}$
$94.6\, kg/mol$	112	$5.1 \cdot 10^{-15}$	$1.9 \cdot 10^{-8}$	$4 \cdot 10^{-5}$	$5.5 \cdot 10^{-3}$
$41.3\, kg/mol$	74	$2.7 \cdot 10^{-14}$	$1.9 \cdot 10^{-8}$	$7.6 \cdot 10^{-6}$	$4.5 \cdot 10^{-4}$
$17.9\, kg/mol$	49	$1.4 \cdot 10^{-13}$	$1.9 \cdot 10^{-8}$	$1.4 \cdot 10^{-6}$	$3.8 \cdot 10^{-5}$
$10\, kg/mol$	36	$4.5 \cdot 10^{-13}$	$1.9 \cdot 10^{-8}$	$4.5 \cdot 10^{-7}$	$7 \cdot 10^{-6}$

Table 4.2. Characteristic time constants, calculated center-of-mass diffusion coefficients and gyration radii for PEO samples at $T = 353K$.

Build-up functions.

$I^{DC}(t)$ and $I^{SE}(t)$ are obtained for all the prepared samples using the pulse sequences described in the previous paragraph. In Figure 4.21 $I^{SE}(t)$ and rescaled $I^{DC}(t)$ are plotted for the fully protonated PEO $M_w = 220\ kg/mol$ at $T = 353K$ and $393K$. Ratio $\frac{I^{SE}(t)}{I^{DC}(t)} = 2.1$ and 2 is found, which in good agreement with the theoretical value of 2 according to eq. (4.5).

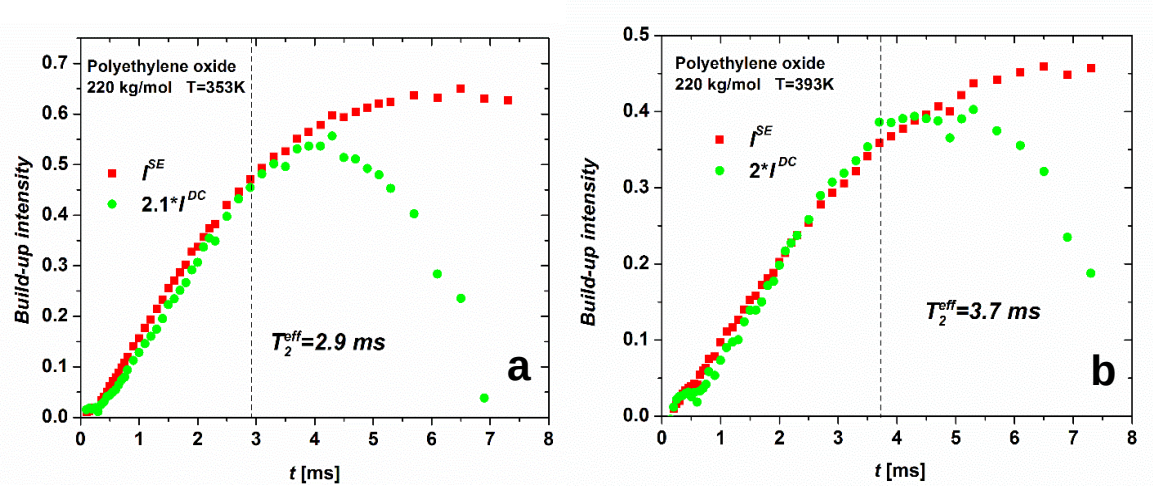

Figure 4.21. Solid-echo $I^{SE}(t)$ and rescaled dipolar-correlation $I^{DC}(t)$ build-up function obtained in the protonated PEO $M_w = 220\ kg/mol$ at (a) $353K$ and (b) $393K$.

Segmental mean squared displacement.

MSD is determined from the intermolecular parts of $I^{SE}(t)$ and $I^{DC}(t)$ as in the previous paragraphs, as well as from the field-cycling NMR relaxometry data based on eq. (3.88)-(3.91). FC measurements are carried out on Stelar Spinmaster FFC2000 in the proton Larmor frequency range of $5KHz \leq \vartheta_0 \leq 20MHz$. All the spin-lattice relaxation curves are found to be monoexponential at least in one order of magnitude. According to the values of τ_d, SE, DC and FC methods can be applied to the investigation of PEO $220\ kg/mol$, $94.6\ kg/mol$, and only the FC data can be evaluated for PEO $41.3\ kg/mol$, since for this sample the time scale accessible to the DC and SE methods lies in the region $t > \tau_d$ (exponential transverse relaxation decay, no build-up behavior, normal diffusion regime). TTS master curves comprising MSD calculated from $\frac{1}{T_1^{inter}}$ obtained by means of the FC NMR at $T = 355K$ and from the intermolecular contribution to $I^{SE}(t)$ and $I^{DC}(t)$ measured at $T = 353K, 393K, 423K$ are shown in Figures 4.22 (a), (b) and (c). Applied temperature shifts are taken from the dependence of $\tau_s(T)$ presented in [143]. Note that for PEO $94.6\ kg/mol$ exponential decays and disappearance of the build-up behavior inherent to the normal diffusion regime is observed at $T = 423K$. Its time scale actually coincides with the calculated τ_d. In Figure 4.22 (d) all the three molecular weights are compared (field-cycling and SE data are used for this plot).

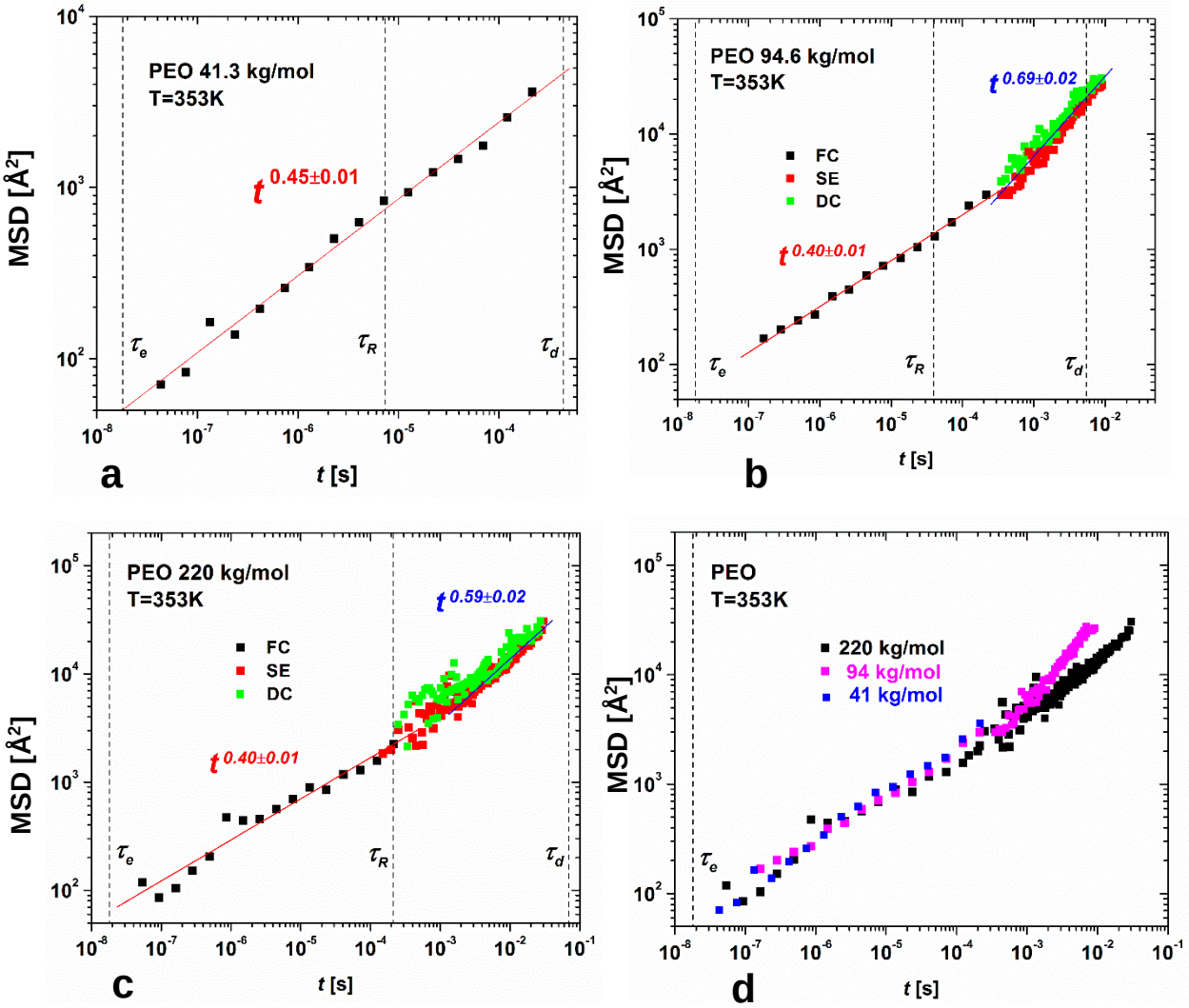

Figure 4.22 Segmental MSD obtained by FC, DC and SE methods in PEO (a) $41.3\ kg/mol$, (b) $94.6\ kg/mol$, (c) $220\ kg/mol$. Characteristic times from Table 4.1 are marked and exponents of the fitted power laws are shown. (d) is a comparison of the three molecular weights (FC and SE data).

In the case of PEO $\tau_e \cong 1.9 \cdot 10^{-8} s$ is rather short, as a consequence all the obtained MSDs lie in the region $t > \tau_e$ corresponding to the regimes of the entangled anisotropic dynamics in the framework of the tube-reptation model. Data obtained by independent methods of the field-cycling relaxometry and the DC and SE formalism coincide well. Surprisingly, no signs of the power law $\propto t^{0.25}$ that is predicted for the regime of the incoherent reptation by the tube-reptation model and was fully observed in PEP in the previous paragraph are found. Consistent values of the MSD time dependence power law's exponent $\alpha = 0.4 \ldots 0.45$ are provided by the FC relaxometry in the time interval $\tau_e < t < \tau_R$, no molecular weight dependence is observed (see Figure 4.22 (d)). It also holds for $M_w = 17.9\ kg/mol$, MSD of which is not shown in Figure 4.22. These results are in good agreement with FC data obtained in PEO $M_w = 178\ kg/mol, 436\ kg/mol$ and $460\ kg/mol$ by Kehr et al. [100]. The value of the MSD at $t = \tau_e$ found by extrapolation of $\langle r^2(t) \rangle$ curves can be used to evaluate the tube diameter for a polyethylene oxide melt, as was done in the case of PEP. Calculation yields $d_t \cong 14$Å, which is significantly lower than the

estimated value $d_t = N_e^{1/2} b \cong 43\text{Å}$. However, it is not clear if one can speak about the determination of the tube diameter given the fact that no features of the incoherent reptation regime corresponding to the constrained motion within the tube are found.

For the larger molecular weights $M_w = 94.6\ kg/mol$ and $220\ kg/mol$ transition towards a power law with the higher exponents $\alpha = 0.69 \pm 0.02$ and 0.59 ± 0.02 is found using DC and SE methods. Time scale of this transition correlates with τ_R. Note that this is at the limit of the applicability of the current formalism due to the condition $\alpha < \frac{2}{3}$. Molecular weight dependence in the time range $\tau_R < t < \tau_d$ is clearly visible in Figure 4.22 (d) as expected from the model for the coherent reptation regime. At longer times, the MSD time dependence demonstrates an onset towards normal diffusion. It is actually reached for PEO $94.6\ kg/mol$ at $T = 423K$. In case of PEO $41.3\ kg/mol$ time scale of the probed MSD is in the proximity of τ_d, however, no apparent onset towards a normal diffusion power law $\langle r^2(t)\rangle \propto t$ is found. Values of $\langle r^2(\tau_d)\rangle$ are $\approx 5 \cdot 10^3 \text{Å}^2$ for $41.3\ kg/mol$, $\approx 2.5 \cdot 10^4 \text{Å}^2$ for $94.6\ kg/mol$ and $\approx 6 \cdot 10^4 \text{Å}^2$ for $220\ kg/mol$. They are almost identical to the values of $2\langle R_g^2\rangle$ taken from Table 4.1, which correspond to the displacement caused by the internal motions at the long-time limit.

Center-of-mass diffusion coefficient.

As was shown in *Chapter 3.5*, at times $t > \tau_D$ the center-of-mass diffusion coefficient D_{cm} of a polymer chain in a melt can be extracted from the intermolecular contribution to the normalized Hahn echo decay using eq. (3.95). This calculation was done for PEO $10\ kg/mol, 17.9\ kg/mol, 41.3\ kg/mol$ and $94.6\ kg/mol$ with the aid of the following relation for the intermolecular part of the Hahn echo decay:

$$g^{HE;inter}(t) = \left(\frac{g_p^{HE}(t)}{g_\beta^{HE}(t)}\right)^{\frac{1}{1-\beta}}, \tag{4.6}$$

where $g_p^{HE}(t)$ and $g_\beta^{HE}(t)$ are the normalized Hahn echo decays for the fully protonated and the isotopically diluted sample with the proton concentration β. For PEO $94.6\ kg/mol$ Hahn echo decay measured at $T = 423K$ is used, since it is observed to reflect the dynamics of the normal diffusion regime, as was mentioned previously. Dependence $D_{cm}(M_w)$ is plotted in Figure 4.23 in a double-logarithmic scale. Power law $D_{cm} \propto M_w^{-1.65\pm0.02}$ is obtained, which slightly weaker than $\propto M_w^{-2}$ as predicted by the tube-reptation model. It is noted that the value for $M_w = 94.6\ kg/mol$ can be overestimated since, first, it is obtained from the Hahn echo decay at the higher temperature than for other molecular weights, second, the protonated chains in this sample are diluted in the deuterated matrix of a lower $M_w = 74.1\ kg/mol$, which is characterized by faster motion. Moreover, limit of the long times $t > \tau_d$ assumed in the course of the derivation of eq. (3.95) might not be completely fulfilled in this case, because $t \approx \tau_d$ as can be seen in Figure 4.22 (b). Fitting only the first three points without $M_w = 94.6\ kg/mol$ yields the power law $D_{cm} \propto M_w^{-1.82\pm0.09}$. Values of D_{cm} are remarkably close to the ones calculated based on the literature data in Table 4.2. These results are extremely promising as they demonstrate the feasibility of the novel elegant method of determining the center-of-mass diffusion coefficients of highly entangled polymer melts based on the intermolecular contribution to the Hahn echo decay. The range of dynamics accessible to this approach demands for the large values of the magnetic field gradient and, consequently,

for a sophisticated hardware, whereas results presented in Figure 4.23 can be obtained on a conventional low-field benchtop relaxometer, such as Bruker Minispec mq20.

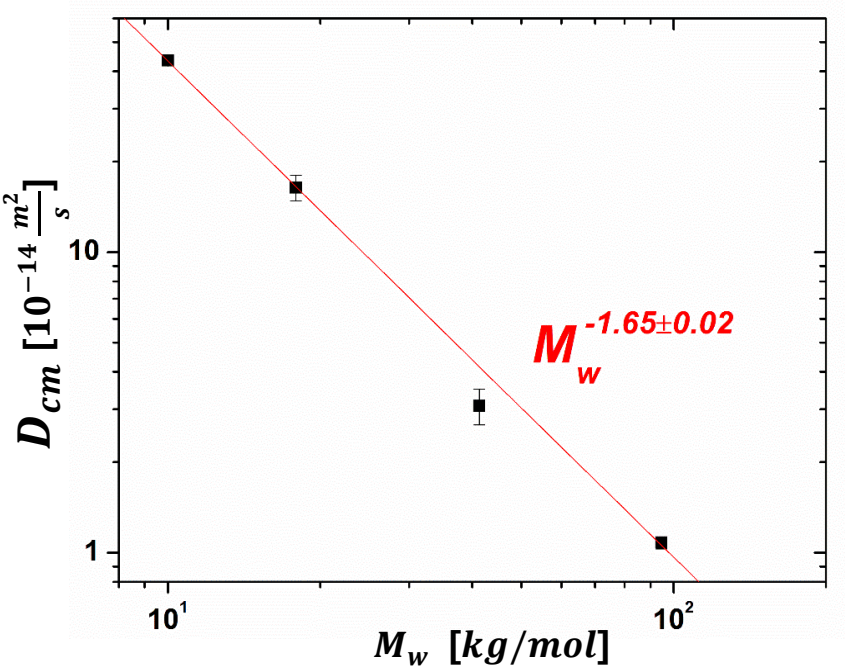

Figure 4.23. Center-of-mass diffusion coefficients obtained from the intermolecular contribution to the normalized Hahn echo decay according to eq. (3.95) as a function of polymer's molecular weight.

Inter- and intramolecular dipole-dipole interactions.

Ratio $\frac{A^{inter}}{A^{intra}}$ of the inter- over intramolecular interactions is obtained from the normalized Hahn echo decays as in the previous paragraphs according to eq. (4.3) for PEO $94.6\ kg/mol$ and $220\ kg/mol$. FC data is used to obtain the ratio for PEO $41.3\ kg/mol$ and $17.9\ kg/mol$ as $\frac{A^{inter}}{A^{intra}} = \left(\frac{1}{T_1^{inter}}\right) / \left(\frac{1}{T_1^{intra}}\right)$. Their dependence on the RMSD is shown in Figure 4.24. Similar to the cases of polybutadiene and poly(ethylene-alt-propylene) none of the samples demonstrate decrease of the relative intermolecular contribution in the regimes of anisotropic entangled dynamics $\tau_e < t < \tau_d$ as is expected from the theory. The highest molecular weights $94.6\ kg/mol$ and $220\ kg/mol$ tend to reach a plateau at longer times. It is noted that data for $220\ kg/mol$ is rather noisy due to the small amount of this sample in the isotopically diluted mixture. Values of $\frac{A^{inter}}{A^{intra}}$ are surprisingly large for this particular sample, almost reaching 10 at long times. It should be kept in mind that this can be caused by the use of the deuterated matrix of a much higher molecular weight (see Table 4.1) possibly leading to an overestimation of the intermolecular interactions. Nevertheless, qualitative behavior is still quite pronounced and is very similar to the one seen in the data obtained in the other highly entangled polymer melts (polybutadiene $196\ kg/mol$, PEP $200\ kg/mol$ and PEO $94.6\ kg/mol$), which hints at a possible common feature of the dipolar interactions in such systems. It is emphasized that this behavior in the course of the current work is systematically shown to be at variance with the predictions of the tube-reptation model.

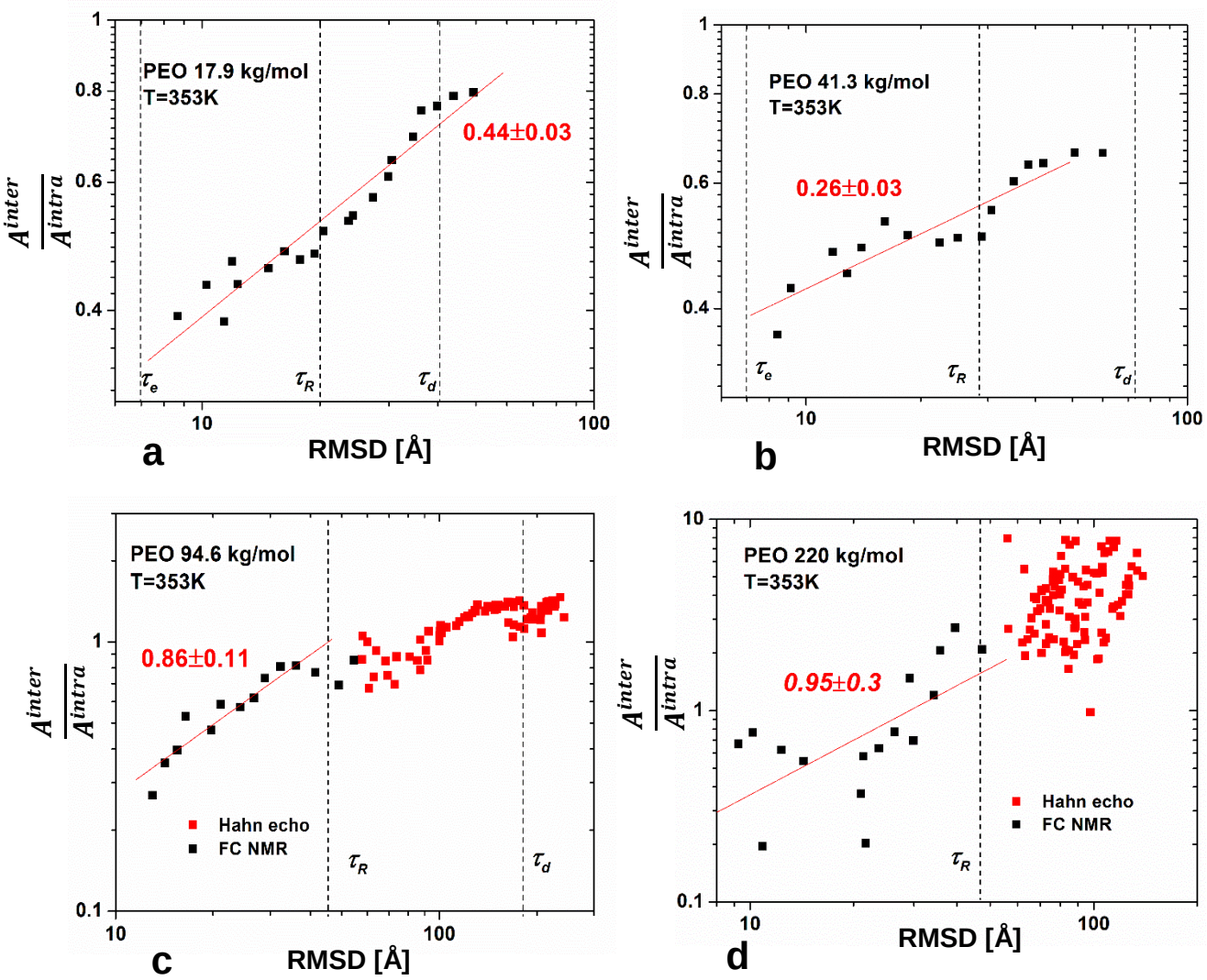

Figure 4.24. Ratio of the inter- over intramolecular dipolar interactions $\frac{A^{inter}}{A^{intra}}$ obtained from the FC data for PEO 17.9 kg/mol (a) and 41.3 kg/mol (b), and from the FC data and the Hahn echo based on eq. (4.3) for PEO 94.6 kg/mol (c) and 220 kg/mol (d) plotted as a function of the root mean squared displacement $\langle r^2(t)\rangle^{\frac{1}{2}}$.

Summary.

The solid-echo and the dipolar-correlation build-up function formalism is applied alongside with the field-cycling NMR relaxometry to obtain the time dependence of the segmental mean squared displacement weights from the intermolecular contribution to the corresponding NMR signals in polyethylene oxide of different molecular. Similar to the previously shown cases of polybutadiene and poly(ethylene-alt-propylene), data yielded by these methods is in good agreement, thereby allowing for probing segmental dynamics of the entangled PEO in the range of over 5 orders of magnitude in time. Interestingly, no signs of entangled dynamics corresponding to the anisotropic motion inside of a fictitious tube as predicted by the tube-reptation model are found. Observed exponent of the MSD time dependence power law $\alpha = 0.4 \dots 0.45$ for the time range $\tau_e < t < \tau_R$ is significantly higher than $\alpha = 0.25$ expected for the incoherent reptation regime. This variance with the model prediction is consistent for all the molecular weights. It is noted that these results are supported by the findings in [100] for PEO $178\ kg/mol, 436\ kg/mol$ and $460\ kg/mol$ obtained by means of the FC NMR relaxometry. Data in [144] provided by the field-gradient NMR for PEO $5000\ kg/mol$ also yield the power-law exponent α significantly larger than 0.25 in the incoherent reptation regime. Given the fact that $\alpha \cong 0.2$ corroborated by the FC and by the NSE is found in PEP in the whole time scale of the regime II, it raises a question of the universal applicability of the dynamics models for different polymer species.

The same methods are used to estimate the relative contribution of the intermolecular dipolar interaction to the spin-lattice and the spin-spin relaxation signals. Their ratio $\frac{A^{inter}}{A^{intra}}$ clearly demonstrates qualitatively the same behavior for all the PEO samples, as well as for polybutadiene and poly(ethylene-alt-propylene). Relative contribution of the intermolecular dipolar interactions tends to increase at small displacements ($10 \div 60$Å) / short times and to reach a plateau at larger displacements (> 100Å) / longer times. For PEO $94.6\ kg/mol$ and PEP $200\ kg/mol$ this plateau value is found to be $\frac{A^{inter}}{A^{intra}} \cong 1$, which corresponds to approximately equal contributions of the inter- and intramolecular dipolar interactions to the spin relaxation.

It is very important to emphasize that the observed behavior of $\frac{A^{inter}}{A^{intra}}$ does not display features expected for the highly restricted anisotropic motion in a fictitious tube according to the tube-reptation model. This variance with the model is found in all the polymer species studied in this work. In the case of PEO it means that nor can MSD time dependence, neither $\frac{A^{inter}}{A^{intra}}$ dependence on the RMSD be explained by the tube-reptation formalism.

In addition to that, determination of the center-of-mass diffusion coefficient D_{cm} from the intermolecular contribution to the normalized Hahn echo decay in accordance with eq. (3.95), which has been derived in this work, is carried out in the normal diffusion regime. The values of D_{cm} are found to be in good agreement with the ones extrapolated from the literature data for PEO. This opens up a new opportunity for extracting the center-of-mass diffusion coefficients of entangled polymer melts on a simple benchtop relaxometer. It is noted that this method can be further improved by measuring the residual proton Hahn echo decay in the deuterated polymers. Low concentration of the proton spins and low probability of their occurrence at the same macromolecule ensures the fact that only intermolecular dipolar interactions contribute to the transverse relaxation.

Obtained dependence of the center-of-mass diffusion coefficient on the molecular weight $D_{cm} \propto M_w^{-1.65\pm0.02}$ is rather close to the well-known $D_{cm} \propto M_w^{-2}$ power law predicted by the tube-reptation model (especially, taking into account possible deviations for the highest measured M_w discussed previously). This characteristic dependence has been verified by different methods in entangled polymers in general [25,44,145,146] and in PEO in particular [141,144,147]. Generally, predictions of the tube-reptation model for the macroscopic characteristics, such as center-of-mass diffusion coefficient, terminal relaxation time, zero-shear viscosity, shear modulus plateau etc., are corroborated by the experimental findings rather well. However, NMR spin relaxation is the only technique that directly provides information about microscopic segmental motions in polymer melts on the time scale of the entangled dynamics. This is due to the fact that the spin relaxation rate and the shape of the relaxation curves are directly related to the fluctuations of the local magnetic fields caused by the dipolar interactions between the spins, which in turn reflect their orientation and spatial position (see *Chapter 2).* Another technique capable of probing such a microscopic spin dynamics is incoherent quasi-elastic neutron scattering, however, maximal displacements and times accessible to this method are limited (see *Chapter 3.5*), thereby not allowing for the investigation of the entangled polymer dynamics in a sufficient time range.

Interestingly, apparent contradiction between the microscopic characteristics (segmental MSD in case of PEO and $\frac{A^{inter}}{A^{intra}}$ ratio for PB, PEP and PEO) and the tube-reptation model predictions does not interfere with the fact that the macroscopic characteristics (D_{cm}, τ_d) obtained with the DC and SE methods support the model calculations.

Conclusion

In the course of this work it has been attempted to demonstrate the whole complexity and versatility of problems encountered in polymer dynamics, which are magnified even more in the case of entangled macromolecular melts. Nevertheless, an elegant model of the tube-reptation can be quite successfully employed to theoretically describe thermal motion of the polymer segments and of the macromolecular chains as wholes in a molten state. Over the years of an extensive research devoted to this problem a lot of experimental findings in polymer melts both supporting as well as contradicting the predictions of the tube-reptation model have been accumulated. A number of methods, brief overview of which was presented in *Chapter 2.5*, is conventionally employed for this purpose. Among them Nuclear magnetic resonance plays an important role providing an informative insight onto the time range corresponding to the entangled segmental dynamics.

During the last years a novel theoretical finding corroborated by experimental evidence appeared in the field of polymer dynamics, namely, character of the dipolar interactions in melts of macromolecules was significantly reconsidered. Evidently, underestimation of the intermolecular constituent of these interactions had been taking place while explaining experimental data before. Taking use of this crucial outcome, a novel theoretical and experimental formalism is proposed in this work. It is based on the NMR spin echo experiments and operates with the time evolution of the spin magnetization in a transverse plane. A central experimental concept of this approach is the construction of the solid-echo and the dipolar-correlation build-up functions, which combine the corresponding spin echo signals. It is demonstrated explicitly that the contribution of the intermolecular dipolar interactions, which are mostly determined by the translational diffusion of spins, is connected to the displacements of segments belonging to different macromolecules. The only necessary condition for the application of this approach is an anomalous character of diffusion, described by $\langle r^2(t)\rangle \propto t^{\alpha}$ with the requirement for the exponent: $\alpha < \frac{2}{3}$. The time scale of the segmental dynamics directly probed by this method is on the order of $10^{-4}s < t < 10^{-2}s$. This range is actually hardly accessible to other conventional techniques widely applied to the investigation of the translation segmental motion, such as quasi-elastic neutron scattering, field-gradient NMR and field-cycling NMR relaxometry.

Elaborate analysis of the behavior of the dipolar-correlation and the solid-echo build-up functions shows that their initial rise at short times is consistent even in the presence of small amount of highly mobile fractions as well as in the systems where the spins are not magnetically equivalent (possessing different spin relaxation times), which are the conditions usually encountered in real polymers.

As an extension of this approach to a normal diffusion regime ($\langle r^2(t)\rangle \propto t$), the method based solely on analyzing the intermolecular contribution to the Hahn echo signal is introduced. It allows determination of the center-of-mass diffusion coefficient of an entangled polymer melt provided that condition $t > \tau_d$ is satisfied. This approach combined with the dipolar-correlation and the solid-echo formalism represents a powerful tool for the investigation of polymer dynamics. Employing a time-temperature superposition provides access to a broad range of times and displacements. One of the remarkable merits of this formalism is that the corresponding experiments can be performed on a typical low-field benchtop relaxometer, there is no demand for the sophisticated hardware and the bulky pulse sequences.

Due to unavailability of a high-temperature relaxometer at the moment of this work, new device based on the Halbach magnet has been assembled and used for the part of the measurements (up to $150°C$). Its design and important characteristics are described in *Chapter 4.1.* This allowed for getting a

better picture of polymer dynamics, playing particularly important role in the case of samples with the highest molecular weights, which are subjected to the long-time correlations.

Construction of the dipolar-correlation build-up function is first attempted in polybutadiene $196\ kg/mol$ melt. Separation of the intermolecular and the intramolecular contributions is achieved by means of the isotopic dilution procedure described thoroughly in *Chapter 4.4.* It relies on the proportionality of the relative part of the intermolecular dipolar interactions to the concentration of the protonated chains in the deuterated matrix. This assumption is later on shown to be valid on the series of polyethylene oxide $41.3\ kg/mol$ and $220\ kg/mol$ melts. Segmental mean squared displacement extracted from the intermolecular part of the dipolar-correlation build-up function is corroborated well by the field-cycling NMR data that is taken as a proof of the experimental validity of the proposed novel method.

Having established its feasibility, the dipolar-correlation approach together with the solid-echo method is applied to a comprehensive investigation of entangled poly(ethylene-alt-propylene) and polyethylene oxide melts, which are polymer species with a rather simple structure, thus representing the perfect targets for testing the basic features of polymer dynamics and the validity of the tube-reptation model. Probed time scale of segmental dynamics accessed in poly(ethylene-alt-propylene) ranges over 6 orders of magnitude effectively covering most of the entangled dynamics regime, which is not possible with other conventional techniques. Importantly, at short times when the dipolar-correlation and the solid-echo methods overlap with the field-cycling NMR relaxometry and the neutron spin echo, the obtained displacements are in good agreement. Three distinct regimes of dynamics attributed to the Rouse, the incoherent and the coherent reptation regimes in the framework of the tube-reptation model are observed in poly(ethylene-alt-propylene) melt. Exponents of the corresponding power laws coincide well with the predictions of the model. Transition from the incoherent to the coherent reptation is observed for the first time in this polymer species of such a high molecular weight. Extremely slow segmental diffusion $\langle r^2(t)\rangle \propto t^{0.20\pm0.01}$ that is found in a wide time range $10^{-5}s < t < 10^{-1}s$ and that is explained well by the restricted motion within a tube, actually, is not seen in any of the entangled polyethylene oxide melts studied in this work. Significantly faster dynamics $\langle r^2(t)\rangle \propto t^{0.40\div0.45}$ is observed in this case in the same time range $\tau_e < t < \tau_R$ by means of the field-cycling NMR relaxometry and the novel DC and SE methods. This finding is consistent for all the measured molecular weights $17\ kg/mol, 41.3\ kg/mol, 94.6\ kg/mol, 220\ kg/mol$ and is supported by the field-gradient NMR data obtained in polyethylene oxide of a higher molecular weight $5000\ kg/mol$.

A crucial difference in the behavior of the segmental MSD time dependence in polyethylene oxide and poly(ethylene-alt-propylene) raises a question: if the tube concept is valid, is it universally applicable to all the polymer species? Further testing of the tube-reptation model is carried out by looking into the features of the inter- and intramolecular dipolar interactions in the studied systems. This is done by investigating the ratio of the inter/intra contribution to the Hahn echo decay, which essentially reflects the time dependence of the corresponding dipolar interactions. Interestingly, behavior of this ratio is found to be universal in polybutadiene, poly(ethylene-alt-propylene) and in polyethylene oxide of all the molecular weights. Moreover, it is found to be in contradiction to what is expected for the anisotropic wriggling and reptation of a chain in the tube as predicted by the tube-reptation model for the corresponding regimes of dynamics. Now the question can be rephrased: is the tube concept generally valid in polymer melts?

Additional information about the translational diffusion is provided by the molecular weight dependence of the center-of-mass diffusion coefficients in polyethylene oxide melts. They are obtained

by the previously mentioned novel method based on the analysis of the intermolecular part of the Hahn echo decay in a normal diffusion regime. Values of the diffusion coefficients found using this approach are in good agreement with the ones extrapolated from the field-gradient NMR data on polyethylene oxide of a lower molecular weight, proving the feasibility of the introduced method and its potential for the application in the field of polymer physics. The molecular weight dependence of the center-of-mass diffusion coefficient in polyethylene oxide is shown to be rather close to the prediction of the tube-reptation model for the normal diffusion regime.

Thus, results provided by NMR methods are in contradiction with the tube-reptation model in the regime of entangled dynamics, at the same time being in agreement in the normal diffusion regime. The latter is actually corroborated by results obtained by a number of independent methods. However, it is very important to emphasize that most of the techniques conventionally applied to investigation of polymer melts probe solely the macroscopic characteristics of the sample, to which belongs as well the center-of-mass diffusion coefficient. Most of the properties of these characteristics are predicted successfully by the tube-reptation model. On the other hand, there are just a few methods capable of looking into the microscopic dynamics of a polymer melt. In the case of long entangled chains, as was discussed in *Chapter 3.5*, only the NMR spin relaxation can provide information about thermal segmental motions, since they are reflected in the fluctuations of the local dipolar fields that, in turn, are directly encoded in the spin relaxation times and the features of the relaxation curves. Therefore, findings obtained by the novel NMR approaches in the course of this work can actually bear exclusive information about microscopic processes in entangled polymer melts.

Whereas it is definitely not justified to completely neglect the tube-reptation model, nevertheless, the results of this work allow to claim that its ansatz of the anisotropic restriction motion within the fictitious tube is called in question. Possibly, the lack of a complete theoretical formalism always incriminated to the tube-reptation concept is the key problem that causes the observed discrepancies. The new methods introduced here are designed to facilitate the study of this issue and hopefully to help find a proper explanation.

Acknowledgements

First of all, I would like to thank my scientific supervisor Prof. Siegfried Stapf for the full support and the extremely valuable guidance that I have received during my PhD research. I have been absolutely enjoying the work in our lab and I have been very lucky to spend these three years working with such a great supervisor.

I am very thankful to Prof. Nail Fatkullin who during my Bachelor studies evoked the passion for the fundamental science in me. His brilliant lectures played a key role in my decision to pursue a scientific career and to go into the field of nuclear magnetic resonance and polymer physics. His scientific work is a great inspiration for me and discussions with him have always been motivating me to never stop learning more.

I would also like to express my special gratitude to Carlos Mattea who has not only been guiding me in my work, but also helped to create a unique amazing atmosphere in our lab, which I will treasure. He was one of my greatest motivators, who always believed in my abilities to overcome any obstacle. I feel that I was able to learn a lot from Carlos, both in science and in general philosophy of life.

I am very grateful to my parents, Aida and Rudolf, who have always supported me in all my intentions. Their belief in me is what helps me reach new levels.

I express my gratitude to my greatest colleagues Jessica, Kerstin, Amin, Oliver, Erik, Oleg, Ingemar, Kevin, Dr. Denner and especially Bulat, who had enough patience to bear with me in our office while I was fiercely analyzing data.

Valuable discussions with Prof. Rainer Kimmich, Prof. Kay Saalwächter and Prof. Ernst Rössler are highly appreciated. They helped a lot to shape my understanding of NMR in polymer physics.

I am also thankful to Rob Dyer for his amazing work on the 3D-positioning system and to Michael Mämpel and Volker Hems from the Workshop of TU Ilmenau for their help and consultation in construction of some parts of our spectrometer.

Appendix

DC build-up function and mean relaxation rate

Mathematical formalism that lies behind the construction of the dipolar-correlation build-up function $I^{DC}(t)$ allows for another useful application not connected with the way it was previously used in this work. Consider a system consisting of different types of molecules that are characterized by relaxation rates (spin-spin or spin-lattice) $R_i = \frac{1}{T_i}$ with respective fractions φ_i. In this case the total relaxation decay for this system is multiexponential and is given by a normalized function:

$$g(t) = \sum_i \varphi_i exp(-R_i t) = \langle exp(-R_i t) \rangle \quad \text{(A1)}$$

The dipolar-correlation build-up function can then be written as:

$$I^{DC}(t) = 1 - \frac{g(t)g(0)}{g(\frac{t}{2})^2} = 1 - \frac{\langle exp(-R_i t) \rangle}{\langle exp\left(-\frac{1}{2}R_i t\right) \rangle^2} \quad \text{(A2)}$$

At $t \to 0$ the exponentials in eq. (A2) can be expanded into the Taylor series. Keeping only the terms $\propto t^3$ one can translate eq. (A2) to

$$I^{DC}(t) = -\langle (\delta R_i)^2 \rangle \frac{t^2}{4} + \langle (\delta R_i)^3 \rangle \frac{t^3}{8}, \quad \text{(A3)}$$

where $\langle (\delta R_i)^2 \rangle = \langle (R_i - \langle R_i \rangle)^2 \rangle = \langle R_i^2 \rangle - \langle R_i \rangle^2$ is a variance of the relaxation rate. Importantly, $I^{DC}(t)$ in this case contains no terms proportional to the mean relaxation rate $\langle R_i \rangle$.

Consider the logarithm of the normalized decay function given by eq. (A1). In the limit $t \to 0$ it can be calculated similarly to $I^{DC}(t)$ and is equal to:

$$ln\big(g(t)\big) = ln \langle exp(-R_i t) \rangle = -\langle R_i \rangle t + \langle (\delta R_i)^2 \rangle \frac{t^2}{2} - \langle (\delta R_i)^3 \rangle \frac{t^3}{6} \quad \text{(A4)}$$

This expression contains $\langle R_i \rangle$, which is often necessary to be determined when dealing with a multiexponential relaxation decay. However eq. (A4) is of little help for this purpose since it also has a quadratic term $\langle (\delta R_i)^2 \rangle \frac{t^2}{2}$, which strongly affects its behavior. In order to diminish its effect, Eq. (A3) and (A4) can be combined in the following way:

$$F(t) = 1 + ln\big(g(t)\big) + 2I^{DC}(t) = 1 - \langle R_i \rangle t + \langle (\delta R_i)^3 \rangle \frac{t^3}{12} \quad \text{(A5)}$$

Function $F(t)$ thus bears information about the mean relaxation rate $\langle R_i \rangle$ and at the same time does not depend on quadratic terms $\propto \langle (\delta R_i)^2 \rangle t^2$. Therefore time dependence in eq. (A5) can be used to obtain the mean relaxation rate $\langle R_i \rangle$, or, more generally, the initial slope of the decay $g(t)$ in case of its multiexponentiality.

Consider now a three-exponential relaxation decay described by $g(t) = \frac{1}{3} * exp(-Rt) + \frac{1}{3} * exp(-0.5Rt) + \frac{1}{3} * exp(-0.01Rt)$. Dipolar-correlation build-up function $I^{DC}(t)$ can be constructed for this function and it used to obtain $F(t)$ in accordance with eq. (A5). In Figure A1 $F(t)$ is plotted as a function of the normalized time $\frac{t}{T}$, where $T = \frac{1}{R}$. The mean relaxation rate $\langle R_i \rangle$ is then determined by fitting the curve with eq. (A5) and neglecting the cubic term. Value obtained in this way is equal to the actual mean value $\langle R_i \rangle \cong 0.0503R$. For comparison, function $ln\big(g(t)\big)$ is plotted in Figure A1 as well. It is clear that $F(t)$ is approximately linear in the essentially longer time interval than is the function $ln(g(t)))$, thus allowing for the more robust determination of the mean value of the relaxation rate.

Note that this approach can be applied not only to the evaluation of the spin-spin and spin-lattice magnetization decays, but also to the calculation of the mean diffusion coefficient in spin-echo experiments in systems with a distribution of diffusion coefficients. The relaxation rate in this case can be presented as $R_i = D_i k^2 = D_i \gamma^2 \delta^2 G^2$, where $\vec{k}$ is an effective wave vector of the corresponding spin-echo experiment. The normalized diffusion decay obtained in the experiment is $g(t) = \langle exp(-D_i \gamma^2 \delta^2 G^2 t) \rangle$. For instance, in the stimulated spin-echo experiment (D_i is the diffusion coefficient of the i^{th} component, G and δ are the strength and the length of the magnetic field gradient pulse) [87].

This application of $I^{DC}(t)$ was first proposed and described in [109]

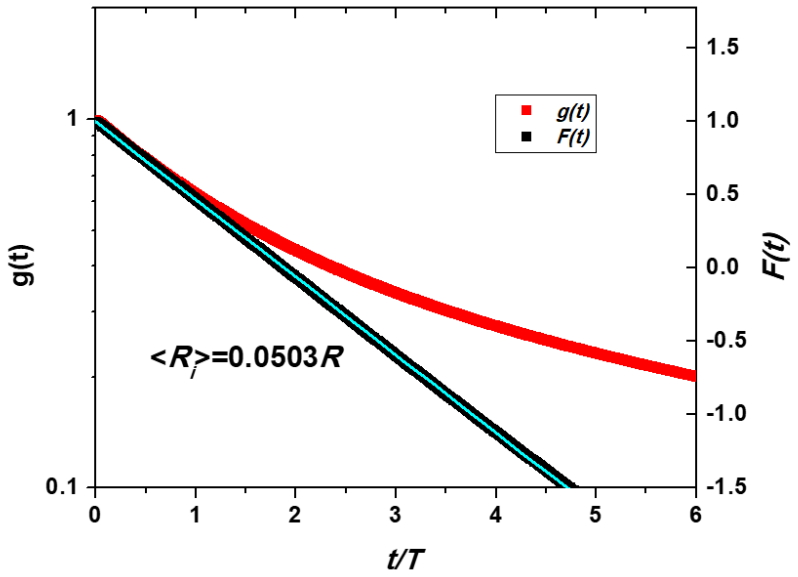

Figure A1. Comparison of the function $F(t)$ given by eq. (A5) with the logarithm of the normalized decay function $ln(g(t))$ in the case of the system with three characteristic relaxation rates $g(t) = \frac{1}{3} * exp(-Rt) + \frac{1}{3} * exp(-0.5Rt) + \frac{1}{3} * exp(-0.01Rt)$. The prolonged linear part of the $F(t)$ time dependence provides a mean value of the relaxation rate $\langle R_i \rangle$.

Bibliography

1. H. Staudinger, European Journal of Inorganic Chemistry, 53(6), 1073 (1920)
2. W. Kuhn, Kolloid-Z, 76, 258 (1936)
3. W. Kuhn, Kolloid-Z, 87, 3 (1939)
4. P.J. Flory, Principles of Polymer Chemistry. Cornell University Press, Ithaca (1953)
5. P.J. Flory, Statistical Mechanics of Chain Molecules, Interscience, New York (1969)
6. M.V. Volkenstein. The configurational statistics of polymeric chains. Journal of Polymer Science Part A: Polymer Chemistry, 29(120), 441 (1958)
7. H. Yamakawa Modern theory of polymer solutions. Harper & Row (1971)
8. J.D. Ferry, Viscoelastic properties of polymers. John Wiley & Sons (1980)
9. W. Schärtl, Light scattering from polymer solutions and nanoparticle dispersions. Springer Science & Business Media (2007)
10. J.S. Higgins, H.C. Benoit, Polymers and Neutron Scattering. United Kingdom: Clarendon Press (1994)
11. L.E. Alexander, X-ray Diffraction Methods in Polymer Science. John Wiley & Sons (1969)
12. M. Rubinstein, R.H. Colby. Polymer physics. Oxford University Press, New York (2003)
13. J.E. Mark, Physical Properties of Polymers Handbook. Springer, New York (2007)
14. W. Kuhn, Kolloid-Z, 68, 2 (1934)
15. O. Kratky, G. Porod, Rec. Trav. Chim. Pays-Bas, 68, 1106 (1949)
16. P.G. de Gennes, Scaling Concepts in Polymer Physics, Cornell University Press (1979)
17. M. Doi, S.F. Edwards, The Theory of Polymer Dynamics, Oxford University Press, New York (1986)
18. A.Y. Grosberg, A.R. Khoklov, Statistical Physics of Macromolecules, AIP Press (1994)
19. A. Yamamoto, M. Fujii, G. Tanaka, H. Yamakawa, Polymer Journal, 2(6), 799 (1971)
20. M. Fukuda, M. Fukutomi, Y. Kato, T. Hashimoto, Journal of Polymer Science Part B: Polymer Physics, 12(5), 871 (1974)
21. Y. Miyaki, Y. Einaga, H. Fujita, Macromolecules, 11(6), 1180 (1978)
22. V.A. Kargin, G.L. Slonimskii, Journal Fizhimii (USSR), 23, 563 (1949)
23. P.J. Rouse, Journal of Chemical Physics, 21, 1272 (1953)
24. L.D. Landau, E.M. Lifshitz, Course of theoretical physics, vol 1. Butterworth-Heinemann, Burlington (1976)
25. R. Kimmich, N. Fatkullin, Polymer Chain Dynamics and NMR. NMR, 3D Analysis, Photopolymerization. Springer Berlin Heidelberg, pp. 1-113, (2004)
26. N. Fatkullin, R. Kimmich, H.W. Weber, Physical Review E 47.6, 4600 (1993)
27. H.W. Weber, R. Kimmich, Macromolecules 26, 2597 (1993)
28. C. Mattea, N. Fatkullin, E. Fischer, U. Beginn, E. Anoardo, M. Kroutieva, R. Kimmich, Applied Magnetic Resonance, 27, 371 (2004)
29. S. Kariyo, A. Brodin, C. Gainaru, A. Herrmann, J. Hintermeyer, H. Schick, V.N. Novikov, E.A. Rössler, Macromolecules, 41(14), 5313 (2008)
30. E.A. Rössler, S. Stapf, N. Fatkullin, Current Opinion in Colloid and Interface Science, 18(3), 172 (2013)

31. G. Fleischer, Colloid & Polymer Science, 265 (2), 89 (1987)
32. P.J. Flory, Journal of Chemical Physics, 17, 303 (1949)
33. T.G. Fox, P.J. Flory, Journal of Chemical Physics, 53, 197 (1949)
34. B.H. Zimm, The Journal of Chemical Physics 24, 269 (1956)
35. J. G. Kirkwood, J. Riseman, The Journal of Chemical Physics, 16, 565 (1948)
36. T.A. Knox, W.I. Lee, J.D.G. McAdam, Polymer 14 (4), 151 (1973)
37. C.C. Han, A.Z. Akcasu, Macromolecules, 14(4), 1080 (1981)
38. L.J. Fetters, D.J. Lohse, D. Richter, T.A. Witten, A. Zirkel, Macromolecules, 27(17), 4639 (1994)
39. S.F. Edwards, Proceedings of the Physical Society, 92(1), 9 (1967)
40. P.G. de Gennes, The Journal of Chemical Physics, 55(2), 572. (1971)
41. M. Doi, S.F. Edwards, J. Chem. Soc., Faraday Trans. 2 74, 1789 (1978)
42. G.C. Berry, T.G. Fox, Advances in Polymer Science, 5, 261 (1968)
43. A. Casale, R.S. Porter, J.F. Johnson, J. Macromol. Sci. Rev. Macromol. Chem. C5, 387 (1971)
44. J. Klein, Nature, 271 (5641), 143 (1978)
45. G. Fleischer, Polymer Bulletin, 11(1), 75 (1984)
46. R. Bachus, R. Kimmich, Polymer, 24(8), 964 (1983)
47. C.R. Bartels, B. Crist, W.W. Graessley, Macromolecules, 17(12), 2702 (1984)
48. A. Wischnewski, M. Monkenbusch, L. Willner, D. Richter, G. Kali, Physical Review Letters 90(5), 58302 (2003)
49. A. Lozovoi, C. Mattea, M. Hofmann, K. Saalwächter, N. Fatkullin, S. Stapf, Journal of Chemical Physics 146 (22), 224901 (2017)
50. B. Kresse, M. Hofmann, A.F. Privalov, N. Fatkullin, F. Fujara, E.A. Rössler, Macromolecules 48(13), 4491 (2015)
51. M. Hofmann, B. Kresse, A.F. Privalov, L. Heymann, L. Willner, N. Aksel, N. Fatkullin, F. Fujara, E.A. Rössler, Macromolecules 49, 7945 (2016)
52. M.Kehr, N. Fatkullin, R. Kimmich, J. Chem. Phys. 126, 094903 (2007)
53. A. Lozovoi, C. Mattea, N. Fatkullin, S. Stapf (submitted)
54. R. Kimmich, R. Bachus, Colloid & Polymer Science, 260, 911 (1982)
55. A. Denissov, M. Kroutieva, N. Fatkullin, R. Kimmich, Journal of Chemical Physics 116, 5217 (2002)
56. R. Kimmich, R.-O. Seitter, U. Beginn, M. Möller, N. Fatkullin, Chem Phys Letters 307, 147 (1999)
57. M. Doi, J. Polym. Sci, Polym. Lett. Ed., 19, 265 (1981)
58. P.G. de Gennes, Macromolecules, 9, 587 (1976)
59. W.W. Graessley, Advances in Polymer Science, 47, 847 (1980)
60. R. Kimmich, Principles of Soft-Matter Dynamics, Springer Science & Business Media (2012)
61. K.S. Schweizer, The Journal of Chemical Physics, 91, 5802 (1989)
62. K.S. Schweizer, The Journal of Chemical Physics, 91, 5822 (1989)
63. R. Zwanzig, Annu. Rev. Phys. Chem, 16, 67 (1965)
64. H. Mori, Prog. Theor. Phys. 33, 423 (1965)
65. N. Fatkullin, R. Kimmich, The Journal of Chemical Physics, 101, 822 (1994)
66. W. Gerlach, O. Stern, Zeitschrift für Physik, 9, 349 (1922)
67. N. Bohr, Philosophical Magazine, 26, 1 (1913)

68. I.I. Rabi, J.R. Zacharias, S. Millman, P. Kusch, Physical Review, 53, 318 (1938)
69. F. Bloch, W.W. Hansen, M. Packard, Physical Review, 69, 127 (1946)
70. E.M. Purcell, H.C. Torrey, R.V. Pound, Physical Review, 69, 37 (1946)
71. A. Abragam, The principles of nuclear magnetism (No. 32). Oxford university press (1961)
72. C.P. Slichter, Principles of magnetic resonance. Springer Science & Business Media (2013)
73. M.H. Levitt, Spin dynamics: basics of nuclear magnetic resonance. John Wiley & Sons (2001)
74. L.D.Landau, E.M. Lifschitz, Quantum Mechanics: Non-relativistic Theory 3rd ed, Oxford (1977)
75. F. Bloch, Physical Review, 70, 460 (1946)
76. J.H. Van Vleck, Physical Review, 74(9), 1168 (1948)
77. R.K. Wangness, F. Bloch, Physical Review, 89, 728 (1953)
78. F. Bloch, Physical review, 102, 104 (1956)
79. F. Bloch, Physical review, 105, 1206 (1957)
80. A.J. Redfield, IBM Journal of research and Development, 1, 1 (1957)
81. M. Mehring, Principles of High Resolution NMR in Solids, 2nd ed, Springer-Verlag, Berlin, Heidelberg, New York (1983).
82. N. Bloembergen, E.M. Purcell, R.V. Pound, Physical Review, 73, 679 (1948)
83. E.L. Hahn, Physical review, 80(4), 580 (1950)
84. H.Y. Carr, E.M. Purcell, Physical review, *94*(3), 630 (1954)
85. S. Meiboom, D. Gill, Review of scientific instruments, 29(8), 688 (1958)
86. J.G. Powles, P. Mansfield, Physics Letters, 2(2), 58 (1962)
87. R. Kimmich, NMR: tomography, diffusometry, relaxometry. Springer Science & Business Media (2012)
88. R. Kimmich, Bulletin of Magnetic Resonance 1, 195 (1980)
89. F. Noack, Progress in Nuclear Magnetic Resonance Spectroscopy, 18, 171 (1986)
90. R. Kimmich, E. Anoardo, Progress in Nuclear Magnetic Resonance Spectroscopy, 44(3), 257 (2004)
91. G. Bodenhausen, Progress in NMR Spectroscopy, 14, 137 (1981)
92. J. Baum, A. Pines, Journal of the American Chemical Society, 108 (24), 7447 (1986)
93. K. Saalwächter, Progress in Nuclear Magnetic Resonance Spectroscopy, 51(1), 1 (2007)
94. K. Saalwächter, ChemPhysChem, 14(13), 3000 (2013)
95. W.S. Warren, D.P. Weitekamp, A. Pines, The Journal of Chemical Physics, *73*(5), 2084 (1980)
96. K. Saalwächter, P. Ziegler, O. Spyckerelle, B. Haidar, A. Vidal, J.U. Sommer, The Journal of Chemical Physics, 119(6), 3468 (2003).
97. M.G. Brereton, Macromolecules, 22(13), 3667 (1989)
98. J.P. Cohen-Addad, Progress in Nuclear Magnetic Resonance Spectroscopy, 25, 1 (1993)
99. R. Kimmich, N. Fatkullin, R.-O. Seitter, K. Gille, The Journal of Chemical Physics, 108, 2173 (1998)
100. M. Kehr, N. Fatkullin, R. Kimmich, The Journal of Chemical Physics, 126, 094903 (2007)
101. M. Kehr, N. Fatkullin, R. Kimmich, The Journal of Chemical Physics, 127, 084911 (2007)
102. N. Fatkullin, Journal of Experimental and Theoretical Physics 72, 563 (1991)
103. E. Fischer, R. Kimmich, N. Fatkullin, The Journal of Chemical Physics, 106,9883 (1997)
104. N. Fatkullin, A. Gubaidullin, S. Stapf, The Journal of Chemical Physics, 132, 094903 (2010)

105. N. Fatkullin, A. Gubaidullin, C. Mattea, S. Stapf, The Journal of Chemical Physics, 137, 224907 (2012)
106. R. Kimmich, N. Fatkullin, Progress in Nuclear Magnetic Resonance Spectroscopy, 101, 18 (2017)
107. N. Fatkullin, C. Mattea, S. Stapf, The Journal of Chemical Physics, 139, 194905 (2013)
108. A. Lozovoi, C. Mattea, A. Herrmann, E.A. Rössler, S. Stapf, N. Fatkullin, The Journal of Chemical Physics, 144(24), 241101 (2016)
109. A. Lozovoi, L. Petrova, C. Mattea, S. Stapf, E.A. Rössler, N. Fatkullin, The Journal of Chemical Physics, 147(7), 074904 (2017)
110. M.G. Brereton, Macromolecules 23, 1119 (1990)
111. J.P. Cohen-Addad, R. Vogin, Physical Review Letters, 33(16), 940 (1974)
112. J. Collignon, H. Sillescu, H. W. Spiess, Colloid and Polymer Science 259(2), 220, (1981)
113. P.T. Callaghan, E. T. Samulski, Macromolecules 30(1), 113 (1997)
114. R.C. Ball, P.T. Callaghan, E.T. Samulski, The Journal of Chemical Physics 106 7352 (1997)
115. P.W. Anderson, P.R. Weiss, Reviews of Modern Physics, 25, 269 (1953)
116. M. J. Bayro, M. Huber, R. Ramachandran, T. C. Davenport, B. H. Meier, M. Ernst, R.G. Griffin, The Journal of Chemical Physics, 130, 114506 (2009)
117. T.C.B. McLeish, Advances in Physics, 51(6), 1379 (2002)
118. G. Strobl, The Physics of Polymers, Springer-Verlag Berlin, Heidelberg (2007)
119. B. Schmidtke, M. Hofmann, A. Lichtinger, E.A. Rössler, Macromolecules, 48(9), 3005 (2015)
120. S. Kariyo, S. Stapf, B. Blümich, 5, 206(13):1292 (2005)
121. R. Graf, A. Heuer, H.W. Spiess, Physical review letters, 80, 5738 (1998)
122. F.V. Chávez, K. Saalwächter, Physical review letters, 104(19), 198305 (2010)
123. F.V. Chávez, K. Saalwächter, Macromolecules 44(6), 1549 (2011)
124. F.V. Chávez, K. Saalwächter, Macromolecules, 44(6), 1560 (2011)
125. B. Kresse, M. Becher, A.F. Privalov, M. Hofmann, E.A. Rössler, M. Vogel, F. Fujara, Journal of Magnetic Resonance, 277, 79–85 (2017)
126. M. Hofmann, B. Kresse, A.F. Privalov, L. Heymann, L.Willner, N. Aksel, N. Fatkullin, F. Fujara, E.A. Rössler, Macromolecules 49(20), 7945(2016)
127. M. Hofmann, B. Kresse, L. Heymann, A.F. Privalov, L. Willner, N.Fatkullin, N. Aksel,F. Fujara, E.A.Rössler, Macromolecules 49(22), 8622 (2016).
128. P.T. Callaghan, Principles of Nuclear Magnetic Resonance Microscopy, Oxford University Press, (1993)
129. E. Fischer, R. Kimmich, N. Fatkullin, The Journal of Chemical Physics, 106, 9883 (1997)
130. F. Mezei, The principles of neutron spin echo, Neutron Spin Echo, 1 (1980).
131. D. Richter, M. Monkenbusch, A. Arbe, J. Colmenero, Advances in Polymer Science, 174, 1 (2005).
132. E.R. Santee, R. Chang, M. Morton, Journal of Polymer Science Part C: Polymer Letters, 11(7), 449 (1973)
133. H. Raich, P. Blümler, Concepts in Magnetic Resonance Part B: Magnetic Resonance Engineering, 23(1), 16 (2004)
134. K. Halbach, Nuclear Instruments and Methods 169(1), 1 (1980)

135. B.D. Armstrong, M.D. Lingwood, E.R. McCarney, E.R. Brown, P. Blümler, S. Han, Journal of Magnetic Resonance, 191(2), 273 (2008)
136. A. Wischnewski, M. Monkenbusch, L. Willner, D. Richter, G. Kali, Physical Review Letterrs 90(5), 58302 (2003)
137. M. Flämig, M. Becher, M. Hofmann, T. Körber, B. Kresse, A.F. Privalov, L. Willner, D. Kruk, F. Fujara, E.A. Rössler, J. Phys. Chem. B 120, 7754 (2016)
138. F. Furtado, J. Damron, M.-L. Trutschel, C. Franz, K. Schröter, R. C. Ball, K. Saalwaechter, D. Panja, Macromolecules 47(1), 256 (2014)
139. F.E. Bailey Jr, G.M. Powell, K.L. Smith, Industrial and Engineering Chemistry Research, 50 (1), 8 (1958)
140. R. Kimmich, R.O. Seitter, U. Beginn, M. Möller, N. Fatkullin, Chemical physics letters, 307(3), 147. (1999)
141. E. Fischer, R. Kimmich, U. Beginn, M. Moller, N. Fatkullin, Physical Review E, 59, 4079 (1999)
142. G.D. Smith, D.Y. Yoon, R.L. Jaffe, R.H. Colby, R. Krishnamoorti, L.J. Fetters, Macromolecules, 29, 3462 (1996)
143. M. Roland, Viscoelastic Behaviour of Rubbery Materials, Oxford University Press (2011)
144. E. Fischer, R. Kimmich, N. Fatkullin, G. Yatsenko, Physical Review E, 62, 775 (2000)
145. D.S. Pearson, G. Ver Strate, E. von Meerwall, F.C. Schilling, Macromolecules, 20(5), 1133 (1987)
146. D.S. Pearson, L.J. Fetters, W.W. Graessley, G. Ver Strate, E. von Meerwall. Macromolecules 27, 3, 711 (1994)
147. M. Appel, G. Fleischer, Macromolecules, 26(20), 5520 (1993)